

# MAGNETOM Flash

Issue Number 79 · 2/2021  
RSNA Edition

[siemens-healthineers.com/magnetom-world](https://siemens-healthineers.com/magnetom-world)

Page 4

Editorial Comment

**The Roadmap to 10-fold**

**Accelerated Routine**

**Musculoskeletal MRI Exams**

*Jan Fritz*

Page 23

**Clinical Implementation of Deep Learning-Accelerated HASTE and TSE**

*Judith Herrmann,  
Ahmed Othman, et al.*

Page 28

**Fast and Reliable Liver Imaging Using Deep Learning HASTE**

*Alain Luciani, Sébastien Mulé, et al.*

Page 37

**Accelerated 3D T2 SPACE CAIPIRINHA with Iterative Denoising for the Assessment of Deep Infiltrating Endometriosis**

*Lamia Jarboui, et al.*

Page 45

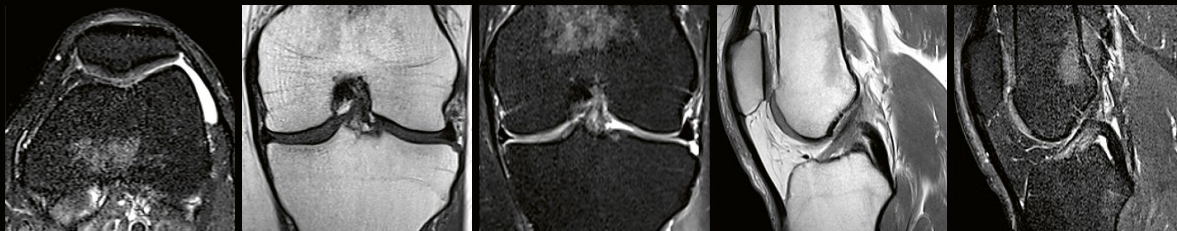
**Clinical Utility of High-Bandwidth Inversion Recovery Sequences in Patients with Cardiac Implanted Electronic Devices**

*Hajnalka Vágó, et al.*

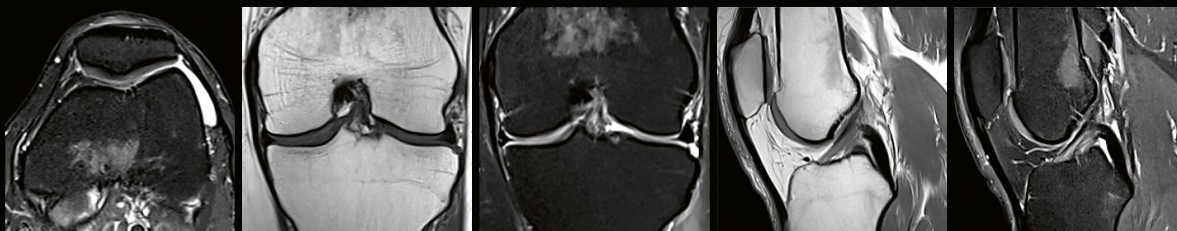
Page 66

**Ultrafast Brain Imaging with Deep Learning Multi-Shot EPI**

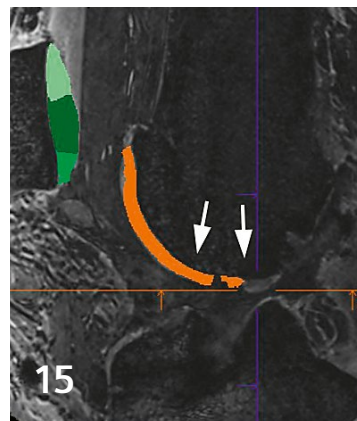
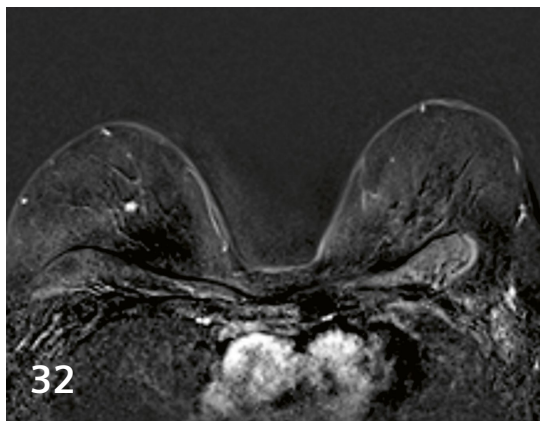
*John Conklin, et al.*



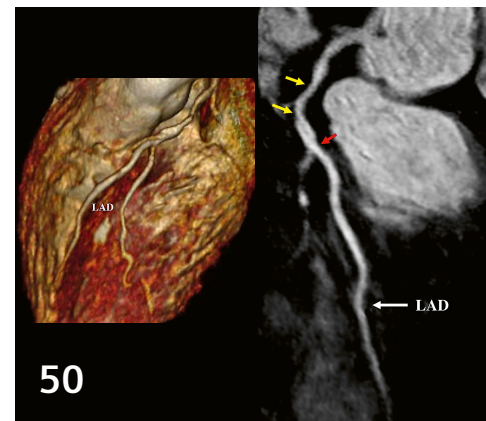
↓ Deep Learning Image Reconstruction ↓



6-fold SMS2-PAT3 Accelerated Turbo Spin-Echo MRI

MR Chondral Health<sup>1</sup>

MR Mammography

Coronary MR Angiography<sup>1</sup>

## Editorial Comment

- 4 Boldly Going Where No One Has Gone Before – The Roadmap to 10-fold Accelerated<sup>1</sup> Routine Musculoskeletal MRI Exams**

Jan Fritz

New York University, Grossman School of Medicine,  
NYU Langone Health, New York, NY, USA

## Musculoskeletal Imaging

- 15 Initial Experience with Automatic Knee Cartilage Segmentation using MR Chondral Health<sup>1</sup>**

Vladimir Juras, Siegfried Trattnig, et al.

High Field MR Centre, Medical University of Vienna,  
Austria

- 23 Clinical Implementation of Deep Learning-Accelerated HASTE<sup>1</sup> and TSE**

Ahmed Othman, Judith Herrmann, et al.

University Medical Center, Mainz / Eberhard Karls University Tuebingen, Germany

## Abdominal Imaging

- 28 Fast and Reliable Liver Imaging Using Deep Learning HASTE<sup>1</sup>**

Alain Luciani, Sébastien Mulé, et al.

Hôpitaux Universitaires Henri-Mondor, Crêteil, France

## Women's Health Imaging

- 32 Full-scale vs. Abbreviated Sequences in MR Mammography – The best of both worlds**

Clemens Kaiser

University Medical Center Mannheim, Germany

- 37 Accelerated 3D T2 SPACE CAIPIRINHA with Iterative Denoising<sup>1</sup> for the Assessment of Deep Infiltrating Endometriosis**

Lamia Jarboui, et al.

Centre Imagerie du Nord, Clinique du Landy, Ramsay-Générale de Santé, Saint-Ouen, France

## Cardiovascular Imaging

- 45 Clinical Utility of High-Bandwidth Inversion Recovery Sequences in Patients with Cardiac Implanted Electronic Devices**

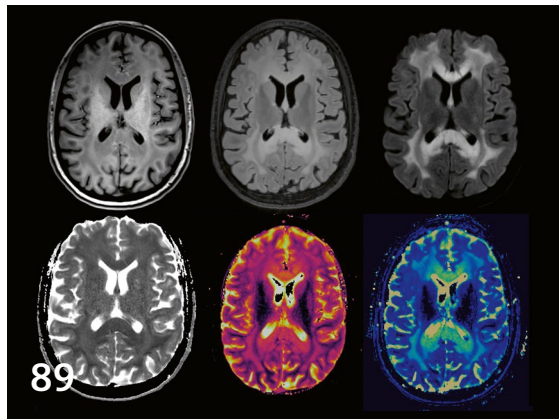
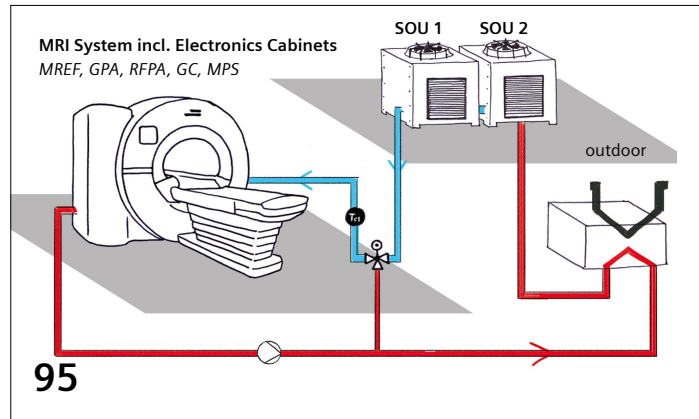
Hajnalka Vágó, et al.

Semmelweis University, Heart and Vascular Center, Budapest, Hungary

- 50 High Spatial Resolution Coronary Magnetic Resonance Angiography<sup>1</sup>: A Single Center Experience**

Reza Hajhosseiny, René M. Botnar, et al.

School of Biomedical Engineering and Imaging Sciences, King's College London, United Kingdom

Quantitative neuroimaging with MR Fingerprinting<sup>2</sup>

Cooling system of DryCool magnets

## Neurologic Imaging

- 60 Updates on Advanced Whole-Brain Vessel Wall Imaging in Stroke Patients**  
Qi Yang, et al.  
Beijing Chaoyang Hospital, Capital Medical University, Beijing, China
- 66 Ultrafast Brain Imaging with Deep Learning Multi-Shot EPI<sup>1</sup>: Preliminary Clinical Evaluation**  
John Conklin, et al.  
Massachusetts General Hospital, Boston, MA, USA
- 71 A Comparison of Post-Contrast 3D T1 SPACE, 3D SPACE FLAIR, and 3D T1 MPRAGE Sequences in Various Brain Parenchymal and Meningeal Pathologies at 3T MRI**  
S. Babu Peter  
Rajiv Gandhi General Hospital, Chennai, India
- 79 T1 Relaxation-Enhanced Steady-State (T1RESS)<sup>1</sup>: An Improved Three-Dimensional Method for Contrast-Enhanced Imaging of Brain Tumors**  
Robert R. Edelman, et al.  
NorthShore University HealthSystem, Evanston, IL, USA
- 83 HASTE Diffusion-weighted Imaging at 3 Tesla: Evaluation of Non-EPI Diffusion for the Detection of Cholesteatomas**  
Thomas Troalen, Frederik Testud, et al.  
Siemens Healthineers

## 89 Magnetic Resonance Fingerprinting<sup>2</sup> – The Future of Quantitative MR Neuroimaging

Gregor Kasprian, Victor Schmidbauer

Department of Biomedical Imaging and Image-guided Therapy, Medical University of Vienna, Austria

## Technology

### 95 MAGNETOM Free.Max: Keeping a Hot System Cool

Stephan Biber

Siemens Healthineers, Erlangen, Germany

## Meet Siemens Healthineers

### 99 Introducing Cheng Shi

Application development at 0.55T

Siemens Healthineers, Shenzhen, China

Cover courtesy of Jan Fritz, M.D., P.D., D.A.B.R., R.M.S.K. New York University, Grossman School of Medicine, NYU Langone Health, Department of Radiology, New York, NY, USA

<sup>1</sup> Work in progress. The application is currently under development and is not for sale in the U.S. and in other countries. Its future availability cannot be ensured.

<sup>2</sup> MR Fingerprinting is not commercially available in some countries. Due to regulatory reasons its future availability cannot be ensured.



**Jan Fritz, M.D.**, is a full-time musculoskeletal radiologist, Associate Professor, and the Division Chief of Musculoskeletal Radiology at the NYU Grossman School of Medicine in New York City, USA. His research and practice focus on the development and clinical integration of novel and rapid musculoskeletal MRI techniques, metal artifact reduction MRI, MR Neurography, interventional MR imaging, and machine learning techniques. He has authored over 200 peer-reviewed scientific articles, reviews, and book chapters, and has lectured at many national and international meetings. He serves on the editorial boards of *Skeletal Radiology*, *Current Radiology Reports*, *PlosONE*, and *Investigative Radiology*.

# Boldly Going Where No One Has Gone Before – The Roadmap to 10-fold Accelerated Routine Musculoskeletal MRI Exams

*“One man cannot summon the future.”*

– Lt. Cmdr. S'chn T'gai Spock

*“But one man can change the present!”*

– Capt. James Tiberius Kirk

Have you ever wondered about the excitement that Captain James T. Kirk, Kathryn Janeway, Jonathan Archer, Jean-Luc Picard, and their crews felt onboard a brand-new starship equipped with disruptive new technologies, ready to embark on a pioneering mission to *boldly go where no one has gone before?*

The Star Trek saga is built on quantum-leap-type technological advances that symbolize gatekeepers and door openers to new horizons in space and time. With every technological advancement, such as fusion reactor plasma-driven impulse engine, spacetime continuum-distorting warp-field drive, or organic displacement-activated mycelial spore network propulsion – Starfleet and the United Federation of Planets overcame boundaries, crossed distant frontiers, and reached new horizons.

The evolution of MRI has notable similarities. Multiple significant technological advancements have overcome

technological boundaries and have successfully translated into clinical MRI applications that have continuously improved patient care. In terms of hardware, these advances include 3T field strength, high-gain receiver chains, high-performance gradients, fast radiofrequency pulse techniques, multi-channel technology, and high-density surface coil technologies [1]. In terms of pulse sequences, they include fast and turbo spin-echo acquisition techniques [2], parallel imaging acceleration [3], and simultaneous multi-slice acquisition [4].

While time and the time-space continuum are constants for us, a deep dive into the building blocks of the value of MRI identifies scan efficiency as central to almost every value component. MRI efficiency is a cornerstone for growing the availability and accessibility of MRI worldwide, improving the tolerability for patients undergoing MRI scans, limiting degrading motion artifacts

on MR images, reducing the need for sedation and anesthesia in pediatric patients<sup>1</sup>, decreasing contact and patient dwell times during the COVID-19 pandemic, and augmenting throughput for busy academic institutions and private centers [5].

At the dawn of this new decade image reconstruction and post-processing techniques artificial intelligence (AI) and machine learning mark the next technological breakthrough and affect almost every aspect of MRI [6] (Fig. 1).

Particularly machine-learning-based image reconstruction and post-processing technologies will permit never-before-seen gains in scan-time efficiency and image-quality enhancements and further potentiate synergies with existing acceleration strategies, including echo-train compaction, parallel imaging, and simultaneous multi-slice acquisitions [5, 7].

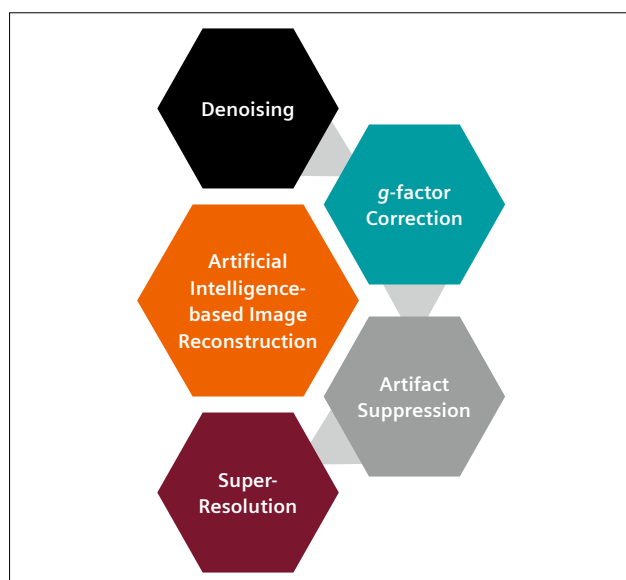
Musculoskeletal MRI has achieved extraordinary gains in efficiency and image quality over the past decade with substantial contributions coming from the now widely used 3T field strength, high-performance surface coils, and the combined use of advanced acceleration techniques with fast and turbo spin-echo pulse sequences, which are essentially part of every musculoskeletal MRI protocol [1]. Effective and optimized use of these technologies is fundamental to maximizing the gains of machine-learning-based MRI.

For example, the optimized combined use of parallel imaging and simultaneous multi-slice now permits clinically

available 4-fold accelerated musculoskeletal turbo spin-echo MRI in any contrast variation [4, 8]. This includes T1-weighted, proton density-, intermediate-, and T2-weighted tissue contrast, and multiple fat suppression techniques, including spectral, Dixon, and inversion-recovery fat suppression. Combining the above techniques with machine-learning-based image reconstruction will unlock multiple synergies, with 8-fold and even 10-fold accelerated turbo spin-echo pulse sequences in stellar image quality as the next breachable frontier – which could reduce 20-minute MRI exams to under 3 minutes (Table 1).

Imaging scientists and radiologists alike have already embarked on a momentous journey to new horizons in musculoskeletal MRI with unprecedented MRI efficiencies and acquisition speeds. It is my distinct honor to be a crew member on this journey – and even more so to editorialize this fine RSNA edition of MAGNETOM Flash. In addition to shining a spotlight on what is ahead, the purpose of this editorial is to highlight key components for the journey to 10-fold accelerated musculoskeletal turbo spin-echo pulse sequences and to sub-5-minute musculoskeletal MRI exams.

*So, in the spirit of Captain Jean-Luc Picard: "Engage!"*



- 1** Deep neural networks for artificial intelligence-based image reconstructions can include various components based on their training and intended use.

Acceleration Factor	Protocol Time [mm:ss]	Pulse-Sequence Time [mm:ss]
unaccelerated	20:00	04:00
2-fold	10:00	02:00
3-fold	06:40	01:20
4-fold	05:00	01:00
5-fold	04:00	00:48
6-fold	03:20	00:40
7-fold	02:51	00:34
8-fold	02:30	00:30
9-fold	02:13	00:27
10-fold	02:00	00:24

**Table 1:** Effect of acceleration factor on the acquisition times of MRI protocols and pulse sequences.

<sup>1</sup> MR scanning has not been established as safe for imaging fetuses and infants less than two years of age. The responsible physician must evaluate the benefits of the MR examination compared to those of other imaging procedures.

## Resistance is futile: Artificial intelligence-driven image reconstruction

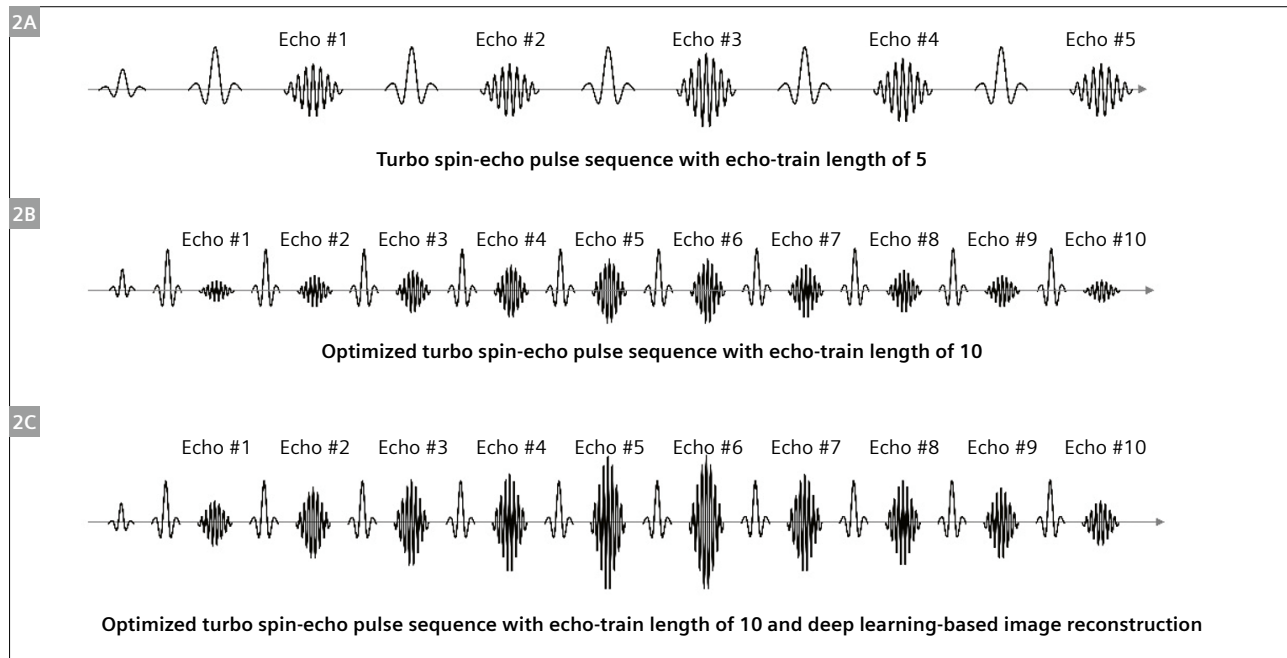
Deep neural networks used for artificial intelligence-based image reconstruction can include various components based on their training and intended use, such as denoising capabilities and *g*-factor corrections to increase the signal-to-noise ratio, artifact suppression techniques to correct aliasing artifacts of parallel imaging and interslice leakage of simultaneous multi-slice acquisition, as well as super-resolution techniques to increase image detail (Fig. 1) [9].

## Make it so: Preparing pulse sequences for new frontiers

Regardless of whether one employs conventional or advanced acquisition schemes, image reconstruction techniques, or post-processing methods, using optimally designed pulse sequences for a specific application (such as a knee MRI protocol) remains fundamental to achieving the fastest scan times (Fig. 2).

In fact, pulse-sequence optimization before applying advanced techniques becomes even more important and rewarding as time savings arising from an optimally played pulse sequence multiply and could even potentiate when applying and combining higher-level acceleration techniques, such as parallel imaging, simultaneous multi-slice acquisition, elliptical scanning, and compressed-sensing-based undersampling. For example, a 10-second time saving achieved through careful optimization of the echo train could multiply to 80 seconds with subsequent 8-fold acceleration.

For musculoskeletal MRI, turbo spin-echo pulse-sequence techniques may be considered the *Bird of Prey*, as their versatility, technical performance, and diagnostic accuracy are unrivaled. Turbo spin-echo pulse sequences are a perfect target for next-generation acceleration because of their ability to generate true T1- and T2-weighted contrasts, and to combine favorably with many techniques, such as 2D and 3D acquisition schemes [10, 11], spectral, Dixon, and short-tau inversion recovery (STIR) fat suppression [12], high-bandwidth, view-angle-tilting (VAT), and SEMAC metal artifact suppression<sup>2</sup> [13], as well as acceler-



**2** Effects of echo-train compaction of a turbo spin-echo pulse sequence and deep learning-based image reconstruction.

(2A) Turbo spin-echo pulse sequence with an echo-train length of five, acquiring five signals for every repetition time.

(2B) Optimized turbo spin-echo pulse sequence via echo-train compaction with fast radiofrequency pulses, high-performance gradients, and high receiver bandwidth permits acquiring ten signals for the same echo-train duration, which constitutes a factor two acceleration compared to the top row sequence.

(2C) The application of deep learning-based image reconstruction effectively results in higher visible signal gains, simplified here as relative gains of echo amplitudes.

<sup>2</sup>The MRI restrictions (if any) of the metal implant must be considered prior to patient undergoing MRI exam. MR imaging of patients with metallic implants brings specific risks. However, certain implants are approved by the governing regulatory bodies to be MR conditionally safe. For such implants, the previously mentioned warning may not be applicable. Please contact the implant manufacturer for the specific conditional information. The conditions for MR safety are the responsibility of the implant manufacturer, not of Siemens Healthineers.

ation methods including parallel imaging, simultaneous multi-slice acquisition [4], and compressed sensing-based sampling [11, 14].

Proton density and intermediate-(PD)-weighted turbo pulse sequences with and without fat suppression are frequently used in musculoskeletal MRI due to their ability to maximize signal gain, to display fluid brightly for reliable detection of edema, inflammation, and collections, and to achieve high-contrast differentiation of ligaments, tendons, and articular and fibrocartilage, which naturally have lower concentrations of protons, and long T1 and short T2 constants.

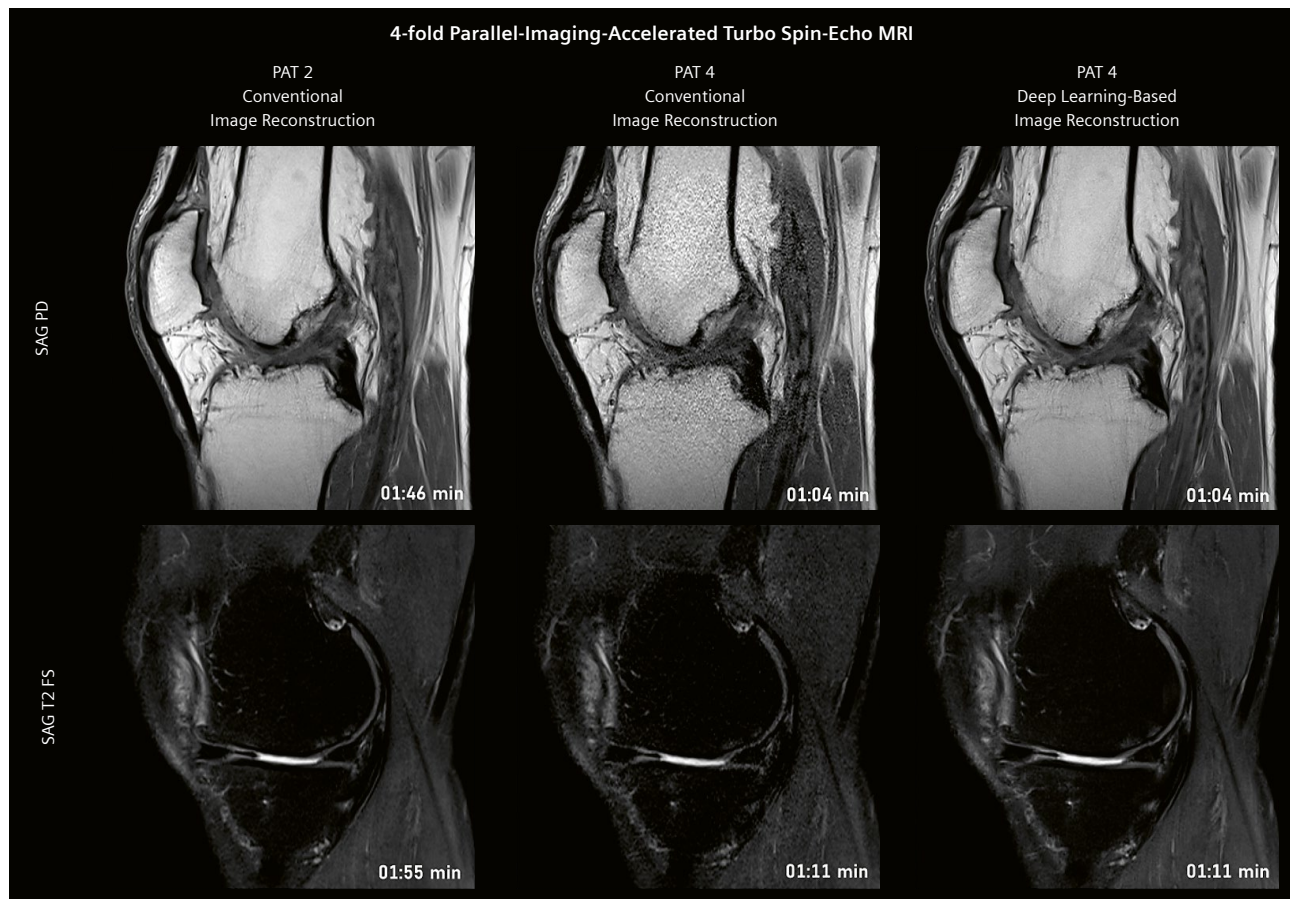
Creating compact echo trains is crucial for optimal turbo spin-echo pulse sequences. Echo-train compaction describes a concept based on optimizing pulse-sequence parameters so that the maximum number of refocusing echoes can be applied in the shortest length of time needed

to complete the echo train, resulting in the sampling of higher signal echoes and minimizing the introduction of image blur (Fig. 2).

The shorter the time between neighboring echoes (echo spacing), the more echoes can be sampled per time unit and within a certain length of time of an echo train. Shortening echo spacing will permit sampling of more echoes in the same length of time, or of the same number of echoes in a shorter time.

The three most important parameters for compacting echo trains are a fast radiofrequency pulse, maximum gradient performance, and high receiver bandwidth. All three factors substantially affect the baseline acquisition time, although they might not be specifically mentioned in commonly used pulse-sequence time equations.

Modern scanners allow users to choose how fast radiofrequency pulses will be executed within a turbo spin-



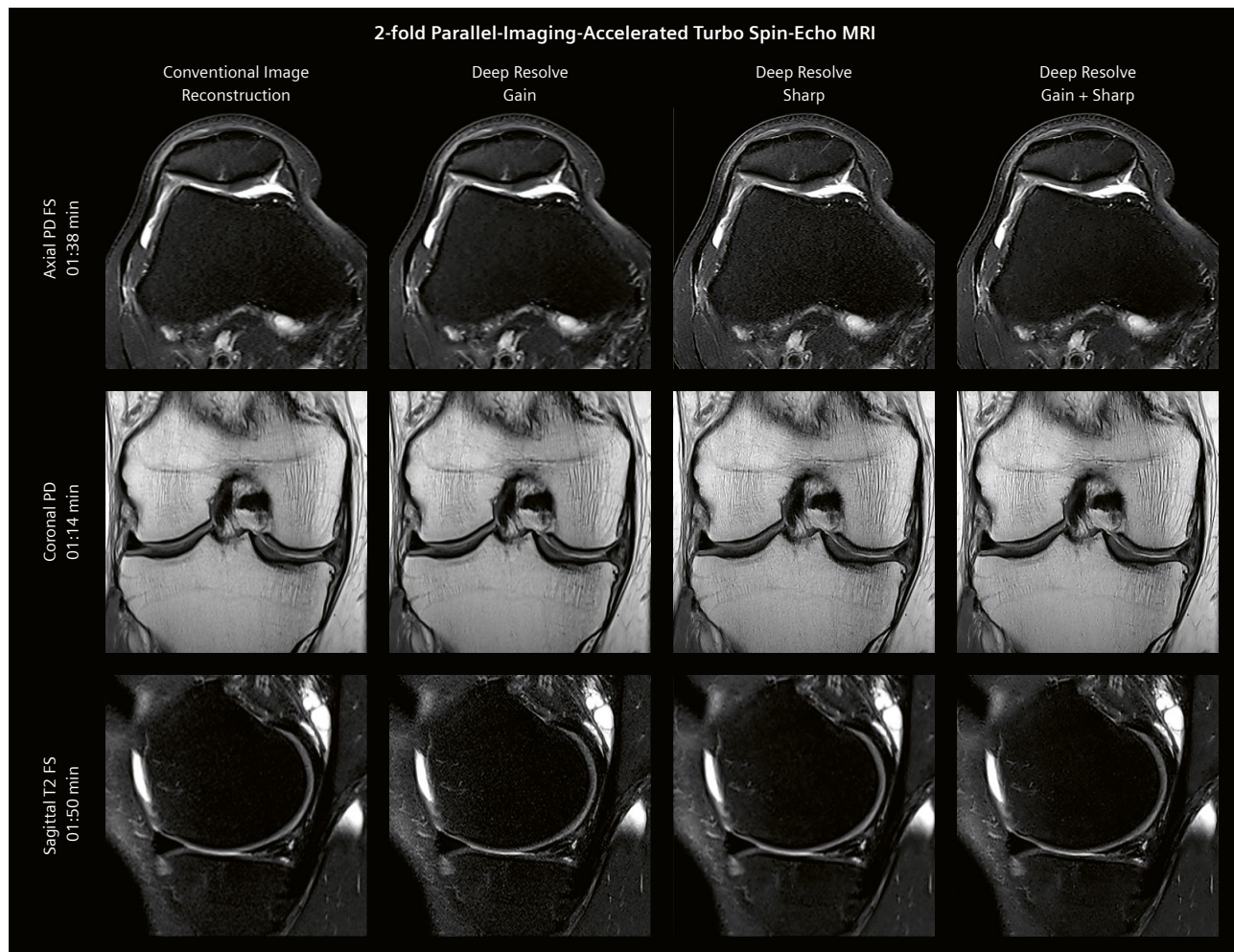
**3** 3-Tesla MRI of the knee with echo-train-compacted turbo spin-echo pulse sequences using 2-fold and 4-fold parallel imaging acceleration (PAT) and conventional and deep learning-based image reconstructions. Application of deep learning-based image reconstruction using an algorithm developed by Facebook AI Research (FAIR) and NYU Langone Health [17] achieves similar or better image quality with 4-fold parallel-imaging-accelerated datasets than 2-fold parallel-imaging-accelerated datasets using conventional image reconstruction. The sagittal PD MR images show a partially torn anterior cruciate ligament. The sagittal fat-suppressed T2-weighted MR images show a torn anterior meniscus segment and high-grade articular cartilage loss of the central femoral condyle. The MR images were obtained with a 3 Tesla MAGNETOM Skyra MRI system and a 1-transmit-channel-15-receiver-channel knee coil. PD = proton density weighting, T2 FS = fat-suppressed T2-weighting, PAT= parallel acquisition technique using GRAPPA (GeneRalized Autocalibrating Partial Parallel Acquisition)

echo pulse sequence. Radiofrequency pulses with shorter durations occupy less time, shorten echo spacing, and result in faster sampling. Compared to slower modes, faster radiofrequency pulses may impart more energy and increase the specific absorption rate (SAR).

The quality of a gradient system is indicated by the gradient speed (slew rate, [T/m/s]) and gradient strength [mT/m], which indicate how quickly and how powerfully gradient effects can be achieved [15]. Modern clinical MRI scanners with slew rates of 150–200 T/m/s and gradient strengths of 35–80 mT/m permit executing turbo spin-echo pulse sequences much faster than previous generations. Gradients have no direct effects on the SAR but may induce nerve-stimulating effects, which are usually well tolerated during musculoskeletal MRI. The “performance” gradient mode now gives users access to the highest gradient performance.

High receiver bandwidths enable faster sampling of MR signals and can therefore substantially contribute to short echo spacing and echo trains. Additional effects that are especially favorable to musculoskeletal MRI and the detection of small abnormalities are reduced chemical shift artifacts and improved sharpness of MR images. High receiver bandwidth results in overall lower strength of the MR signal and reduced SNR. However, the associated shortening of echo spacing leads to an earlier sampling of stronger MR signals, limiting signal losses.

The combined use of high-performance gradients, fast radiofrequency pulses, and high receiver bandwidth can substantially shorten the echo spacing of turbo spin-echo pulse sequences. Short acquisition times translate to shorter possible minimum required repetition times and higher possible echo-train lengths, which lays the foundation for multiplying and potentiating gains with advanced



**4** 3-Tesla MRI of the knee with echo-train-compacted turbo spin-echo pulse sequences using 2-fold parallel imaging acceleration (PAT) and conventional and Deep Resolve image reconstructions. Application of Deep Resolve Gain reduces perceived image noise. Deep Resolve Sharp increases image detail. The MR images show a patellar cartilage fissure and complex meniscus tear. The MR images were obtained with a 3T MAGNETOM Skyra MRI system and a 1-transmit-channel-15-receiver-channel knee coil. Parallel imaging acquisition was performed with GRAPPA (GeneRalized Autocalibrating Partial Parallel Acquisition). PD = proton density weighting, PD FS = fat-suppressed proton density weighting, T2 FS = fat-suppressed T2 weighting

techniques. Carefully optimized turbo spin-echo pulse sequences that employ echo-train compaction can often yield a 2-fold acceleration factor.

## Live long and prosper: Artificial intelligence-driven parallel imaging

Parallel imaging has proven to be one of the most effective and easy-to-use methods of accelerating turbo spin-echo pulse sequences. Based on sensitivity profile encoding of multi-element receiver coils, parallel imaging permits the undersampling of time-consuming phase-encoding steps. Effectively, parallel imaging saves acquisition time by sampling only every second (2-fold acceleration), third (3-fold acceleration), or even fourth (4-fold acceleration) phase-encoding step while keeping the field-of-view, matrix size, and spatial resolution unchanged. The number of omitted phase-encoding steps is proportional to the acceleration factor and will directly reduce the acquisition time (Table 1).

The SNR of an MR image will reduce proportionally to the square root of the acceleration factor. Hence, with conventional image reconstruction, acceleration factors above two often result in a detrimental increase in image noise and additional aliasing artifacts depending on the coil geometry (Fig. 3). Considering  $g$ -factor-related effects, 2-fold, 3-fold, and 4-fold parallel imaging accelerations result in approximately 29–36%, 41–48%, and 50–58% less SNR in musculoskeletal structures, respectively [7].

Deep Resolve is an artificial intelligence-based reconstruction method that combines targeted denoising and deep learning-based image reconstruction by incorporating noise maps acquired with the original data in a time-neutral fashion [16]. Deep Resolve Gain applies advanced denoising by extracting individually heterogeneous noise distributions, regaining SNR to better advantage than conventional denoising techniques. Deep Resolve Sharp utilizes a deep neural network to increase the sharpness of the reconstructed image (Fig. 4).

As a rule of thumb, aliasing artifacts and visible heterogenous noise enhancement are expected to occur when the acceleration factor exceeds the number of coil elements across the phase-encoding direction of the pulse sequence. For example, a parallel imaging acceleration factor of four will likely overwhelm the geometry of an 18-channel knee coil consisting of three rings in head-to-foot direction, and will therefore result in additional aliasing artifacts (Fig. 3).

Deep learning-based image reconstruction techniques that combine intelligent denoising and aliasing correction can reconstruct 4-fold accelerated MR image datasets with higher quality than achieved by conventional image reconstruction algorithms reconstructing 2-fold parallel-imaging-accelerated datasets [17] (Fig. 3).

## Beam me up, Scotty: Artificial intelligence-driven simultaneous multi-slice acceleration

Simultaneous multi-slice acquisition of turbo spin-echo pulse sequences is a key technology for achieving artificial intelligence-based ultrafast musculoskeletal MRI as it favorably combines with parallel imaging acceleration and elliptical scanning, thereby multiplying acceleration factors [4].

While conventional turbo spin-echo pulse sequences obtain slice signals one after the other, simultaneous multi-slice acquisition techniques can acquire signals from multiple slices at the same time. Sharing some similarities with parallel imaging, dedicated deconvolution algorithms such as CAIPIRINHA [18] separate the mixed MR signals from the originating slices, using coil-sensitivity profiles, field-of-view shifts, and gradient encoding.

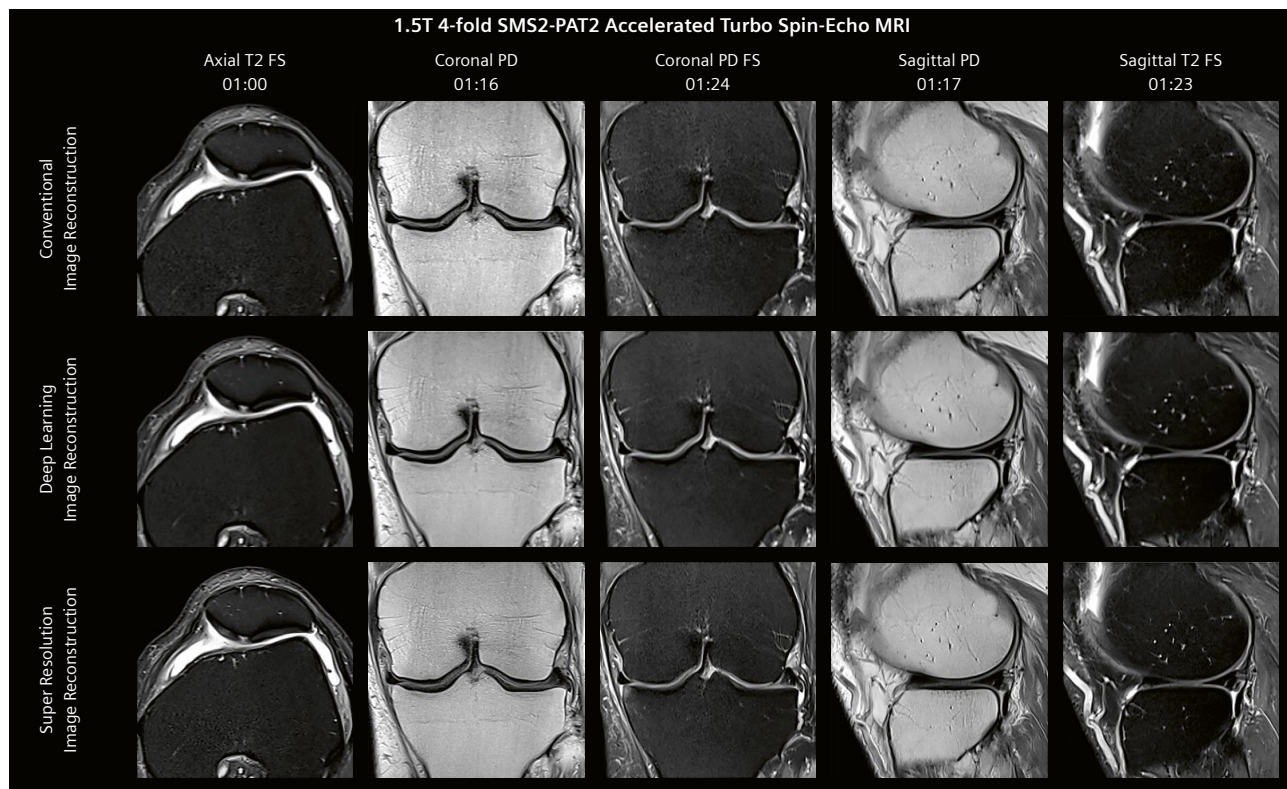
Simultaneous multi-slice acquisition effectively reduces the total repetition time of a multi-slice turbo spin-echo pulse sequence, which translates into direct and indirect time savings, including shorter possible repetition times, obviating concatenations and permitting longer echo trains, simultaneous acquisition of in-phase and opposed-phase echoes within Dixon-based acquisitions, as well as time-neutral use of a higher number of slices or reduction of interslice gaps, and repetition of time-consuming SPAIR fat suppression.

Simultaneous multi-slice acquisition synergizes favorably with parallel imaging acceleration [4]. In contrast to parallel imaging acceleration, simultaneous multi-slice acquisition is linked only to  $g$ -factor-associated signal loss, which is a fraction of the SNR loss of parallel imaging. On the other hand, SMS may result in higher SAR values because of the sum of simultaneously imparted radiofrequency pulses. However, dedicated radiofrequency pulse designs, flip angles of 125–150 degrees, and local transmit coils can substantially reduce SAR levels in peripheral joints.

When used in combination, the acceleration factors contributed by each technique multiply. For example, the combined use of simultaneous multi-slice acquisition and parallel imaging acceleration enables artifact-free, 4-fold accelerated turbo spin-echo acceleration for rapid 5-sequence knee MRI at 1.5T (Fig. 5 and Table 2), and at 3T (Fig. 6 and Table 3) with a much higher average SNR than 4-fold accelerated parallel imaging [8]. Combining deep learning-based image reconstruction with 4-fold accelerated simultaneous multi-slice acquisition and parallel imaging results in substantial SNR gains (Figs. 5, 6)<sup>3</sup>.

Since deep neural networks have already been shown to reconstruct 4-fold parallel-imaging-accelerated datasets with image quality exceeding a conventionally recon-

<sup>3</sup>Work in progress: the application is currently under development and is not for sale in the U.S. and in other countries. Its future availability cannot be ensured.

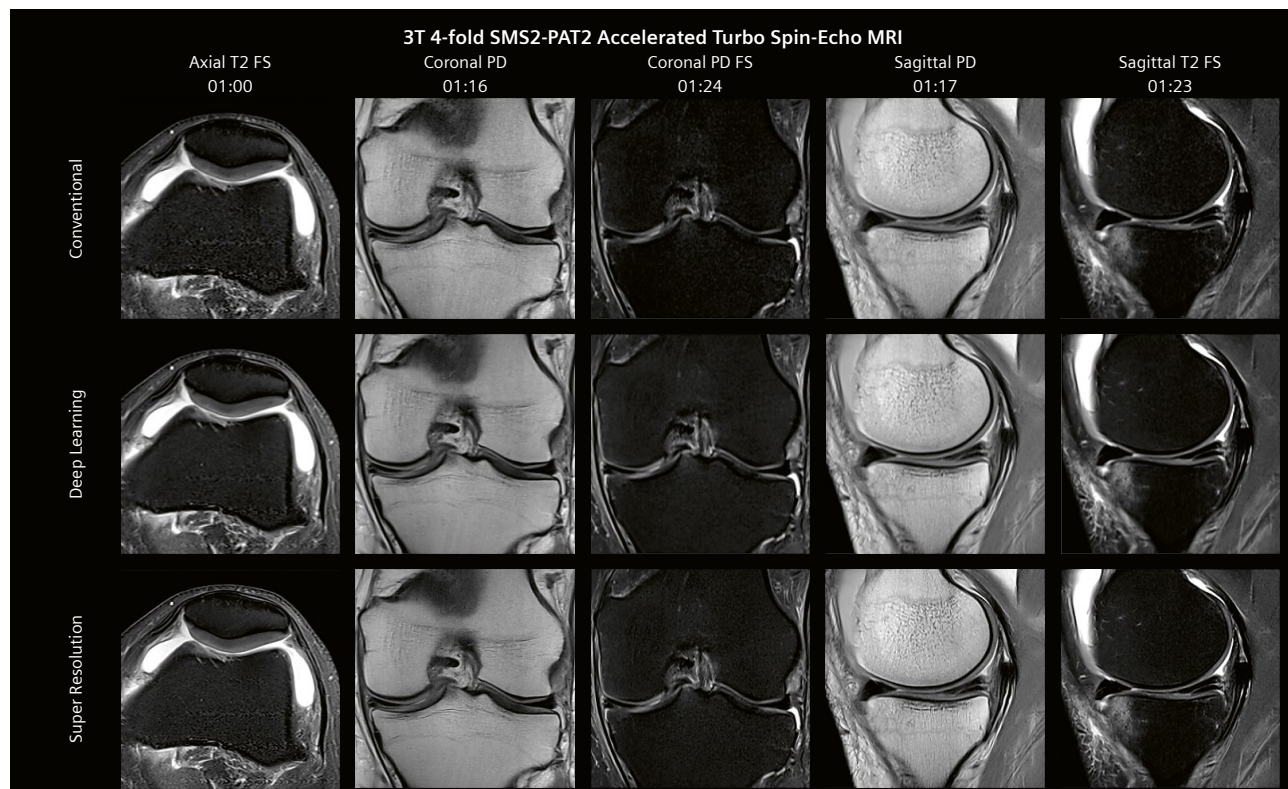


**5** 1.5-Tesla MRI of the knee with echo-train-compacted turbo spin-echo pulse sequences using combined 2-fold parallel imaging and 2-fold simultaneous multi-slice acquisition acceleration and conventional and deep learning image reconstructions<sup>3</sup>. Application of deep learning-based image and super-resolution reconstruction substantially decreases image noise, increases perceived signal and contrast, and increases image detail. The MR images show a patellar cartilage defect and lateral meniscus tear with a displaced fragment in the inferior meniscosynovial recess. The MR images were obtained with a 1.5T MAGNETOM Sola MRI system and a 1-transmit-channel-18-receiver-channel knee coil. The MRI protocol is given in Table 2. PD = proton density weighting, PD FS = fat-suppressed proton density weighting, T2 FS = fat-suppressed T2 weighting

Parameter	Ax T2 FS	Cor PD	Cor PD FS	Sag PD	Sag T2 FS
Repetition/echo time [ms]	4000/54	4000/37	3500/31	4000/37	4000/53
PI	2	2	2	2	2
SMS / FOV shift	2/2	2/2	2/2	2/2	2/2
Echo-train length	14	11	11	15	14
Bandwidth (Hz/px)	159	200	159	200	159
Echo spacing [ms]	10.8	9.31	10.3	9.31	10.6
FOV [mm]	160 × 160	160 × 160	160 × 160	160 × 160	160 × 160
Voxel size [mm]	0.55 × 0.69 × 3.0	0.45 × 0.56 × 3.0	0.56 × 0.69 × 3.0	0.45 × 0.56 × 3.0	0.56 × 0.69 × 3.0
Slices	40	40	40	36	36
Concatenations	1	1	1	1	1
Phase direction	right-to-left	right-to-left	head-to-foot	head-to-foot	head-to-foot
Acquisition time [mm:ss]	00:58	00:55	01:18	01:18	01:11

**Table 2:** NYU 1.5-Tesla 4-fold SMS2-PAT2 accelerated knee MRI protocol.

Ax = axial, Cor = coronal, sag = sagittal, PD = proton density weighted, FS = fat suppression, PI = parallel imaging acceleration factor, SMS = simultaneous multislice acquisition acceleration factor, TSE = turbo spin-echo, FOV = field-of-view



**6** 3-Tesla MRI of the knee with echo-train compacted turbo spin echo pulse sequences using combined 2-fold parallel imaging and 2-fold simultaneous multi-slice acquisition acceleration and conventional and deep learning image reconstructions<sup>3</sup>. Application of deep learning-based image and super-resolution reconstruction substantially decreases image noise, increases perceived signal and contrast, and increases image detail. The MR images show intact patellar articular cartilage and a nondisplaced horizontal medial meniscus tear. The MR images were obtained with a 3 Tesla MAGNETOM Vida MRI system and 1-transmit-channel-18-receiver-channel knee coil. The MRI protocol is given in Table 3. PD = proton density weighting, PD FS = fat-suppressed proton density weighting, T2 FS = fat-suppressed T2 weighting

Parameter	Ax T2 FS	Cor PD	Cor PD FS	Sag PD	Sag T2 FS
Repetition/echo time [ms]	3600/57	4000/23	4000/35	4000/23	3700/56
PI	2	2	2	2	2
SMS / FOV shift	2/2	2/4	2/4	2/4	2/4
Echo-train length	11	11	11	11	9
Bandwidth (Hz/px)	296	354	301	354	301
Echo spacing [ms]	7.51	7.05	8.03	7.05	8.03
FOV [mm]	140 × 140	140 × 140	140 × 140	140 × 140	140 × 140
Voxel size [mm]	0.5 × 0.6 × 3.0	0.4 × 0.5 × 3.0	0.5 × 0.6 × 3.0	0.4 × 0.5 × 3.0	0.5 × 0.6 × 3.0
Slices	38	36	36	38	38
Concatenations	1	1	1	1	1
Phase direction	right-to-left	right-to-left	head-to-foot	head-to-foot	head-to-foot
Acquisition time [mm:ss]	01:00	01:16	01:24	01:17	01:23

**Table 3:** NYU 3-Tesla 4-fold SMS2-PAT2 accelerated knee MRI protocol.

Ax = axial, Cor = coronal, sag = sagittal, PD = proton density weighted, FS = fat suppression, PI = parallel imaging acceleration factor, SMS = simultaneous multislice acquisition acceleration factor, TSE = turbo spin-echo, FOV = field-of-view

structed 2-fold parallel-imaging-accelerated dataset [17], the door is now open to teaching deep neural networks to reconstruct SMS2-PAT3, SMS3-PAT3, SMS2-PAT4, and SMS3-PAT4, which may exceed a total acceleration factor of 10 (Fig. 9)<sup>3</sup>.

## Set phasers to stun: Artificial intelligence-driven matrix interpolation and super-resolution images

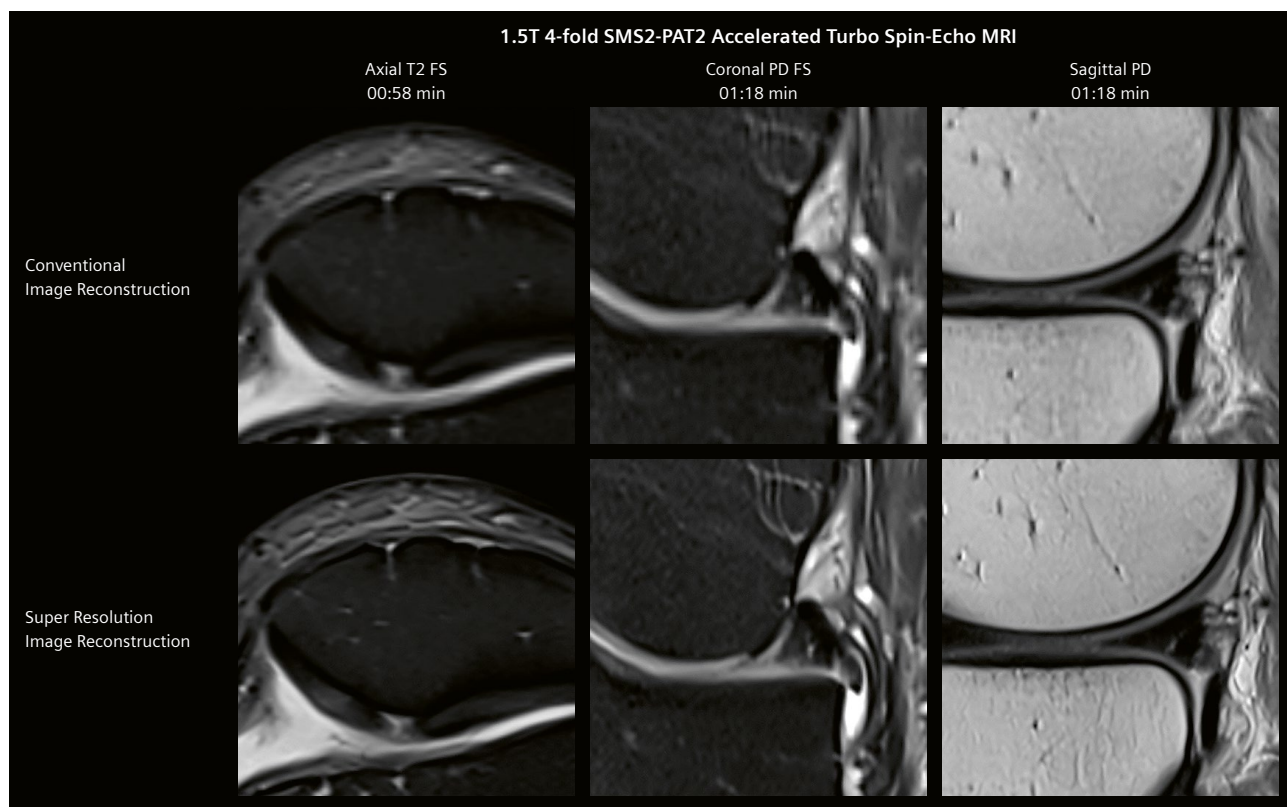
Acquiring MR images with higher spatial resolution to resolve small musculoskeletal structures and abnormalities with greater detail is a costly endeavor because of the inverse square-root relationship between increasing spatial resolution and SNR loss.

Hence, technologies that can accurately convert MR images from an acquired lower resolution to calculate or predict higher spatial resolutions could substantially increase scan efficiency [5]. MRI datasets could then be acquired with lower matrix resolution in shorter acquisition times. Conversely, higher image quality could be achieved without the need for longer scan times.

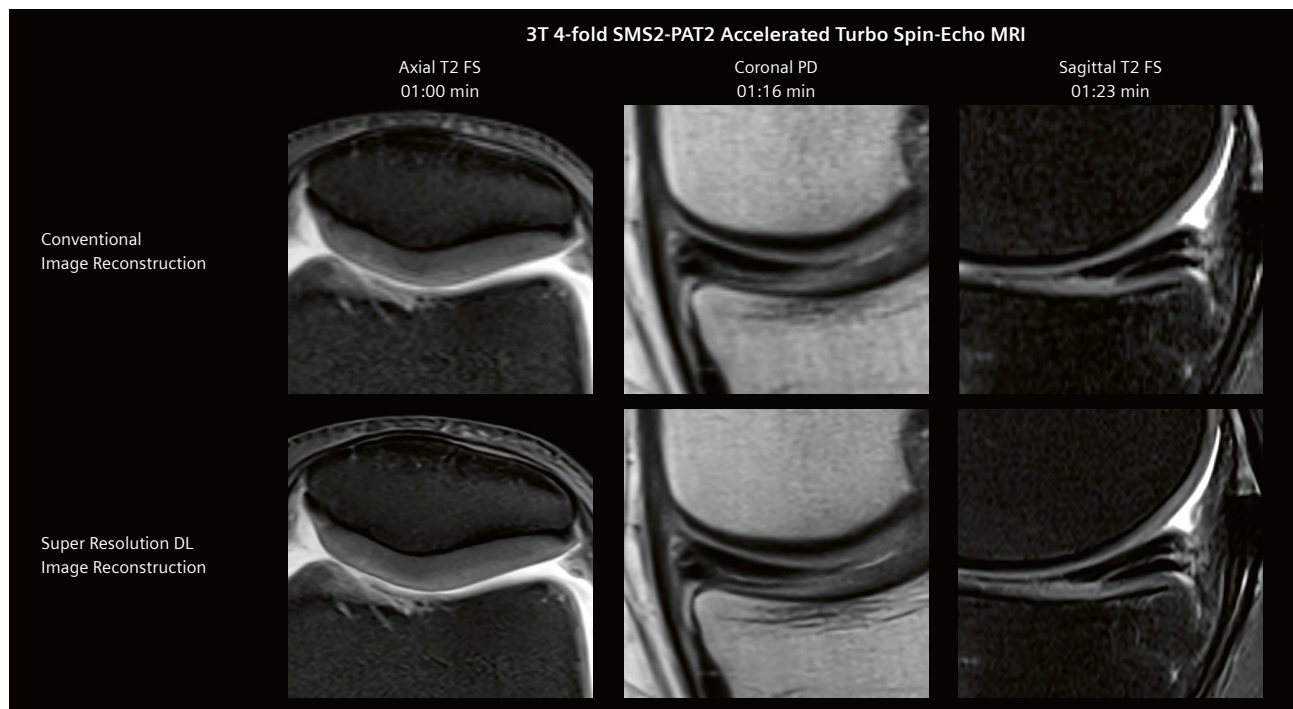
Various conventional *k*-space- and image-domain-based matrix interpolation techniques have been applied in the past, including adding empty data (zero filling) or mathematically estimated data. While basic interpolation techniques may not add information, improved edge sharpness and reduced partial volume effects have been achieved in some cases.

Deep Resolve Sharp is a super-resolution algorithm based on deep neural networks that increases image detail and sharpness of MR images acquired with various pulse sequences and image contrast [16]. The algorithm combines matrix expansion and accurately predicts higher spatial resolution information based on its extensive training with many pairs of low-resolution and high-resolution MRI datasets.

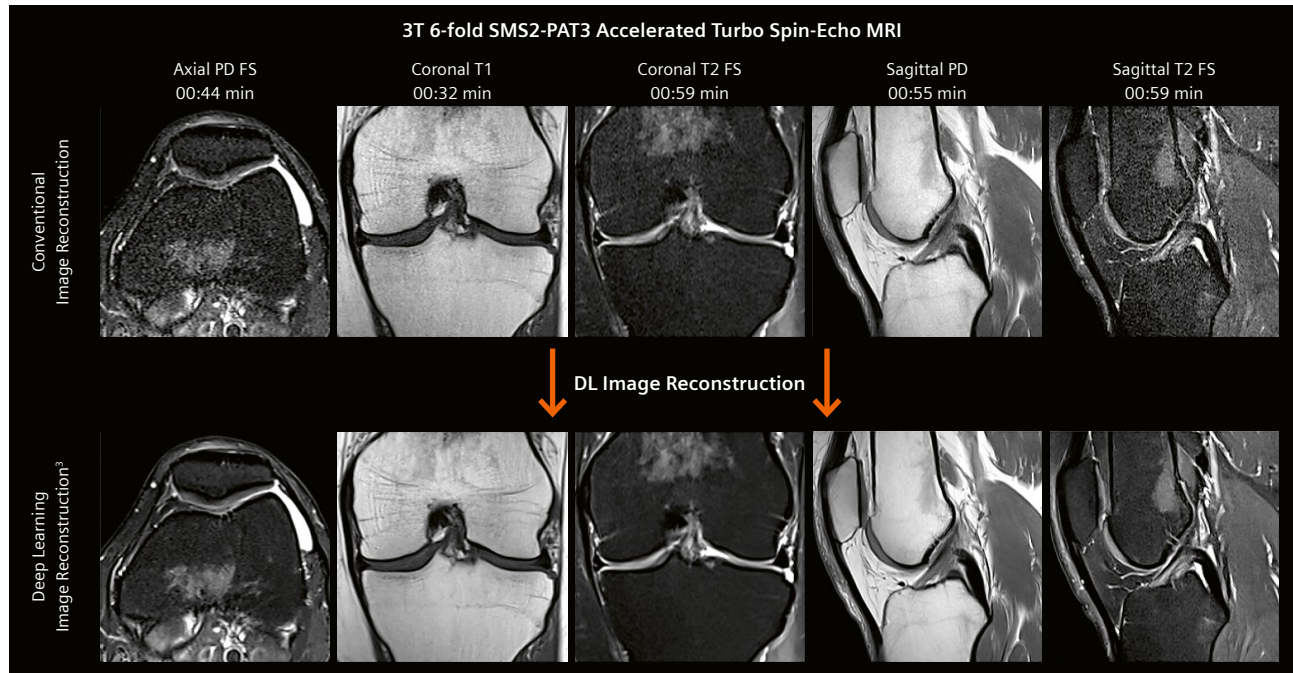
Deep Resolve Sharp can be combined with other deep learning-based image reconstruction algorithms and acceleration techniques, such as combined parallel imaging and simultaneous multi-slice acquisition with, indeed, *stunning* increases in sharpness, detail, and overall image quality (Figs. 7, 8).



**7** 1.5-Tesla MRI of the knee with echo-train-compacted turbo spin-echo pulse sequences using combined 2-fold parallel imaging and 2-fold simultaneous multi-slice acquisition acceleration and conventional and deep learning image reconstructions. The application of Deep Resolve Sharp super-resolution reconstruction greatly increases the detail of the patellar cartilage defect and the displaced lateral meniscus tear. The MR images were obtained with a 1.5T MAGNETOM Sola MRI system and a 1-transmit-channel-18-receiver-channel knee coil.  
PD = proton density weighting, PD FS = fat-suppressed proton density weighting, T2 FS = fat-suppressed T2 weighting



- 8** 3-Tesla MRI of the knee with echo-train-compacted turbo spin-echo pulse sequences using combined 2-fold parallel imaging and 2-fold simultaneous multi-slice acquisition acceleration and conventional and deep learning image reconstructions. The application of Deep Resolve Sharp super-resolution reconstruction greatly increases the detail of the intact patellar articular cartilage and nondisplaced horizontal medial meniscus tear. The MR images were obtained with a 3T MAGNETOM Vida MRI system and a 1-transmit-channel-18-receiver-channel knee coil. PD = proton density weighting, PD FS = fat-suppressed proton density weighting, T2 FS = fat-suppressed T2 weighting



- 9** 3-Tesla MRI of the knee with echo-train-compacted turbo spin-echo pulse sequences using combined 2-fold simultaneous multi-slice acquisition and 3-fold parallel imaging acceleration and conventional and deep learning image reconstructions<sup>3</sup>. The application of deep learning image reconstruction permits artifact-free MR image reconstruction with high signal, low noise, and high anatomical detail. The MR images were obtained with a 3T MAGNETOM Vida MRI system and a 1-transmit-channel-18-receiver-channel knee coil. PD = proton density weighting, PD FS = fat-suppressed proton density weighting, T2 FS = fat-suppressed T2 weighting

## Things are only impossible until they're not: Conclusion

Driven by synergies of high-performance scanner technologies, advanced acceleration techniques, and artificial intelligence-based image and super-resolution reconstructions, we are already well on our way to new horizons and to crossing new musculoskeletal MRI frontiers with acceleration factors that no one believed were possible. Each parsec of the journey will add a value component to MRI, ultimately benefiting patients, institutions, and societies in multiple ways. *We are, indeed, boldly going where no one has gone before!*

Live long and prosper 



Jan Fritz

## References

- 1 Khodarahmi I, Fritz J. The Value of 3 Tesla Field Strength for Musculoskeletal MRI. *Invest Radiol.* 2021; 56(11):749-763.
- 2 Hennig J, Nauerth A, Friedburg H. RARE imaging: a fast imaging method for clinical MR. *Magn Reson Med.* 1986; 3(6):823-833.
- 3 Griswold MA, Jakob PM, Heidemann RM, Nittka M, Jellus V, Wang J, et al. Generalized autocalibrating partially parallel acquisitions (GRAPPA). *Magn Reson Med.* 2002; 47(6):1202-1210.
- 4 Fritz J, Fritz B, Zhang J, Thawait GK, Joshi DH, Pan L, Wang D. Simultaneous Multislice Accelerated Turbo Spin Echo Magnetic Resonance Imaging: Comparison and Combination With In-Plane Parallel Imaging Acceleration for High-Resolution Magnetic Resonance Imaging of the Knee. *Invest Radiol.* 2017; 52(9):529-537.
- 5 Del Grande F, Guggenberger R, Fritz J. Rapid Musculoskeletal MRI in 2021: Value and Optimized Use of Widely Accessible Techniques. *AJR Am J Roentgenol.* 2021; 216(3):704-717.
- 6 Fritz J, Kijowski R, Recht MP. Artificial intelligence in musculoskeletal imaging: a perspective on value propositions, clinical use, and obstacles. *Skeletal Radiol.* 2021 May 13. Online ahead of print.
- 7 Fritz J, Guggenberger R, Del Grande F. Rapid Musculoskeletal MRI in 2021: Clinical Application of Advanced Accelerated Techniques. *AJR Am J Roentgenol.* 2021; 216(3):718-733.
- 8 Del Grande F, Rashidi A, Luna R, Delcogliano M, Stern SE, Dalili D, Fritz J. Five-Minute Five-Sequence Knee MRI Using Combined Simultaneous Multislice and Parallel Imaging Acceleration: Comparison with 10-Minute Parallel Imaging Knee MRI. *Radiology.* 2021; 299(3):635-646.
- 9 Lin DJ, Johnson PM, Knoll F, Lui YW. Artificial Intelligence for MR Image Reconstruction: An Overview for Clinicians. *J Magn Reson Imaging.* 2021; 53(4):1015-1028.
- 10 Fritz J, Fritz B, Thawait GG, Meyer H, Gilson WD, Raithel E. Three-Dimensional CAIPRINHA SPACE TSE for 5-Minute High-Resolution MRI of the Knee. *Invest Radiol.* 2016; 51(10):609-617.
- 11 Fritz J, Raithel E, Thawait GK, Gilson W, Papp DF. Six-Fold Acceleration of High-Spatial Resolution 3D SPACE MRI of the Knee Through Incoherent k-Space Undersampling and Iterative Reconstruction-First Experience. *Invest Radiol.* 2016; 51(6):400-409.
- 12 Horger W, Kiefer B. Fat Suppression Techniques – a Short Overview. *MAGNETOM Flash* (46) 1/2011:56-59.
- 13 Fritz J, Ahlawat S, Demehri S, Thawait GK, Raithel E, Gilson WD, Nittka M. Compressed Sensing SEMAC: 8-fold Accelerated High Resolution Metal Artifact Reduction MRI of Cobalt-Chromium Knee Arthroplasty Implants. *Invest Radiol.* 2016; 51(10):666-676.
- 14 Fritz J, Fritz B, Thawait GK, Raithel E, Gilson WD, Nittka M, Mont MA. Advanced metal artifact reduction MRI of metal-on-metal hip resurfacing arthroplasty implants: compressed sensing acceleration enables the time-neutral use of SEMAC. *Skeletal Radiol.* 2016; 45(10):1345-1356.
- 15 Blasche M. Gradient Performance and Gradient Amplifier Power. *MAGNETOM Flash* (69) 3/2017.
- 16 Behl N. Deep Resolve – Mobilizing the Power of Networks. *MAGNETOM Flash* (78) 1/2021: 29-35.
- 17 Recht MP, Zbontar J, Sodickson DK, Knoll F, Yakubova N, Sriram A, et al. Using Deep Learning to Accelerate Knee MRI at 3 T: Results of an Interchangeability Study. *AJR Am J Roentgenol.* 2020; 215(6):1421-1429.
- 18 Breuer F, Blaimer M, Griswold MA, Jakob P. CAIPRINHA – Revisited. Simultaneous Multi-Slice Supplement *MAGNETOM Flash* (63) 3/2015: 8-15.

# Initial Experience with Automatic Knee Cartilage Segmentation using MR Chondral Health

Vladimir Juras, Ph.D.; Pavol Szomolanyi, Ph.D.; Veronika Janáčová, MSc; Siegfried Trattnig, M.D.

High Field MR Centre, Department of Biomedical Imaging and Image-guided Therapy, Medical University of Vienna, Vienna, Austria

## Abstract

Osteoarthritis (OA) is a degenerative disease affecting the articular cartilage characterized by slow cartilage loss over time. Magnetic resonance imaging (MRI) provides a noninvasive and sensitive tool for examining structures involved in OA disease. Both morphological and quantitative MRI techniques are helpful in the diagnosis and treatment monitoring of OA patients. In MR imaging, cartilage segmentation is an important evaluation step to define cartilage loss in disease progression or cartilage volume increase as a response to treatment. This step, however, presents a significant and substantial burden in large cohort trials. Here, we present our initial experience using automated segmentation software, MR Chondral Health<sup>1</sup>, which is capable of automatically segmenting the whole knee cartilage on isotropic MRI scans.

## Key points

1. Automated cartilage segmentation is an essential tool for improving the detection of early osteoarthritis in patients at risk of OA and, in particular, in treatment monitoring of newly developed cartilage regenerative drugs.
2. MR Chondral Health<sup>1</sup> provides robust and reproducible automated knee cartilage segmentation that can be performed on the most common 3D isotropic MR sequences.
3. Automated quantitative MRI data extraction can be added to the automated cartilage segmentation as it provides valuable information about collagen fibers and glycosaminoglycans.

## Background

Osteoarthritis (OA), the most common form of arthritis, is a complex, multifactorial condition that causes disability in the older population [1]. In terms of pathophysiology, OA refers to disease of the entire joint including breakdown

of cartilage and the associated alterations in the underlying bone. This leads to joint deformity, disability, and debilitating joint symptoms of all joint structures such as cartilage, bone, menisci, ligaments, and tendons. Studies have shown that the morphometric assessment of the cartilage structure, such as volume and thickness, from MR images provides an accurate measurement of OA progression [2–4]. Although a number of quantitative MRI techniques [5–8] have recently been developed for the detection of early cartilage degeneration, one of the major hurdles for clinical translation of these advanced quantitative techniques is the time-consuming and tedious task of manual or semiautomatic cartilage segmentation. In addition, manual segmentation is typically subject to relatively high inter- and intra-reader variability. Over the years, a number of different techniques for automated cartilage segmentation have been developed, including deformable models [9], clustering [10], intensity and edge detection-based [11, 12] approaches, and atlas-/graph-based methods [13]. The use of convolutional neural networks (CNNs) in knee articular cartilage segmentation has become very popular in recent years [14]. The model-based cartilage segmentation approach developed by Fripp et al. [15] has been implemented in the MR Chondral Health application (Siemens Healthcare, Erlangen, Germany) and provides

<span style="background-color: #80B1A8; border: 1px solid black; padding: 2px 5px;"></span>	Patella lateral superior	<span style="background-color: #0072BD; border: 1px solid black; padding: 2px 5px;"></span>	Tibia lateral posterior
<span style="background-color: #006400; border: 1px solid black; padding: 2px 5px;"></span>	Patella lateral central	<span style="background-color: #E64A19; border: 1px solid black; padding: 2px 5px;"></span>	Femur medial anterior
<span style="background-color: #008000; border: 1px solid black; padding: 2px 5px;"></span>	Patella lateral inferior	<span style="background-color: #F0A040; border: 1px solid black; padding: 2px 5px;"></span>	Femur medial central
<span style="background-color: #004000; border: 1px solid black; padding: 2px 5px;"></span>	Patella medial superior	<span style="background-color: #FFF176; border: 1px solid black; padding: 2px 5px;"></span>	Femur medial posterior
<span style="background-color: #008000; border: 1px solid black; padding: 2px 5px;"></span>	Patella medial central	<span style="background-color: #F08040; border: 1px solid black; padding: 2px 5px;"></span>	Femur trochlea lateral
<span style="background-color: #008000; border: 1px solid black; padding: 2px 5px;"></span>	Patella medial inferior	<span style="background-color: #FFF176; border: 1px solid black; padding: 2px 5px;"></span>	Femur trochlea medial
<span style="background-color: #1A237E; border: 1px solid black; padding: 2px 5px;"></span>	Tibia medial anterior	<span style="background-color: #FFC107; border: 1px solid black; padding: 2px 5px;"></span>	Femur trochlea central
<span style="background-color: #1A237E; border: 1px solid black; padding: 2px 5px;"></span>	Tibia medial central	<span style="background-color: #FFF176; border: 1px solid black; padding: 2px 5px;"></span>	Femur lateral anterior
<span style="background-color: #1A237E; border: 1px solid black; padding: 2px 5px;"></span>	Tibia medial posterior	<span style="background-color: #FFC107; border: 1px solid black; padding: 2px 5px;"></span>	Femur lateral central
<span style="background-color: #1A237E; border: 1px solid black; padding: 2px 5px;"></span>	Tibia lateral anterior	<span style="background-color: #E64A19; border: 1px solid black; padding: 2px 5px;"></span>	Femur lateral posterior
<span style="background-color: #1A237E; border: 1px solid black; padding: 2px 5px;"></span>	Tibia lateral central		

- 1** The color codes of 21 cartilage regions automatically segmented using MR Chondral Health.

<sup>1</sup>Work in progress. The product is still under development and not commercially available yet. Its future availability cannot be ensured.

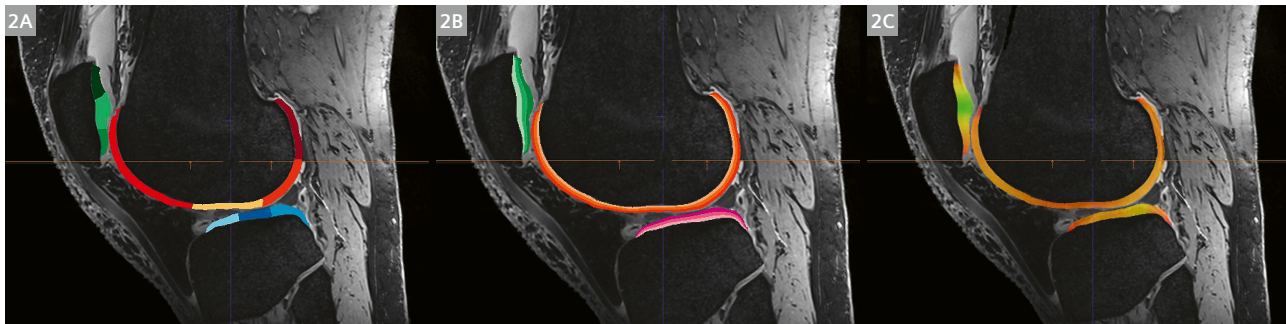
automated knee cartilage segmentation, which is further divided into twenty-one subregions. Here we present an overview of the basic features of MR Chondral Health and our experience of its application in clinical trials.

## Segmentation workflow

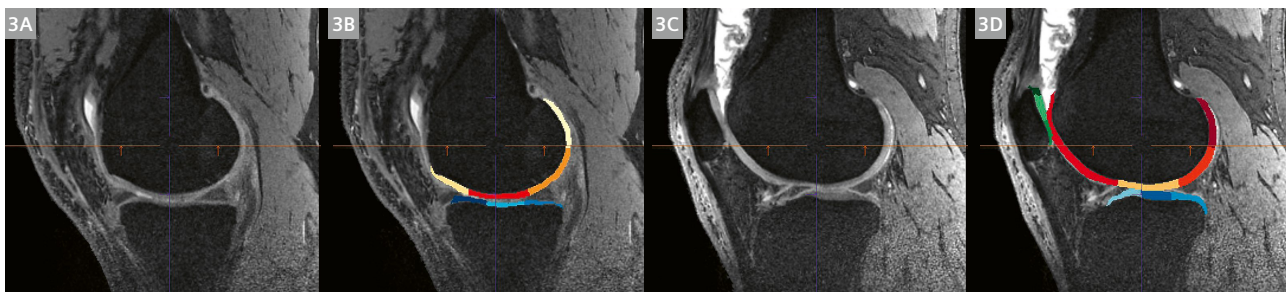
Knee cartilage was segmented using the prototype MR Chondral Health software (version 2.1.0, Siemens Healthcare, Erlangen, Germany), which uses a model-based segmentation algorithm [15]. The basic scheme consists of four stages: preprocessing (bone-cartilage interface (BCI) determination), atlas alignment, bone segmentation, and cartilage segmentation [15]. According to anatomical landmarks introduced by Surowiec et al., knee cartilage is divided into six patellar, six tibial, and nine femoral subregions [16]. These anatomical landmarks are visible on MR images as well as during arthroscopy. The color codes used are shown in Figure 1. Each segment can be further divided into three layers defined as three-thirds along the surface bone-cartilage interface (BCI) axis, if needed. The software is also capable of calculating a global and mean volume and thickness for each region – it is calculated as an average of the thickness values of the pixels lying on the BCI through all slices of a certain cartilage

region. If a quantitative MRI measurement is available, it can be loaded into the software along with the morphological image, and after image registration, quantitative MRI values can be automatically extracted. Any of the 3D morphological sequences can be used for automated segmentation, preferably 3D-DESS (Double-Echo Steady State), but we successfully segmented cartilage on 3D-GRE (Gradient Echo), 3D-TrueFISP (Balanced Steady-State GRE), 3D-MERGE (Multiple Echo Recombined Gradient Echo), and 3D-WAT images (T1-weighted gradient echo with water-selective excitation). On average, a single knee segmentation step takes approximately 5–15 minutes, depending on the pixel resolution and number of slices (tested on a standard workstation equipped with an Intel Xeon W-2225 CPU @ 4.10 GHz with 4 cores, 16 GB of physical memory and an AMD Radeon R7 450 graphical unit). The example of automated cartilage segmentation from 3D-DESS and 3D-GRE morphological images are shown in Figure 2 and 3 respectively.

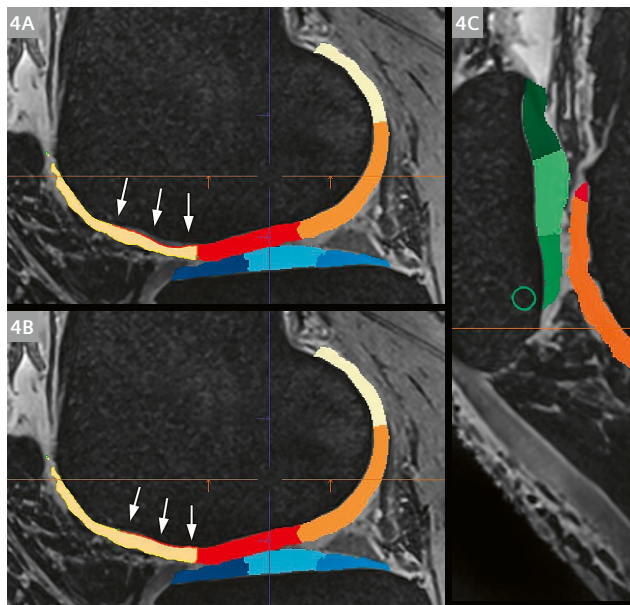
After coarse initial segmentation, the software allows the user to edit the individual cartilage regions manually. Two editing modes are available: paint mode, which uses brushes of selectable size and shape and adds or removes parts of the selected region, and nudge mode, which is applied to the contours of the selected region, which can



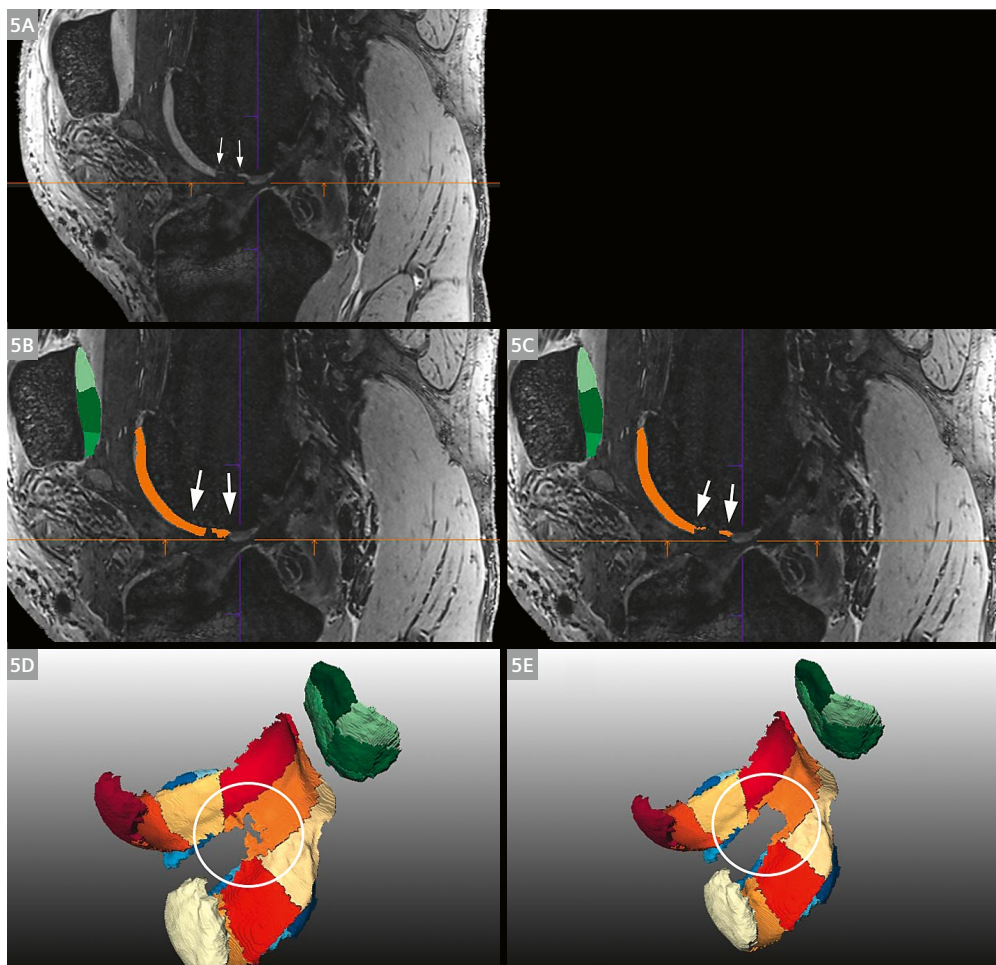
**2** (2A) Automated segmentation of the knee cartilage on 3D-DESS images (7-tesla MRI, echo time 2.55 ms, repetition time 8.68 ms, acquisition matrix 320 × 320, pixel spacing 0.25 × 0.25 mm, slice thickness 0.5 mm). (2B) Three-layer representation of the segmentation (deep, middle, and superficial cartilage zones), (2C) cartilage thickness map.



**3** (3A, B) Automated segmentation of the medial condyle on 3D-GRE images (3-tesla MRI, echo time 4.92 ms, repetition time 16.3 ms, acquisition matrix 320 × 320, pixel spacing 0.5 × 0.5 mm, slice thickness 0.7 mm). (3C, D) Automated segmentation of the lateral condyle on 3D-GRE images of the same subject scanned with the same protocol.



**4** Segmentation post-editing in nudge mode – an inaccurately segmented region can be selected (4A) and dragged as required (4B), the white arrows point to the selected region. Alternatively, post-editing in paint mode can be used; in this example, a circular six-pixel diameter brush was selected (4C).



**5** A 39-year-old female patient after ACI procedure; (5A) 3D-DESS image (7-tesla MRI, echo time 2.55 ms, repetition time 8.23 ms, acquisition matrix 384 x 384, pixel spacing 0.22 x 0.22 mm, slice thickness 0.45 mm), arrows indicate the donor site from which the cartilage was harvested. (5B) Unedited automated segmentation of the corresponding slice; (5C) Edited automated segmentation of the corresponding slice using paint mode; 3D rendering of an unedited (5D) and edited (5E) automated segmentation (donor site in the white circle).

be altered using a Bézier curve. An example of the editing mode is shown in Figure 4. Typically, post-editing is not necessary if high-quality DESS images are used. If low-resolution or low SNR images are used, editing takes approximately 5 to 20 minutes.

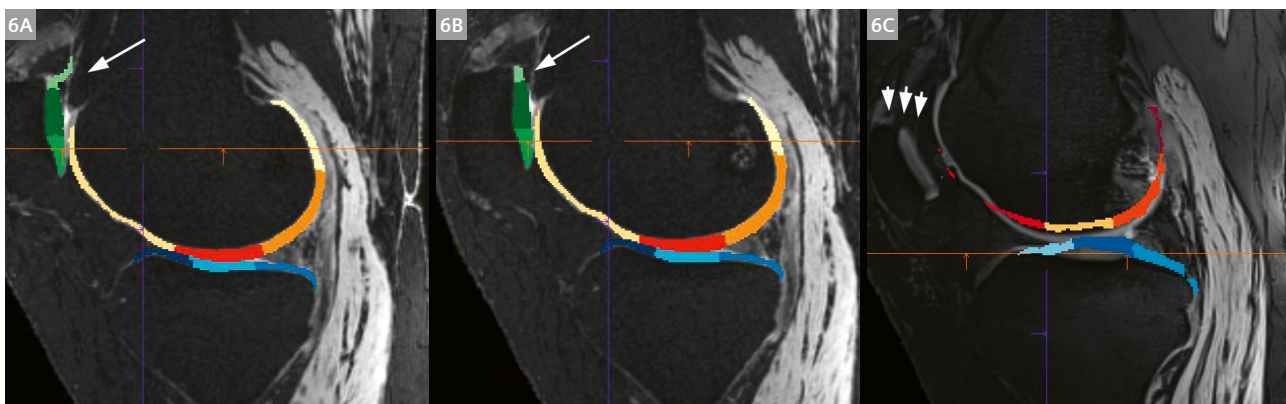
## Automated cartilage segmentation in patients with autologous chondrocyte implantation

Autologous chondrocyte implantation (ACI) is a surgical procedure used to treat full-thickness articular cartilage defects of the knee [17]. It is a two-stage procedure: In the first stage, the surgeon harvests a small piece of articular cartilage from the patient's knee from which the chondrocytes are enzymatically isolated. In the second stage, open surgery is performed in which a scaffold of a different type, seeded with cells that have been harvested and cultivated, is inserted into the articular cartilage defect. The chondrocytes should induce matrix synthesis and, at best,

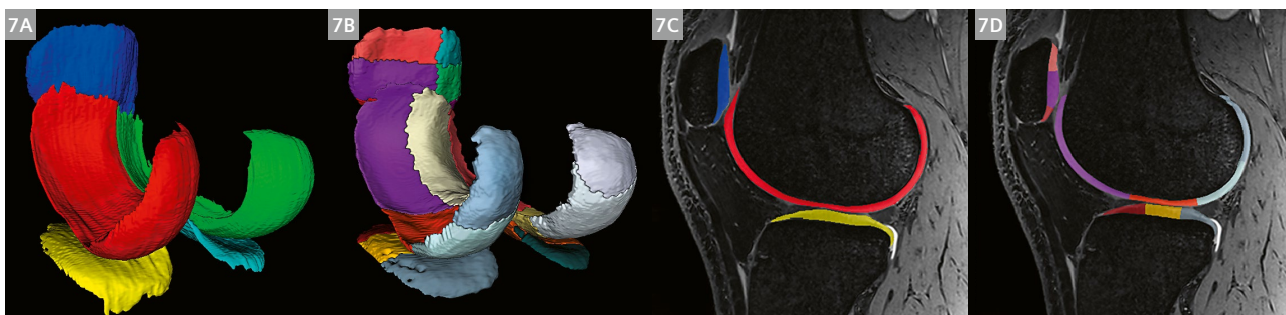
produce hyaline cartilage repair tissue. The transplanted part of cartilage typically fills the whole lesion and hence does not cause any problems for automated segmentation. The harvested part of the cartilage in a non-weight bearing region leaves a full-thickness hole in the cartilage which gradually fills up with fibrous tissue. Segmentation of the cartilage subregion encompassing the donor site can be used to indirectly assess refilling of the cartilage defect over time. The software clearly identifies cartilage interruption. However, the boundaries are not accurately segmented. In the example shown in Figure 5, the donor site was covered by approximately 15 slices, hence post-editing took less than five minutes per case.

## Automated segmentation in patients treated with disease-modifying osteoarthritis drugs

The key potential of automated cartilage segmentation lies in the evaluation of patients treated with newly developed chondrotherapies, which can have a direct or indirect



**6** Automated knee cartilage segmentation of cadaver knees. If the patella (long arrow) has not substantially shifted (**6A**), the resulting automated segmentation can be relatively easily edited (**6B**). However, if the patella has shifted several centimeters caudally (three short arrows), further editing is needed (**6C**).



**7** 3D rendering of a manual (**7A**) and automated (**7B**) knee cartilage segmentation and example slices of manual (**7C**) and automated (**7D**) segmentation overlaid on 3D-DESS images (7-tesla MRI, echo time 2.55 ms, repetition time 8.86 ms, acquisition matrix 320 x 320, pixel spacing 0.25 x 0.25 mm, slice thickness 0.5 mm).

	Fully-automated cartilage segmentation		Fully-automated cartilage segmentation with post-editing	
Cartilage region	Jaccard	Dice	Jaccard	Dice
Patella	0.706	0.855	0.823	0.879
Lateral tibia	0.700	0.850	0.788	0.861
Medial tibia	0.702	0.825	0.832	0.828
Femur	0.722	0.882	0.845	0.895
All regions combined	0.710	0.834	0.822	0.866

**Table 1:** A comparison of automated and manual cartilage segmentation using the Jaccard coefficient and the Dice coefficient. Both options, fully automated and fully automated with post-editing, are listed. *Reproduced from [19].*

Smallest detectable change							
PATELLA							
	LatSup	LatCent	LatInf	MedSup	MedCent	MedInf	all combined
T2 (in ms)	2.62	2.42	2.35	4.11	2.26	2.60	2.73
Volume (in mm <sup>3</sup> )	75.9	70.9	51.6	101.6	102.6	38.6	73.5
Thickness (in mm)	0.14	0.22	0.26	0.17	0.25	0.12	0.19
TIBIA							
	MedAnt	MedCent	MedPost	LatAnt	LatCent	LatPost	all combined
T2 (in ms)	2.55	3.23	3.07	1.85	3.05	2.73	2.74
Volume (in mm <sup>3</sup> )	47.66	68.14	39.43	64.18	63.00	96.07	63.08
Thickness (in mm)	0.11	0.21	0.05	0.12	0.24	0.12	0.14
FEMUR							
	MedAnt	MedCent	MedPost	TrochLat	TrochMed	TrochCent	LatAnt
T2 (in ms)	3.28	1.92	1.89	0.81	1.67	1.56	1.53
Volume (in mm <sup>3</sup> )	45.81	201.04	187.04	73.93	64.20	178.29	88.72
Thickness (in mm)	0.18	0.20	0.21	0.09	0.12	0.09	0.21
	LatCent	LatPost	all combined				
	1.96	2.47	1.90				
	165.68	151.05	128.42				
	0.22	0.18	0.16				

**Table 2:** Test-retest of automated cartilage segmentation and automated 3D-TESS T2 extractions from baseline scan and scan repeated after eight days. *Reproduced from [19].*

effect on the cartilage volume. Therefore, the MR Chondral Health (MRCH) software was employed for MRI knee examinations (3-tesla) performed at baseline and at a few follow-up timepoints over the course of one year after treatment. The effect of the treatment was assessed in an exploratory analysis of the additive volume within the weight-bearing area of the medial femur [18]. The data generated from the MRCH software in this study was found to be potentially more sensitive than that obtained by the manual segmentation approach.

## Automated cartilage segmentation of cadaver knees

MR Chondral Health was also tested on cadaver knees from six donors. Automated segmentation of such knees can be challenging for several reasons. First, the MRI image contrast differs from in-vivo knees even when the same MRI protocol is used because of post-mortem changes of the soft tissue. Second, as the patellar tendon is typically cut in cadaver knees, the patella slips caudally, which results in unusual knee anatomy. The example of automated cartilage segmentation of cadaver knees with dislocated patella is shown in Figure 6.

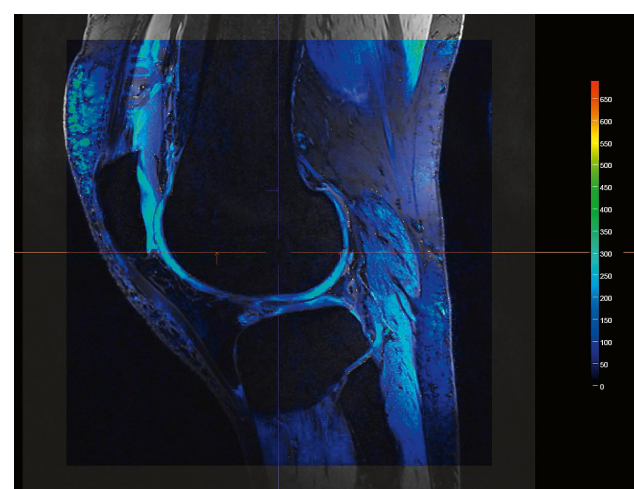
## Validating segmentation

In order to evaluate the accuracy of automated knee cartilage segmentation, the images of thirteen patients with a grade I and grade II femoral cartilage defect in the lateral or medial condyle (six females,  $50.8 \pm 4.4$  years and seven males,  $50.2 \pm 6.1$  years) were manually segmented by an experienced radiologist and automatically segmented using the MR Chondral Health application. To calculate test-retest variability, the MRI examinations were performed twice: at baseline and after eight days. The MRI protocol consisted of 3D-DESS, 3D-TESS T2 mapping (triple-echo steady state) [19], and CPMG T2 mapping (Carr-Purcell-Meiboom-Gill, i.e. multiecho spin-echo sequence). Manual segmentation was performed for bulk femoral, patellar, and tibial lateral and medial cartilage rather than for all twenty-one cartilage subregions separately, since reproducing the exact perimeters of the subregions defined automatically is a difficult task and might introduce a significant bias (Fig. 7). While testing for the similarity between the manual and automatic datasets, a mean Jaccard coefficient of  $0.709 \pm 0.010$  and a mean Dice coefficient of  $0.848 \pm 0.025$  were found when using the unedited data from the automated segmentation. When using data from the edited automated segmentation, the mean Jaccard and Dice coefficients

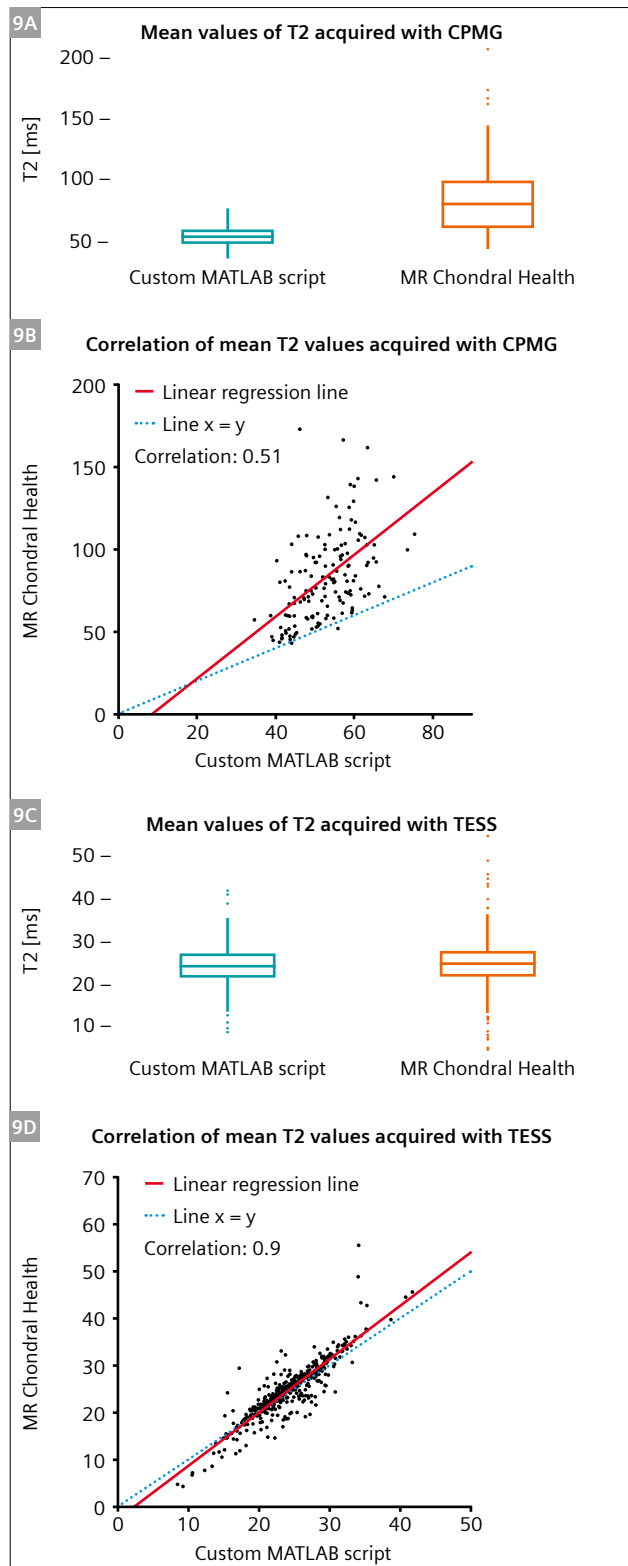
increased to  $0.822 \pm 0.024$  and  $0.863 \pm 0.027$  respectively [20]. Details of the Jaccard and Dice coefficients for individual cartilage regions are listed in Table 1. The test-retest variability was also expressed as the smallest detectable change individually for cartilage volume, thickness, and T2 values (listed in Table 2).

## Validating the accuracy of biochemical image registration

When biochemical images (such as those acquired with T2 mapping) are loaded into MR Chondral Health, the software registers the images, extracts the values, and displays them in the final output table (Fig. 8). In order to validate the accuracy of the registration, it was compared with an algorithm developed in MATLAB (version 2019b, The MathWorks, Inc, Natick, MA, USA). This algorithm uses a multimodal co-registration method, which was applied using spatial mapping of fixed images (DESS) and moving images (T2-TESS and T2-CPMG). Affine transformation with 12 degrees of freedom was used. Optimizer function parameters were determined by a previous iterative process, while a similarity index map was used as a quantitative co-registration quality marker (initial radius = 0.001; epsilon = 1.5e-4; growth factor = 1.01; and maximum iterations = 300). Two registering methods were compared across the twenty-one subregions in seven subjects using descriptive statistics and the Pearson correlation coefficient (Fig. 9). In the case of 3D-TESS T2 mapping, there was a high correlation between MR Chondral Health and MATLAB registration. However, in the case of 3D-CPMG T2 mapping, the correlation was substantially lower. In 3D-CPMG T2



**8** A screenshot from MR Chondral Health depicting a 3D-DESS image overlaid with a registered CPMG-T2 map.



- 9** The comparison of two biochemical image (T2 mapping) registration methods: MR Chondral Health and custom-written MATLAB script; mean values of T2 acquired with TESS (9A) and CPMG (9C), and a correlation between these two methods of CPMG-T2 and TESS-T2 (9B).

mapping, MR Chondral Health slightly misregistered the maps onto bone; this introduced some outliers resulting in T2 overestimation. MR Chondral Health allows the user to adjust registration manually; however, this tool is rather cumbersome.

## Conclusion and outlook

Fully automatic tissue segmentation is an essential step toward applying quantitative MRI techniques in a clinical setting. These advances in MR imaging may contribute to the development and evaluation of effective therapeutic strategies that target early structural changes. MR Chondral Health provides robust and reproducible automated segmentation of articular knee cartilage images from wide range of 3D MRI sequences. Automated extraction of quantitative MRI values is a promising feature of the software, but the registration algorithm used in this version still requires some improvement. (According to our information, this issue has been resolved with MR Chondral Health Version 2.2, which is to be released soon). A remaining question still to be evaluated is the accuracy of automated cartilage segmentation in late-stage OA, which is manifested by cartilage thinning and forming of osteophytes.

## References:

- 1 Sarzi-Puttini, P., M.A. Cimmino, R. Scarpa, R. Caporali, F. Parazzini, A. Zaninelli, F. Atzeni, and B. Canesi, Osteoarthritis: an overview of the disease and its treatment strategies. *Semin Arthritis Rheum*, 2005. 35(1 Suppl 1): pp. 1–10.
- 2 Ambellan, F., A. Tack, M. Ehlke, and S. Zachow, Automated segmentation of knee bone and cartilage combining statistical shape knowledge and convolutional neural networks: Data from the Osteoarthritis Initiative. *Med Image Anal*, 2019. 52: pp. 109–118.
- 3 Hou, W., J. Zhao, R. He, J. Li, Y. Ou, M. Du, X. Xiong, B. Xie, L. Li, X. Zhou, P. Zuo, E. Raithel, Z. Zhang, and W. Chen, Quantitative measurement of cartilage volume with automatic cartilage segmentation in knee osteoarthritis. *Clin Rheumatol*, 2021. 40(5): pp. 1997–2006.
- 4 Iranpour-Boroujeni, T., A. Watanabe, R. Bashtar, H. Yoshioka, and J. Duryea, Quantification of cartilage loss in local regions of knee joints using semi-automated segmentation software: analysis of longitudinal data from the Osteoarthritis Initiative (OAI). *Osteoarthr Cartil*, 2011. 19(3): pp. 309–14.
- 5 Liess, C., S. Lusse, N. Karger, M. Heller, and C.C. Gluer, Detection of changes in cartilage water content using MRI T-2-mapping in vivo. *Osteoarthr Cartil*, 2002. 10(12): pp. 907–913.
- 6 Watkins, L.E., E.B. Rubin, V. Mazzoli, S.D. Uhrlrich, A.D. Desai, M. Black, G.K. Ho, S.L. Delp, M.E. Levenston, G.S. Beaupre, G.E. Gold, and F. Kogan, Rapid volumetric gagCEST imaging of knee articular cartilage at 3 T: evaluation of improved dynamic range and an osteoarthritic population. *Nmr in Biomedicine*, 2020. 33(8).
- 7 Welsch, G.H., S. Trattnig, K. Scheffler, P. Szomontanyi, S. Quirbach, S. Marlovits, S. Domayer, O. Bieri, and T.C. Mamisch, Magnetization transfer contrast and T2 mapping in the evaluation of cartilage repair tissue with 3T MRI. *J Magn Reson Imaging*, 2008. 28(4): pp. 979–986.

- 8 Zbyn, S., V. Mlynarik, V. Juras, P. Szomolanyi, and S. Trattnig, Evaluation of cartilage repair and osteoarthritis with sodium MRI. *Nmr in Biomedicine*, 2016. 29(2): pp. 206–215.
- 9 Tang, J., S. Millington, S.T. Acton, J. Crandall, and S. Hurwitz, Surface extraction and thickness measurement of the articular cartilage from MR images using directional gradient vector flow snakes. *IEEE Trans Biomed Eng*, 2006. 53(5): pp. 896–907.
- 10 Folkesson, J., E.B. Dam, O.F. Olsen, P.C. Pettersen, and C. Christiansen, Segmenting articular cartilage automatically using a voxel classification approach. *IEEE Trans Med Imaging*, 2007. 26(1): pp. 106–15.
- 11 Cashman, P.M., R.I. Kitney, M.A. Gariba, and M.E. Carter, Automated techniques for visualization and mapping of articular cartilage in MR images of the osteoarthritic knee: a base technique for the assessment of microdamage and submicro damage. *IEEE Trans Nanobioscience*, 2002. 1(1): pp. 42–51.
- 12 Kshirsagar, A.A., P.J. Watson, J.A. Tyler, and L.D. Hall, Measurement of localized cartilage volume and thickness of human knee joints by computer analysis of three-dimensional magnetic resonance images. *Invest Radiol*, 1998. 33(5): pp. 289–99.
- 13 Shim, H., S. Chang, C. Tao, J.H. Wang, C.K. Kwoh, and K.T. Bae, Knee cartilage: efficient and reproducible segmentation on high-spatial-resolution MR images with the semiautomated graph-cut algorithm method. *Radiology*, 2009. 251(2): pp. 548–56.
- 14 Ebrahimkhani, S., M.H. Jaward, F.M. Cicuttini, A. Dharmaratne, Y. Wang, and A.G.S. de Herrera, A review on segmentation of knee articular cartilage: from conventional methods towards deep learning. *Artif Intell Med*, 2020. 106: pp. 101851.
- 15 Fripp, J., S. Crozier, S.K. Warfield, and S. Ourselin, Automatic segmentation and quantitative analysis of the articular cartilages from magnetic resonance images of the knee. *IEEE Trans Med Imaging*, 2010. 29(1): pp. 55–64.
- 16 Surowiec, R.K., E.P. Lucas, E.K. Fitzcharles, B.M. Petre, G.J. Dornan, J.E. Giphart, R.F. LaPrade, and C.P. Ho, T2 values of articular cartilage in clinically relevant subregions of the asymptomatic knee. *Knee Surg Sports Traumatol Arthrosc*, 2014. 22(6): pp. 1404–14.
- 17 Harris, J.D., R.A. Siston, X. Pan, and D.C. Flanigan, Autologous chondrocyte implantation: a systematic review. *J Bone Joint Surg Am*, 2010. 92(12): pp. 2220–33.
- 18 Trattnig, S., C. Scotti, D. Laurent, D. Juras, S. Hacker, B. Cole, L. Pasa, R. Lehovec, P. Szomolanyi, E. Raithel, F. Sixer, J. Praestgaard, F. La Gamba, J. L. Jiménez, D. Sanchez Ramos, R. Roubenoff, and M. Schieker, POS0277 Anabolic effect of LNA043, a novel disease-modifying osteoarthritis drug candidate: results from an imaging-based proof-of-concept trial in patients with focal articular cartilage lesions, in *Annals of the Rheumatic Diseases*. 2021, BMJ Publishing Group Ltd., <http://dx.doi.org/10.1136/annrheumdis-2021-eular.447>: Online. p. 277.
- 19 Heule, R., C. Ganter, and O. Bieri, Triple echo steady-state (TESS) relaxometry. *Magn Reson Med*, 2014. 71(1): pp. 230–7.
- 20 Juras, V., P. Szomolanyi, M.M. Schreiner, K. Unterberger, A. Kurekova, B. Hager, D. Laurent, E. Raithel, H. Meyer, and S. Trattnig, Reproducibility of an Automated Quantitative MRI Assessment of Low-Grade Knee Articular Cartilage Lesions. *Cartilage*, 2020: pp. 1947603520961165.

## Contact

Vladimir Juras, Ph.D.  
Medical University of Vienna  
Department of Biomedical Imaging  
and Image-guided Therapy  
High Field MR Centre  
Währinger Gürtel 18–20  
1090 Vienna  
Austria  
Phone: +43 1 40 400 64660  
vladimir.juras@meduniwien.ac.at



Vladimir Juras



Pavol Szomolanyi



Veronika Janacova



Siegfried Trattnig

# Clinical Implementation of Deep Learning-Accelerated HASTE and TSE

Judith Herrmann<sup>1</sup>; Andreas Lingg<sup>1</sup>; Matthias Kündel<sup>1</sup>; Sebastian Gassenmaier<sup>1</sup>; Saif Afat<sup>1</sup>; Haidara Al-Mansour<sup>1</sup>; Dominik Nickel<sup>2</sup>; Gregor Koerzdoerfer<sup>2</sup>; Ahmed Othman<sup>1,3</sup>

<sup>1</sup>Department of Diagnostic and Interventional Radiology, Tuebingen, Germany

<sup>2</sup>MR Applications Predevelopment, Siemens Healthineers, Erlangen, Germany

<sup>3</sup>Department of Neuroradiology, University Medical Center, Mainz, Germany

## Introduction

Magnetic resonance imaging (MRI) has become a modality of choice for the diagnosis of several diseases and is currently indispensable in healthcare. One big disadvantage of MRI is the long duration of the examination, usually ranging between 20 and 60 minutes for body trunk imaging. Long acquisition times come with downsides, such as decreased image quality due to motion artifacts, increased costs, and reduced patient throughput [1]. In view of the limited availability of MRI scanners in general, MRI remains a scarce and more expensive resource than other imaging techniques with limited access to patients in need.

In order to improve this situation, over the past few decades, different acceleration strategies such as compressed sensing (CS) and parallel imaging (PI) have been proposed and established. Recently a revolutionary development based on artificial intelligence has been implemented to further accelerate the acquisition and improve the image quality at the same time: Deep Learning (DL) reconstruction has come to the fore and is gradually being implemented in clinical routine [2–4].

The aim of this report is to describe the first clinical implementation of DL-accelerated, T2-weighted (T2w) half-Fourier single-shot turbo spin echo (HASTE)<sup>1</sup> sequences of the upper abdomen as well as T2w and proton density (PD)-weighted turbo spin echo (TSE) sequences for musculoskeletal imaging in routine daily workflow. The novel DL-accelerated sequences are evaluated in terms of feasibility and image quality compared to standard sequences.

<sup>1</sup>Work in progress. The application is currently under development and is not for sale in the U.S. and in other countries. Its future availability cannot be ensured.

## MRI technique

### Acceleration strategies for Deep Learning-reconstructed TSE and HASTE<sup>1</sup>

To accelerate the image acquisition, a conventional undersampling pattern known from parallel imaging is used for both sequences [5, 6]. Besides the data acquisition for the actual image data, calibration data for the coil-sensitivity estimation need to be acquired. For the TSE sequence, these data are acquired as part of the imaging scan. For the HASTE sequence, these are separately acquired using a second echo train covering only the region around the *k*-space center. In both sequences, a fraction of the *k*-space's periphery is not acquired to further reduce the acquisition time.

For TSE acquisitions, DL-reconstructed MRI can be used to improve on a combination of image resolution, acquisition time, and SNR, while maintaining the original contrast. In contrast to this, for the HASTE sequence, the improved DL reconstruction enables an improved image

Demographics	
Total (male/female), n	20 (8/12)
Age, mean $\pm$ SD (range), y	59 $\pm$ 13 (27–79)
Sequence and body region, n	HASTE, upper abdomen, 10 PD TSE, knee, 5 PD TSE, shoulder, 5

Table 1: Demographics of participating individuals

SD indicates standard deviation; y, years; n, number; HASTE, half-Fourier single-shot turbo spin echo; PD, proton density; TSE, turbo spin echo.

contrast. Specifically, with a higher acceleration factor the duration of the echo train can be shortened and therefore the effect of T2 decay can be reduced. As an additional benefit, the specific absorption rate (SAR) is reduced along with the number of refocusing pulses required. This allows for further sequence optimizations in the form of larger gaps between consecutively acquired slices and reduced repetition time.

### Deep Learning image reconstruction

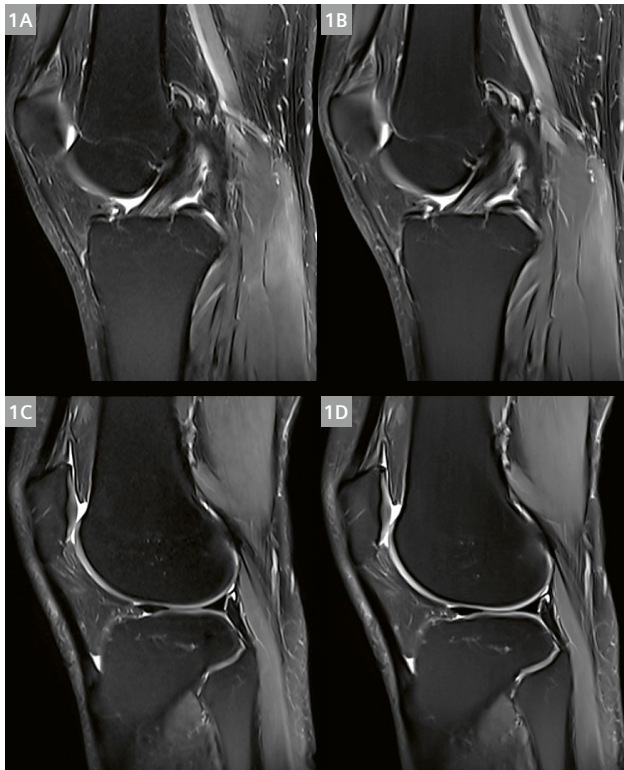
For both sequences, the image reconstruction comprises a fixed iterative reconstruction scheme or variational network [6, 7], alternating between data consistency and a Convolutional Neural Network (CNN)-based regularization. The regularization model's architecture is based on a novel hierarchical design of an iterative network that repeatedly decreases and increases the resolution of the feature maps, allowing for a more memory-efficient model than conventional CNNs. Coil sensitivity maps are estimated from the calibration data in advance as a pre-processing step. For the image reconstruction, undersampled  $k$ -space

data, bias field correction, and coil sensitivity maps are inserted into the variational network.

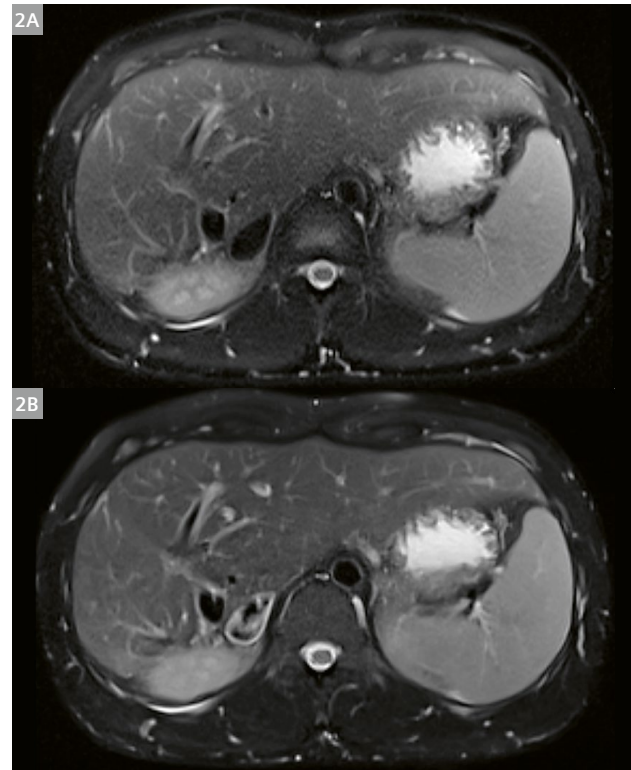
The reconstruction was trained using volunteer acquisitions consisting of about 10,000 slices for each sequence type using conventional HASTE and TSE protocols acquired on various clinical 1.5T and 3T scanners (MAGNETOM scanners, Siemens Healthcare, Erlangen, Germany).

### Implementation of DL image reconstruction in clinical workflow

To apply the DL reconstruction on clinically used MRI scanners, the network was converted to a C++ implemented inference framework. For the CPU-only reconstruction, inference needed about 2 seconds per slice for the protocol settings used. As the reconstruction was triggered after the end of the acquisition, the resulting perceived reconstruction time was 2–3 minutes including additional pre and post-processing. A GPU-based reconstruction is expected to reduce this duration to approximately 10 seconds, but was not available on the clinical scanners used.



**1** 31-year-old female participant with MRI of the knee in coronal (upper row) and sagittal (lower row) plane at 3T. Standard reconstructed PD-weighted TSE (1A and 1C) show more noise compared to Deep Learning-reconstructed PD-weighted TSE (1B and 1D). The delineation and assessment of anatomic structures, such as the anterior cruciate ligament, is comparable in both reconstructions.



**2** 20-year-old male participant with MRI of the liver in axial plane at 1.5T. Image noise and edge sharpness of anatomical structures are improved in Deep Learning-reconstructed HASTE (2B) compared to standard reconstructed HASTE (2A). Furthermore, the acquisition of the Deep Learning-reconstructed HASTE is possible within just one breath-hold.

### Image quality analysis

Institutional review board approval was obtained for this prospective monocentric study. All study procedures were conducted in accordance with the ethical standards as laid down in the 1964 Declaration of Helsinki and its later amendments.

Accelerated MR images with DL reconstruction were prospectively acquired along with standard MR images on 1.5T and 3T MRI scanners (MAGNETOM Prisma<sup>fit</sup>, MAGNETOM Vida, MAGNETOM Skyra, MAGNETOM Avanto, and MAGNETOM Aera, Siemens Healthcare, Erlangen, Germany) and an exemplary sample of 20 participants were included in this analysis (see Table 1). Two radiologists with three to ten years of experience in MRI who were blinded to participant information, acquisition parameters, and image reconstruction rated in consensus both standard MR images and accelerated MR images with DL reconstruction by using a random order. Overall image quality, artifacts, edge sharpness, and diagnostic confidence ratings were performed on an ordinal 5-point Likert scale ranging from one to five, with five being best. Reading scores were considered sufficient when reaching  $\geq 3$ .

Image analysis was performed on a PACS workstation (GE Healthcare Centricity™ PACS RA1000, Milwaukee, WI, USA).

Statistical analysis was performed using SPSS version 26 (IBM Corp, Armonk, NY, USA). Besides descriptive statistics, comprising median and interquartile range (IQR), nonparametric paired Wilcoxon signed-rank tests

were used to analyze Likert scores for image quality, artifacts, edge sharpness, and diagnostic confidence assessments. P-values less than 0.05 were considered statistically significant.

### Results

The aim of this report was to describe the implementation of a DL image reconstruction in clinical workflow and evaluate its obtainable image quality in daily clinical routine. All sequences with DL image reconstruction were successfully implemented in clinical workflow and DL sequences were successfully acquired in all participants in all body parts. Fat suppression could be applied successfully for the TSE and HASTE sequences implemented with DL image reconstruction.

For TSE sequences, DL enabled a time saving of  $\geq 50\%$ . As expected, SAR did not exceed normal levels. For HASTE sequences, DL allowed for an acquisition time reduction of  $> 50\%$ . As a single-shot sequence with a long train of refocusing pulses, HASTE is impaired by high power deposition, which limits its use at high resolutions and high field strengths, particularly if combined with acceleration techniques such as PI [8]. The DL algorithm used effectively reduced TA while staying within the SAR limitations. An overview of exemplary acquisition parameters is displayed in Table 2.

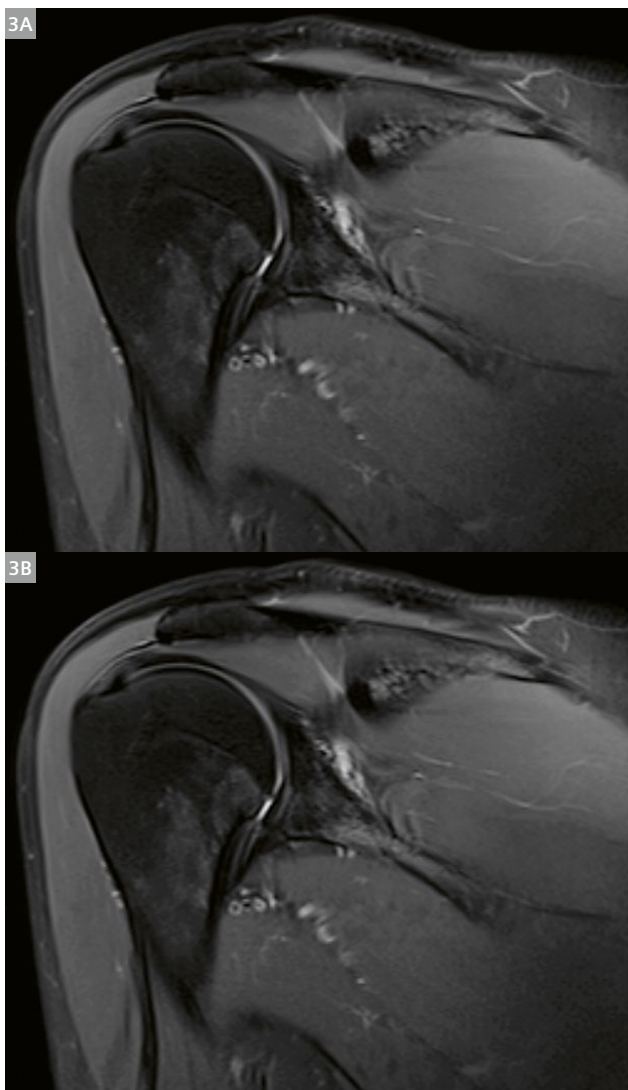
Radiologists rated the overall image quality of HASTE and PD TSE with DL reconstruction as excellent (median 5, IQR 4.25–5) and even superior to standard HASTE and

Sequence	HASTE		PD TSE FS	
	standard	DL	standard	DL
Body part	upper abdomen	upper abdomen	knee	knee
Tesla	1.5T	1.5T	3T	3T
Orientation	axial	axial	coronal	coronal
TA, min	1:28–1:44	0:16	3:11	1:33
FOV, mm	293 × 360	293 × 360	150	150
Voxel size, mm	1.13 × 1.13 × 6.0	1.13 × 1.13 × 6.0	0.2 × 0.2 × 3.0	0.2 × 0.2 × 3.0
TR, ms	1400	500	3790	3580
TE, ms	94	94	44	41
FA, degree	160	160	150	150

**Table 2: Exemplary acquisition parameters of standard and vv sequences**

HASTE indicates half-Fourier single-shot turbo spin echo; PD, Proton Density; TSE, turbo spin echo; FS, fat saturation; DL, deep learning; T, Tesla; TA, time of acquisition; FOV, field of view; TR, repetition time; TE, echo time; FA, flip angle.

PD TSE sequences (median 4, IQR 4–5,  $p<0.05$ ). No severe artifacts occurred when using DL reconstruction as no difference was found in the extent of artifacts between standard (median 5, IQR 4–5) and DL-reconstructed sequences (median 5, IQR 4.25–5,  $p=0.157$ ). Edge sharpness was improved with the DL reconstruction (median 5, IQR 5–5) compared to standard sequences (median 5, IQR 4–5,  $p<0.05$ ). Diagnostic confidence was rated as comparable between the sequences (median 5, IQR 4.25–5,  $p=0.317$ ). Image examples are given in Figures 1–3.



**3** 35-year-old female participant with MRI of the shoulder in coronal plane at 3T. Image noise and edge sharpness are improved in Deep Learning-reconstructed PD-weighted TSE (3B) compared to standard reconstructed PD-weighted TSE (3A).

## Discussion

Although MRI has evolved to become a modality of choice for the diagnosis of several diseases, its availability is still limited for reasons closely related to long examination times [1]. One promising approach to solve this shortcoming is to use novel techniques, including artificial intelligence (AI) and machine learning, to accelerate the acquisition of MR images. AI is in the public focus more than ever due to enormous innovations in the last decade, especially in the field of radiology. Novel AI techniques and new algorithms have not only been developed and trained to detect pathologies, but also to improve and accelerate image acquisition and reconstruction [9, 10]. Despite the rapid progress of all technological advances, especially in radiology, there is still a lack of widespread implementation in daily clinical routine. Therefore, the aim of this report was to describe the implementation of DL image reconstruction in daily routine and evaluate the obtainable image quality.

Our investigation demonstrates the successful implementation of DL reconstruction techniques in daily clinical workflow with a substantial reduction of TA and at the same time even higher image quality and improved edge sharpness compared to standard sequences. Effects of the implementation of these new techniques are primarily based on the reduction of TA without compromising regarding the extent of artifacts and diagnostic confidence. The reduction in TA of more than 50%, in particular, yields enormous potential for workflow optimization, increased availability of MRI, and improvement of healthcare.

One central issue in MRI has always been the shortage of scanners. Drastic acceleration and reduction of examination times might provide one piece of the big puzzle of how to enhance healthcare and balance the weight of supply and demand. This is of particular interest in low-income countries where there is only limited access to high-quality diagnostic MRI. DL reconstructions are mostly not very demanding regarding the technical specifications and can therefore also be applied in countries with less-developed technical infrastructures. Another issue that merits consideration is the increasing importance of MRI in standard of care diagnostic procedures. MRI has become increasingly important in many pathologies for diagnosis, biopsy planning, therapy surveillance, and follow-up [11–14].

One of the most challenging tasks in medicine has always been finding a compromise between best medical care and best economic outcome. As most healthcare systems worldwide are insurance based, they all face the same problem: shortage of money versus increase in

demand due to development of new expensive therapies, increased life expectancy, and new diagnostic possibilities. Reduction in acquisition time might allow a higher number of examinations per day.

As we successfully implemented DL sequences in imaging of different body regions, this report is intended to motivate radiologists to establish new AI techniques in everyday clinical practice to further accelerate MRI and improve access to MRI for more patients. For this report we selected some illustrative examples of the DL examinations conducted to provide a brief introduction into how DL sequences are implemented in daily routine. Systematic analyses of the different body regions are in progress and will be outlined in separate studies.

To conclude, DL image reconstruction can be implemented in clinical workflow and enables accelerated image acquisition while maintaining excellent image quality.

## References

- 1 Vanderby S, Badea A, Pena Sanchez JN, Kalra N, Babyn P. Variations in Magnetic Resonance Imaging Provision and Processes Among Canadian Academic Centres. *Can Assoc Radiol J.* 2017 Feb;68(1):56–65.
- 2 Knoll F, Hammernik K, Zhang C, Moeller S, Pock T, Sodickson DK, et al. Deep-Learning Methods for Parallel Magnetic Resonance Imaging Reconstruction: A Survey of the Current Approaches, Trends, and Issues. *IEEE Signal Proc Mag.* 2020 Jan;37(1):128–140.
- 3 Lin DJ, Johnson PM, Knoll F, Lui YW. Artificial Intelligence for MR Image Reconstruction: An Overview for Clinicians. *Journal of Magnetic Resonance Imaging.* 2020 Feb 12.
- 4 Hyun CM, Kim HP, Lee SM, Lee S, Seo JK. Deep learning for undersampled MRI reconstruction. *Phys Med Biol.* 2018 Jul;63(13).
- 5 Knoll F, Hammernik K, Kobler E, Pock T, Recht MP, Sodickson DK. Assessment of the generalization of learned image reconstruction and the potential for transfer learning. *Magn Reson Med.* 2019 Jan;81(1):116–128.
- 6 Hammernik K, Klatzer T, Kobler E, Recht MP, Sodickson DK, Pock T, et al. Learning a variational network for reconstruction of accelerated MRI data. *Magn Reson Med.* 2018 Jun;79(6):3055–3071.
- 7 Schlemper J, Caballero J, Hajnal JV, Price AN, Rueckert D. A Deep Cascade of Convolutional Neural Networks for Dynamic MR Image Reconstruction. *IEEE Trans Med Imaging.* 2018 Feb;37(2):491–503.
- 8 Schulz J, Marques JP, Ter Telgte A, van Dorst A, de Leeuw FE, Meijer FJA, et al. Clinical application of Half Fourier Acquisition Single Shot Turbo Spin Echo (HASTE) imaging accelerated by simultaneous multi-slice acquisition. *Eur J Radiol.* 2018 Jan;98:200–206.
- 9 Wichmann JL, Willemink MJ, De Cecco CN. Artificial Intelligence and Machine Learning in Radiology: Current State and Considerations for Routine Clinical Implementation. *Invest Radiol.* 2020 Sep;55(9):619–627.
- 10 Weikert T, Cyriac J, Yang S, Nesic I, Parmar V, Stieljes B. A Practical Guide to Artificial Intelligence-Based Image Analysis in Radiology. *Invest Radiol.* 2020 Jan;55(1):1–7.
- 11 Petralia G, Padhani AR, Pricolo P, Zugni F, Martinetti M, Summers PE, et al., Italian Working Group on Magnetic R. Whole-body magnetic resonance imaging (WB-MRI) in oncology: recommendations and key uses. *Radiol Med.* 2019 Mar;124(3):218–233.
- 12 Gillessen S, Omlin A, Attard G, de Bono JS, Efstatithiou E, Fizazi K, et al. Management of patients with advanced prostate cancer: recommendations of the St Gallen Advanced Prostate Cancer Consensus Conference (APCCC) 2015. *Ann Oncol.* 2019 Dec;30(12):e3.
- 13 Beets-Tan RG, Beets GL, Vliegen RF, Kessels AG, Van Boven H, De Bruine A, et al. Accuracy of magnetic resonance imaging in prediction of tumour-free resection margin in rectal cancer surgery. *Lancet.* 2001 Feb 17;357(9255):497–504.
- 14 Balleyguier C, Sala E, Da Cunha T, Bergman A, Brkljacic B, Danza F, et al. Staging of uterine cervical cancer with MRI: guidelines of the European Society of Urogenital Radiology. *Eur Radiol.* 2011 May;21(5):1102–10.

## Contact



Judith Herrmann, M.D.  
Eberhard Karls University Tuebingen  
Department of Diagnostic and Interventional Radiology  
Hoppe-Seyler-Strasse 3  
72076 Tuebingen  
Germany  
judith.herrmann@med.uni-tuebingen.de



Ahmed Othman, M.D.  
University Medical Center  
Department of Neuroradiology  
55131 Mainz  
Germany  
ahmed.e.othman@googlemail.com

# Fast and Reliable Liver Imaging Using Deep Learning HASTE

Sébastien Mulé, M.D., Ph.D.<sup>1,2,3</sup>; Aurélien Massire, Ph.D.<sup>4</sup>; Pierre Zerbib<sup>1</sup>; Dominik Nickel, Ph.D.<sup>5</sup>;  
Alain Luciani, Ph.D., M.D.<sup>1,2,3</sup>

<sup>1</sup>Service d'Imagerie Médicale, AP-HP, Hôpitaux Universitaires Henri Mondor, Créteil, France

<sup>2</sup>Faculté de Santé, Université Paris-Est Créteil, Créteil, France

<sup>3</sup>INSERM IMRB, U 955, Equipe 18, Créteil, France

<sup>4</sup>Siemens Healthcare SAS, Saint-Denis, France

<sup>5</sup>Siemens Healthineers, Erlangen, Germany

## Introduction

With its superb ability to detect, characterize, and differentiate focal lesions in the liver, magnetic resonance imaging (MRI) has become the gold standard and problem-solving modality in diagnostic abdominal imaging. Despite its indisputable clinical value, however, MRI is not as robust and reliable as other modalities, e.g., CT scans. This is mainly due to breathing-induced motion during the time-consuming data sampling process and the long scan time of 25–30 minutes.

## Triggered and breath-hold acquisitions

Different strategies to minimize the susceptibility to artifacts have been developed over the last decades. The most routinely used ones are: (multiple-)breath-hold acquisitions; prospectively and retrospectively triggered acquisitions where only data in specific states of the respiratory cycle is acquired or used for reconstruction; and data sampling trajectories which are inherently less susceptible to motion, such as radial or BLADE sampling. Each approach has certain advantages and disadvantages: With triggered acquisitions, the data sampling rate over time is low and scan times can easily exceed five minutes per acquisition, particularly in patients with irregular or shallow breathing patterns. On the other hand, triggered acquisitions do not require major compromises in spatial resolution, as data sampling does not have to be “squeezed” into a single or a few breath-holds. Non-Cartesian sampling schemes such as radial trajectories are very robust because they simply average out motion effects, but they may show image blurring and streaking artifacts.

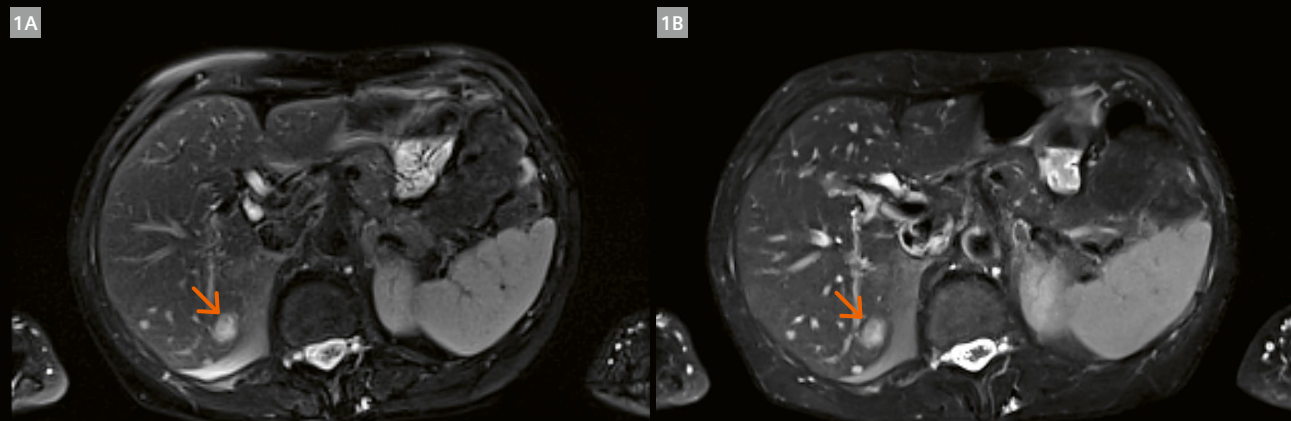
The advent and clinical adoption of MR acceleration techniques that use “intelligent” *k*-space subsampling and parallel data sampling – such as SENSE, GRAPPA, CAIPIRINHA, SMS, and Compressed Sensing – have drastically reduced breath-hold durations and data sampling times for most of the relevant imaging contrasts in abdominal MRI. However, they are only applicable to certain contrast weightings and sequence types.

One of the remaining weak points of a typical, routine liver MRI protocol (with T2-weighted imaging, diffusion-weighted imaging, T1-weighted in- and opposed-phase imaging, dynamic contrast-enhanced T1-weighted scanning, and post-contrast T1-weighted scans) is the acquisition of high-resolution, high-quality T2-weighted TSE images in a short scan time. To achieve appropriate T2-weighting, long TRs have to be chosen, which require several breath-holds or long respiratory-triggered protocols to cover multiple segments of the *k*-space and thereby achieve sufficient *k*-space sampling to reconstruct high-resolution images. Modified segmented Cartesian sampling schemes in which several rotated, overlapping bundles of parallel *k*-space lines are acquired and combined are available from all vendors (PROPELLER, MultiVane, BLADE) and have been shown to improve robustness and SNR compared to conventional TSE scanning. Scan times, however, remain a challenge for both triggered and multiple-breath-hold acquisitions.

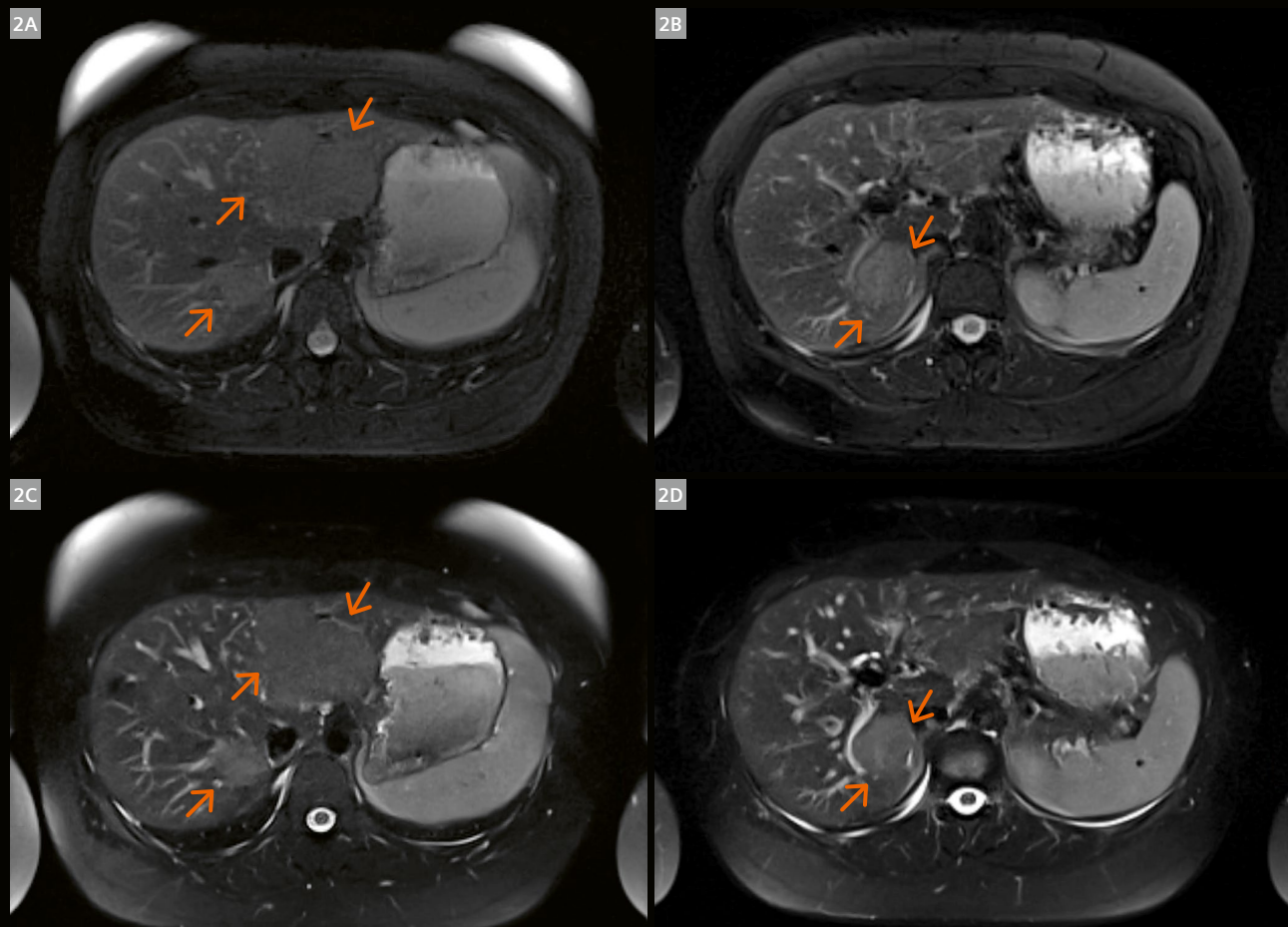
## Single-shot acquisition

A more radical approach is to acquire data for a complete imaging slice in a single shot, as implemented in the half-Fourier acquisition single-shot turbo spin-echo (HASTE) sequence. Since data acquisition requires just fractions of a second, motion artifacts do not pose any problem. Breath-holds or synchronization with breathing are only required to achieve uniform slice coverage across the abdomen. On the downside, reading out the entire *k*-space in a single shot requires a compromise in spatial resolution as the echo train length (which scales with spatial resolution) makes HASTE prone to T2-decay-related blurring and SNR reduction. Accordingly, HASTE images are not typically considered adequate for high-resolution T2-weighted imaging of the abdomen. They are mostly used to provide a quick overview or to acquire “something” in challenging cases, e.g., pediatric patients<sup>1</sup>.

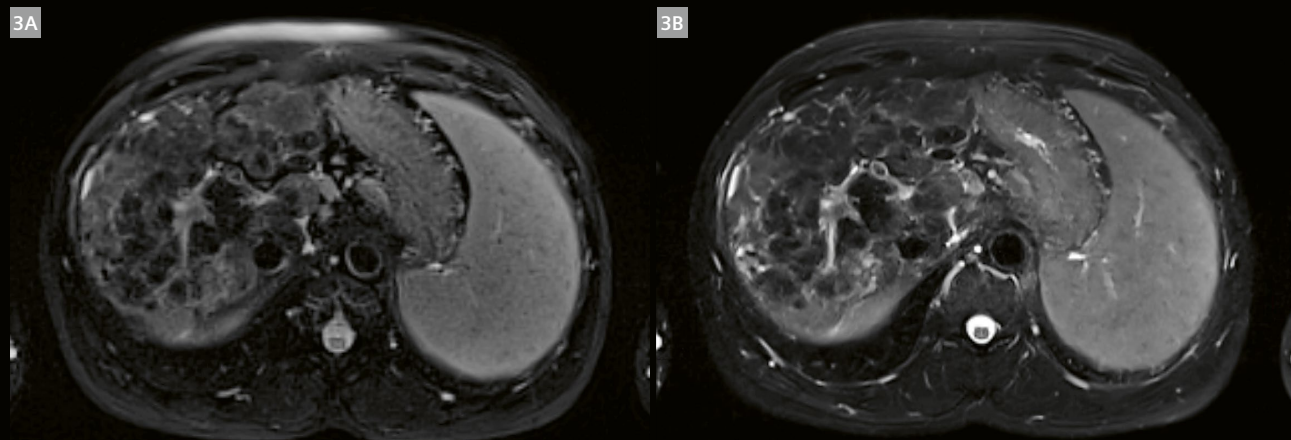
<sup>1</sup>MR scanning has not been established as safe for imaging fetuses and infants younger than two years of age. The responsible physician must evaluate the benefits of the MR examination compared to those of other imaging procedures.



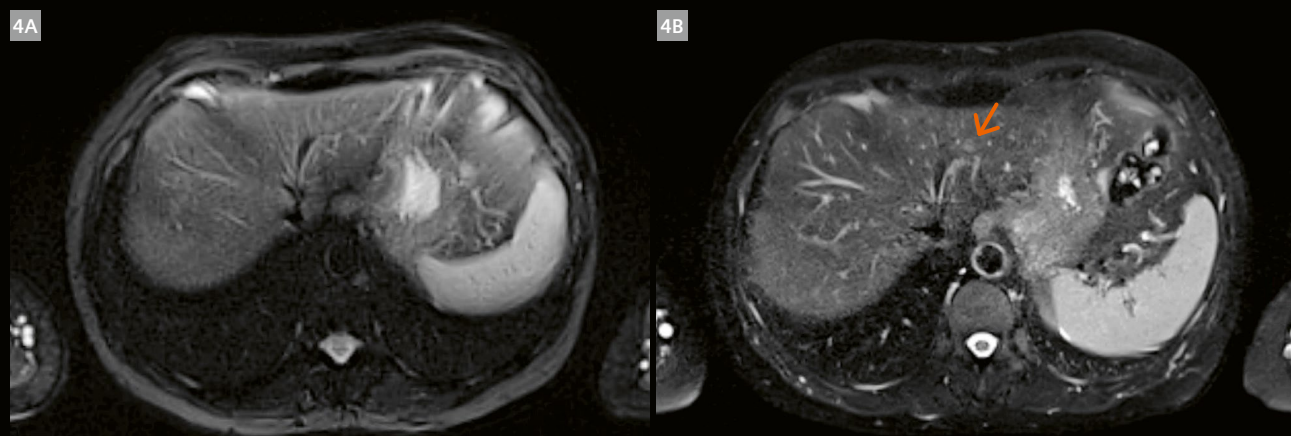
**1** An 82-year-old female patient with hepatic angiomyolipoma.  
(1A) T2-weighted FS BLADE TSE and (1B) T2-weighted FS DL HASTE. Similar lesion conspicuity with significantly reduced acquisition time for DL HASTE, and higher SNR in the liver on DL HASTE images.



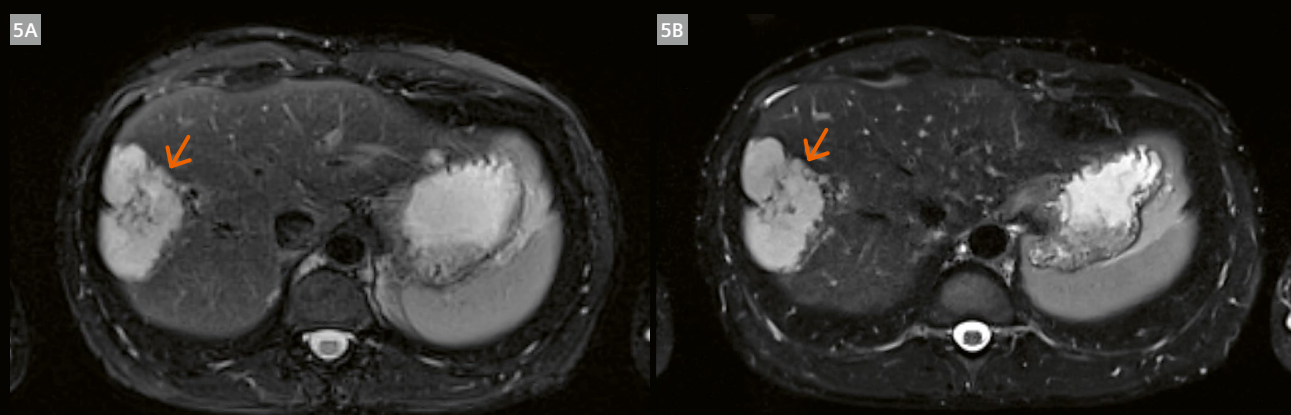
**2** A 31-year-old female patient with focal nodular hyperplasia.  
(2A, B) T2-weighted FS BLADE TSE and (2C, D) T2-weighted FS DL HASTE. DL HASTE provides higher lesion-to-liver contrast and sharper lesion delineation.



**3** A 49-year-old male patient with sarcoidosis nodules.  
(3A) T2-weighted FS BLADE TSE and (3B) T2-weighted FS DL HASTE. There is higher lesion conspicuity and lesion-to-liver CNR of multiple hypointense liver nodules on the DL HASTE images.



**4** A 72-year-old female patient with focal nodular hyperplasia.  
(4A) T2-weighted FS BLADE TSE and (4B) T2-weighted FS DL HASTE. The lesion is not seen on the BLADE image (4A) but is individualized on the DL HASTE image (4B).



**5** A 48-year-old male patient with atypical hemangioma.  
(5A) T2-weighted FS BLADE TSE and (5B) T2-weighted FS DL HASTE. The DL HASTE image shows sharper lesion conspicuity and higher liver SNR.

## Deep learning HASTE

The introduction of a novel image reconstruction method usually referred to as deep learning reconstruction [2, 3] can potentially overcome the abovementioned challenge in HASTE imaging (and other MR imaging problems). Instead of a conventional Fourier transformation of the acquired  $k$ -space data, a deep neural network is used to translate frequency information into the image domain as described in detail elsewhere [4]. In short, high-quality HASTE raw data and respective images were acquired as ground truth information. A neural network was then trained to "associate" down-sampled raw data (achieved by retrospectively removing  $k$ -space data, thereby simulating higher parallel imaging factors) with high-quality output images. If the trained network is then presented with highly undersampled input data, high-quality images can be reconstructed while conventional reconstruction would result in artifacts and low SNR. The main advantages of Deep Learning HASTE are increased SNR, improved image contrast, and reduced T2 blurring by shortening the echo train with parallel imaging. Another advantage is the reduction in the specific absorption rate (SAR often presents a challenge in HASTE acquisitions, particularly at 3T), which allows substantial reductions in TR and therefore acquisition time.

## Materials and methods

At our institution, we had access to a prototypical implementation of the DL HASTE sequence<sup>2</sup>. All patients underwent a multiphase liver MRI examination in a clinical 1.5T MR system (MAGNETOM Avanto<sup>fit</sup>, Siemens Healthcare, Erlangen, Germany) in supine position with an 18-channel body array and a 32-channel spine array. We used two sequences:

- Multiple-breath-hold, fat-suppressed Turbo Spin-Echo T2-weighted (TSE BLADE) with an average acquisition time of ~ 2.5 minutes
- Single-breath-hold, fat-suppressed Half-Fourier Acquisition Single-shot Turbo Spin-Echo T2-weighted sequence with deep learning reconstruction (DL HASTE), with an average acquisition time of ~ 18 seconds

We present a series of clinical cases which show that DL HASTE provides similar image quality and diagnostic information as the longer conventional, triggered BLADE acquisition, which is the clinical standard at our institution. These results are also in line with the published literature, which has reported remarkable time savings, as well as comparable image quality and diagnostic confidence for staging hepatic pathologies and characterizing hepatic lesions [4].

<sup>2</sup>Work in progress. The application is currently under development and is not for sale in the U.S. and in other countries. Its future availability cannot be ensured.

A usual and reasonable concern is that deep learning reconstruction may result in loss of fine structures, eradication of focal lesions, or hallucination of structures that do not exist. Therefore, it is worth mentioning that the reconstruction pipeline is set up in a similar way to clinically accepted and well-established methods, such as compressed sensing reconstruction: several iterations for image improvement are performed within clear and strict boundaries so as not to conflict with physical reality and data integrity.

Both our cohort and the literature gave us confidence that the DL HASTE method is not affected by the above-mentioned issues and provides reliable, robust, and high-quality image information in a single breath-hold. We believe the method holds great potential for saving valuable scan time in abdominal MRI studies and beyond.

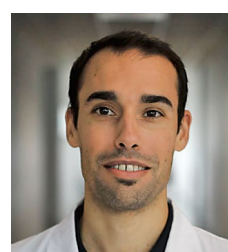
## References

- 1 Rosenkrantz AB, Mannelli L, Mossa D, Babb JS. Breath-hold T2-weighted MRI of the liver at 3T using the BLADE technique: impact upon image quality and lesion detection. Clin Radiol. 2011;66(5):426–33.
- 2 Schlemper J, Caballero J, Hajnal JV, Price AN, Rueckert D, et al. A Deep Cascade of Convolutional Neural Networks for Dynamic MR Image Reconstruction. IEEE Trans Med Imaging. 2018;37(2):491–503.
- 3 Hammernik K, Klatzer T, Kobler E, Recht MP, Sodickson DK, Pock T, et al. Learning a variational network for reconstruction of accelerated MRI data. Magn Reson Med. 2018;79(6):3055–3071.
- 4 Herrmann J, Gassenmaier S, Nickel D, Arberet S, Afat S, Lingg A, et al. Diagnostic Confidence and Feasibility of a Deep Learning Accelerated HASTE Sequence of the Abdomen in a Single Breath-Hold. Invest Radiol. 2021;56(5):313–319.



## Contact

Professor Alain Luciani, Ph.D., M.D.  
Hôpital Henri-Mondor  
HU Henri Mondor,  
Medical Imaging Department,  
APHP, UPEC University  
51 Avenue Mal De Lattre De Tassigny  
94000 Créteil  
France  
alain.luciani@aphp.fr



Sébastien Mulé, M.D., Ph.D.  
HU Henri Mondor  
Medical Imaging Department,  
APHP, UPEC University  
51 Avenue Mal De Lattre De Tassigny  
94000 Creteil  
France  
sebastien.mule@aphp.fr

# Full-scale vs. Abbreviated Sequences in MR Mammography – the Best of Both Worlds

Clemens Kaiser, M.D.

Department of Radiology and Nuclear Medicine, University Medical Center Mannheim, Germany

## Background

According to the current state of the literature, MR Mammography detects breast cancer with the highest accuracy of all imaging techniques. Since 1984, when the first scientific results were published, more than 15,000 publications have followed, proving the diagnostic benefit of this method [1].

MRI offers unique soft-tissue contrast that can be enhanced using contrast agents to reliably detect tumor-angiogenic processes and carcinomas from a size of 2–3 mm [2, 3]. A significant portion of carcinomas are verifiable by MR Mammography only [4–6]. In addition, this method enables the dependable detection of carcinomas in an early stage [6–8]. This can be prognostically very important for patients.

Literature has shown that preoperative staging with MR Mammography reduces the local rate of recurrence

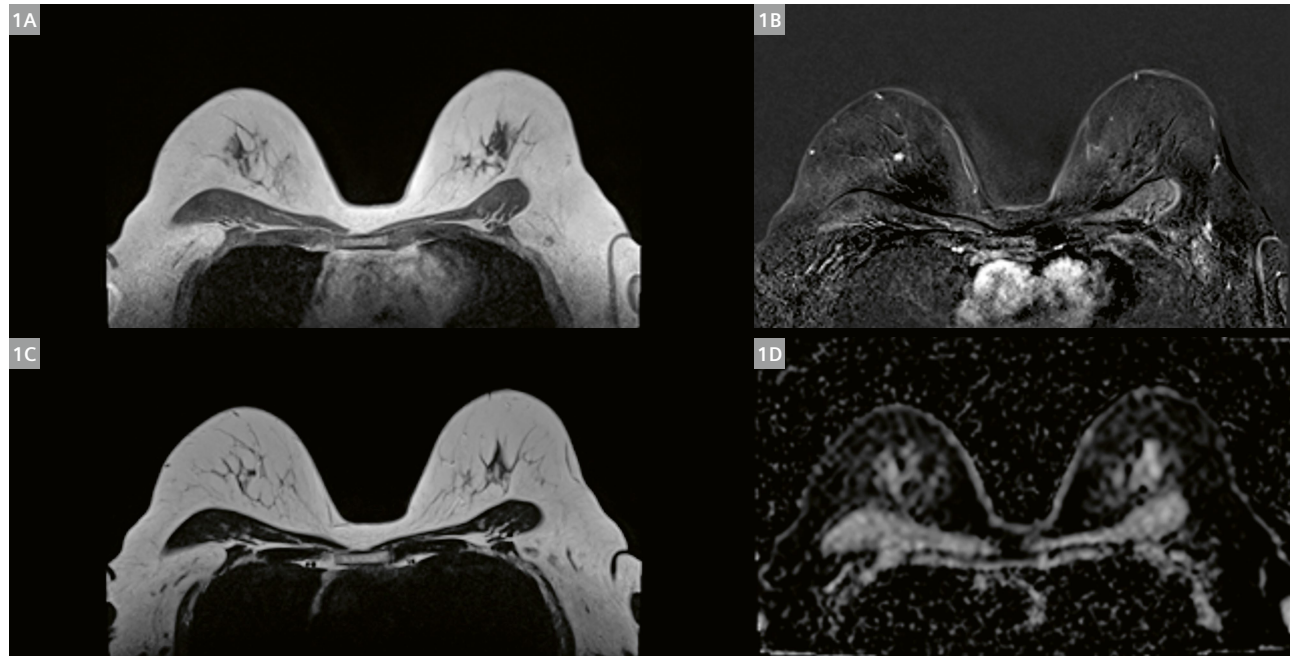
and influences therapy decisions significantly [9–12]. In 3% of all cases, this led to detection of contra-lateral carcinomas, too.

With a negative predictive value of 100% [13], MR Mammography can, moreover, exclude invasive carcinomas with certainty, impacting on biopsy rates and leading to reduced patient stress due to a more reliable diagnosis.

## Screening women with dense breast tissue

Despite these well-known diagnostic benefits, only a few patients get to profit from MR Mammography in Germany (and many other countries) because the examination is currently only indicated and reimbursed in a few exceptional indications, e.g., high-risk screening collectives [14].

At the same time, conventional breast cancer screening programs have not managed to decrease mortality



**1** (1A) First minute post application of 1 mmol/kg Gd; (1B) First min subtraction, (1C) T2-weighted scan; (1D) ADC map. The scan reveals a 3 mm carcinoma in the upper inner quadrant. The lesion shows a type 3 curve, pos. Root Sign and hypointensity in T2. Due to its size and the resolution it is not visible in the ADC map.

rates from breast cancer significantly – neither nationally nor internationally [15]. This could indicate a possible new diagnostic role for MR Mammography, especially as a screening tool for women of average risk of developing breast cancer but with dense breast tissue, following the experience of, for example, Dutch screening algorithms.

There has, however, been critical discussion in the past of the financial aspects in particular, as these present the main barriers to the acceptance of MR Mammography as a screening tool.

In 2019, extensive new data on the screening of women with dense breast tissue using MR Mammography was published, indicating a significant reduction in interval carcinomas [7, 8] and giving a first hint of evidence of a reduction in mortality through the use of MR Mammography as a screening tool with interval carcinomas as an accepted surrogate marker for mortality.

## Cost-effective MR Mammography

In addition to delivering gratifying clinical results, these data also enabled a cost-effectiveness analysis that showed that MR Mammography is cost-effective [16].

Early detection of small carcinomas in the breast saves on subsequent additional therapy costs. Especially for women with breast tissue of high density, MR Mammography offers a cost-efficient and accurate screening tool. That is why its role in prevention should be reconsidered.

An additional approach to reduce the costs of examination with MRI, is "abbreviated protocol magnetic resonance imaging" (AB-MRI). The aim of AB-MRI is to reduce scan time and thereby the costs of examinations by omitting some sequences for better use in high-throughput screening settings.

As early as 2012, Fischer et al. proposed [17] that acquiring just pre- and post-gadolinium (Gd) injection T1-weighted sequences could reduce scan times and costs significantly while at the same time benefiting from the high negative predictive value of MR Mammography as breast cancer could be excluded without evidence of Gd enhancement. In cases when gadolinium enhancement is visible, a full-scale examination, including T2-weighted images and a complete dynamic series is required. This results in additional costs and nevertheless a second charge of contrast medium.

Further publications, for example by Kuhl et al. [18], showed that such an approach represents a full-featured alternative to conventional diagnostic mammography and is at least equivalently cost-effective in comparison.

Over the last 10 years, more and more publications have investigated various approaches to reducing costs by applying different sets of selected sequences, sometimes relying on diffusion-weighted images only, and have reported varying results.

## Abbreviated vs. full-scale protocols

As of today, there is still a lack of definition of abbreviated protocols. The major studies commonly agree on a pre-contrast and a post-contrast image as well as T2-weighted images if the total length of the protocol does not exceed 10 minutes in total length [19].

While the study has impressively demonstrated that AB-MRI allows to detect significantly more invasive carcinomas at an earlier point in time than digital breast tomosynthesis (DBT) in women with dense breast [19] it remains unknown how the overall performance characteristics would have been improved with a full scale MR Mammography protocol.

MR scanners from Siemens Healthineers with NumarisX software now offer new acquisition techniques that enable radiologists to perform a full-scale MR examination in under 10 minutes, the time frame of abbreviated protocols and far below regular acquisition times of full-scale protocols.

## The best of both worlds

At University Hospital Mannheim, a 1.5T MAGNETOM Sola is being used for standard MR Mammography examinations. This scanner is equipped with the Turbo Suite Excelerate package that includes the Simultaneous Multi-Slice (SMS) acquisition technique.

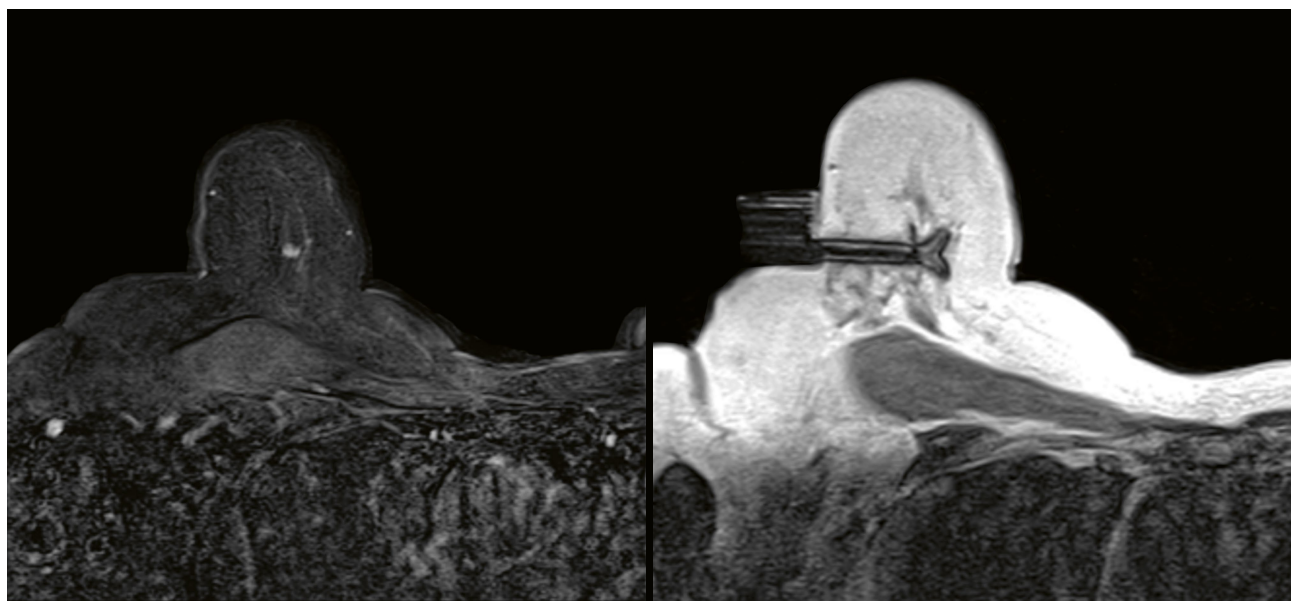
With SMS, it is possible to excite and readout multiple slices simultaneously, effecting a remarkable acceleration. SMS can be used for TSE sequences as well as for diffusion-weighted imaging (DWI) and can also be combined with iPAT.

MR Mammography for clinical diagnostic routine was set up with the following protocols:

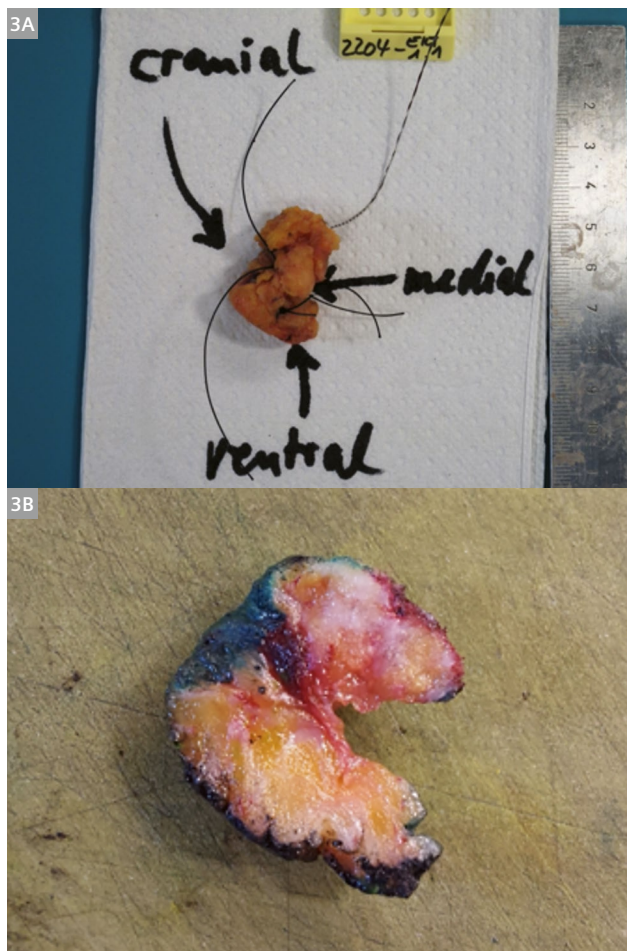
- 3 mm axial T2 TSE with iPAT 2 and SMS 2.  
Inplane resolution:  $0.8 \times 0.8 \text{ mm}^2$ , 56 slices,  
TA: 1:36 min.
- 3 mm axial EPI Diffusion ( $b$ -values  $50 \text{ s/mm}^2$  and  $800 \text{ s/mm}^2$ ) 3-scan trace with iPAT 2 and SMS 2.  
Inplane resolution:  $1.5 \times 1.5 \text{ mm}^2$  (interpolated), 56 sl.,  
TA: 1:46 min.
- 1.5 mm axial T1 fl3d as dynamic series  
(1+5, 20s delay), with iPAT 3.  
Inplane resolution:  $0.9 \times 0.9 \text{ mm}^2$ , 112 sl., TA: 6:21 min.

The .exar1 protocol is available for download at:  
[www.siemens-healthineers.com/magnetom-world](http://www.siemens-healthineers.com/magnetom-world)  
> Clinical Corner > Protocols > Breast MRI

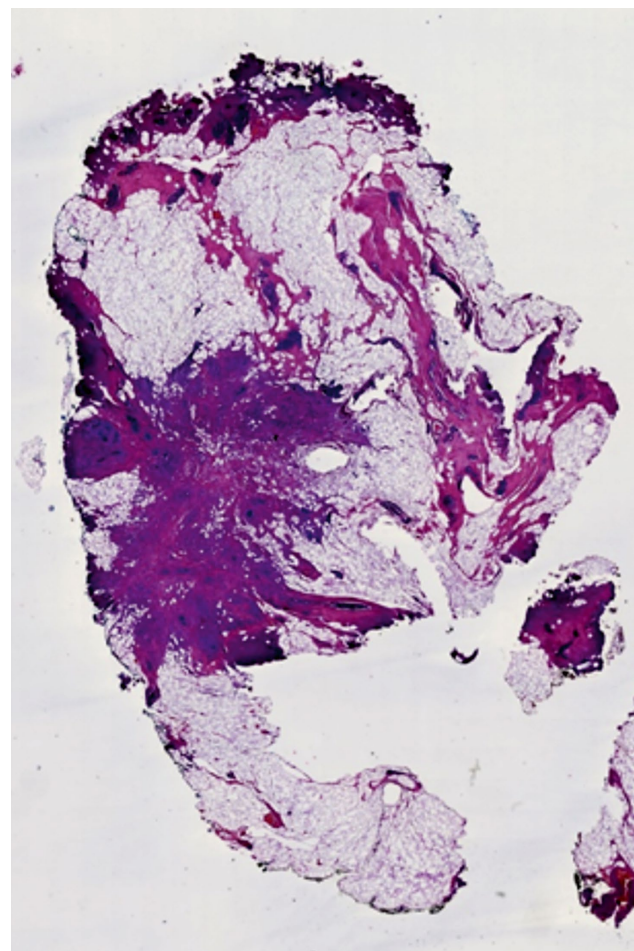
At our institution we are using an 18-channel BI Mammography coil; the program, however, may also be used with other (high-channel) MR Mammography coils with very similar or the same parameters.



**2** MR-guided wire localization before open surgical excision.



**3** (3A) Excised specimen, (3B) excised specimen after coloring.



**4** Histopathological slice revealing an invasive ductal carcinoma, 3 mm.

The full set of dynamic T1-weighted sequences (pre-injection and 5 minutes post injection of 1 mmol/kg Gd) with a time resolution of exactly 1 minute each is hereby adopted from standing protocols as suggested in the BIRADS Lexicon. The full dynamic set covering 6 minutes enables the reader to evaluate kinetic details in depth, a key requirement in optimizing the specificity of MR Mammography. Depicting all 6 minutes has been considered most time-consuming in the formation of abbreviated sequences and was therefore the main subject of protocol abbreviation.

T2-weighted sequences – as they are indicated in abbreviated as well as in full-scale protocols – are essential in assessing morphological aspects of lesions as they usually cover the field of view with a significantly higher resolution. T2-weighted sequences also deliver highly important diagnostic information, such as micro bleeding, perifocal, or prepectoral edema [20, 21].

Diffusion-weighted imaging enables the assessment of diffusibility and offers additional room to increase specificity [22–25], although a certain resolution bias makes assessing small and non-focal lesions difficult.

Both T2- and diffusion-weighted sequences can be acquired without significant loss of image quality in half the acquisition time using SMS [26], paving the way to a full-scale protocol in under 10 minutes and making screening women outside current indications feasible.

## Conclusion

With SMS the need for abbreviated protocols may be overrated. You no longer need to decide between full-scale or abbreviated protocols, because the measurement time is now so short that you can confidently run a full-scale protocol just as efficiently as an abbreviated one.

This should be a giant step towards a feasible solution for screening women outside current indications.

## Acknowledgments

I highly appreciate the support of Thomas Illigen, Siemens Healthineers, Erlangen, Germany, in setting up the protocol and supporting this manuscript.

## References

- Kaiser WA, Zeitler E (1989) MR imaging of the breast: fast imaging sequences with and without Gd-DTPA. Preliminary observations. *Radiology* 170:681–686.
- Folkman J, Watson K, Ingber D, Hanahan D (1989) Induction of angiogenesis during the transition from hyperplasia to neoplasia. *Nature* 339:58–61.
- Buadu LD, Murakami J, Murayama S, et al. (1996) Breast lesions: correlation of contrast medium enhancement patterns on MR images with histopathologic findings and tumor angiogenesis. *Radiology* 200:639–649.
- Kuhl C, Weigel S, Schrading S, et al. (2010) Prospective multicenter cohort study to refine management recommendations for women at elevated familial risk of breast cancer: the EVA trial. *J Clin Oncol Off J Am Soc Clin Oncol* 28:1450–1457.
- Sardanelli F, Podo F, Santoro F, et al. (2011) Multicenter surveillance of women at high genetic breast cancer risk using mammography, ultrasonography, and contrast-enhanced magnetic resonance imaging (the high breast cancer risk Italian 1 study): final results. *Invest Radiol* 46:94–105.
- Riedl CC, Luft N, Bernhart C, et al. (2015) Triple-modality screening trial for familial breast cancer underlines the importance of magnetic resonance imaging and questions the role of mammography and ultrasound regardless of patient mutation status, age, and breast density. *J Clin Oncol Off J Am Soc Clin Oncol* 33:1128–1135.
- Bakker MF, de Lange SV, Pijnappel RM, et al (2019) Supplemental MRI Screening for Women with Extremely Dense Breast Tissue. *N Engl J Med* 381:2091–2102.
- Veenhuizen SGA, de Lange SV, Bakker MF, et al. (2021) Supplemental Breast MRI for Women with Extremely Dense Breasts: Results of the Second Screening Round of the DENSE Trial. *Radiol* 299(2):278–286.
- Fisher B, Anderson S, Redmond CK, et al. (1995) Reanalysis and results after 12 years of follow-up in a randomized clinical trial comparing total mastectomy with lumpectomy with or without irradiation in the treatment of breast cancer. *N Engl J Med* 333:1456–1461.
- Jacobson JA, Danforth DN, Cowan KH, et al. (1995) Ten-year results of a comparison of conservation with mastectomy in the treatment of stage I and II breast cancer. *N Engl J Med* 332:907–911.
- Fowble BL, Solin LJ, Schultz DJ, Goodman RL (1991) Ten year results of conservative surgery and irradiation for stage I and II breast cancer. *Int J Radiat Oncol Biol Phys* 21:269–277.
- Haffty BG, Goldberg NB, Rose M, et al. (1989) Conservative surgery with radiation therapy in clinical stage I and II breast cancer. Results of a 20-year experience. *Arch Surg Chic Ill* 1960 124:1266–1270.
- Bennani-Baiti B, Baltzer PA (2017) MR Imaging for Diagnosis of Malignancy in Mammographic Microcalcifications: A Systematic Review and Meta-Analysis. *Radiology* 283:692–701.
- (2020) S3-Leitlinie Mammakarzinom. 453
- Krebs - Brustkrebs. [https://www.krebsdaten.de/Krebs/DE/Content/Krebsarten/Brustkrebs/brustkrebs\\_node.html](https://www.krebsdaten.de/Krebs/DE/Content/Krebsarten/Brustkrebs/brustkrebs_node.html) Accessed 3 Mar 2020
- Kaiser CG, Dietzel M, Vag T, Froelich MF (2020) Cost-effectiveness of MR-Mammography vs. conventional Mammography in screening patients at intermediate risk of breast cancer - A model-based economic evaluation. *Eur J Radiol*. 136:109355.
- Fischer U, Korthauer A, Baum F, et al. (2012) Short first-pass MRI of the breast. *Acta Radiol* 53:267–269.
- Kuhl CK, Schrading S, Strobel K, et al. (2014) Abbreviated breast magnetic resonance imaging (MRI): first postcontrast subtracted images and maximum-intensity projection-a novel approach to breast cancer screening with MRI. *J Clin Oncol Off J Am Soc Clin Oncol* 32:2304–2310.

- 19 Comstock CE, Gatsonis C, Newstead GM, et al. (2020) Comparison of Abbreviated Breast MRI vs Digital Breast Tomosynthesis for Breast Cancer Detection Among Women With Dense Breasts Undergoing Screening. *JAMA* 323:746–756.
- 20 Baltzer P a. T, Dietzel M, Gajda null, et al. (2012) A systematic comparison of two pulse sequences for edema assessment in MR-mammography. *Eur J Radiol* 81:1500–1503.
- 21 Kaiser CG, Herold M, Baltzer PAT, et al. (2015) Is “prepectoral edema” a morphologic sign for malignant breast tumors? *Acad Radiol* 22:684–689.
- 22 Hatakenaka M, Soeda H, Yabuuchi H, et al. (2008) Apparent diffusion coefficients of breast tumors: clinical application. *Magn Reson Med Sci MRMS Off J Jpn Soc Magn Reson Med* 7:23–29.
- 23 Kuroki Y, Nasu K (2008) Advances in breast MRI: diffusion-weighted imaging of the breast. *Breast Cancer Tokyo Jpn* 15:212–217.
- 24 Wenkel E, Geppert C, Schulz-Wendland R, et al. (2007) Diffusion weighted imaging in breast MRI: comparison of two different pulse sequences. *Acad Radiol* 14:1077–1083.
- 25 Woodhams R, Matsunaga K, Iwabuchi K, et al. (2005) Diffusion-weighted imaging of malignant breast tumors: the usefulness of apparent diffusion coefficient (ADC) value and ADC map for the detection of malignant breast tumors and evaluation of cancer extension. *J Comput Assist Tomogr* 29:644–649.
- 26 Riffel J, Kannengiesser S, Schoenberg SO, et al. (2021) T2-weighted Imaging of the Breast at 1.5T Using Simultaneous Multi-slice Acceleration. *Anticancer Res* 41:4423–4429.

## Contact

PD Dr. med. Clemens Kaiser, M.D.  
Section Chief Breast  
Department of Radiology  
and Nuclear Medicine  
University Medical Center Mannheim  
Theodor-Kutzer-Ufer 1-3  
68167 Mannheim  
Phone: +49 (0)621 383-0  
clemens.kaiser@umm.de



Advertisement

## View the Women's Health Session from the 11th MAGNETOM World Summit

**DENSE Trial – Implications for Breast Cancer Screening**  
Carla van Gils (University Medical Center Utrecht, The Netherlands)

**Repetitive HR-MRI of the Breast at Intervals of 24 Months – a way to Reduce Mortality?**  
Uwe Fischer (Diagnostisches Brustzentrum Göttingen, Germany)

**Implementing Abbreviated MRI Screening into a Breast Imaging Practice**  
Donna Plecha (University Hospitals Cleveland, OH, USA)

**Abbreviated Breast MRI. The Royal Melbourne Journey**  
Angela Agostinelli (The Royal Melbourne Hospital, Parkville, Victoria, Australia)

**Treatment Response Assessment with MRI**  
Susan Weinstein (Penn Medicine, University of Pennsylvania, Philadelphia, PA, USA)

**MRI in Breast Cancer: From Bench to Bedside & Beyond. MRI-derived Parameters for Hormone Receptors**  
Katja Pinker-Domenig (Medical University Vienna, Austria / Memorial Sloan Kettering Cancer Center, New York, NY, USA)

[Siemens-Healthineers.com/MWS2020-recordings](https://www.siemens-healthineers.com/MWS2020-recordings)



Graphic recording: www.gabriele-heinzel.com

# Accelerated 3D T2 SPACE CAIPIRINHA with Iterative Denoising for the Assessment of Deep Infiltrating Endometriosis

Alexis Vaussy<sup>1</sup>; Marie Florin<sup>3</sup>; Laurent Macron<sup>3</sup>; Fabrice Harritchague<sup>3</sup>; Guillaume Masson<sup>3</sup>; Stephan Kannengiesser<sup>2</sup>; Elisabeth Weiland<sup>2</sup>; Alto Stemmer<sup>2</sup>; Lamia Jarboui<sup>3</sup>

<sup>1</sup>Siemens Healthineers, Saint-Denis, France

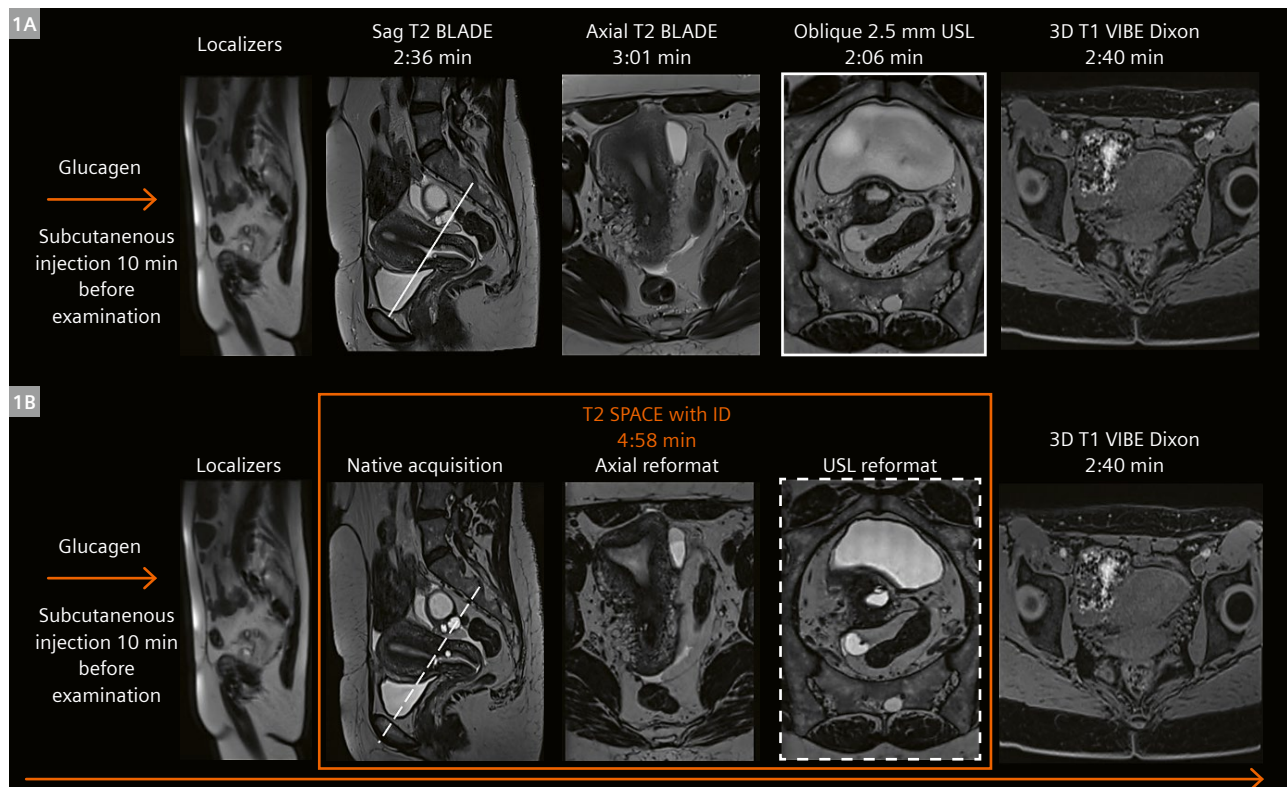
<sup>2</sup>Siemens Healthineers, Erlangen, Germany

<sup>3</sup>Centre Imagerie du Nord, Clinique du Landy, Radiology Department, Ramsay-Générale de Santé, Saint-Ouen, France

## Introduction

Deep infiltrating endometriosis (DIE) is a common gynecological inflammatory disease that primarily affects women of reproductive age, with a prevalence of 10% [1]. This pathology can be defined as functional ectopic endometrial tissue outside the uterine cavity. The most common locations of DIE include the torus, uterosacral ligaments,

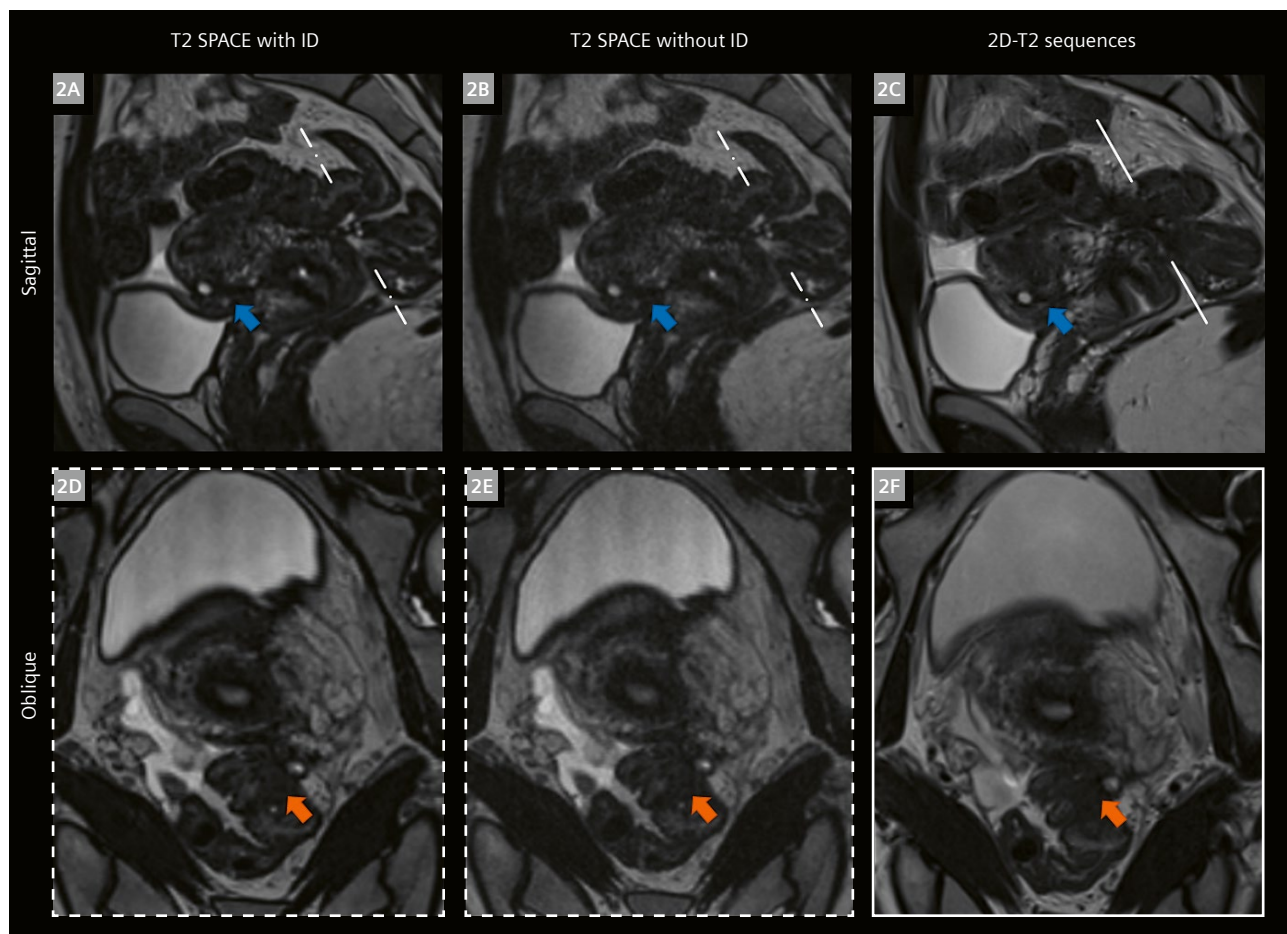
rectosigmoid colon, and vagina [2]. According to the European Society of Urogenital Radiology guidelines (ESUR) [3], magnetic resonance imaging (MRI) is considered one of the most effective techniques for the evaluation of pelvic endometriosis with transvaginal ultrasonography. Nowadays, the most commonly used



**1** Illustration of the protocol strategy used for endometriosis assessment. (1A) First routine protocol used until 2019 for the assessment of endometriosis (scan time = 10 min 23 sec). (1B) New optimized protocol from March 2020 using a T2 SPACE with ID reconstruction (scan time = 7 min 38 sec).

MRI protocol for endometriosis includes 2-dimensional turbo spin echo (TSE) T2-weighted (2D T2) sequences in addition to 2D T1-weighted sequences with and without fat suppression. Additional 2.5 mm thin oblique 2D T2 slices can improve the assessment of uterosacral ligaments (USL) and parametrial endometriosis locations [4]. However, the spatial localization of USL is variable and needs to be carefully adapted for each patient. Furthermore, the visualization of small endometriosis lesions remains limited by the thick slice thickness of 2D imaging and the resulting partial volume effect.

For that reason, 3-dimensional (3D) TSE sequences are of high interest as they offer the possibility to reconstruct any multiplanar view from a high-resolution isotropic volume [5, 6]. However, the visualization of small endometriosis lesions would require a sub-millimetre voxel size and complete coverage of the uterine cavity, which would considerably lengthen the scan time. Furthermore, the detection of subtle T2 contrast changes induced by endometriosis lesions may be masked by the extended echo train length used with the Sampling Perfection with Application-optimized Contrasts using different flip angle Evolutions (SPACE) technique [6]. Recently, a suc-



**2 Representative images comparing T2 SPACE with/without ID reconstruction and conventional 2D T2 sequences.** A 28-year-old patient seen for follow-up of known moderate endometriosis after appearance of new symptoms (dyspareunia, dysuria, and dyschezia). Corresponding T2 SPACE acquisition with oblique reformatted plans (dotted line) with ID (2A, 2D) and without ID reconstructions (2B, 2E) and separately acquired sagittal and oblique (full line) 2D T2 sequences (2C, 2F). From (2A) to (2C), an endometriosis location is visible on the vesico-uterine pouch (blue arrow), while a digestive location is identified on rectosigmoid area (orange arrow) from (2D) to (2F). In both cases, the fibrous endometriosis component is identified as an hypointensity in close contact with anatomical structures. Both endometriosis locations are better depicted with T2 SPACE with ID reconstruction, which displays a sharper image quality and lower partial volume effect. Additionally, the identification of endometriotic cysts visible as hypersignal intensity between dotted lines in (2A) and (2B) is carried out more easily than on the conventional 2D T2 sequence (2C).

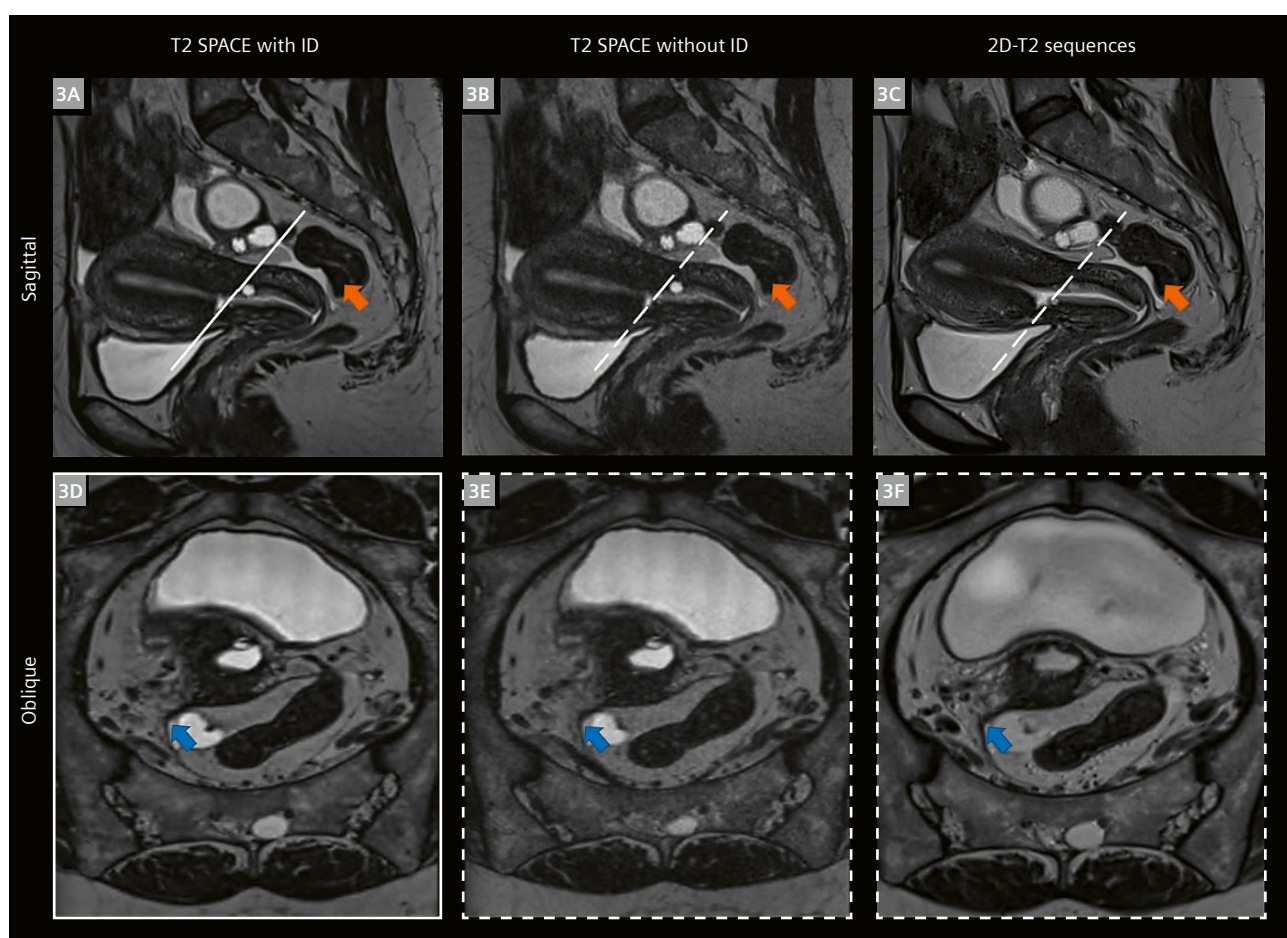
cessful combination of SPACE acquisition with Controlled Aliasing In Parallel Imaging Results IN Higher Acceleration (CAIPIRINHA) acceleration [8–10], reconstructed with a prototype iterative denoising (ID) algorithm [11], demonstrated tremendous results in several applications, such as brain and musculoskeletal imaging [12, 13].

Very recently, the setup, optimization, and evaluation of a 3D T2 SPACE accelerated with CAIPIRINHA parallel imaging with prototypal ID reconstruction (T2 SPACE with ID)<sup>1</sup> was carried out at "Centre d'Imagerie du Landy" by Florin et al. in close collaboration with MR application developers and the local clinical scientist [14]. From

<sup>1</sup>Work in progress. The application is currently under development and is not for sale in the U.S. and in other countries. Its future availability cannot be ensured.

December 2019 to March 2020, 90 female patients with suspected endometriosis were prospectively enrolled. We performed a systematic evaluation of the diagnostic performance of the optimized T2 SPACE with ID against conventional 2D T2 sequences. MRI was performed on a 1.5T MAGNETOM Aera scanner (Siemens Healthcare, Erlangen, Germany) using a 30-channel phased array coil in combination with a 32-channel spine coil. In this study, we demonstrated similar intra- and interobserver agreements between T2 SPACE with ID and conventional 2D T2 sequences with a scan time reduction of 36%.

In this article, we propose to share our workflow for patient preparation, sequence parameter optimization, and slab positioning. We also present several clinical cases to demonstrate the diagnostic value of T2 SPACE with ID in the context of deep infiltrating endometriosis.



**3** Representative images comparing T2 SPACE with/without ID reconstruction and conventional 2D T2 sequences. A 47-year-old woman presented with suspected endometriosis. Corresponding T2 SPACE acquisition with oblique reformatted plans (dotted line) with (3A, 3D) and without ID reconstructions (3B, 3E) and separately acquired sagittal and oblique (full line) 2D T2 sequences (3C, 3F). From (3A) to (3C), an endometriosis location is visible on rectosigmoid area (orange arrow), while another location is visible on the right USL from (3D) to (3F). Of note, the thinner slice thickness of the T2 SPACE with ID offers a better delineation of the USL structures compared to the conventional oblique 2D T2 sequence.

## High-resolution T2 SPACE for female pelvis imaging: How we do it

### 2D vs. T2 SPACE strategies

The routine protocol used until 2019 for the assessment of endometriosis integrated a manual positioning of each 2D T2 sequences. It included two orthogonal T2 BLADE sequences (sagittal and axial) for the whole uterine cavity and a thin T2 section oblique to the cervix for USL evaluation (total scan time of the three 2D T2 sequences: 7 minutes 43 seconds). However, the spatial localization of USL is variable according to the pelvis anatomy and needs to be carefully adapted for each patient. A 3D gradient-echo T1-weighted sequence with and without fat suppression using a two-point Dixon technique was additionally performed at the end of the examination for the diagnosis of endometriotic cysts and blood identification. The whole protocol lasts 10 minutes 23 seconds (Fig. 1A).

Since March 2020, the new protocol, including the optimized T2 SPACE with ID, has provided a real benefit by allowing the acquisition of a unique set of volumetric T2 images that could be reconstructed in any plane, eliminating the possibility of a suboptimal plane [14]. Furthermore, the scan time of the T2 SPACE with ID is 36% shorter than the separately acquired sagittal, oblique, and axial 2D T2 sequences (Fig. 1B). Figures 2 and 3 present two relevant clinical cases to highlight the advantages of the new T2 SPACE with ID for the assessment of DIE compared to conventional 2D T2 sequences.

### 3D T2 SPACE settings

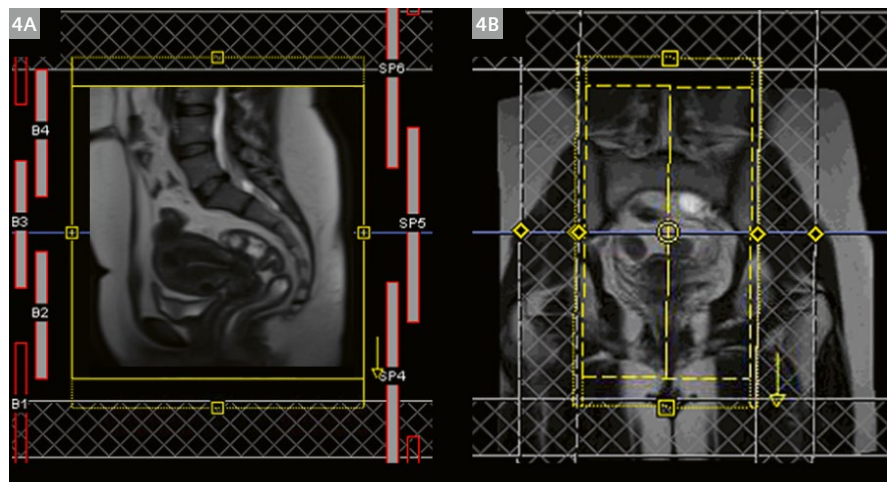
The sequence parameters of the T2 SPACE with ID sequence are presented in Table 1. The SPACE technique

is an optimized 3D TSE sequence, which allows increasing the duration of the echo train (and thereby reducing the acquisition time) by using short non-spatially selective radiofrequency pulses and variable flip angle schemes. In this study, the scan time of the T2 SPACE with ID sequence was shortened using a 4-fold CAIPIRINHA acceleration factor, while the g-factor penalty and SNR drop were compensated with the ID prototype algorithm. The sequence was set up to cover the whole pelvis cavity using full Fourier sampling and a voxel size of  $0.8 \times 0.8 \times 0.9 \text{ mm}^3$  to ensure the visualization of fine anatomical details and multiplanar reconstruction in any desirable reformats. Finally, the SPACE variable flip angle mode was set to constant, while the echo

### T2 SPACE with ID

Orientation	Sagittal
Field of view	$256 \times 256 \times 176 \text{ mm}$
Matrix	$320 \times 320 \text{ pixels}$
Acquired voxel size	$0.8 \times 0.8 \times 1.0 \text{ mm}^3$
No. averages	1.4
TR/TE	1360/152 ms
Turbo factor	72
Bandwidth	679 Hz/pixel
Accelerator factor	CAIPIRINHA 2 × 2
Scan time	4:58 min

Table 1: T2 SPACE with ID reconstruction sequence



**4** Sequence positioning on the MR console. The volume (yellow box) is positioned in sagittal orientation to cover the whole pelvis cavity on sagittal (4A) and coronal (4B) localizers. The phase encoding direction is set from head to feet to reduce motion breathing artifacts. Four saturation bands are placed along the phase encoding direction (manual positioning in front of the activated coils) and slice direction (automated positioning) to reduce the fold-over artifact from the upper abdomen, thumbs, and hips. The automated coil selection is set to "Minimize" to prevent any additional risks of folding artifacts.

train length was significantly reduced to 265 ms using a low turbo factor of 72 and a high bandwidth of 679 Hz/Px. This setting allowed to reproduce the desired contrast of the conventional 2D T2 sequences.

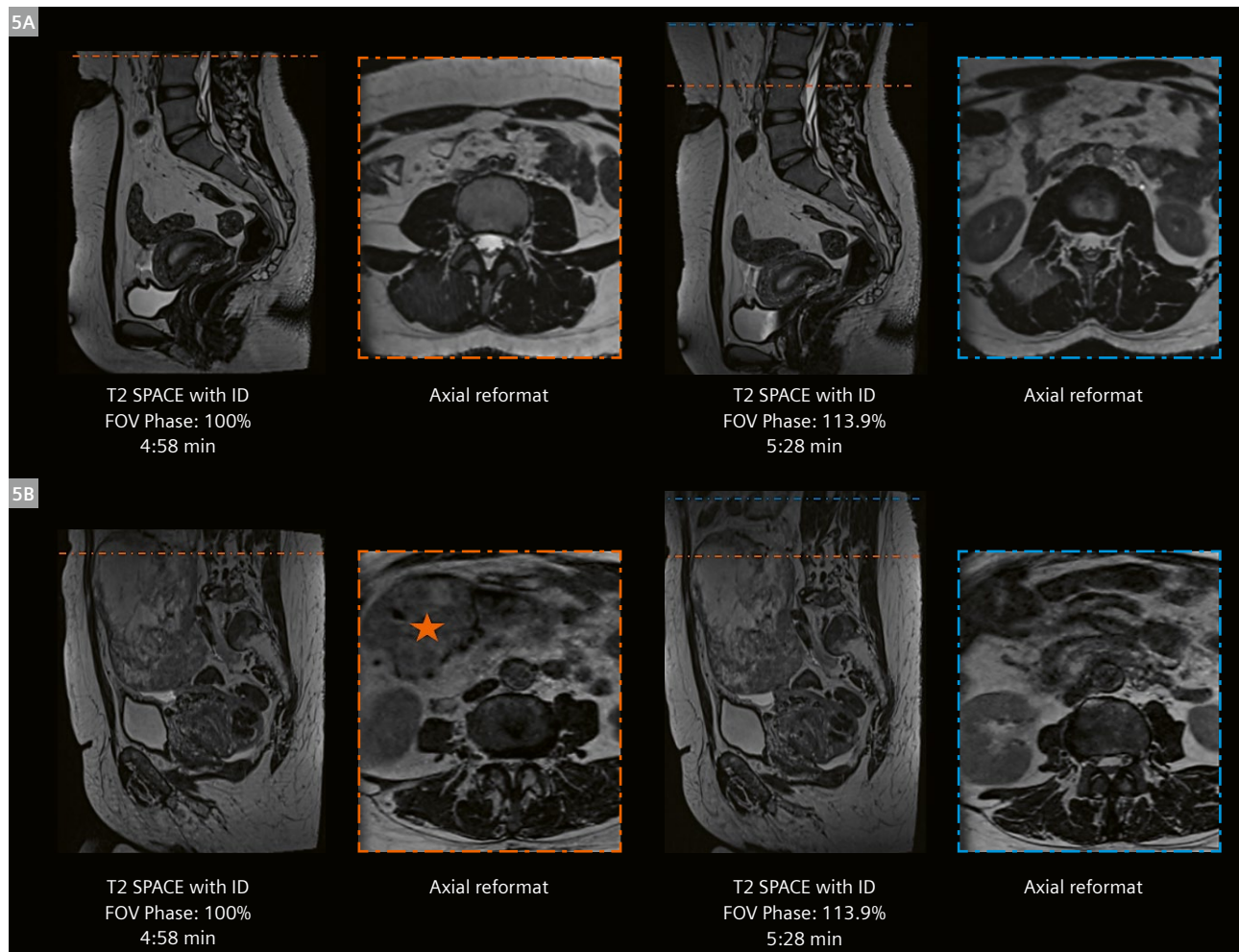
While this may at first seem counterintuitive, the phase encoding direction is set from head to feet with a phase oversampling of only 20% to maintain a clinically compatible scan time. This choice is made to minimize artifacts caused by breathing and to avoid the saturation band placement on the straight muscle of the abdomen, which could hide an endometriosis location. To reduce the fold-over artifact from the upper abdomen and the thumbs, two saturation bands are positioned in front of the activated coil elements not covered by the phase oversampling (Fig. 4). Two

additional parallel sat bands are placed along the slice direction. The automatic coil selection is set to "Minimize" to prevent any additional risks of folding artifacts.

Moreover, an easy adaptation of the phase field of view parameter can be performed, depending on patient anatomy and pathology context (Fig. 5), without compromising voxel size and image quality, at the cost of a slightly increased scan time.

#### Patient preparation

According to the latest ESUR guidelines, the use of antiperistaltic agent is recommended in the evaluation of DIE to reduce bowel peristalsis [3]. However, there is currently no performance recommendation regarding the best



**5** Effect of the phase encoding direction to easily adapt the FOV according to patient anatomy and clinical indications. In (5A), due to patient height, the FOV phase was increased from 100% to 113.9% to explore the complete pelvis cavity from iliac crest to the pyelo-calyceal cavities in the context of endometriosis. In (5B), the head to feet coverage did not offer a complete visualization of the uterine fibrosis borders (orange star), corrected with the increased FOV. Please note that this operation would slightly increase the scan time without any impact on the acquired voxel size.

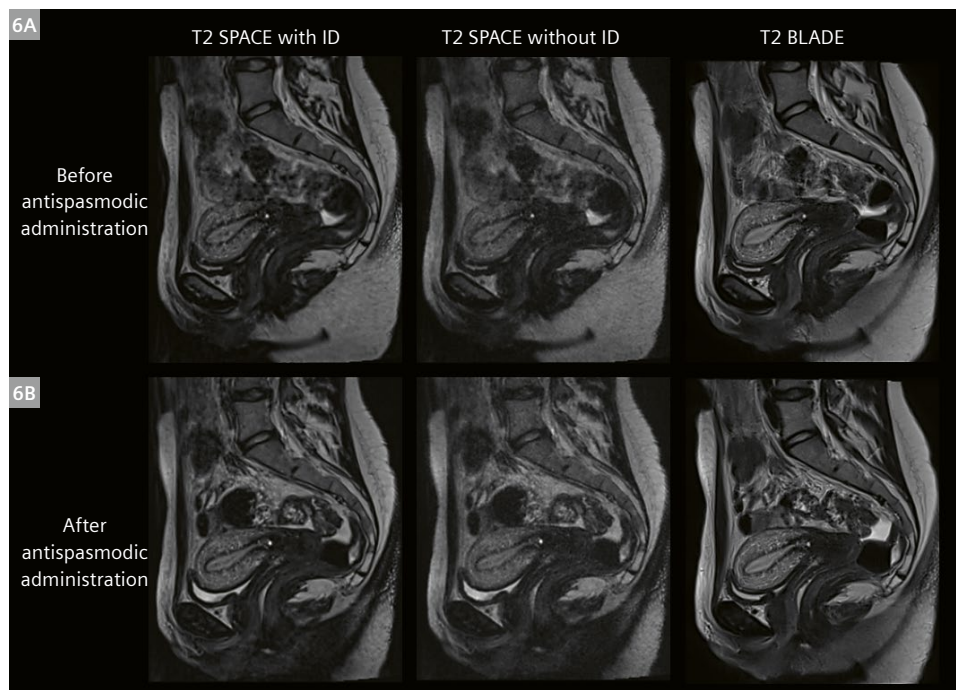
administration procedure and timing. Figure 6 shows the impact of the antispasmodic drugs on T2 SPACE with ID image quality, compared to the reduced motion sensitivity of the conventional T2 BLADE. For that reason, precise timing is required between the antispasmodic administration and the acquisition of the T2 SPACE with ID. At our center, a single dose of antispasmodic subcutaneous injection (Glucagen, 1 mg/mL, Novo Nordisk, Paris, France) is administrated in the patient preparation room 10 minutes before MRI examination. Furthermore, before each examination, patients are asked to perform an intestinal toilette (Normacol). Patients are positioned in supine position, arms along the body. An abdominal strapping is used to reduce artifacts caused by respiratory movement, as recommended by ESUR guidelines.

#### **Future perspectives: fusion imaging between MRI and ultrasound**

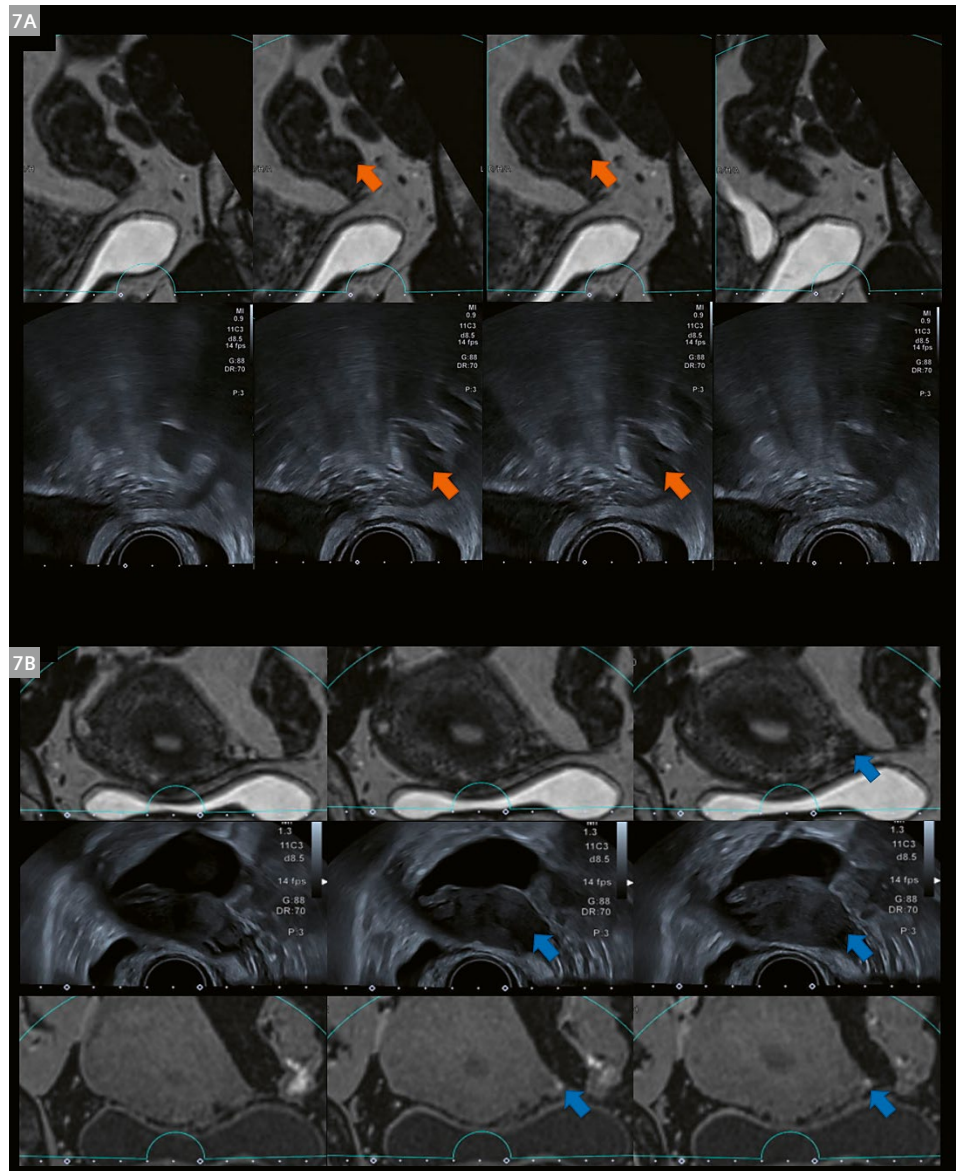
MRI and ultrasound (US) complement each other in the screening and diagnosis of DIE and are considered the best non-invasive techniques for this indication. While US is considered a first-line technique, owing to its widespread availability and cost effectiveness, the modality suffers from higher interobserver variability in the diagnosis of pelvic endometriosis, and its performance is highly dependent on the radiologist's experience [15]. In contrast, MRI provides a visualization of the whole pelvis, an excellent tissue contrast resolution [16], and

is also considered less biased and more reproducible than US [17, 18]. Therefore, fusion imaging has great potential in the assessment of endometriosis as it combines the advantages of US and MRI modalities, and overcomes their weaknesses by providing superior spatial, contrast, and temporal resolution to that possible with each modality technique alone. As a result, MRI can be used to locate the targeted structures with US.

Despite the promising and encouraging results of DIE assessment by fusion imaging [19], it was demonstrated that MRI-US fusion imaging could not be readily implemented into daily practice as a routine evaluation of DIE due to the lack of accuracy between both modalities' datasets [20]. However, it must be noted that these studies used standard 2D T2 sequences, and that the sets of images needed to be synchronized manually using only one anatomical plane and reference point. The optimized T2 SPACE with ID proposed in this study may bring useful anatomical information to obtain a perfect fusion calibration independently of the desired reformatted plan required for US exploration. Figure 7 shows some preliminary clinical cases where the T2 SPACE with ID was used and fused with US in the context of DIE. This additional value of the MRI and US fusion using this novel MRI sequence will be further evaluated in a dedicated study.



**6** **Illustration of the impact of antispasmodic on image quality for T2 SPACE with/without ID and T2 BLADE sequence.** (6A) shows the high peristaltic sensitivity and reduced image quality of T2 SPACE with/without ID before antispasmodic administration compared to conventional T2 BLADE. After antispasmodic administration (6B), the image quality of the T2 SPACE with ID is similar to conventional T2 BLADE, while the image quality of T2 SPACE without ID remains unacceptable for clinical examination.



**7** Simultaneous fusion imaging between magnetic resonance imaging (MRI) and transvaginal ultrasonography (US). Fusion imaging of intestinal endometriosis (7A, orange arrows) and superficial endometriosis (7B, blue arrows) with simultaneous display of corresponding planes obtained by MRI (reformatted T2 SPACE, first row) and transvaginal ultrasonography (US, second row). Intestinal endometriosis appears as a thickened structure associated with hypointense and hypoechoic signals on MRI and US images, respectively. The same structure identification can be performed for superficial endometriosis facilitated by the additional hyperintense signal delineation offered by 3D T1 VIBE Dixon (7B, third row).

## Conclusion

As outlined in this article, recent advances in 3D T2 SPACE imaging technique have given clinicians powerful tools to diagnose endometriosis pathologies. These tools can range from better MRI identification of endometriosis lesions to the most advanced perspectives, such as MRI and US fusion imaging. In our study, the combination of SPACE acquisition with a CAIPIRINHA sampling pattern and ID reconstruction offered a 36% scan time reduction compared to conventional 2D T2 sequences without

compromising image quality. According to the World Health Organization, there is a need to improve early diagnosis of endometriosis as almost 190 million reproductive age women may be affected by this disease. We believe T2 SPACE with ID to be a promising tool to handle the growing challenges of this pathology management by providing all relevant information in only one sequence. Further investigations are needed to validate these results on a larger scale and to confirm the diagnostic performance of this sequence with surgical findings.

## References

- 1 WHO key facts on Endometriosis. <https://www.who.int/news-room/fact-sheets/detail/endometriosis>, accessed October 6, 2021.
- 2 Bazot M, Daraï E, Hourani R, Thomassin I, Cortez A, Uzan S, et al. Deep Pelvic Endometriosis: MR Imaging for Diagnosis and prediction of Extension of Disease. *Radiology*. 2004 Aug; 232(2):379–89.
- 3 Bazot M, Bharwani N, Huchon C, Kinkel K, Cunha TM, Guerra A, et al. European society of urogenital radiology (ESUR) guidelines: MR imaging of pelvic endometriosis. *Eur Radiol*. 2017 Jul;27(7):2765–75.
- 4 Bazot M, Gasner A, Ballester M, Daraï E. Value of thin-section oblique axial T2-weighted magnetic resonance images to assess uterosacral ligament endometriosis. *Hum Reprod*. 2011 Feb;26(2):346–53.
- 5 Agrawal G, Riherd JM, Busse RF, Hinshaw JL, Sadowski EA. Evaluation of uterine anomalies: 3D FRFSE cube versus standard 2D FRFSE. *AJR Am J Roentgenol*. 2009 Dec;193(6):W558–562.
- 6 Bazot M, Stivalet A, Daraï E, Coudray C, Thomassin-Naggara I, Poncelet E. Comparison of 3D and 2D FSE T2-weighted MRI in the diagnosis of deep pelvic endometriosis: preliminary results. *Clin Radiol*. 2013 Jan;68(1):47–54.
- 7 Mugler JP. Optimized three-dimensional fast-spin-echo MRI. *J Magn Reson Imaging*. 2014 Apr;39(4):745–67.
- 8 Breuer FA, Blaimer M, Mueller MF, Seiberlich N, Heidemann RM, Griswold MA, et al. Controlled aliasing in volumetric parallel imaging (2D CAIPRINHA). *Magn Reson Med*. 2006 Mar;55(3):549–56.
- 9 Breuer F, Blaimer M, Griswold M, Jakob P, Habas C. Controlled Aliasing in Parallel Imaging Results in Higher Acceleration (CAIPRINHA). *MAGNETOM Flash* (49) 1/2012;135–42.
- 10 Fritz J, Fritz B, Thawait GG, Meyer H, Gilson WD, Raithel E. Three-Dimensional CAIPRINHA SPACE TSE for 5-Minute High-Resolution MRI of the Knee. *Invest Radiol*. 2016 Oct;51(10):609–17.
- 11 Kannengiesser S, Mailhe B, Mariappan N, Huber S, Kiefer B. Universal iterative denoising of complex-valued volumetric MR image data using supplementary information. In: ISMRM Annual Meeting Proceedings [conference proceedings on the Internet].
- 12 Vaussy A, Eliezer M, Menjot de Champfleur N, Le Bars E, Nguyen T, Habas C, et al. Iterative Denoising Applied to 3D SPACE CAIPRINHA: A New Approach to Accelerate 3D Brain Examination in Clinical Routine. *MAGNETOM Flash - MAGNETOM Free.Max special issue* 2020;26–34.
- 13 Rebbah S, Hlaihel C, Le Rumeur Y, Kannengiesser S, Stemmer A, Troalen T. Iterative Denoising Applied to 3D SPACE CAIPRINHA: An Application to Musculoskeletal Imaging. *MAGNETOM Flash* (78) 1/2021;53–60.
- 14 Florin M, Vaussy A, Macron L, Bazot M, Stemmer A, Pinar U, et al. Evaluation of Iterative Denoising 3-Dimensional T2-Weighted Turbo Spin Echo for the Diagnosis of Deep Infiltrating Endometriosis. *Invest Radiol*. 2021 Oct 1;56(10):637–44.
- 15 Bazot M, Daraï E, Biau DJ, Ballester M, Dessolle L. Learning curve of transvaginal ultrasound for the diagnosis of endometriomas assessed by the cumulative summation test (LC-CUSUM). *Fertil Steril*. 2011 Jan;95(1):301–3.
- 16 Bazot M, Daraï E, Hourani R, Thomassin I, Cortez A, Uzan S, et al. Deep pelvic endometriosis: MR imaging for diagnosis and prediction of extension of disease. *Radiology*. 2004 Aug;232(2):379–89.
- 17 Saba L, Guerrero S, Sulcis R, Ajossa S, Melis G, Mallarini G. Agreement and reproducibility in identification of endometriosis using magnetic resonance imaging. *Acta Radiol*. 2010 Jun;51(5):573–80.
- 18 Saba L, Guerrero S, Sulcis R, Pilloni M, Ajossa S, Melis G, et al. Learning curve in the detection of ovarian and deep endometriosis by using Magnetic Resonance: comparison with surgical results. *Eur J Radiol*. 2011 Aug;79(2):237–44.
- 19 Millischer A-E, Salomon LJ, Santulli P, Borghese B, Dousset B, Chapron C. Fusion imaging for evaluation of deep infiltrating endometriosis: feasibility and preliminary results. *Ultrasound Obstet Gynecol*. 2015 Jul;46(1):109–17.
- 20 Berger J, Henneman O, Rhemrev J, Smeets M, Jansen FW. MRI-Ultrasound Fusion Imaging for Diagnosis of Deep Infiltrating Endometriosis - A Critical Appraisal. *Ultrasound Int Open*. 2018 Sept;4(3):E85–90.

## Contact

Dr. Lamia Jarboui, M.D.  
Centre Imagerie du Nord  
Clinique du Landy  
23 Rue du Landy  
93400 Saint Ouen  
France  
ljarboui@ccnradio.fr



Alexis Vaussy  
Siemens Healthcare SAS,  
40 Avenue des Fruitières  
93210 Saint Denis  
France  
alexis.vaussy@siemens-healthineers.com



# Clinical Utility of High-Bandwidth Inversion Recovery Sequences in Patients with Cardiac Implanted Electronic Devices

Zsófia Dohy<sup>1</sup>; Liliána Szabó<sup>1</sup>; Máté Kiss<sup>2</sup>; Xiaoming Bi<sup>3</sup>; Csilla Czimbalmos<sup>1</sup>; Ferenc Imre Suhai<sup>1</sup>; Attila Tóth<sup>1</sup>; Vencel Juhász<sup>1</sup>; Roland Papp<sup>1</sup>; László Gellér<sup>1</sup>; Béla Merkely<sup>1</sup>; Hajnalka Vágó<sup>1</sup>

<sup>1</sup>Semmelweis University, Heart and Vascular Center, Budapest, Hungary

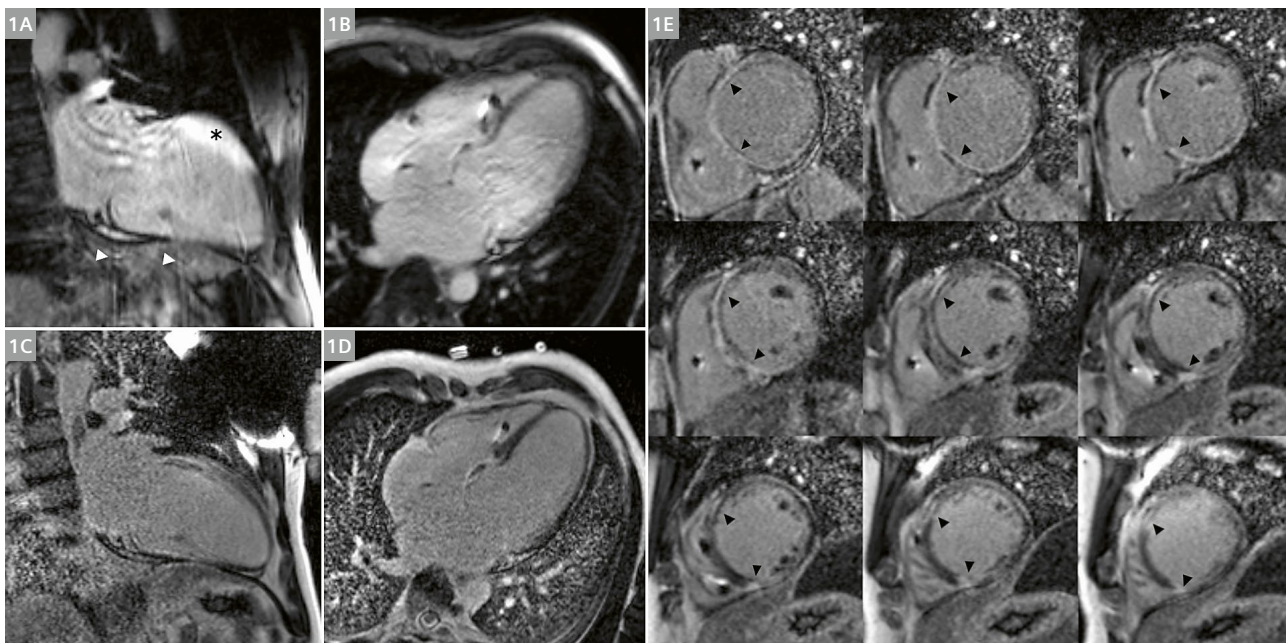
<sup>2</sup>Siemens Healthineers, Budapest, Hungary

<sup>3</sup>Siemens Medical Solutions, Los Angeles, USA

## Introduction

Myocardial scar detection using cardiac magnetic resonance (CMR) imaging with late gadolinium enhancement (LGE) facilitates diagnosis and clinical management in various cardiac conditions. For instance, it can help determine the etiology of heart failure and arrhythmias, assess myocardial viability, differentiate among cardiomyopathies, and guide electrophysiological interventions

[1–4]. In patients with scar-related ventricular tachycardia (VT), performing CMR imaging before radiofrequency catheter ablation can help pre-procedural planning and scar mapping [5]. However, many patients with an indication for VT ablation already have an implantable cardioverter defibrillator (ICD)<sup>1</sup>, and this may be a contraindication to a CMR examination. The population of patients



**1** (1A, B) Standard LGE images in 2-chamber (1A) and 4-chamber (1B) views with hyperintensity (black asterisk) and breathing (white arrowheads) artifacts. (1C–E) Wideband LGE images in 2-chamber (1C), 4-chamber (1D), and short axis (1E) views with mid-myocardial contrast enhancement in the basal and midventricular anterior, septal, and inferior segments (black arrowheads).

<sup>1</sup>The MRI restrictions (if any) of the metal implant must be considered prior to patient undergoing MRI exam. MR imaging of patients with metallic implants brings specific risks. However, certain implants are approved by the governing regulatory bodies to be MR conditionally safe. For such implants, the previously mentioned warning may not be applicable. Please contact the implant manufacturer for the specific conditional information. The conditions for MR safety are the responsibility of the implant manufacturer, not of Siemens Healthineers.

with different cardiac implanted electronic devices (CIEDs)<sup>1</sup> is growing. Because CIED patients with electrical abnormalities often have underlying structural heart disease, the indications for CMR examinations are expanding in this patient population.

In the past, CMR was contraindicated in patients with CIEDs due to safety concerns. With the advent of MR-conditional CIEDs and the establishment of appropriate and strict safety protocols which allow CMR imaging in patients with CIEDs [6, 7], the number of these examinations is growing. However, device- and lead-related artifacts can limit image interpretability and the clinical applicability of CMR in CIED patients, especially in the case of ICDs and cardiac resynchronization therapy pacemakers (CRT-Ps) or defibrillators (CRT-Ds) [8, 9]. There are two basic device artifacts in late gadolinium enhancement (LGE) imaging:

- 1) Hyperintense regions which were not inverted due to the limited inversion bandwidth
- 2) Signal voids due to dephasing, caused by gradient generally along the widest voxel dimension [10].

A high-bandwidth inversion recovery sequence uses wideband (WB) techniques to reduce susceptibility artifacts<sup>2</sup>. This extends the benefit of tissue characterization to device patients, enabling them to receive diagnostically robust imaging that visualizes myocardial injury. Wideband LGE CMR techniques have been developed to attenuate these image artifacts and enhance the diagnostic value of CMR in CIED patients [10, 11].

At our institution we are using a 1.5T MR scanner (MAGNETOM Aera, Siemens Healthcare, Erlangen, Germany) and two types of WB protocols to reduce susceptibility and off-resonance artifacts in examinations with CIEDs. The spatial resolution is the same for both protocols: 1.4 x 1.4 x 8.0 mm<sup>3</sup>. The first protocol is a shorter single-shot breath-controlled sequence. The second uses a single-shot data acquisition method in combination with phase-sensitive inversion recovery (PSIR) and motion correction (MoCo) for reconstruction, which allows measurements to be taken under free-breathing conditions [12]. Signal-to-noise ratio (SNR) loss from the accelerated single-shot acquisition is offset by increasing the number of averages. For ICD imaging with more severe artifacts, we suggest at least 24 averages (with thinner slices – e.g., 4 mm). For pacemakers – where the artifacts are less intense – we can reduce the number of averages to 16. Free-breathing measurements take slightly longer, but they provide more stable image quality without SNR loss or device-related image artifacts.

The following two clinical cases demonstrate the clinical impact of the high-bandwidth inversion recovery sequence in everyday routine.

## Case 1

A 45-year-old male patient with a CRT-D was referred for CMR imaging before VT ablation for scar mapping.

Patient history: In 2015, the patient had syncope. An electrocardiogram (ECG) showed wide QRS and first-degree AV block, and 24-hour Holter monitoring detected polymorphic ventricular premature beats. The CMR examination in 2015 showed dilated cardiomyopathy with extended LGE with a non-ischemic pattern. During the electrophysiological examination, sustained VT could be induced. After radiofrequency catheter ablation, the VT persisted with altered morphology, which indicated ICD implantation. Over the years, appropriate ICD shocks were detected on several occasions. Because of the progression of heart failure, VT ablation was repeated in 2020 and the ICD was upgraded to a CRT-D (St. Jude Quadra Assura 3371-40C).

The patient has since had repeated VTs, which necessitated another VT ablation and a CMR examination for scar mapping. Before CMR scanning, the patient – who has a non-conditional CIED – underwent device interrogation. As the patient was pacemaker-dependent, the pacing mode was programmed to DOO-RV-only asynchronous bipolar pacing with high pacing energy (5.0 V/1.0 msec). All tachyarrhythmia detection and therapies were switched off. Protocols developed for safely performing CMR imaging in patients with CIEDs were followed [13, 14]. Intraprocedural monitoring was performed with a continuous electrocardiogram, pulse oximetry, and non-invasive blood pressure measurements. The specific absorption rate was limited to 2.0 W/kg. No adverse events occurred. Following completion of the CMR scan, the original device settings were reinstated.

The CMR examination was performed in a 1.5T scanner (MAGNETOM Aera, Siemens Healthcare, Erlangen, Germany). After standard scout slices, spoiled gradient echo imaging was performed to assess cardiac volumes and function. An intravenous bolus of gadobutrol (0.15 mmol/kg) was injected. Ten minutes after the injection, standard LGE and free-breathing WB LGE images were acquired in 2-, 3-, and 4-chamber views. WB LGE images were acquired, as well as short-axis images with full coverage of the left ventricle with free breathing and the MoCo algorithm.

Hyperintensity artifacts in the anterior segments, as well as breathing artifacts, limited the interpretability of standard LGE images (Figs. 1A, B). No artifacts affected the left ventricular segments on the WB LGE images, and midmyocardial contrast enhancement was present in the basal and midventricular anterior, septal, and inferior segments (Figs. 1C–E). The WB LGE images were processed with ADAS-3D software (Galgo Medical SL, Barcelona,

<sup>2</sup>High-bandwidth Inversion Recovery is a product with software version syngo MR XA 30/31. The sequence used in the article was a prototype.

Spain) for channel detection. Following semiautomatic endo- and epicardial contour detection, ten concentric surface layers were created automatically from endocardium to epicardium. A 3D shell was created for each layer. Based on signal intensities, scar core, border zone, and healthy myocardium were identified. A conducting channel was defined as a corridor in the border zone between two scar-core areas [5].

After invasive electroanatomic mapping (EAM) – supported by the CMR images – VT ablation was repeated in the septal region. During a four-month clinical follow-up, no ventricular arrhythmias were detected.

## Case 2

A 64-year-old male patient with prior myocardial infarction and ICD (Biotronic Itrevia 5 VR-T DX) implantation was referred for CMR imaging. The patient had an ST-elevated myocardial infarction in 2016, and a percutaneous coronary intervention with stent implantation in the right coronary artery was performed. Six months later, monomorphic VT occurred. Coronary angiography showed in-stent restenosis, which required reintervention with stent implantation. As the VT recurred, VT ablation and ICD implantation were performed in 2016. In 2020 and 2021, appropriate ICD therapies occurred several times, which indicated a repeated VT ablation.

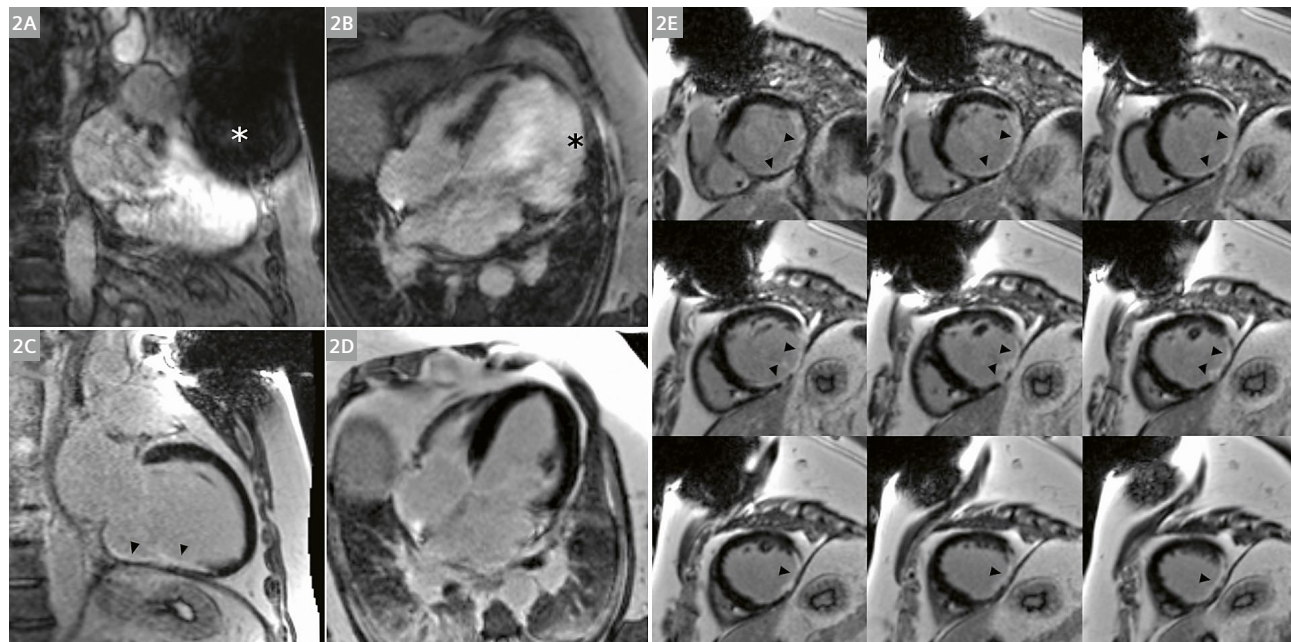
Prior to the VT ablation, CMR for scar mapping was performed with the same protocol described in our first case report. As the patient was not pacemaker-dependent, the MR-conditional ICD was turned off during the CMR examination.

Taking into account the proximity of the ICD, we detected large susceptibility and off-resonance artifacts at the left ventricular anterior and anterolateral segments on the standard LGE images (Figs. 2A, B). Such artifacts would make the correct diagnosis impossible. However, the high-bandwidth inversion recovery sequence allowed us to completely diminish both the off-resonance and susceptibility artifacts, and to detect transmural contrast enhancement in the inferior and inferolateral segments corresponding to the previous myocardial infarction (Figs. 2C–E). Potentially arrhythmogenic conducting channels were identified using the ADAS 3D software (Fig. 3).

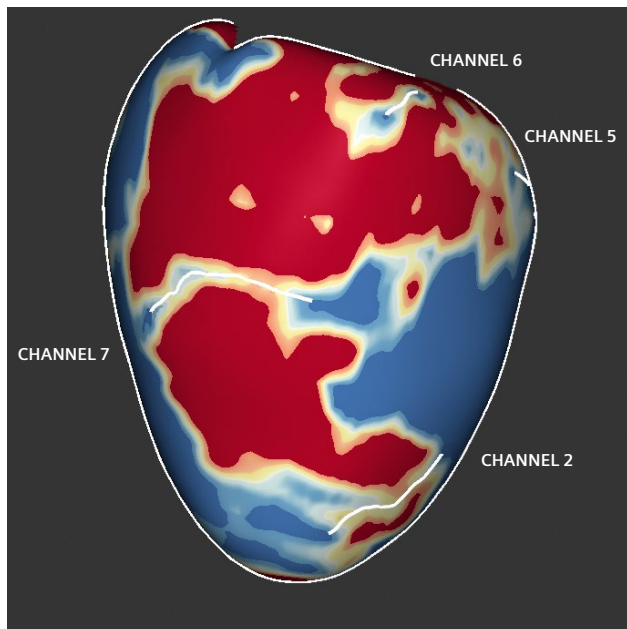
Using the EAM and CMR images, extended epi- and endocardial ablation was performed in the inferior region. During a five-month clinical follow-up, no VT was detected by the ICD.

## Discussion

LGE-CMR can accurately identify fibrotic myocardium and the potential arrhythmogenic substrate. It is therefore a



**2** (2A, B) Standard LGE images in 2-chamber (2A) and 4-chamber (2B) views with hyperintensity off-resonance artifacts (black asterisk) in the anterior and anterolateral segments, and susceptibility artifacts (white asterisk) in the anterior segments. (2C–E) Wideband LGE images in 2-chamber (2C), 4-chamber (2D), and short axis (2E) views with transmural contrast enhancement in the inferior and inferolateral segments (black arrowheads).



**3** Detection of scar in red, border zones in yellow, and normal tissue in blue using ADAS 3D software. Conducting channels were identified as a corridor in the border zone between two core areas.

widely used technique for planning ablation procedures [15, 16]. Previous data demonstrated that CMR-aided VT ablation was associated with a lower need for radiofrequency delivery, lower VT inducibility after substrate ablation, and lower VT recurrence rate [5]. Nevertheless, most patients referred to VT ablation already have a CIED. With conventional CMR, the quality of LGE images is usually poor due to metal-induced artifacts, especially in the left ventricular anterior segments [9]. The device generator causes off-resonance hyperintensity artifacts within the myocardium. These artifacts appear similar to the LGE of scar tissue, which can lead to false diagnoses.

In this report, we presented two patient cases: one with a non-MR-conditional CRT-D, and one with an MR-conditional ICD. The safety protocols were followed and no adverse events occurred. We found that using WB LGE increased the image quality independently of the type of device. Do et al. investigated the safety of CMR and the interpretability of images using WB LGE in 111 patients with a non-MR-conditional CIED, using a self-developed wideband pulse sequence. In 87% of the study population, the WB technique yielded artifact-free images; just 3% of cases had significant artifacts that limited or undermined interpretation of the study [17].

In the CMR studies presented here, free-breathing WB LGE was performed. Previous data suggest that free-breathing WB single-shot LGE and WB-segmented LGE produce similarly improved image quality compared to standard LGE. Schwartz et al. found that the percentage

of diagnostically interpretable myocardial segments was 72% for standard LGE, 89% for WB-segmented LGE, and 94% for free-breathing WB single-shot LGE [18]. According to our experiences, CIED patients may have difficulties with breath-holds because of underlying heart disease. The high-bandwidth inversion recovery application can diminish both the device-related artifacts and the breathing artifacts. However, acquisition times are longer in the free-breathing WB sequence than in a single-shot breath-controlled sequence.

Several studies have demonstrated the clinical benefit of using WB LGE in CIED patients. Bhuvan et al. found that WB LGE resulted in changed clinical management in 75% of ICD patients and 19% of pacemaker patients when compared to imaging with standard LGE sequences, based on 136 CMR studies [10]. Singh et al. investigated the agreement between LGE images (standard and WB) and invasive EAM in 27 patients with ICD who underwent VT ablation. With standard LGE, the presence and location of LGE agreed with at least one focus of scar on EAM in 10 out of the 27 cases. In contrast, agreement with EAM was noted in 21 of the 27 cases when WB LGE was used [19]. In another study, conducting channels were identified using ADAS 3D software before VT ablation, based on WB LGE images in 13 ICD patients and on standard LGE images in 26 patients without CIED. The two groups were matched according to the type of cardiomyopathy, scar location, and age. The agreement between CMR and EAM was 85.1% and 92.2% in the WB group and the standard LGE group, respectively. The researchers found no differences in false-positive rates or false-negative rates between the two groups [20].

## Conclusion

In this report, we presented our experience with the new high-bandwidth inversion recovery sequence in CIED patients. By reporting on the cases of two patients – one with non-ischemic and one with ischemic cardiac disease – we demonstrated that WB LGE sequences have a substantial impact on diagnosis and treatment in CIED patients.

### Funding

Project no. NVKP\_16-1-2016-0017 ('National Heart Program') has been implemented with the support provided from the National Research, Development and Innovation Fund of Hungary, financed under the NVKP\_16 funding scheme. The research was financed by the Thematic Excellence Programme (2020-4.1.1.-TKP2020) of the Ministry for Innovation and Technology in Hungary, within the framework of the Therapeutic Development and Bioimaging thematic programmes of the Semmelweis University. LS was supported by the ÚNKP-20-3-II-SE-61 New National Excellence Program of the Ministry for Innovation and Technology from the source of the National Research, Development and Innovation Fund. ZD and LS were supported by the "Development of scientific workshops of medical, health sciences and pharmaceutical educations" project. Project identification number: EFOP-3.6.3-VEKOP-16-2017-00009.

## References

- 1 Hundley WG, Bluemke DA, Finn JP, Flamm SD, Fogel MA, Friedrich MG, et al. ACCF/ACR/AHA/NASCI/SCMR 2010 expert consensus document on cardiovascular magnetic resonance: a report of the American College of Cardiology Foundation Task Force on Expert Consensus Documents. *J Am Coll Cardiol.* 2010;55(23):2614–62.
- 2 Bello D, Shah DJ, Farah GM, Di Luzio S, Parker M, Johnson MR, et al. Gadolinium cardiovascular magnetic resonance predicts reversible myocardial dysfunction and remodeling in patients with heart failure undergoing beta-blocker therapy. *Circulation.* 2003;108(16):1945–53.
- 3 Kim RJ, Wu E, Rafael A, Chen EL, Parker MA, Simonetti O, et al. The use of contrast-enhanced magnetic resonance imaging to identify reversible myocardial dysfunction. *N Engl J Med.* 2000 Nov;343(20):1445–53.
- 4 Klem I, Weinsaft JW, Bahnson TD, Hegland D, Kim HW, Hayes B, et al. Assessment of myocardial scarring improves risk stratification in patients evaluated for cardiac defibrillator implantation. *J Am Coll Cardiol.* 2012;60(5):408–20.
- 5 Andreu D, Penela D, Acosta J, Fernández-Armenta J, Perea RJ, Soto-Iglesias D, et al. Cardiac magnetic resonance–aided scar dechanneling: Influence on acute and long-term outcomes. *Heart Rhythm.* 2017;14(8):1121–1128.
- 6 Russo RJ, Costa HS, Silva PD, Anderson JL, Arshad A, Biederman RWW, et al. Assessing the Risks Associated with MRI in Patients with a Pacemaker or Defibrillator. *N Engl J Med.* 2017;376(8):755–764.
- 7 Nazarian S, Hansford R, Rahsepar AA, Weltin V, McVeigh D, Gucuk Ipek E, et al. Safety of Magnetic Resonance Imaging in Patients with Cardiac Devices. *N Engl J Med.* 2017;377(26):2555–2564.
- 8 Sasaki T, Hansford R, Zviman MM, Kolandaivelu A, Bluemke DA, Berger RD, et al. Quantitative assessment of artifacts on cardiac magnetic resonance imaging of patients with pacemakers and implantable cardioverter-defibrillators. *Circ Cardiovasc Imaging.* 2011;4(6):662–70.
- 9 Mesubi O, Ahmad G, Jeudy J, Jimenez A, Kuk R, Salaris A, et al. Impact of ICD artifact burden on late gadolinium enhancement cardiac MR imaging in patients undergoing ventricular tachycardia ablation. *Pacing Clin Electrophysiol.* 2014;37(10):1274–83.
- 10 Bhuvu AN, Kellman P, Graham A, Ramlall M, Boubertakh R, Feuchter P, et al. Clinical impact of cardiovascular magnetic resonance with optimized myocardial scar detection in patients with cardiac implantable devices. *Int J Cardiol.* 2019;279:72–8.
- 11 Rashid S, Rapacchi S, Vaseghi M, Tung R, Shivkumar K, Finn JP, et al. Improved late gadolinium enhancement MR imaging for patients with implanted cardiac devices. *Radiology.* 2014;270(1):269–74.
- 12 Kellman P, Xue H, Hansen MS. Free-breathing Late Enhancement Imaging: Phase Sensitive Inversion Recovery (PSIR) with Respiratory Motion Corrected (MOCO) Averaging. *MAGNETOM Flash.* 2016;66(3):65–73.
- 13 Nazarian S, Roguin A, Zviman MM, Lardo AC, Dickfeld TL, Calkins H, et al. Clinical utility and safety of a protocol for noncardiac and cardiac magnetic resonance imaging of patients with permanent pacemakers and implantable cardioverter defibrillators at 1.5 tesla. *Circulation.* 2006;114(12):1277–84.
- 14 Gupta SK, Ya'qoub L, Wimmer AP, Fisher S, Saeed IM. Safety and Clinical Impact of MRI in Patients with Non-MRI-conditional Cardiac Devices. *Radiol Cardiothorac Imaging.* 2020;2(5):e200086.
- 15 Acosta J, Fernández-Armenta J, Penela D, Andreu D, Borras R, Vassanelli F, et al. Infarct transmurality as a criterion for first-line endo-epicardial substrate-guided ventricular tachycardia ablation in ischemic cardiomyopathy. *Heart Rhythm.* 2016;13(1):85–95.
- 16 Andreu D, Ortiz-Pérez JT, Boussy T, Fernández-Armenta J, De Caralt TM, Perea RJ, et al. Usefulness of contrast-enhanced cardiac magnetic resonance in identifying the ventricular arrhythmia substrate and the approach needed for ablation. *Eur Heart J.* 2014;35(20):1316–26.
- 17 Do DH, Eyvazian V, Bayoneta AJ, Hu P, Finn JP, Bradfield JS, et al. Cardiac magnetic resonance imaging using wideband sequences in patients with nonconditional cardiac implanted electronic devices. *Heart Rhythm.* 2018;15(2):218–25.
- 18 Schwartz SM, Pathrose A, Serhal AM, Ragin AB, Charron J, Knight BP, et al. Evaluation of image quality of wideband single-shot late gadolinium-enhancement MRI in patients with a cardiac implantable electronic device. *J Cardiovasc Electrophysiol.* 2021;32(1):138–47.
- 19 Singh A, Kawaji K, Goyal N, Nazir NT, Beaser A, O'Keefe-Baker V, et al. Feasibility of Cardiac Magnetic Resonance Wideband Protocol in Patients With Implantable Cardioverter Defibrillators and Its Utility for Defining Scar. *Am J Cardiol.* 2019;123(8):1329–35.
- 20 Roca-Luque I, Van Breukelen A, Alarcon F, Garre P, Tolosana JM, Borras R, et al. Ventricular scar channel entrances identified by new wideband cardiac magnetic resonance sequence to guide ventricular tachycardia ablation in patients with cardiac defibrillators. *Europace.* 2020;22(4):598–606.



## Contact

Hajnalka Vágó, M.D.  
Semmelweis University  
Heart and Vascular Center  
Gáál József út 9  
Budapest 1122  
Hungary  
Phone: +36-20-825-8058  
vago.hajnalka@med.semmelweis-univ.hu

# High Spatial Resolution Coronary Magnetic Resonance Angiography: A Single Center Experience

Reza Hajhosseiny<sup>1</sup>; Aurélien Bustin<sup>1</sup>; Imran Rashid<sup>1</sup>; Gastao Cruz<sup>1</sup>; Karl P. Kunze<sup>1,2</sup>; Radhouene Neji<sup>1,2</sup>; Ronak Rajani<sup>3</sup>; Claudia Prieto<sup>1</sup>; René M. Botnar<sup>1</sup>

<sup>1</sup>School of Biomedical Engineering and Imaging Sciences, King's College London, London, United Kingdom

<sup>2</sup>MR Research Collaborations, Siemens Healthcare Limited, Frimley, United Kingdom

<sup>3</sup>School of Cardiovascular Medicine and Sciences, King's College London, London, United Kingdom

## Abstract

Coronary magnetic resonance angiography (CMRA) could potentially offer a safe, non-invasive alternative for the anatomical assessment of coronary artery disease (CAD), which is free of ionizing radiation and iodinated contrast agents. However, image acquisition with conventional free-breathing CMRA frameworks is limited by long and unpredictable scan times, whilst image degradation due to respiratory motion remains a challenge. Here we outline a CMRA framework, that aims to overcome some of these challenges by incorporating a highly undersampled Cartesian acquisition with a two-dimensional (2D) image navigator to enable 100% respiratory scan efficiency, 2D translational motion correction, and three-dimensional (3D) non-rigid motion estimation, which is then fully reconstructed using a 3D patch-based low-rank regularization framework (PROST)<sup>1</sup>. We recently validated this framework against coronary computed tomography angiography (CCTA) in a single-center trial of 50 patients with suspected CAD. Diagnostic image quality was obtained in 95% of all coronary segments. The sensitivity, specificity, and negative predictive value were as follows: per-patient, 100%, 74%, and 100%; per-vessel, 81%, 88%, and 97%; and per-segment, 76%, 95%, and 99%, respectively. These findings emphasize the growing potential of this CMRA framework as a viable alternative to CCTA and invasive X-ray angiography for the anatomical assessment of CAD.

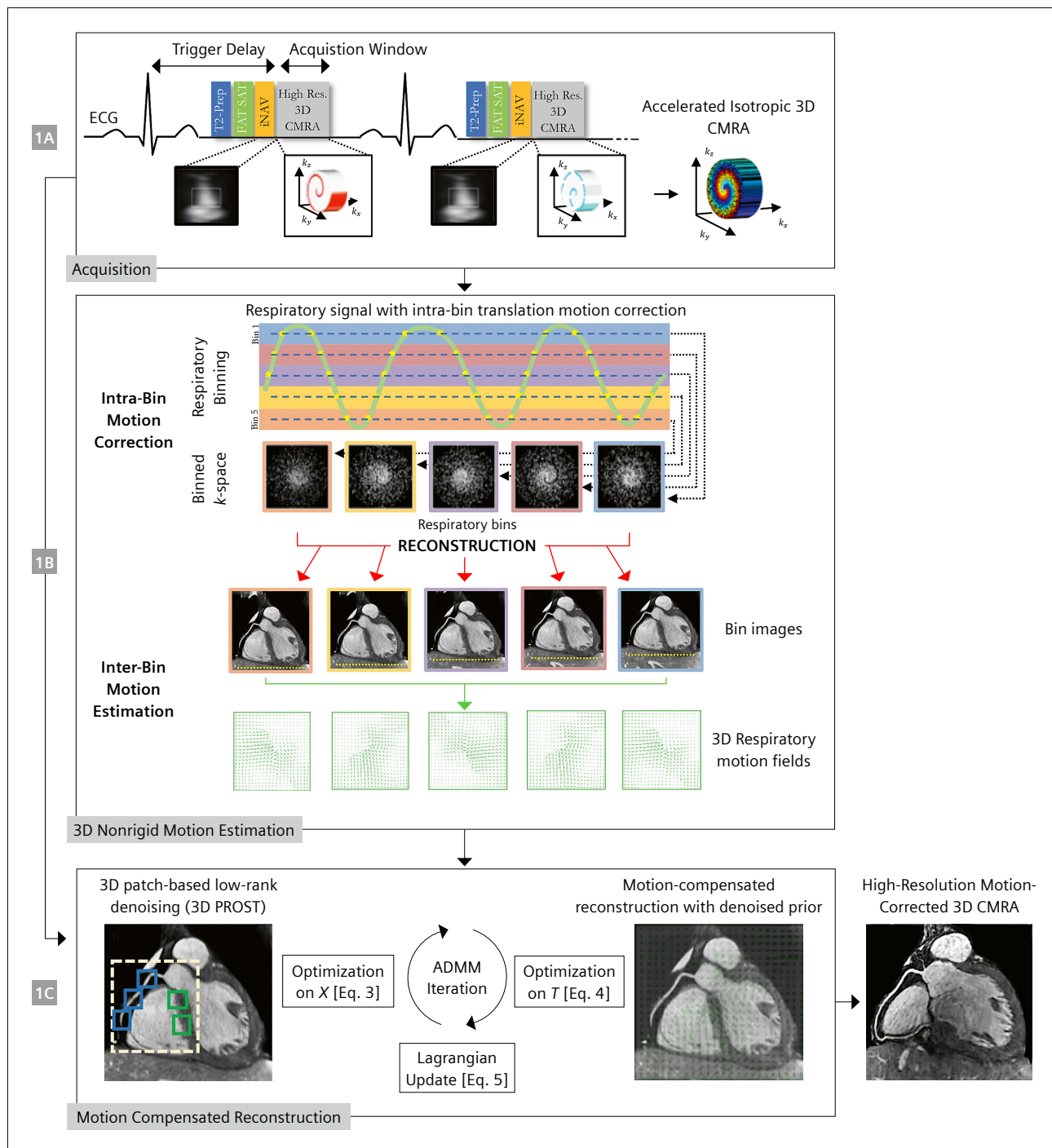
## Introduction

Cardiovascular disease is the leading cause of mortality worldwide [1]. Among all causes of cardiovascular disease, atherosclerotic coronary artery disease (CAD) accounts for approximately half of all cases [1]. The early detection and long-term monitoring of CAD enable targeted risk stratification and prophylactic treatment of patients most at risk of progressing toward acute coronary syndromes. Invasive X-ray coronary angiography and non-invasive coronary computed tomography angiography (CCTA) are the gold standard imaging modalities for the assessment of CAD [2–7]. Despite being highly diagnostic, X-ray coronary angiography is limited by invasive complications (e.g., death, stroke, myocardial and vascular injury, pain, and bleeding), whilst both X-ray coronary angiography and CCTA are limited by the risks from ionizing radiation and contrast-mediated nephropathy. There is therefore a clear need for an alternative imaging modality for the early detection and long-term monitoring of CAD, which is free of the risks associated with X-ray coronary angiography and CCTA.

## Coronary magnetic resonance angiography

Cardiovascular magnetic resonance (CMR) could be a safe, non-invasive alternative for the imaging of coronary artery stenosis without ionizing radiation or iodinated contrast

<sup>1</sup>Work in progress. The application is currently under development and is not for sale in the U.S. and in other countries. Its future availability cannot be ensured.



**1** Schematic overview of the proposed accelerated free-breathing 3D CMRA acquisition with sub-millimeter isotropic resolution, 100% scan efficiency, and non-rigid motion-compensated PROST reconstruction. **(1A)** CMRA acquisition is performed with an undersampled 3D variable density spiral-like Cartesian trajectory with golden angle between spiral-like interleaves (VD-CASPR), preceded by 2D image navigators (iNAV) to allow for 100% scan efficiency, and beat-to-beat translational respiratory-induced motion correction of the heart. **(1B)** Foot-head respiratory signal is estimated from the 2D iNAs and used to assign the acquired data to 5 respiratory bins and translation-corrected respiratory bins. Subsequent reconstruction of each bin is performed using soft-gated SENSE, and 3D non-rigid motion fields are then estimated from the 5 reconstructed datasets. **(1C)** The final 3D whole-heart motion-corrected CMRA image is obtained using the proposed 3D patch-based (PROST) non-rigid motion-compensated reconstruction.

**Abbreviations:** CMRA = coronary magnetic resonance angiography; PROST = patch-based undersampled reconstruction; ADMM = alternating direction method of multipliers.

Adapted and reproduced with permission from Bustin et al. [22].

agent. Large multi-center studies have demonstrated the clinical potential of coronary magnetic resonance angiography (CMRA) against X-ray coronary angiography for the anatomical assessment of CAD with per-patient sensitivity, specificity, and negative predictive value of up 94%, 82%, and 92% respectively [8–10]. However, widespread clinical implementation of CMRA is currently limited to suspected anomalous coronary arteries, suspected coronary artery aneurysms (e.g., Kawasaki's disease), coronary artery graft patency assessment, assessment of the proximal coronary arteries, and patients with renal impairment who are unable to receive iodinated contrast [11–13]. The very limited and specific clinical use of CMRA is due to long and unpredictable acquisition times, cumbersome scan planning, lower spatial resolution (usually 1–2 mm anisotropic), and motion-related (cardiac, respiratory, and patient) degradation of image quality.

In a similar fashion to CCTA, CMRA overcomes cardiac motion artifacts by using prospective electrocardiographic (ECG) gating to acquire data during the quiescent phase of the cardiac cycle when coronary artery motion is minimal [11], usually in mid-to-late diastole. In cases of cardiac arrhythmias and variable heart rates, which disproportionately impact the diastolic phase of the cardiac cycle, systolic imaging is the preferred option [11]. An alternative retrospective ECG gating approach is to continuously acquire data throughout the cardiac cycle and then reconstruct multiple cardiac phases and select the phase with the sharpest images or fewest motion artefacts [14, 15].

To compensate for the respiratory motion artifacts during free-breathing acquisitions, conventional CMRA estimates the respiratory displacement and deformation of the heart and surrounding tissues using the diaphragmatic 1D navigator approach [11, 16–18]. Here the liver-diaphragm interface lends itself for motion tracking, with the increased signal-to-noise ratio (SNR) of the right hemi diaphragm used as a surrogate to track the superior-inferior motion of the heart during the respiratory cycle, and with respiratory gating enabled to obtain image data at the quiescent phase of end of expiration [16, 19, 20, 17]. However, there is a non-linear relationship between the displacement of the diaphragm and the heart, requiring a patient-specific correction factor, which is usually set at 0.6 (population average) when gating is combined with respiratory motion correction [16]. Furthermore, only data within a small (end-expiration) respiratory gating window is accepted, significantly reducing scan efficiency and leading to prolonged and unpredictable acquisition times [21]. Moreover, prospective or retrospective translational motion compensation can only be applied in the superior-inferior direction [21]. Finally, this approach

adds complexity as detailed scan planning and defining separate imaging parameters for the navigator acquisition are required, further increasing scan time and costs [16]. In addition, a fully sampled 3D whole-heart CMRA acquisition at high spatial resolution is associated with long acquisition times (up to 30 minutes), regardless of cardiac and respiratory motion gating, which leads to patient discomfort and patient-related motion artifacts.

To overcome these limitations, we have leveraged recent advances in CMR technology including trajectory design, motion correction, and undersampled reconstruction techniques – to propose a novel, highly accelerated, high-spatial-resolution (sub-1 mm<sup>3</sup>), free-breathing, non-contrast, 3D whole-heart CMRA framework in a clinically feasible and 100% predictable acquisition time.

## Proposed coronary magnetic resonance angiography framework

The proposed CMRA framework was developed on a 1.5T CMR scanner (MAGNETOM Aera, Siemens Healthcare, Erlangen, Germany) with a dedicated 32-channel spine coil and an 18-channel body coil. It combines a highly undersampled variable-density Cartesian acquisition with an image navigator (iNAV) to enable model-free 2D translational and 3D non-rigid motion estimation, and finally deploys a motion-corrected 3D patch-based low-rank image reconstruction (PROST) algorithm<sup>1</sup> to reconstruct the undersampled acquisition. These steps are outlined in more detail in the following sections and in the article by Bustin et al. [22].

### Accelerated CMRA acquisition

An undersampled (3- to 4-fold) free-breathing 3D whole-heart, balanced steady-state free-precession (bSSFP) sequence with a 3D variable-density spiral-like Cartesian trajectory (VD-CASPR) with golden-angle step was employed as previously proposed [23] (Fig. 1). A low-resolution 2D iNAV preceded each spiral-like interleave to allow 100% scan efficiency, predictable scan time, and 2D translational motion estimation of the heart on a beat-to-beat basis. The 2D iNAVs were obtained by spatially encoding the startup profiles of the bSSFP sequence [24]. A spectrally selective SPIR (Spectral Presaturation with Inversion Recovery) fat saturation pulse with a constant flip angle (FA) of 130° was used to improve coronary depiction and minimize fat-related aliasing artifacts. An adiabatic T2 preparation pulse [25, 26] was played at each heartbeat in order to enhance the contrast between blood and cardiac muscle and to avoid the use of extracellular contrast agents.

<sup>1</sup>Work in progress. The application is currently under development and is not for sale in the U.S. and in other countries. Its future availability cannot be ensured.

### Beat-to-beat 2D translational motion estimation

Beat-to-beat 2D translational motion correction was performed as previously proposed in [27, 28]. Briefly, foot-head (FH) and right-left (RL) translational respiratory motion of the heart was extracted from the iNAVs using a template-matching algorithm with normalized cross-correlation as similarity measure [24]. The reference template was manually selected during scan planning on a region encompassing the subject's heart. The FH respiratory signal was used to sort the acquired data into five respiratory states or bins. Intra-bin 2D translational motion estimation was performed by correcting the data for each bin to the same respiratory position (taken as the bin center) (Fig. 1). This correction was implemented by modulating the  $k$ -space data with a linear phase shift according to the previously estimated respiratory motion [27].

### Bin-to-bin non-rigid motion estimation

In this framework, the acquired 3D CMRA data is undersampled (3- to 4-fold), with the resulting binned  $k$ -spaces being highly accelerated (~15- to 20-fold). Soft-gating iterative sensitivity encoding reconstruction [27] was employed to reconstruct each respiratory bin. Bin-to-bin 3D non-rigid motion estimation was subsequently performed using spline-based free-form deformation [29], considering the end-expiration bin as reference image (Fig. 1).

### 3D patch-based non-rigid motion-compensated reconstruction (non-rigid PROST)

Following this step, the estimated 3D non-rigid motion fields are then directly incorporated into a general matrix description reconstruction framework [30, 31]. In contrast to previous CMRA studies where the data are acquired either fully sampled [27] or with modest undersampling factors [28], our proposed high-resolution ( $0.9 \text{ mm}^3$ ) CMRA framework exploits higher undersampling factors (3- to 4-fold) to reach approximately 10-minute acquisition time. 3D patch-based low-rank undersampled reconstruction (3D PROST) has been proposed to highly accelerate sub-mm CMRA imaging with translational motion correction only [23]. 3D PROST reconstruction exploits the inherent redundancies of the complex 3D anatomy of the coronary arteries on a local (i.e., within a patch) and non-local (i.e., between similar patches within a neighborhood) basis, through an efficient iterative low-

rank decomposition and singular value thresholding. The proposed non-rigid PROST framework combines 3D PROST with the matrix formalism for non-rigid motion correction, and can be formulated as the unconstrained optimization (found at the bottom of the page), where  $X$  is the non-rigid motion-corrected 3D CMRA volume (or "motion-free" image),  $K$  is the 2D translational motion-corrected  $k$ -space data,  $E$  is the encoding operator composed of:  $A_b$  the sampling matrix for bin  $b$ ,  $F$  the 3D Fourier transform,  $S_c$  the coil sensitivities for coil  $c$ ,  $U_b$  the estimated 3D non-rigid motion fields for bin  $b$  and  $N_{bins}$  the number of respiratory bins.  $\|\cdot\|_F$  and  $\|\cdot\|_*$  denote the Frobenius and nuclear norms respectively,  $P_p(\cdot)$  is the patch-selection operator at voxel  $p$ . Equation (1) can be efficiently solved by operator-splitting via alternating direction method of multipliers (ADMM).

## Results from a single-center clinical study

The proposed CMRA framework was assessed in a cohort of patients with suspected CAD at Guy's and St Thomas' Hospitals, London, UK. The full results of this clinical study are described in the article by Hajhosseiny et al. [32]. In summary, 50 consecutive patients between 35 and 77 years of age who were referred for a clinically indicated CTCA were invited to undergo a CMRA within the proposed framework. In the absence of contraindications, each patient was treated with intravenous metoprolol in 5 mg increments with a maximum dose of 30 mg, aiming for a target heart rate (HR)  $< 65 \text{ bpm}$  in order to maximize the diastolic acquisition window, reduce HR variability and cardiac motion artefacts. All patients were given 800 mg of sublingual glyceryl trinitrate to promote coronary vasodilation. To assess diagnostic performance, significant coronary stenosis was visually defined as luminal narrowing of  $\geq 50\%$  in each of the coronary segments using an intention-to-read approach. The image quality of CMRA images (3D whole-heart dataset and individual vessels) was evaluated using the following scale: 0, non-diagnostic; 1, poor (limited coronary vessel visibility or noisy image); 2, average (coronary vessel visible but diagnostic confidence low); 3, good (coronary artery adequately visualized and diagnostic quality image); and 4, excellent (coronary artery clearly depicted).

All CMRA acquisitions were successfully completed in an imaging time of  $10.7 \pm 1.4 \text{ min}$  (range 8.0–13.3 min), with 100% respiratory scan efficiency. All CMRA acquisi-

$$(1) L_{NR-PROST}(X, T, Y) := \underset{X, T_p, Y}{\operatorname{argmin}} \|EX - K\|_F^2 + \lambda \sum_p \|T_p\|_* + \frac{\mu}{2} \sum_p \|T_p - P_p(X) - \frac{Y_p}{\mu}\|_F^2$$

$$(2) E = \sum_b^{N_{bins}} A_b F S_c U_b$$

tions were performed in diastole with an average acquisition window of  $88 \pm 8$  ms (range 81–111 ms). Mean age was  $55 \pm 9$  years, 33/50 (66%) were male, and 12/50 (24%) had significant CAD on CTCA.

In total, 95% of CMRA segments were deemed diagnostic, while all left main stem segments were diagnostic on CMRA. Furthermore, 97%, 96%, and 87% of right coronary artery, left anterior descending artery, and left circumflex artery segments were diagnostic on CMRA. Finally, 97%, 97%, and 90% of proximal, middle, and distal CMRA segments were of diagnostic quality.

The sensitivity, specificity, positive predictive value, negative predictive value, and diagnostic accuracy of CMRA for detecting significant CAD were as follows:

- per-patient

100% (95% CI: 76–100%), 74% (95% CI: 58–85%), 55% (95% CI: 35–73%), 100% (95% CI: 88–100%), and 80% (95% CI: 67–89%) respectively;

- per-vessel

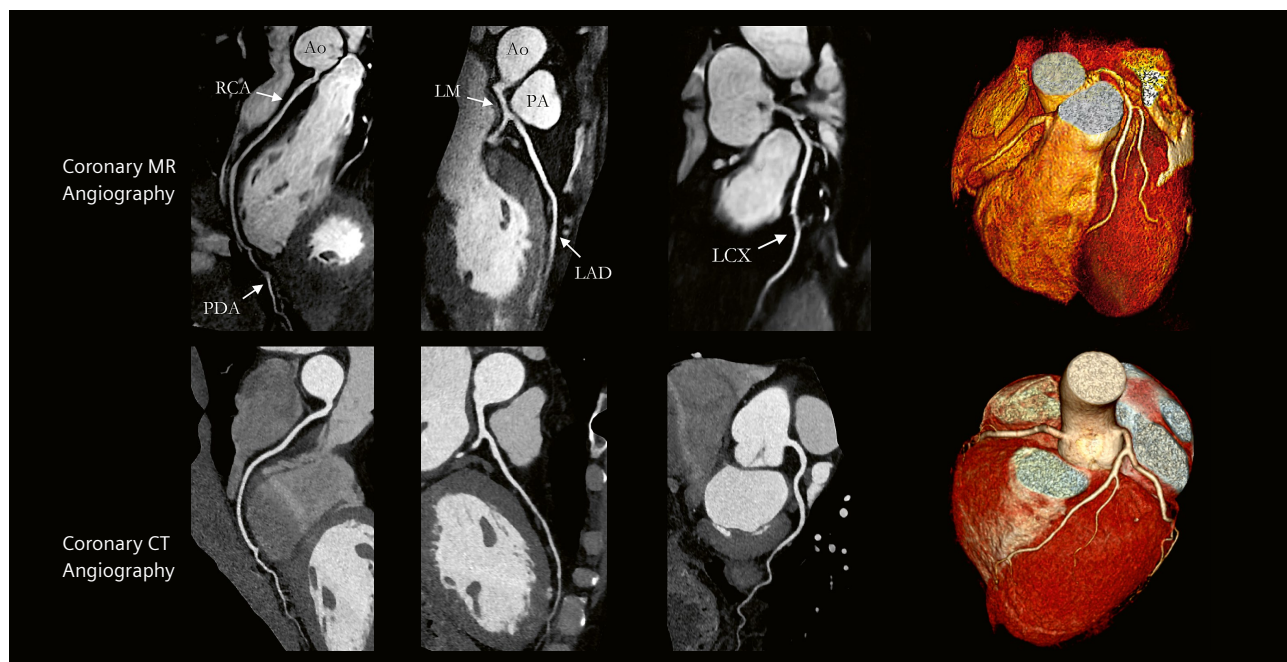
81% (95% CI: 57–93%), 88% (95% CI: 82–93%), 46% (95% CI: 30–64%), 97% (95% CI: 93–99%), and 88% (95% CI: 81–92%) respectively;

- per-segment

76% (95% CI: 55–89%), 95% (95% CI: 92–97%), 44% (95% CI: 30–60%), 99% (95% CI: 97–99%), and 94% (95% CI: 91–96%) respectively.

Example images from selected patients with suspected CAD are shown in Figures 2–8.

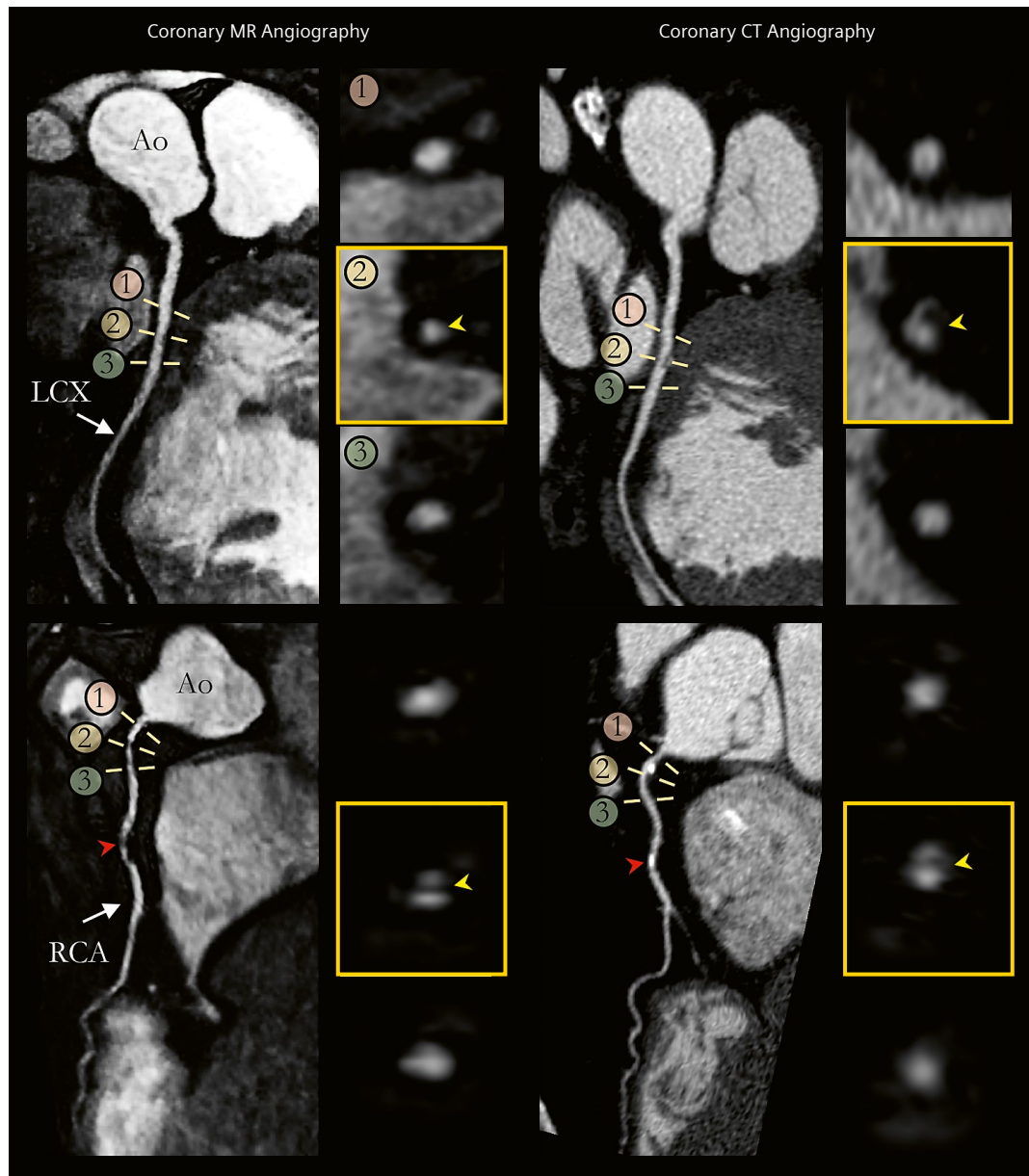
The proposed CMRA framework (without PROST regularization) has been implemented in-line in the scanner software, providing non-rigid motion corrected reconstructions in ~2–5 min (CPU).



**2** Non-contrast whole-heart sub-millimeter isotropic CMRA images of a 53-year-old male patient with normal coronary arteries. Accelerated free-breathing CMRA images acquired and reconstructed with the proposed framework are shown in the top row, revealing the LAD, RCA, and LCX territories. The corresponding reformatted images obtained with contrast-enhanced CCTA are shown in the bottom row. 3D volume-rendered images for both modalities are shown in the right-hand column.

**Abbreviations:** CMRA = coronary magnetic resonance angiography; CCTA = coronary computed tomography angiography; LAD = left anterior descending artery; RCA = right coronary artery; LCX = left circumflex artery; PDA = posterior descending artery; PA = pulmonary artery; Ao = aorta.

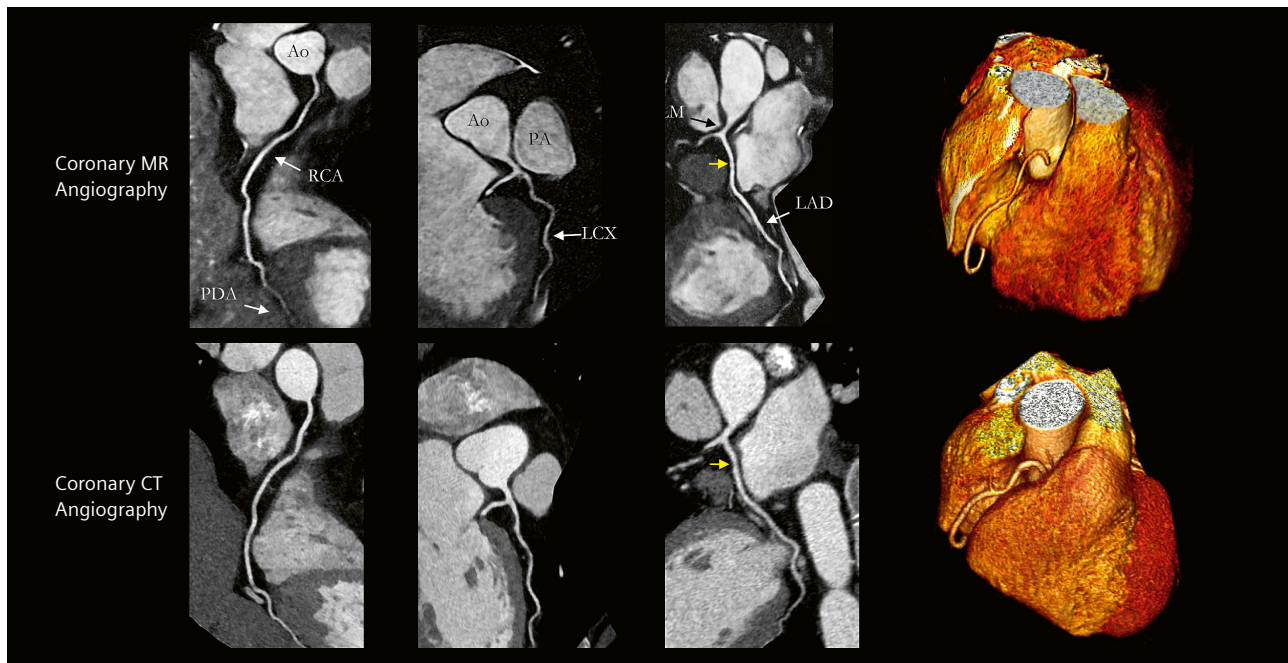
Adapted and reproduced with permission from Bustin et al. [22].



- 3** Reformatted non-contrast whole-heart sub-millimeter isotropic CMRA (left) and contrast-enhanced CCTA (right) images along the LCX (top) and RCA (bottom) are shown for a 54-year-old male patient. The CCTA images demonstrate mild (< 50%) disease with a calcified plaque within the proximal RCA, severe disease (> 50%) with a partially calcified plaque in the mid-segment of the RCA (red arrows), and mild (< 50%) disease with calcified plaque in the mid-segment of the LCX. Luminal narrowing is seen on the cross-sectional views at the sites of coronary plaque on the CMRA images (yellow arrows).

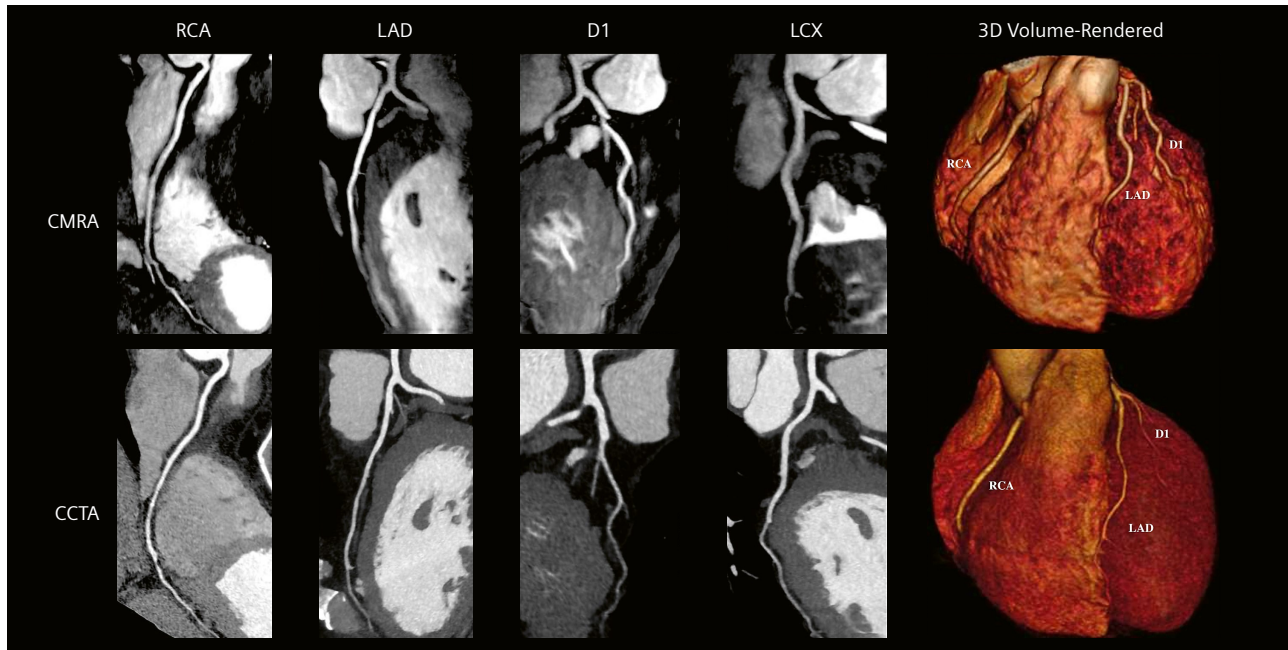
**Abbreviations:** CMRA = coronary magnetic resonance angiography; CCTA = coronary computed tomography angiography; LAD = left anterior descending artery; RCA = right coronary artery; LCX = left circumflex artery; Ao = aorta.

*Adapted and reproduced with permission from Bustin et al. [22].*



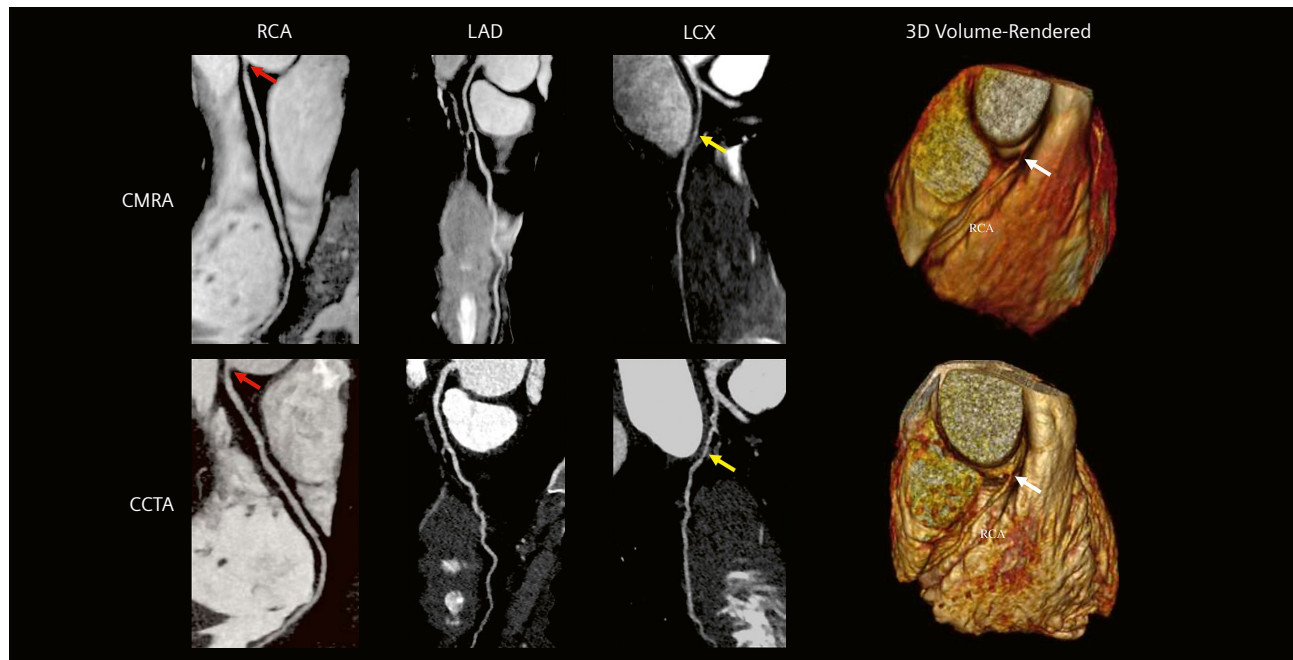
**4** Non-contrast whole-heart sub-millimeter isotropic CMRA images of a 35-year-old male patient with normal coronary arteries. The CMRA images acquired and reconstructed with the proposed framework are shown in the top row, revealing the LAD and RCA. The corresponding reformatted images obtained with contrast-enhanced CCTA are shown in the bottom row. The 3D volume-rendered images are shown in the right-hand column, which were both correctly visualized on the CMRA images.  
**Abbreviations:** CMRA = coronary magnetic resonance angiography; CCTA = coronary computed tomography angiography; LAD = left anterior descending artery; RCA = right coronary artery; LCX = left circumflex artery; LM = left main stem; PDA = posterior descending artery; PA = pulmonary artery; Ao = aorta.

Adapted and reproduced with permission from Bustin et al. [22].



**5** Curved multiplanar reformat and 3D volume-rendered non-contrast CMRA and contrast-enhanced CCTA in a 54-year-old male with no significant stenosis.  
**Abbreviations:** CMRA = coronary magnetic resonance angiography; CCTA = coronary computed tomography angiography; RCA = right coronary artery; LAD = left anterior descending artery; D1 = first diagonal artery; LCX = left circumflex artery.

Adapted and reproduced with permission from Hajhosseiny et al. [32].

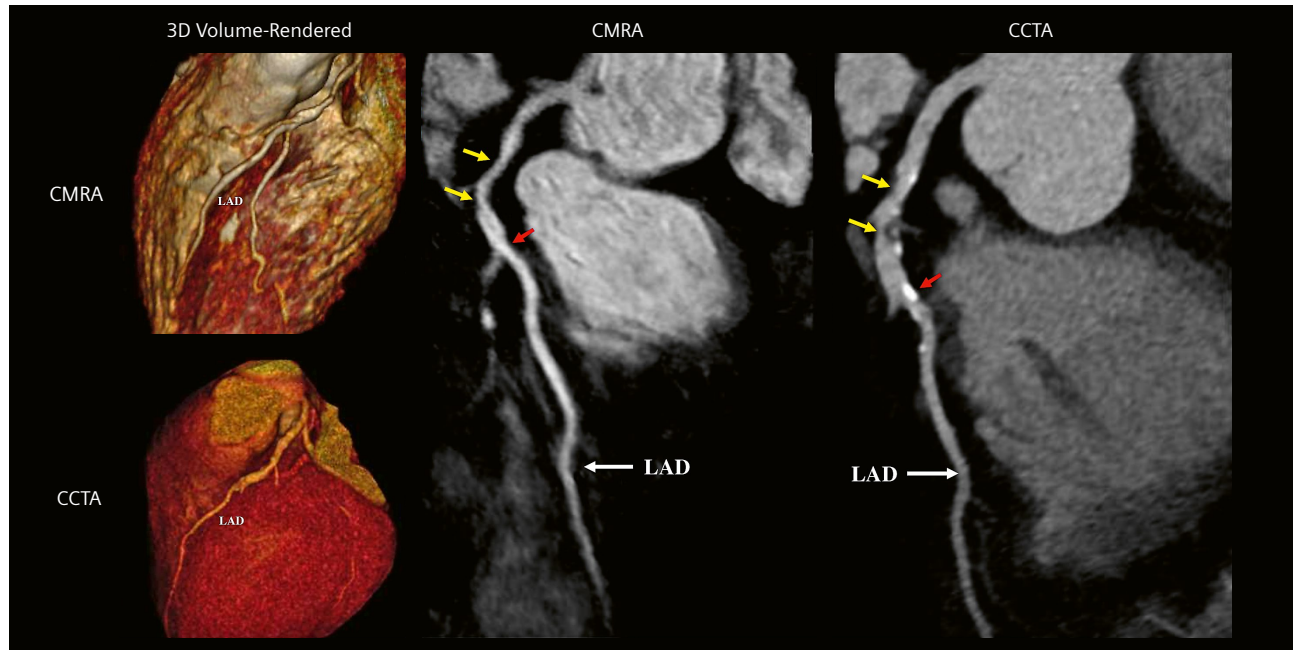


- 6** Curved multiplanar reformat and 3D volume-rendered non-contrast CMRA and contrast-enhanced CCTA in a 44-year-old male with > 50% non-calcified stenosis in the ostial RCA (red arrows). This can also be seen in the 3D volume-rendered images (white arrows). The yellow arrows represent a > 50% stenosis in the proximal/mid LCX.

**Abbreviations:** CMRA = coronary magnetic resonance angiography; CCTA = coronary computed tomography angiography;

RCA = right coronary artery; LAD = left anterior descending artery; LCX = left circumflex artery.

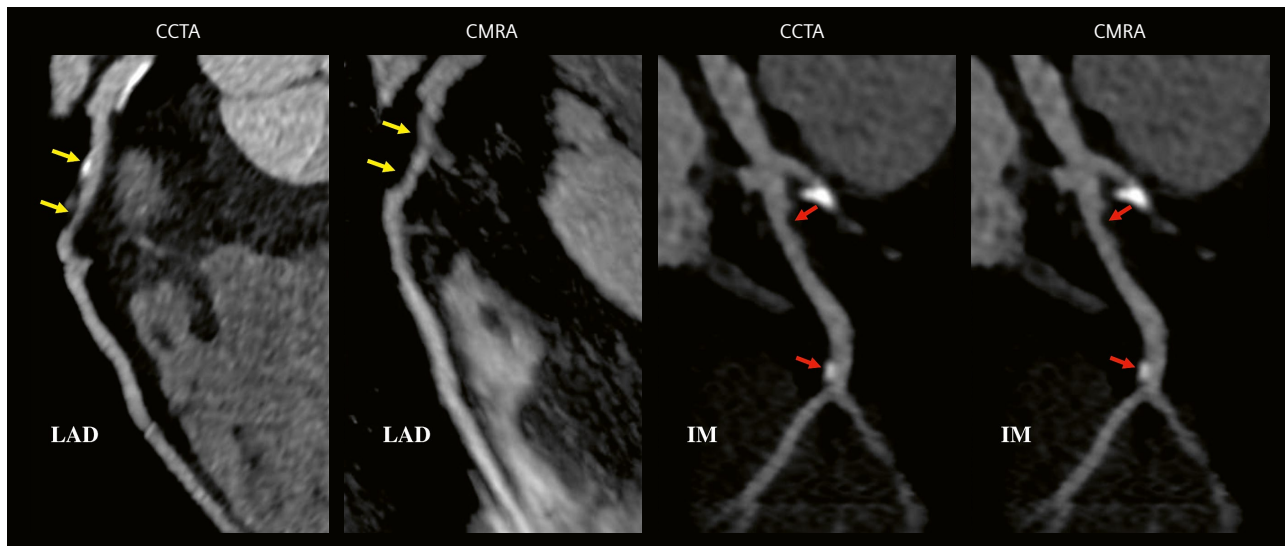
Adapted and reproduced with permission from Hajhosseini et al. [32].



- 7** Curved multiplanar reformat and 3D volume-rendered non-contrast CMRA and contrast-enhanced CCTA in a 60-year-old male with > 50% partially calcified stenosis in the proximal-to-mid LAD on either side of the first diagonal artery (yellow arrows). The red arrows point to a focal calcified < 50% stenosis just distal to the second diagonal artery.

**Abbreviations:** CMRA = coronary magnetic resonance angiography; CCTA = coronary computed tomography angiography;

LAD = left anterior descending artery. Adapted and reproduced with permission from Hajhosseini et al. [32].



- 8** Curved multiplanar reformat non-contrast CMRA and contrast-enhanced CCTA in a 57-year-old male with > 50% partially calcified stenosis in the proximal LAD (yellow arrows). The red arrows point to focal < 50% stenosis in the proximal and distal ramus intermedius artery.

**Abbreviations:** CMRA = coronary magnetic resonance angiography; CCTA = coronary computed tomography angiography; LAD = left anterior descending artery; IM = ramus intermedius artery. *Adapted and reproduced with permission from Hajhosseiny et al. [32].*

## Conclusions

In this initial single-center clinical study, we have introduced a robust, contrast-free, sub-millimeter CMRA framework with predictable and clinically feasible scan times of approximately 10 minutes, achieving highly diagnostic image quality and diagnostic accuracy for excluding significant disease in patients with suspected CAD. This is the first clinical study to assess the diagnostic performance of a 3D contrast-free CMRA approach that enables a predictable scan time of approximately 10 minutes for 0.9 mm<sup>3</sup> spatial-resolution. This was achieved by employing a robust motion corrected free-breathing acquisition with 100% respiratory scan efficiency, using image navigation for 2D translational motion estimation and respiratory data binning combined with 3D non-rigid motion compensated undersampled reconstruction employing a 3- to 4-fold undersampled Cartesian acquisition and a patched-based low-rank reconstruction. Future work will focus on multi-center clinical assessment of this novel framework to determine its clinical applicability in a larger cohort of patients with a wider spectrum of CAD.

- 2 Kočka V. The coronary angiography – An old-timer in great shape. *Cor Vasa* 2015;57(6):e419–e424. Available at: <https://www.sciencedirect.com/science/article/pii/S0010865015001009>. Accessed August 14, 2018.
- 3 Tavakol M, Ashraf S, Brener SJ. Risks and complications of coronary angiography: a comprehensive review. *Glob J Health Sci.* 2012;4(1):65–93. Available at: <http://www.ncbi.nlm.nih.gov/pubmed/22980117>. Accessed August 14, 2018.
- 4 Kolossváry M, Szilveszter B, Merkely B, Maurovich-Horvat P. Plaque imaging with CT-a comprehensive review on coronary CT angiography based risk assessment. *Cardiovasc Diagn Ther.* 2017;7(5):489–506. Available at: <http://www.ncbi.nlm.nih.gov/pubmed/29255692>. Accessed August 14, 2018.
- 5 Hamilton M, Baumbach A. Non invasive coronary imaging with computed tomography. [journal on the Internet]. 2007; 5(20). Available at: <https://www.escardio.org/Journals/E-Journal-of-Cardiology-Practice/Volume-5/Non-Invasive-Coronary-Imaging-With-Computed-Tomography-Title-Non-Invasive-Cor>. Accessed August 14, 2018.
- 6 Alfakih K, Byrne J, Monaghan M. CT coronary angiography: a paradigm shift for functional imaging tests. *Open Hear.* 2018;5(1):e000754. Available at: <http://www.ncbi.nlm.nih.gov/pubmed/29632679>. Accessed August 14, 2018.
- 7 Doris MK, Newby DE. How should CT coronary angiography be integrated into the management of patients with chest pain and how does this affect outcomes? *Eur Heart J - Qual Care Clin. Outcomes* 2016;2(2):72–80. Available at: <https://academic.oup.com/ehjqcco/article-lookup/doi/10.1093/ehjqcco/qcv027>. Accessed August 14, 2018.
- 8 Kim WY, Danias PG, Stuber M, et al. Coronary magnetic resonance angiography for the detection of coronary stenoses. *N Engl J Med.* 2001;345(26):1863–1869. Available at: <http://www.ncbi.nlm.nih.gov/pubmed/11756576>. Accessed July 26, 2019.
- 9 Yang Q, Li K, Liu X, et al. Contrast-Enhanced Whole-Heart Coronary Magnetic Resonance Angiography at 3.0-T. A Comparative Study With X-ray Angiography in a Single Center. *J Am Coll Cardiol.* 2009;54(1):69–76.

## References

- 1 Benjamin EJ, Virani SS, Callaway CW, et al. Heart disease and stroke statistics-2018 update: A report from the American Heart Association. *Circulation* 2018;137(12):e67–e492. Available at: <http://www.ncbi.nlm.nih.gov/pubmed/29386200>.

- 10 Kato S, Kitagawa K, Ishida N, et al. Assessment of coronary artery disease using magnetic resonance coronary angiography: a national multicenter trial. *J Am Coll Cardiol.* 2010;56(12):983–91. Available at: <http://linkinghub.elsevier.com/retrieve/pii/S0735109710024691>. Accessed September 30, 2018.
- 11 Sriharan M, McParland P, Harden S, Nicol E. Non-Invasive Coronary Angiography. In: Branislav B. Coronary Angiography - Advances in Noninvasive Imaging Approach for Evaluation of Coronary Artery Disease. [book on the Internet]. London: InTech, 2011:99–122. DOI: 10.5772/22475. Available at: <http://www.intechopen.com/books/coronary-angiography-advances-in-noninvasive-imaging-approach-for-evaluation-of-coronary-artery-disease/non-invasive-coronary-angiography>. Accessed August 16, 2018.
- 12 Mangla A, Oliveros E, Williams KA, Kalra DK. Cardiac imaging in the diagnosis of coronary artery disease. *Curr Probl Cardiol.* 2017;42(10):316–366. Available at: <https://www.sciencedirect.com/science/article/pii/S0146280617300725?via%3Dihub#bib116>. Accessed August 16, 2018.
- 13 Hamdy A, Ishida M, Sakuma H. Cardiac MR assessment of coronary arteries. *CVIA* 2017;1(1):49–59. Available at: <https://doi.org/10.22468/cvia.2016.00066>. Accessed December 11, 2018.
- 14 Coppo S, Piccini D, Bonanno G, et al. Free-running 4D whole-heart self-navigated golden angle MRI: Initial results. *Magn Reson Med.* 2015;74(5):1306–1316. Available at: <http://www.ncbi.nlm.nih.gov/pubmed/25376772>. Accessed September 3, 2018.
- 15 Pang J, Bhat H, Sharif B, et al. Whole-heart coronary MRA with 100% respiratory gating efficiency: Self-navigated three-dimensional retrospective image-based motion correction (TRIM). *Magn Reson Med.* 2014;71(1):67–74. Available at: <http://doi.wiley.com/10.1002/mrm.24628>. Accessed August 18, 2018.
- 16 Henningsson M, Botnar RM. Advanced respiratory motion compensation for coronary MR angiography. *Sensors (Basel).* 2013;13(6):6882–99. Available at: <http://www.ncbi.nlm.nih.gov/pmc/articles/PMC3708271/>. Accessed August 17, 2018.
- 17 Ehman RL, Felmlee JP. Adaptive technique for high-definition MR imaging of moving structures. *Radiology* 1989;173(1):255–263. Available at: <http://www.ncbi.nlm.nih.gov/pmc/articles/PMC2781017/>. Accessed August 17, 2018.
- 18 McConnell M V, Khasgiwala VC, Savord BJ, et al. Comparison of respiratory suppression methods and navigator locations for MR coronary angiography. *AJR Am J Roentgenol.* 1997;168(5):1369–1375. Available at: <http://www.ncbi.nlm.nih.gov/pmc/articles/PMC2781017/>. Accessed August 17, 2018.
- 19 Danias PG, McConnell M V, Khasgiwala VC, Chuang ML, Edelman RR, Manning WJ. Prospective navigator correction of image position for coronary MR angiography. *Radiology*. 1997;203(3):733–736. Available at: <http://www.ncbi.nlm.nih.gov/pmc/articles/PMC2781017/>. Accessed August 17, 2018.
- 20 Nehrke K, Börnert P, Groen J, Smink J, Böck JC. On the performance and accuracy of 2D navigator pulses. *Magn Reson Imaging* 1999;17(8):1173–81. Available at: <http://www.ncbi.nlm.nih.gov/pmc/articles/PMC2781017/>. Accessed August 17, 2018.
- 21 Correia T, Ginami G, Cruz G, et al. Optimized respiratory-resolved motion-compensated 3D Cartesian coronary MR angiography. *Magn Reson Med.* 2018;80(6):2618–2629. Available at: <http://www.ncbi.nlm.nih.gov/pmc/articles/PMC2781017/>. Accessed August 17, 2018.
- 22 Bustin A, Rashid I, Cruz G, et al. 3D whole-heart isotropic sub-millimeter resolution coronary magnetic resonance angiography with non-rigid motion-compensated PROST. *J Cardiovasc Magn Reson.* 2020;22(1):<https://doi.org/10.1186/s12968-020-00611-5>.
- 23 Bustin A, Ginami G, Cruz G, et al. Five-minute whole-heart coronary MRA with sub-millimeter isotropic resolution, 100% respiratory scan efficiency, and 3D-PROST reconstruction. *Magn Reson Med.* 2019;81(1):102–115.
- 24 Henningsson M, Koken P, Stehning C, Razavi R, Prieto C, Botnar RM. Whole-heart coronary MR angiography with 2D self-navigated image reconstruction. *Magn Reson Med.* 2012;67(2):437–445. Available at: <http://www.ncbi.nlm.nih.gov/pmc/articles/PMC2781017/>. Accessed August 17, 2018.
- 25 Nezafat R, Stuber M, Ouwerkerk R, Gharib AM, Desai MY, Pettigrew RI. B1-insensitive T2 preparation for improved coronary magnetic resonance angiography at 3T. *Magn Reson Med.* 2006;55(4):858–64.
- 26 Botnar RM, Stuber M, Danias PG, Kissinger K V, Manning WJ. Improved coronary artery definition with T2-weighted, free-breathing, three-dimensional coronary MRA. *Circulation*. 1999;99(24):3139–3148.
- 27 Cruz G, Atkinson D, Henningsson M, Botnar RM, Prieto C. Highly efficient nonrigid motion-corrected 3D whole-heart coronary vessel wall imaging. *Magn Reson Med.* 2017;77(5):1894–1908. Available at: <http://doi.wiley.com/10.1002/mrm.26274>. Accessed August 20, 2018.
- 28 Correia T, Cruz G, Schneider T, Botnar RM, Prieto C. Technical note: Accelerated nonrigid motion-compensated isotropic 3D coronary MR angiography. *Med Phys.* 2018;45(1):214–222.
- 29 Rueckert D, Sonoda LI, Hayes C, Hill DL, Leach MO, Hawkes DJ. Nonrigid registration using free-form deformations: application to breast MR images. *IEEE Trans Med Imaging.* 1999;18(8):712–721.
- 30 Batchelor PG, Atkinson D, Irarrazaval P, Hill DLG, Hajnal J, Larkman D. Matrix description of general motion correction applied to multishot images. *Magn Reson Med.* 2005;54(5):1273–1280.
- 31 Cruz G, Atkinson D, Buerger C, Schaeffter T, Prieto C. Accelerated motion corrected three-dimensional abdominal MRI using total variation regularized SENSE reconstruction. *Magn Reson Med.* 2016;75(4):1484–1498.
- 32 Hajhosseiny R, Rashid I, Bustin A, Munoz C, Cruz G, Nazir M.S., Grigoryan K, Ismail T.F., Preston R, Neji R, Kunze K, Razavi R, Chiribiri A, Masci P.G., Rajani R, Prieto C, Botnar R.M. Clinical comparison of sub-mm high-resolution non-contrast coronary MRA against coronary CTA in patients with low-intermediate risk of CAD: A single center trial. *J Cardiovasc Magn Reson.* 2021; IN PRESS.



## Contact

Reza Hajhosseiny, M.D.  
School of Biomedical Engineering and Imaging Sciences  
King's College London  
3<sup>rd</sup> floor Lambeth Wing  
London, SE1 7EH  
United Kingdom  
Phone: +44 020 7188 7188  
reza.hajhosseiny@kcl.ac.uk  
Twitter: @KCL\_CardiacMR

# Updates on Advanced Whole-Brain Vessel Wall Imaging in Stroke Patients

Fang Wu, M.D.<sup>1</sup>; Yuehong Liu, M.D.<sup>2</sup>; Qi Yang, M.D., Ph.D.<sup>2</sup>

<sup>1</sup>Department of Radiology and Nuclear Medicine, Xuanwu Hospital, Capital Medical University, Beijing, China

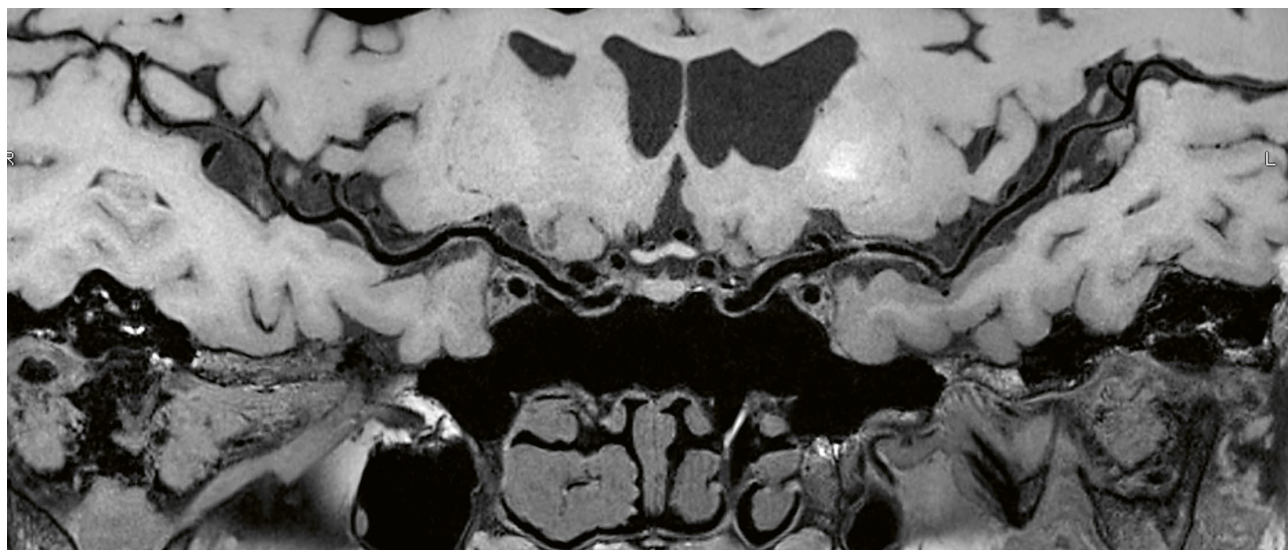
<sup>2</sup>Department of Radiology, Beijing Chaoyang Hospital, Capital Medical University, Beijing, China

## Abstract

Intracranial artery stenosis is one of the common causes of ischemic stroke in Asia. Advances in vessel wall imaging techniques now make it possible to directly visualize the intracranial vessel wall. Several single-center studies have suggested that intracranial vessel wall magnetic resonance imaging (VW-MRI) may provide insights into stroke etiology, vascular pathogenesis, and the risk of recurrent stroke. However, the robustness of intracranial VW-MRI as a valuable tool for the assessment of various cerebrovascular diseases still needs to be validated in a large-scale multicenter study. Thus, our research group initiated a multicenter study in China on February 1, 2017. This study aimed to investigate the clinical utility of whole-brain intracranial VW-MRI in assessing the etiologies in patients with ischemic stroke.

## Introduction

Stroke is one of the most common causes of death and disability in the world, which usually causes an abrupt onset of a neurological deficit [1, 2]. Intracranial artery stenosis has been considered a major cause of ischemic stroke, especially in Asia [3]. Traditionally, intracranial vascular diseases have been evaluated with invasive luminal imaging techniques, such as catheter angiography or non-invasive luminal imaging techniques (MR angiography or CT angiography). However, these techniques indirectly visualize vessel wall abnormalities, and many cerebral vasculopathies may have similar luminal narrowing. VW-MRI has been applied as the only non-invasive technique to directly assess the intracranial vessel wall structure [4, 5]. It can provide derived vessel wall characteristics to help clinicians determine stroke etiology, estimate atherosclerotic plaque burden or vasculitis activity, as well as future cerebrovascular events [6].



1 Curved-planar reformation of three-dimensional vessel wall magnetic resonance imaging (VW-MRI).

## Field strength and pulse sequences

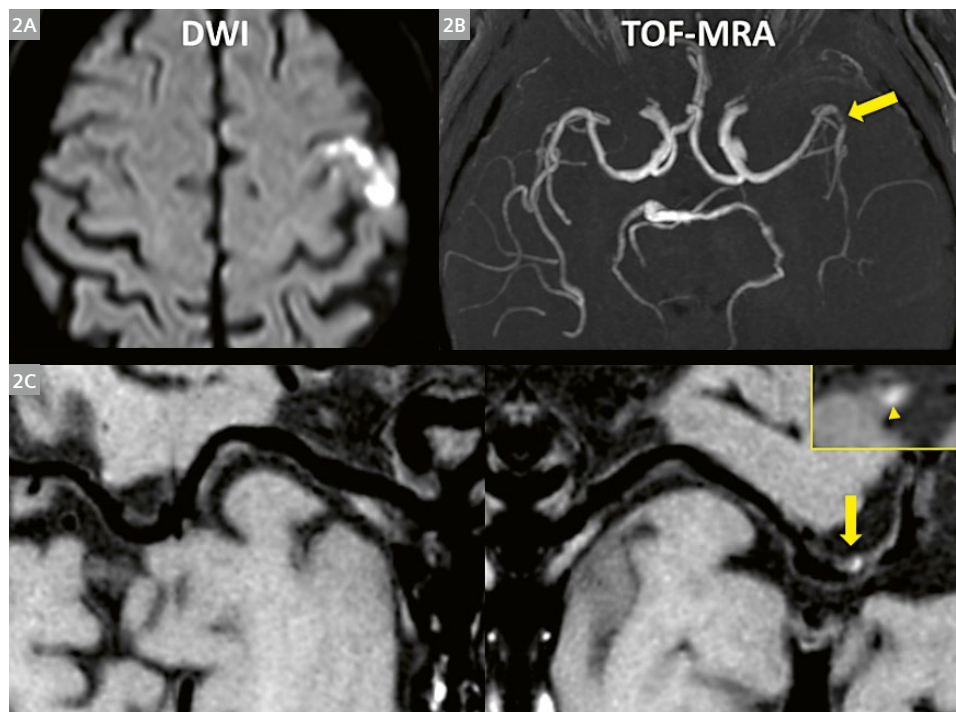
Currently, VW-MRI for intracranial arteries is performed on 3T MRI systems at most centers. Considering the small caliber of intracranial arteries, ultra-high field MRI (7T) may provide an additional value for evaluating intracranial atherosclerotic plaques, as it allows for a high signal-to-noise ratio (SNR), spatial resolution, and contrast-to-noise ratio. Although the feasibility of intracranial VW-MRI at 7T has been demonstrated in several *in-vivo* and *ex-vivo* studies [7, 8], more evidence of additional clinical value of 7T MRI is needed before being used in routine clinical practice. The selection of pulse sequences and protocols remains variable across sites and vendors. To clearly depict the inner and outer boundaries of vessel walls, adequate spatial resolution, as well as excellent blood and cerebrospinal fluid (CSF) suppression are essential for intracranial vessel wall imaging techniques. A two-dimensional (2D) sequence can provide a better in-plane spatial resolution (a voxel size of  $0.4 \times 0.4 \times 2.0 \text{ mm}^3$ ) for targeted vessel wall lesions. However, it is unable to achieve a more global depiction of multiple vessels and detect lesions without luminal stenosis. Literature shows a shift from 2D to 3D volumetric acquisitions. 3D isotropic imaging with a larger coverage of whole-brain vessels makes it possible to perform multi-planar and curved-planar reformations, as well as assess plaque burden and distribution of major intracranial arteries from various perspectives (Fig. 1) [9]. There are numerous technical developments for VW-MRI pulse sequences aimed to reduce blood and CSF flow artifacts.

## Vascular pathologies and their depiction with VW-MRI

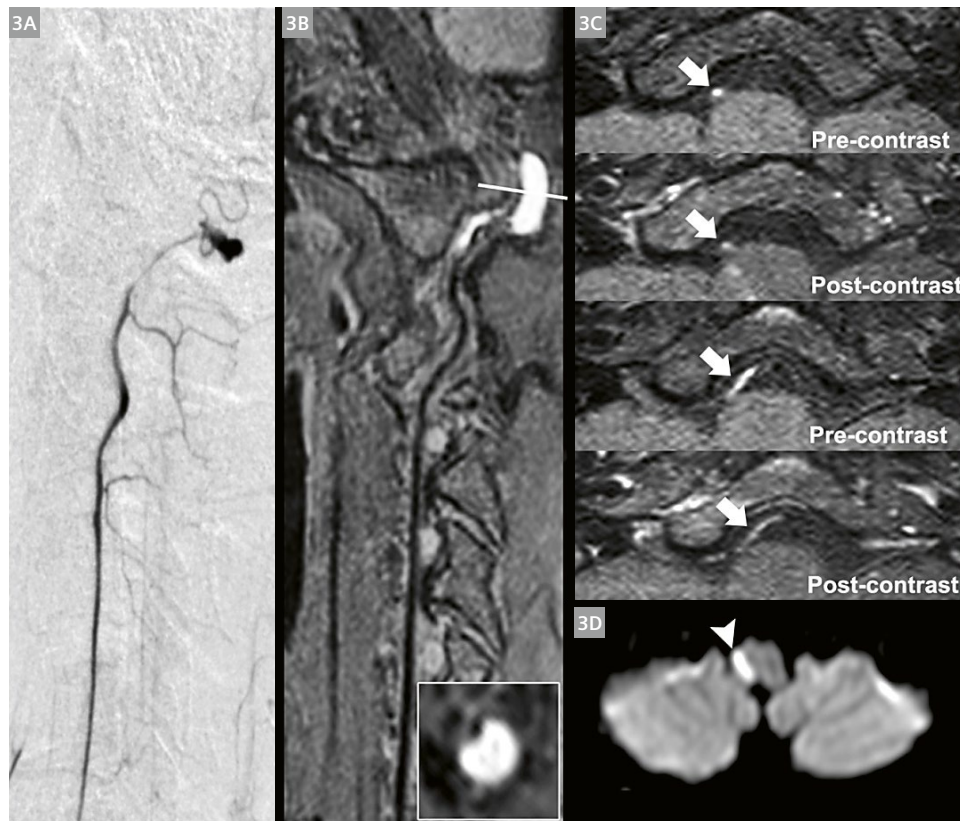
The most important recommendation for intracranial VW-MRI in clinical practice is to assess and differentiate intracranial vasculopathies, such as intracranial atherosclerotic plaque, vasculitis, reversible cerebral vasoconstriction syndrome, arterial dissection, and other causes of intracranial arterial narrowing. Diagnosis of cerebrovascular disease has relied on luminal imaging. However, different vasculopathies usually have similar morphological features on luminal imaging. The advent of VW-MRI offers insights into the pathogenesis of cerebrovascular disease. Furthermore, high diagnostic accuracy of VW-MRI for distinguishing a range of vasculopathies has been presented in several studies [4, 10].

### Atherosclerotic plaque

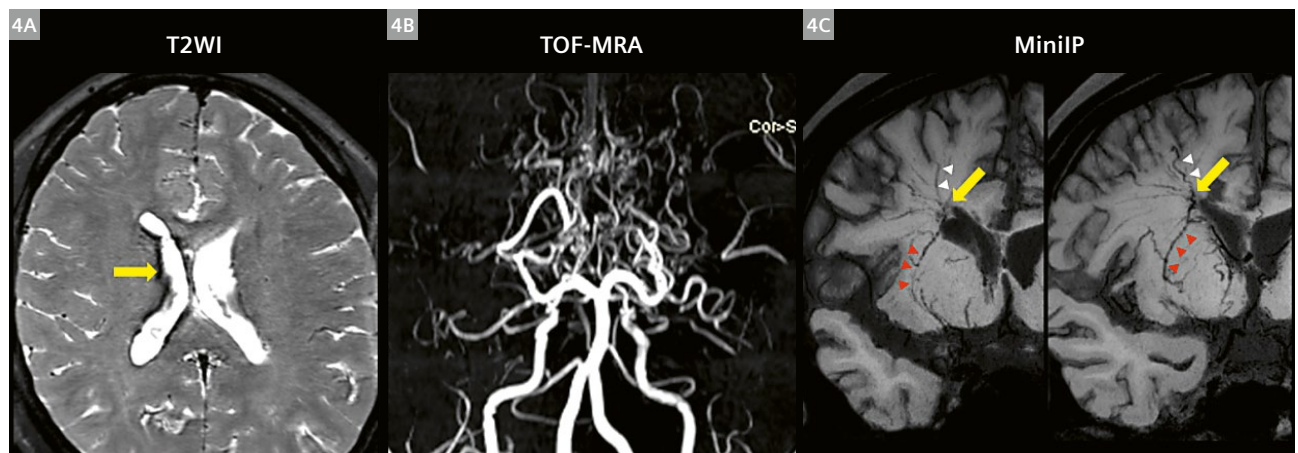
VW-MRI of intracranial atherosclerotic plaque typically demonstrates arterial wall thickening, which eccentrically (nonuniformly) involves the circumference of the arterial wall. Intraplaque hemorrhage (IPH), fissured fibrous cap, lipid-rich necrotic core, neovascularization, and inflammation are considered common features of vulnerable plaques and symptomatic lesions. Identification of plaque components with VW-MRI has the potential to identify vulnerable plaque and predict the risk of rupture and events (Fig. 2). For intracranial atherosclerosis, MRI-pathology correlation was explored in limited studies of postmortem artery specimens. Chen et al. reported that



**2** 70-year-old male patient. (2A) Diffusion-weighted imaging (DWI) showed disseminated spotty high signal intensity lesions in the left cortico-subcortical area of the MCA territory; (2B) time-of-flight magnetic resonance angiography (TOF-MRA) showed severe stenosis on the relevant MCA (arrow); (2C) curved multiplanar reconstruction of pre-contrast VW-MRI showed hyperintense plaque (arrow and arrowhead) on the MCA.



**3** A 35-year-old female patient with cervicocranial artery dissection with lateral dorsal medulla syndrome. (3A) Digital subtraction angiography showed a severe stenosis and occlusion of the V3-V4 segment of the right vertebral artery; (3B) curved planar reformation of VW-MRI demonstrated intramural hematoma (white line) in the vessel wall of the V3 segment of right vertebral artery; (3C) axial VW-MRI detected a distal intraluminal thrombus (arrows) without contrast enhancement of the right vertebral artery; (3D) DWI showed a single infarction in the right part of the medulla oblongata (arrowhead).



**4** A 21-year-old female moyamoya disease patient with right intraventricular hemorrhage. (4A) T2-weighted imaging (T2WI) demonstrated that the origin of hemorrhage was in the right periventricular area (yellow arrow); (4B) TOF-MRA detected occlusion of bilateral MCAs; (4C) minimum intensity projection (MinIP) of VW-MRI revealed an anastomosis (yellow arrow) between the LSAs (red arrowheads) and the medullary arteries (white arrowheads).

high signal on T1-weighted images in specimens at 1.5T was IPH as pathologically-verified in a postmortem case of a Chinese adult [11]. The correlation between the lipid core assessed on histology and low signal on T1-weighted fat-suppressed images within intracranial vessel walls has also been explored [12].

A postmortem study demonstrated that neovascularity can be found in middle cerebral artery (MCA) atherosclerotic plaque and that it was associated with ipsilateral infarction [13]. Gadolinium enhancement of carotid plaques was proven to be associated with vulnerable plaque, neovascularization, macrophages, and loose fibrosis correlating with histopathology [14]. Using VW-MRI, intracranial plaque enhancement can be evaluated and the relationship between plaque enhancement and recent infarction has been established [15].

## Arterial dissection

Intracranial arterial dissection most often occurs as an extension of a cervical artery dissection. Simultaneous high-resolution 3D carotid and intracranial imaging has the potential to identify dissected vessels in the head and neck. VW-MRI features of intracranial arterial dissection include a curvilinear hyperintensity on T2-weighted images (intimal flap), separating the true lumen from the false lumen, and crescent-shaped arterial wall thickening with the signal characteristics of blood (intramural hematoma). Early detection of high-risk imaging characteristics of cervicocranial artery dissection may be useful to aid in the preventive treatment of patients with cervicocranial artery dissection without stroke but at higher risk. In a previous study, we investigated the imaging features that are associated with ischemic stroke in patients with cervicocranial artery dissection. We found that the presence of irregular surface and intraluminal thrombus were related to stroke occurrence in these patients (Fig. 3). Integrated head/neck VW-MRI might give insights into the pathogenesis of ischemic stroke in cervicocranial artery dissection. It may be useful for individual prediction of ischemic stroke early in cervicocranial artery dissection [16].

## Vasculitis and reversible cerebral vasoconstriction syndrome

VW-MRI often demonstrates smooth and concentric arterial wall thickening and enhancement in patients with central nervous system vasculitis, in comparison with the typical eccentric wall thickening of atherosclerotic plaque. Reversible cerebral vasoconstriction syndrome (RCVS) can also result in concentric arterial wall thickening, but the vessel wall in RCVS is typically nonenhancing (or mildly enhancing) compared with the typical intense wall enhancement in active vasculitis [10]. Early differentiation

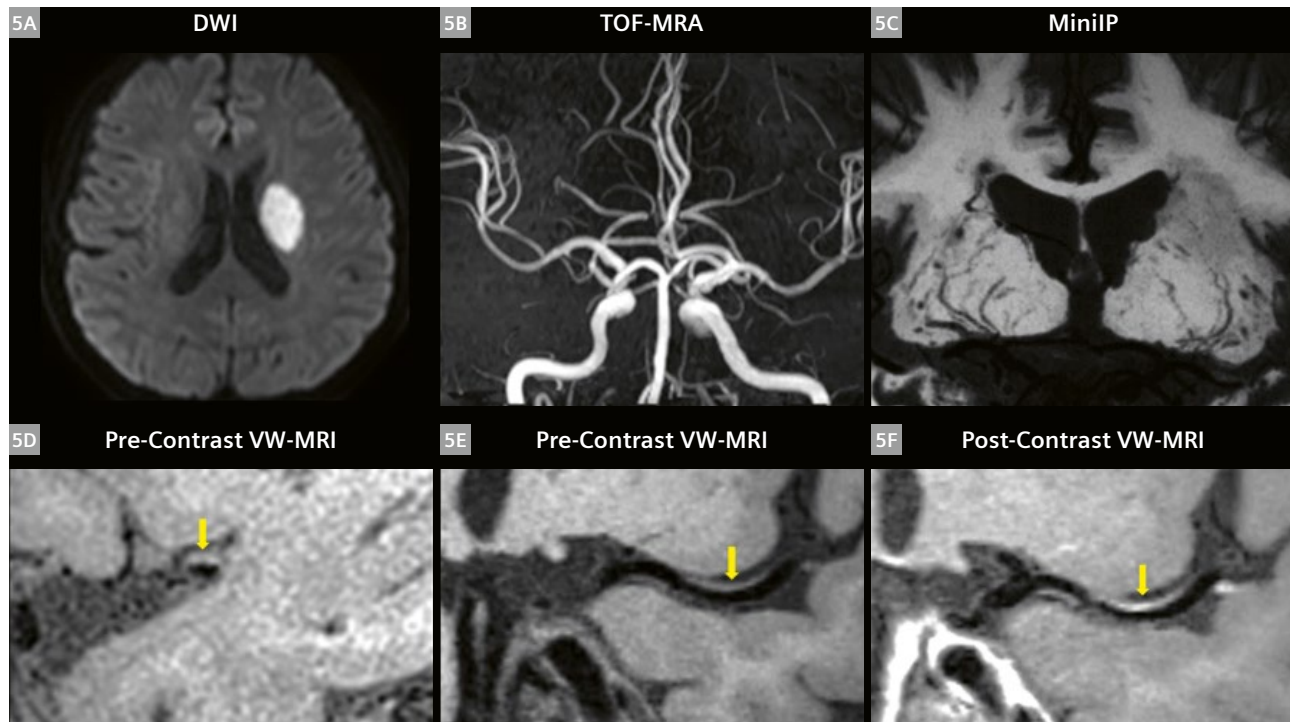
between vasculitis and RCVS is important: RCVS is treated with observation or calcium channel blockers, whereas vasculitis is treated with steroids and immunosuppressive drugs.

## Moyamoya disease

VW-MRI holds significant value in differentiating moyamoya disease and atherosclerotic moyamoya syndrome, which have a significant overlap in luminal morphological patterns. Focal eccentric wall thickening or enhancement was observed in the involved arteries in atherosclerotic moyamoya syndrome, which was different from concentric wall thickening or enhancement in moyamoya disease. Intracranial hemorrhage is one of the most severe complications in patients with moyamoya disease. Moyamoya vessels are the dilated and proliferative perforating arteries serving as collateral circulation, which are more prone to rupture and might be closely associated with intracranial hemorrhage. In a previous study, we investigated the association between dilation, proliferation, and anastomosis of perforating arteries, and intracranial hemorrhage in moyamoya disease patients using VW-MRI. We found that choroidal anastomosis is a valuable imaging biomarker for predicting hemorrhagic events in adult patients with moyamoya disease (Fig. 4). Whole-brain VW-MRI can visualize not only the abnormal collateral vessels but also the anatomy of the parenchymal structure, which may facilitate risk estimates of bleeding in moyamoya disease [17].

## Lenticulostriate artery imaging

The lenticulostriate artery (LSA) supplies blood to the basal ganglia and its vicinity in the brain. Impairment of the LSA is associated with ischemic stroke and small-vessel disease. Visualization of the LSA is essential for understanding the mechanisms of microvascular pathologies and potential guiding therapeutic intervention. Using the T1 VW-MRI technique, we have obtained detailed black-blood angiographic delineation of the LSAs [18]. Single subcortical infarctions with a nonstenotic middle cerebral artery have been considered to be caused by lipohyalinosis and fibrinoid degeneration in small-vessel disease, commonly called lacunar strokes. However, large-artery atherothrombosis that blocks the orifice of the perforating artery may also be an important cause of single subcortical infarctions. Jiang et al. used VW-MRI to quantitatively evaluate the associations between the distribution and characteristics of middle cerebral artery plaque and morphological changes to LSAs in the symptomatic and asymptomatic sides of single subcortical infarction patients. They found that superiorly distributed middle cerebral artery plaques at the LSA origin are closely



**5** A 68-year-old male patient with right limb weakness. (5A) DWI showed a single subcortical infarction in the left LSA territory; (5B) TOF-MRA showed mild stenosis on the relevant MCA; (5C) coronal minimum intensity projection (MinIP) revealed shorter lengths of left lenticulostriate arteries (LSAs) compared with the right side; (5D) the cross-section view of pre-contrast VW-MRI demonstrated a superiorly located plaque (arrow) of MCA; (5E, F) curved multiplanar reconstruction of pre- and post-contrast VW-MRI showed an isointensity plaque with contrast enhancement (arrow).

associated with morphological changes to the LSA in symptomatic middle cerebral arteries, suggesting that the distribution, rather than the inherent features of plaques, determines the occurrence of single subcortical infarctions (Fig. 5) [19].

## Setup of our multicenter study

VW-MRI holds promise of improving our pathological understanding of intracranial artery stenotic disease. The robustness of this technique as a valuable tool for the assessment of various cerebrovascular diseases still needs to be validated in a large-scale multicenter study. We also used the sequence successfully in a multicenter study comprising nine hospitals in China that was initiated by Professor Qi Yang in February 2017. The aim of this study was to accurately classify the etiology of stroke through the scientific research cooperation of various partners, and at the same time carry out early screening and accurate diagnosis of high-risk plaques, thereby providing a new imaging method for the clinical diagnosis and treatment of stroke. The imaging technique used in this project is whole-brain VW-MRI based on sampling perfection with application-optimized contrast using different flip angle evolutions (SPACE) combined with nonselective excitation

and a trailing magnetization flip-down module [20, 21]. This imaging technique in combination with a uniform protocol setting on 3T scanners (MAGNETOM Prisma, MAGNETOM Skyra, Siemens Healthcare, Erlangen, Germany) can perform high-resolution imaging of the intracranial vessel wall, clearly depicting the morphology of the vessel wall and distinguishing high-risk vulnerable plaques. In this multi-center study, each participating site carried out imaging studies ranging from intracranial large arterial to perforating arteriole lesions, focusing on cerebrovascular diseases of different etiologies. Several results of this research have been published [22–26].

## Outlook

The technology of whole-brain VW-MRI has become a new method for stroke classification. The research performed by our group and other groups presents a first step in designing focused trials on individualized treatment and prevention strategies of intracranial stenosis. Further studies are required to investigate the use of selected biomarkers in randomized control trials of secondary prevention and treatment of intracranial artery stenotic disease.

## References

- 1 GBD 2016 Stroke Collaborators. Global, regional, and national burden of stroke, 1990–2016: a systematic analysis for the Global Burden of Disease Study 2016. *Lancet Neurol.* 2019;18:439–458.
- 2 Powers WJ. Acute Ischemic Stroke. *N Engl J Med.* 2020;383:252–260.
- 3 Wu S, Wu B, Liu M, et al. Stroke in China: Advances and challenges in epidemiology, prevention, and management. *The Lancet. Neurology.* 2019;18:394–405.
- 4 Mandell DM, Matouk CC, Farb RI, et al. Vessel wall MRI to differentiate between reversible cerebral vasoconstriction syndrome and central nervous system vasculitis: Preliminary results. *Stroke.* 2012;43:860–862.
- 5 Fan Z, Zhang Z, Chung YC, et al. Carotid arterial wall MRI at 3T using 3D variable-flip-angle turbo spin-echo (TSE) with flow-sensitive dephasing (FSD). *J Magn Reson Imaging.* 2010;31:645–654.
- 6 Mandell DM, Mossa-Basha M, Qiao Y, et al. Intracranial vessel wall MRI: Principles and expert consensus recommendations of the American society of neuroradiology. *AJR Am J Neuroradiol.* 2017;38:218–229.
- 7 Harteveld AA, van der Kolk AG, van der Worp HB, et al. High-resolution intracranial vessel wall MRI in an elderly asymptomatic population: comparison of 3T and 7T. *Eur Radiol.* 2017;27:1585–1595.
- 8 van der Kolk AG, Zwanenburg JJ, Denswil NP, et al. Imaging the intracranial atherosclerotic vessel wall using 7T MRI: initial comparison with histopathology. *AJR Am J Neuroradiol.* 2015;36:694–701.
- 9 Qiao Y, Guallar E, Suri FK, et al. MR Imaging Measures of Intracranial Atherosclerosis in a Population-based Study. *Radiology.* 2016;280:860–868.
- 10 Mossa-Basha M, Shibata DK, Hallam DK, et al. Added value of vessel wall magnetic resonance imaging for differentiation of nonocclusive intracranial vasculopathies. *Stroke.* 2017;48:3026–3033.
- 11 Chen XY, Wong KS, Lam WW, et al. High signal on T1 sequence of magnetic resonance imaging confirmed to be intraplaque hemorrhage by histology in middle cerebral artery. *Int J Stroke.* 2014;9(4):E19.
- 12 Yang WJ, Chen XY, Zhao HL, et al. Postmortem Study of Validation of Low Signal on Fat-Suppressed T1-Weighted Magnetic Resonance Imaging as Marker of Lipid Core in Middle Cerebral Artery Atherosclerosis. *Stroke.* 2016;47:2299–2304.
- 13 Chen XY, Wong KS, Lam WW, et al. Middle cerebral artery atherosclerosis: histological comparison between plaques associated with and not associated with infarct in a postmortem study. *Cerebrovasc Dis.* 2008;25:74–80.
- 14 Millon A, Boussel L, Brevet M, et al. Clinical and histological significance of gadolinium enhancement in carotid atherosclerotic plaque. *Stroke.* 2012;43:3023–3028.
- 15 Qiao Y, Zeiler SR, Mirbagheri S, et al. Intracranial plaque enhancement in patients with cerebrovascular events on high-spatial-resolution MR images. *Radiology.* 2014;271:534–542.
- 16 Wu Y, Wu F, Liu Y, et al. High-Resolution Magnetic Resonance Imaging of Cervicocranial Artery Dissection: Imaging Features Associated With Stroke. *Stroke.* 2019;50:3101–3107.
- 17 Wu F, Han C, Liu Y, et al. Validation of Choroidal Anastomosis on High-Resolution Magnetic Resonance Imaging as Imaging Biomarker in Hemorrhagic Moyamoya Disease. *Eur Radiol.* 2021;31:4548–4556.
- 18 Zhang Z, Fan Z, Kong Q, et al. Visualization of the lenticulostriate arteries at 3T using black-blood T1-weighted intracranial vessel wall imaging: comparison with 7T TOF-MRA. *Eur Radiol.* 2019;29:1452–1459.
- 19 Jiang S, Yan Y, Yang T, et al. Plaque Distribution Correlates With Morphology of Lenticulostriate Arteries in Single Subcortical Infarctions. *Stroke.* 2020;51:2801–2809.
- 20 Fan Z, Yang Q, Deng Z, et al. Whole-brain intracranial vessel wall imaging at 3 Tesla using cerebrospinal fluid-attenuated T1-weighted 3D turbo spin echo. *Magn Reson Med.* 2017;77:1142–1150.
- 21 Yang Q, Deng Z, Bi X, et al. Wholebrain vessel wall MRI: a parameter tune-up solution to improve the scan efficiency of three-dimensional variable flip-angle turbo spin-echo. *J Magn Reson Imaging.* 2017;46:751–757.
- 22 Liu Y, Li S, Wu Y, et al. The Added Value of Vessel Wall MRI in the Detection of Intraluminal Thrombus in Patients Suspected of Craniocervical Artery Dissection. *Aging & Dis.* 2021; Doi:10.14336/AD.2021.0502.
- 23 Jiang S, Yan Y, Yang T, et al. Plaque Distribution Correlates With Morphology of Lenticulostriate Arteries in Single Subcortical Infarctions. *Stroke.* 2020;51(9):2801–2809.
- 24 Wu Y, Wu F, Liu Y, Yang Q, et al. High-Resolution Magnetic Resonance Imaging of Cervicocranial Artery Dissection: Imaging Features Associated with Stroke. *Stroke.* 2019; 50(11):3101–3107.
- 25 Wu F, Ma Q, Song H, et al. Differential Features of Culprit Intracranial Atherosclerotic Lesions: A Whole-Brain Vessel Wall Imaging Study in Patients With Acute Ischemic Stroke. *J Am Heart Assoc.* 2018 Jul 22;7(15).
- 26 Wu F, Song H, Ma Q, et al. Hyperintense plaque on intracranial vessel wall magnetic resonance imaging as a predictor of artery-to-artery embolic infarction. *Stroke.* 2018; 49(4):905–911.



## Contact

Professor Qi Yang, M.D., Ph.D.  
Vice Chair  
Department of Radiology  
Beijing Chaoyang Hospital  
Capital Medical University  
No. 8 Gongti South Road  
Chaoyang District  
Beijing 100020, China  
Phone: +86 (0) 10-8523-1928  
yangyangqiqi@gmail.com

# Ultrafast Brain Imaging with Deep Learning Multi-Shot EPI: Preliminary Clinical Evaluation

Azadeh Tabari<sup>1</sup>, Bryan Clifford<sup>2</sup>, Augusto Lio M. Goncalves Filho<sup>1</sup>, Zahra Hosseini<sup>3</sup>, Thorsten Feiweier<sup>4</sup>, Wei-Ching Lo<sup>2</sup>, Min Lang<sup>1</sup>, Maria Gabriela Figueiro Longo<sup>1</sup>, Kawin Setsompop<sup>5</sup>, Berkin Bilgic<sup>6</sup>, Otto Rapalino<sup>1</sup>, Pamela Schaefer<sup>1</sup>, Stephen Cauley<sup>6</sup>, Susie Huang<sup>1</sup>, John Conklin<sup>1</sup>

<sup>1</sup>Department of Radiology, Massachusetts General Hospital, Boston, MA, USA

<sup>2</sup>Siemens Medical Solutions USA, Boston, MA, USA

<sup>3</sup>Siemens Medical Solutions USA, Atlanta, GA, USA

<sup>4</sup>Siemens Healthineers, Erlangen, Germany

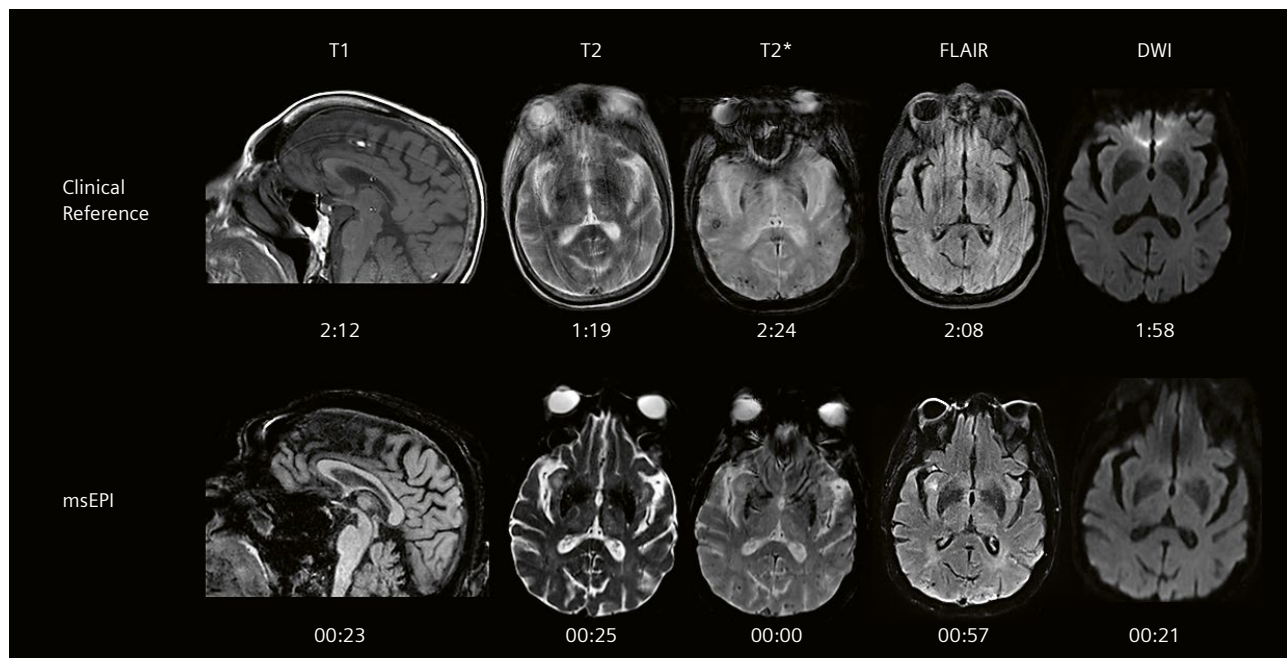
<sup>5</sup>Department of Radiology / Department of Electrical Engineering, Stanford University, Stanford, CA, USA

<sup>6</sup>Department of Radiology, A. A. Martinos Center for Biomedical Imaging, Massachusetts General Hospital, Harvard Medical School, Boston, MA, USA

MR imaging (MRI) is an integral part of the diagnosis and treatment planning of various neurological diseases. However, the long scan time of brain MRI is a major factor that limits its effectiveness, especially in patients who are prone to motion and frequently require sedation. Thus, fast brain MRI protocols with acceptable diagnostic image quality are desired to enable wider clinical applica-

tion of MRI [1, 2]. There is an ongoing clinical need to reduce the scan time of brain MRI, especially for uncooperative or motion-prone patients, and patients with diseases requiring rapid diagnosis such as stroke.

Various efforts have been made to achieve ultrafast MRI for brain imaging by using pulse sequences that rapidly acquire images. One well-known approach is to use



**1** Illustrative example on the comparison of the motion-degraded exam of a 10-minute clinical reference protocol to the proposed 2-minute msEPI protocol in a 73-year-old female with no pathologic findings.

single-shot echo-planar imaging (ssEPI), which acquires  $k$ -space data for an entire 2D image in a single, long readout (shot), following a single RF-excitation pulse [3, 4]. The number of  $k$ -space lines (echoes) collected in a single shot is called the "EPI factor". The technical advances in the design of echo-planar imaging have made ultrafast brain MRI protocols, including a combination of anatomic and functional sequences, possible [5, 6]. ssEPI methods have recently been used to create rapid screening exams with total durations of 1–2 minutes. However, these rapid ssEPI approaches come at the cost of significant geometric distortion, low signal-to-noise ratio (SNR), and reduced tissue contrast [6–8]. In addition, these approaches offer limited flexibility to acquire in different image orientations or to repeat individual contrasts.

Multi-shot EPI (msEPI) acquisitions have been exploited to address these shortcomings. In a msEPI acquisition, data from multiple highly-undersampled shots are combined together. This approach results in reduced geometric distortion, but at the cost of slightly longer scan times. Higher acceleration factors can be used to compensate for this, but can lead to increased  $g$ -factor noise and residual aliasing [9–11]. Recent advancement in artificial intelligence (AI)-powered reconstruction algorithms have proved successful in denoising accelerated MRI data. Deep learning (DL) models, can be applied to reduce noise and residual aliasing during reconstruction [12].

In this article we show preliminary results from a clinical translational study being performed at Massachusetts General Hospital (MGH) for validating the feasibility of prototype DL-accelerated msEPI-based rapid brain protocols<sup>1</sup> in a high-volume emergency and inpatient care setting. The rapid imaging technique combines a novel deep learning algorithm to limit  $g$ -factor noise amplification, magnetization transfer preparation to improve brain tissue contrast, and high per-shot EPI undersampling factors to minimize geometric distortion [12, 13]. A multidisciplinary team of neuroradiologists, MR physicists, and Siemens Healthineers engineers at MGH have developed and optimized acquisition parameters for each of these prototype msEPI-based MRI protocols. Following the optimization of sequence parameters and DL-based reconstruction, an Institutional Review Board approved study was executed. The validation approach comprised prospective comparative studies of emergency and inpatient examinations with a variety of indications. The imaging protocol included T1-, T2-, T2\*-weighted, T2-FLAIR, and DW imaging sequences from the prototype msEPI protocol and the clinical reference standard. Imaging was performed on 3T MRI scanners (MAGNETOM Skyra and MAGNETOM Prisma, Siemens Healthcare, Erlangen, Germany) using a 20-channel

head coil. Fully sampled msEPI training data were acquired with two averages and eight shots across 16 healthy subjects (8 men, 8 women, aged 19–67). A single FLASH auto calibration scan, acquired at the start of each acquisition, allowed for the calculation of coil sensitivity maps, GRAPPA and/or SMS kernels. The data were split into training and validation datasets with 12 and 4 subjects, respectively. The use of fully sampled data allowed networks to be trained for different acceleration factors through retrospective undersampling.

Two board-certified neuroradiologists, blinded to the clinical history and the imaging protocols, evaluated the head-to-head image quality, scan time, and diagnostic performance of DL-accelerated msEPI-based MRI protocols against the respective clinical standard protocols. For diagnostic performance, they assessed six clinically relevant imaging findings in each protocol (intracranial mass-like lesion, intracranial hemorrhage, white matter hyperintensities, subarachnoid FLAIR hyperintensities, diffusion restriction, and hydrocephalus). For image quality, the raters used a 3-point score to evaluate image degradation by noise and artifacts. Qualitative assessment was compared using Wilcoxon signed-rank tests, and the intraclass correlation coefficients (ICCs) were used to test interobserver reproducibility on the diagnostic concordance between two readers.

## Initial clinical experience

The prototype msEPI protocols (T1-, T2-, T2\*-weighted, T2-FLAIR, and DWI) required only 2 minutes of scan time (not including adjustments), while the rapid reference protocols (turbo spin-echo (TSE)-based acquisitions) took 10 minutes for the same number of image contrasts. A total of 26 patients (Male:Female 12:14, mean age  $58 \pm 19$  years old) were included in this preliminary study.

Two board-certified neuroradiologists performed an initial clinical subjective evaluation of the DL-accelerated msEPI-based images. Aside from noticeable mild distortion of soft facial tissues, the msEPI images contained only very minimal distortion of the pons and temporal lobes – areas which are critical for diagnosis. The limited artifacts we observed were most prevalent in the longer echo-time T2\* data and corresponded to cases where patient motion could be identified. Figure 1 illustrates how shorter scan time allows for lower motion artifacts.

Interobserver agreement was 'almost perfect' for the evaluation of intracranial masses (ICC = 1), WM hyperintensities (ICC = 0.83), diffusion restrictions (ICC = 0.83), and hydrocephalus (ICC = 1); and 'substantial' for intracranial hemorrhage (ICC = 0.76) and subarachnoid FLAIR

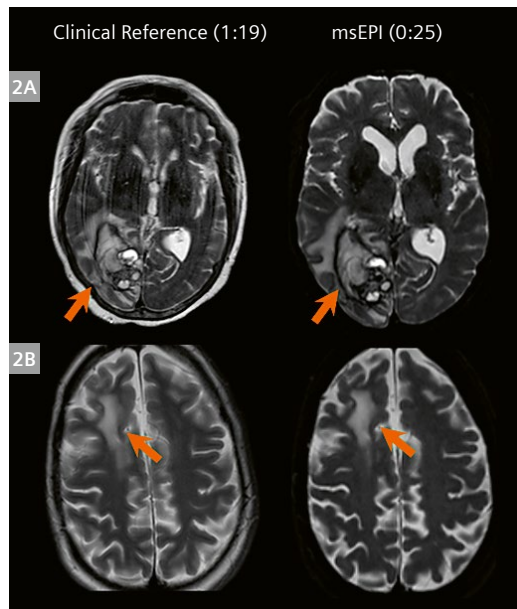
<sup>1</sup>Work in progress. The application is currently under development and is not for sale in the U.S. and in other countries. Its future availability cannot be ensured.

hyperintensities (ICC = 0.65). Head-to-head comparisons of image quality showed increased noise on the msEPI exams for T1, FLAIR, and DWI ( $p < 0.05$ ) and increased artifacts on T2, T2\*, and FLAIR ( $p < 0.05$ ), without compromising the detection of the imaging findings.

Figures 2–6 demonstrate examples of the msEPI images and the corresponding clinical reference images for each image contrast, highlighting the clinical findings in each. As these cases illustrate, the 2-minute DL-accelerated msEPI prototype sequences can offer high clinical efficacy at a significantly shorter acquisition time.

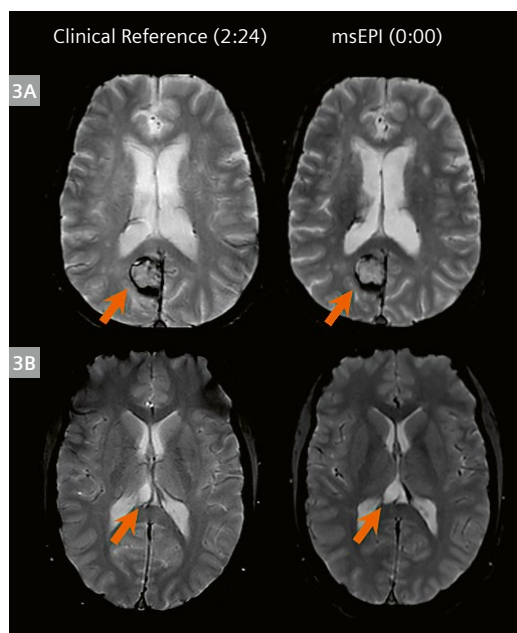
## Conclusion

We have successfully used a DL-accelerated 2-minute msEPI protocol to enable rapid, comprehensive brain MRI evaluation of emergency department and hospitalized patients. In this preliminary study we found high interobserver agreement for major brain MRI findings, similar to that of a 10-minute conventional protocol. The DL-accelerated 2-minute msEPI protocol provided clear depiction of pathologic intracranial findings and comparable tissue contrast to that observed with the five-fold slower clinical reference exam. The msEPI technique is currently being evaluated in a larger clinical study of inpatient and emergency department patients at our institution, which



T2 Sequence	Acquisition Time (m:s)	Resolution (mm <sup>3</sup> )	TR (ms)	TE (ms)	PAT Factor	No. shots	Echo spacing (ms)
TSE	1:19	0.9×0.9×5.0	7060	85	2	–	9.42
msEPI	0:25	1.0×1.0×4.0	4500	86	2	4	1.2

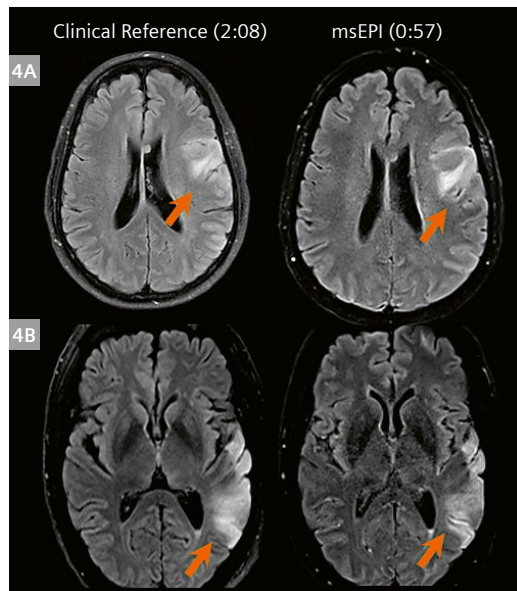
- 2** (2A) Large complex hemorrhagic mass-like lesion within the right occipital lobe that is better seen on msEPI exam. The clinical reference exam that was performed with > 3-fold increase in scan time demonstrates intense motion artifacts.  
**(2B)** Post-surgical changes from right frontal craniotomy with right frontal lobe encephalomalacia.



T2* Sequence	Acquisition Time (m:s)	Resolution (mm <sup>3</sup> )	TR (ms)	TE (ms)	PAT Factor	No. shots	Echo spacing (ms)
GRE	2:24	0.9×0.9×5.0	694	20	1	–	–
msEPI	0:00 <sup>2</sup>	1.0×1.0×4.0	4500	21.2	2	4	1.2

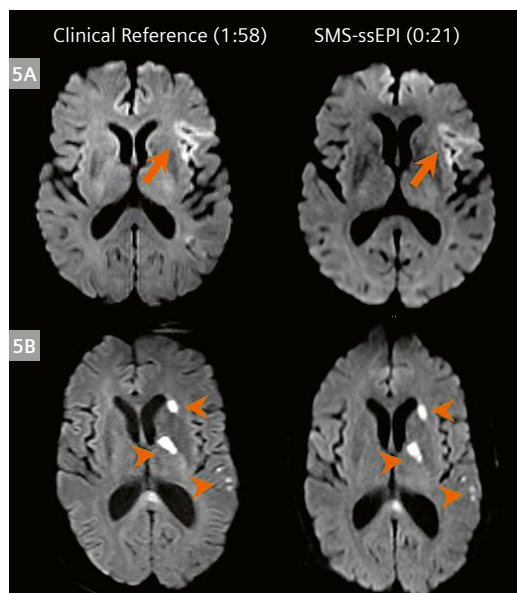
- 3** (3A) Right parietal lobe intraparenchymal hematoma with dependent T2\* hypointense blood products.  
**(3B)** Non-enhancing cystic lesion in the right aspect of the pineal gland.

<sup>2</sup>Acquired in combination with the T2 sequence.



FLAIR Sequence	Acquisition Time (m:s)	Resolution (mm <sup>3</sup> )	TR (ms)	TE (ms)	PAT Factor	No. shots	Echo spacing (ms)
TSE	2:08	0.9×0.9×5.0	9000	85	2	–	7.49
msEPI	0:57	1.0×1.0×4.0	9000	86	2	2	1.19

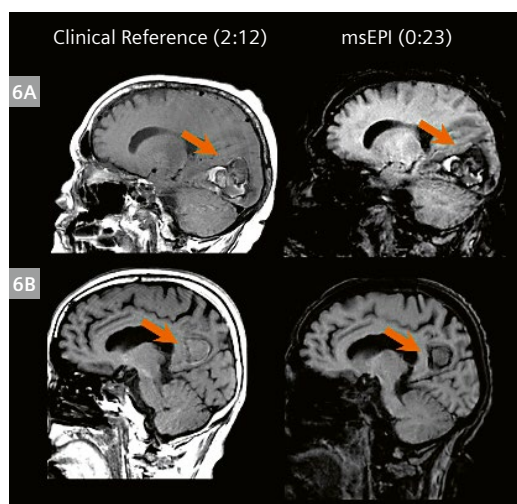
- 4** (4A) Left frontal high-grade glioma.  
(4B) Subacute left temporal lobe infarct (left middle cerebral artery territory).



DWI Sequence	Acquisition Time (m:s)	Resolution (mm <sup>3</sup> )	TR (ms)	TE (ms)	PAT Factor	No. shots	Echo spacing (ms)
ssEPI	1:58	1.4×1.4×5.0	3800	72	2	1	0.72
SMS-ssEPI	0:21	1.4×1.4×4.0	2000	63	2	2	0.93

b-value 1000 s/mm<sup>2</sup>

- 5** (5A) Subacute infarct involving left frontal lobe and insula.  
(5B) Multiple infarcts involving left cerebral hemisphere.



T1 Sequence	Acquisition Time (m:s)	Resolution (mm <sup>3</sup> )	TR (ms)	TE (ms)	PAT Factor	No. shots	Echo spacing (ms)
SE	2:12	0.9×0.9×4.0	400	8.4	1	–	–
msEPI	0:23	1.0×1.0×4.0	1670	12	2	4	1.18

- 6** (6A) Hemorrhagic neoplastic lesion in the right occipital lobe.  
(6B) Right parietal lobe intraparenchymal hematoma.

will provide further insight into the advantages and trade-offs of ultrafast, high-quality brain imaging in this patient population. We envision this protocol could be an effective rapid screening tool for acute intracranial pathology in these often difficult to image and neurologically unstable patients.

## References

- 1 Blystad I, Warntjes JB, Smedby O, et al. Synthetic MRI of the brain in a clinical setting. *Acta Radiol* 2012; 53:1158–1163
- 2 Raja, A. S. et al. Radiology Utilization in the Emergency Department: Trends of the Past 2 Decades. *Am J Roentgenol.* 203, 355–360 (2014).
- 3 Sun K, Zhong Z, Xu Z, et al. In-plane simultaneous multisegment imaging using a 2D RF pulse. *Magn Reson Med.* 2021 Aug 4. doi: 10.1002/mrm.28956. Epub ahead of print. PMID: 34350601.
- 4 Feinberg DA, Moeller S, Smith SM, et al. Multiplexed echo planar imaging for sub-second whole brain fMRI and fast diffusion imaging. *PLoS One.* 2010 Dec 20;5(12):e15710. doi: 10.1371/journal.pone.0015710. Erratum in: *PLoS One.* 2011;6(9).
- 5 Ha JY, Baek HJ, Ryu KH, et al. One-Minute Ultrafast Brain MRI With Full Basic Sequences: Can It Be a Promising Way Forward for Pediatric Neuroimaging? *AJR Am J Roentgenol.* 2020 Jul;215(1):198–205. doi: 10.2214/AJR.19.22378. Epub 2020 Apr 7. PMID: 32255685.
- 6 Setsompop K, Feinberg DA, Polimeni JR. Rapid brain MRI acquisition techniques at ultra-high fields. *NMR Biomed.* 2016 Sep;29(9):1198–221. doi: 10.1002/nbm.3478. Epub 2016 Feb 2. PMID: 26835884; PMCID: PMC5245168.
- 7 Skare S, Sprenger T, Norbeck O, et al. A 1-minute full brain MR exam using a multicontrast EPI sequence. *Magn Reson Med.* 2018;79(6):3045–3054. doi:10.1002/mrm.26974
- 8 Ryu KH, Choi DS, Baek HJ, et al. Clinical feasibility of 1-min ultrafast brain MRI compared with routine brain MRI using synthetic MRI: a single center pilot study. *J Neurol.* 2019;266(2):431–439. doi:10.1007/s00415-018-9149-4
- 9 Liao C, Bilgic B, Tian Q, et al. Distortion-free, high-isotropic-resolution diffusion MRI with gSlider BUDA-EPI and multicoil dynamic B 0 shimming. *Magn Reson Med.* March 2021:mrm.28748. doi:10.1002/mrm.28748
- 10 Chen N, Guidon A, Chang H-C, Song AW. A robust multi-shot scan strategy for high-resolution diffusion weighted MRI enabled by multiplexed sensitivity-encoding (MUSE). *NeuroImage.* 2013;72:41–47. doi:10.1016/j.neuroimage.2013.01.038
- 11 Conklin, J. et al. A comprehensive multi-shot EPI protocol for high-quality clinical brain imaging in 3 minutes. *Proc. Intl. Soc. Magn. Reson. Med.* 6691 (2020).
- 12 Clifford B, Conklin J, Huang S, et al. Clinical evaluation of an AI-accelerated two-minute multi-shot EPI protocol for comprehensive high-quality brain imaging. In: Proceedings of the 28th Annual Meeting of ISMRM, virtual, USA, 2020.
- 13 Demir S, Clifford B, Feiwei T, et al. Optimization of magnetization transfer contrast for EPI FLAIR brain imaging. International Society for Magnetic Resonance in Medicine, 2021. Online virtual meeting.

## Contact

John Conklin, M.D., MS  
Diagnostic Radiologist  
Director of Emergency MRI  
Division of Emergency Imaging  
Department of Radiology  
Massachusetts General Hospital  
326 Cambridge St #410  
Boston, MA 02114  
USA  
Phone: +1617-726-8323  
John.Conklin@MGH.HARVARD.EDU



Advertisement

## Prepare your patients mentally for their MRI exam

Tap the full potential of your facility by preparing your patients for the scan with our Patient Education Toolkit. A video, poster, meditation, and a book for children explain the process of an MRI exam in simple words and answer common questions.

Download the Patient Education Toolkit in your preferred language here:

[magnetomworld.siemens-healthineers.com/toolkit/mri-patient-education](https://magnetomworld.siemens-healthineers.com/toolkit/mri-patient-education)



# A Comparison of Post-Contrast 3D T1 SPACE, 3D SPACE FLAIR, and 3D T1 MPRAGE Sequences in Various Brain Parenchymal and Meningeal Pathologies at 3T MRI

S. Babu Peter, MD DNB MNAMS FICR

Barnard Institute of Radiology, Madras Medical College, Rajiv Gandhi General Hospital, Chennai, India

## Introduction

Contrast-enhanced magnetic resonance imaging (MRI) is well-suited for diagnosing meningeal and brain parenchymal abnormalities at an early stage, and this increases the survival rate of patients [1].

Intravenous magnetic resonance contrast agents are used to detect and characterize central nervous system disorders. The commonly used MR contrast agent gadolinium shortens both the T1 and T2 relaxation times of the tissues in which it has accumulated.

Mechanisms of contrast enhancement vary depending on the site of the lesion: With intra-axial brain lesions, disruption of the blood–brain barrier causes gadolinium to enter the extracellular space; with extra-axial lesions, enhancement occurs due to the relatively high vascularity; and in leptomeningeal regions, contrast leaks from the vessels into the cerebrospinal fluid (CSF).

While in the past, 2D imaging was common practice and protocols have been highly optimized for contrast-enhanced imaging. Nowadays, 3D imaging is becoming more and more popular, multiple 3D sequences are available, and protocols vary between institutions. The choice of 3D sequence can be tailored according to individual needs.

It is possible to acquire high-spatial-resolution 3D T1-weighted data of the brain in a convenient time with spin-echo contrast rather than gradient echo contrast. Variable flip angle refocusing pulses in SPACE reduce the specific absorption rate. In some studies, 3D T1 SPACE images identified a high number of discrete enhancing small lesions, which the MPRAGE sequence missed [3].

Many clinical studies have shown that the post-contrast 3D SPACE FLAIR sequence offers more information than a post-contrast 3D T1 SPACE sequence alone. Thanks to suppression of the CSF signal, no or minimal enhancement of blood vessels, reduction of phase shift artifacts derived from enhanced blood vessels or dural sinuses, and better detection of peritumoral edema, lesions are more conspicuous in 3D SPACE FLAIR sequences [4–6].

However, in post-contrast 3D SPACE FLAIR imaging alone, the observed hyperintense lesion may be less conspicuous due to either T2 lengthening or T1 shortening. This limits the usefulness of the FLAIR sequences, which should therefore be performed with both pre-contrast and post-contrast scans.

## Objectives

We compare post-contrast 3D T1 SPACE, 3D SPACE FLAIR, and 3D MPRAGE sequences in various brain parenchymal and meningeal pathologies.

Specifically, we

- evaluate different meningeal enhancement patterns such as pachymeningeal enhancement, leptomeningeal enhancement, gyral enhancement, folial enhancement, and cisternal enhancement
- identify which MRI sequence is best for detecting conglomerate ring-enhancing lesions, scolices, and multiple lesions

## Literature review

### Post-contrast 3D T1 SPACE sequences

3D T1 SPACE (Sampling Perfection with Application optimized Contrast using different flip-angle Evolutions) sequence is a single-slab 3D TSE sequence with a slab-selective, variable excitation pulse. Enhancing vessels may mimic meningeal enhancement in MPRAGE sequences, which makes differentiation difficult. T1 SPACE is a 3D fast spin echo sequence in which refocusing of the transverse magnetization is done by radiofrequency pulse. It is the least affected by magnetic field inhomogeneities and shows the absence of flow-related signal from vessels [9, 10]. The magnetization effect produced by the pulses provides better delineation of lesions by suppressing white matter signal intensity [11, 12].

### Post-contrast 3D SPACE FLAIR sequences

FLAIR MRI techniques were first described by Hajnal et al. [13]. Long T2 relaxation times improve conspicuity of brain lesions on FLAIR images [14–16]. The usefulness of gadolinium-enhanced FLAIR MRI in revealing enhancement of brain lesions has recently been investigated.

Post-contrast 3D SPACE FLAIR imaging adds significantly more information than post-contrast MPRAGE imaging: The study by Fukuoka et al. [17] showed that 3D SPACE FLAIR was more sensitive to low gadolinium concentrations and less sensitive to high gadolinium concentrations than MPRAGE.

The abnormal enhancement also depends on the amount of contrast given. An intravenous injection of gadolinium at a dose of  $0.1 \text{ mmol kg}^{-1}$  can detect brain lesions effectively. The maximum concentration of gadolinium in the blood after 10 to 60 seconds of intravenous injection of gadolinium at  $0.1 \text{ mmol kg}^{-1}$  of body weight is  $2.0 \pm 1.2 \text{ mmol L}^{-1}$  for the aorta and  $0.6 \pm 0.3 \text{ mmol L}^{-1}$  for the inferior vena cava. Therefore, administration of contrast at a dose of  $0.1 \text{ mmol kg}^{-1}$  is ideal [18].

Since many cases showed abnormalities on both pre-contrast and post-contrast 3D SPACE FLAIR images, only

those that showed up on subtraction images were taken as evidence of abnormal post-contrast FLAIR enhancement.

## Materials and methods

In the period from January to December 2019, a total of 82 patients with high suspicion of brain parenchymal and meningeal abnormalities (excluding cerebrovascular accident and trauma) were evaluated. The study was carried out in Rajiv Gandhi Government General Hospital, Madras Medical College, Chennai, Tamil Nadu, India. Approval was obtained from the institute's ethics committee. Prior informed consent was obtained from the patients who underwent MRI. 60 patients fulfilled the inclusion criteria and underwent pre-contrast and post-contrast 3D T1 SPACE, 3D SPACE FLAIR, and 3D T1 MPRAGE imaging. The images from the three different contrast sequences were evaluated in parallel and a final decision was reached on which sequence showed which lesions most conspicuously.

## Inclusion criteria

All patients with high clinical suspicion of new-onset neurological symptoms and either criteria (a) or (b):

- Multiple parenchymal lesions with abnormal CSF findings or known history of primary tumor
- Suspicious meningeal abnormalities with abnormal CSF findings or known history of primary tumor

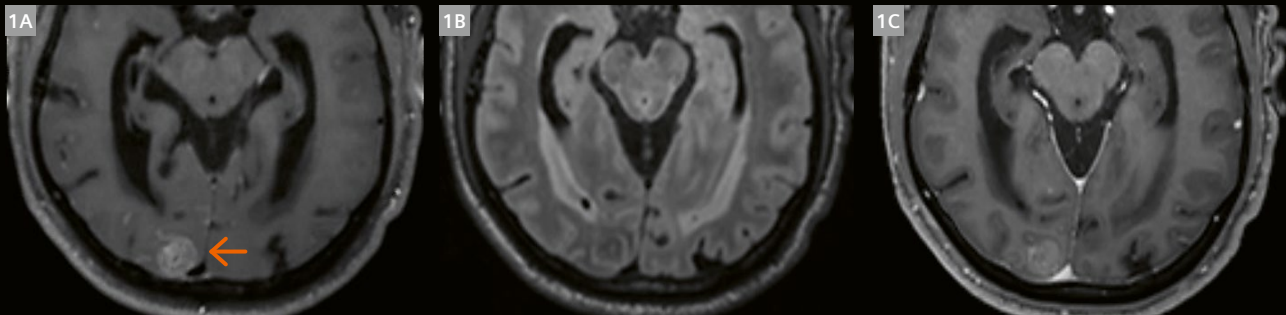
## Exclusion criteria

- All patients with a previous history of neurological disease
- Patients with a previous history of brain surgery
- Patients with diffusion abnormalities corresponding to vascular territory

## Imaging technique

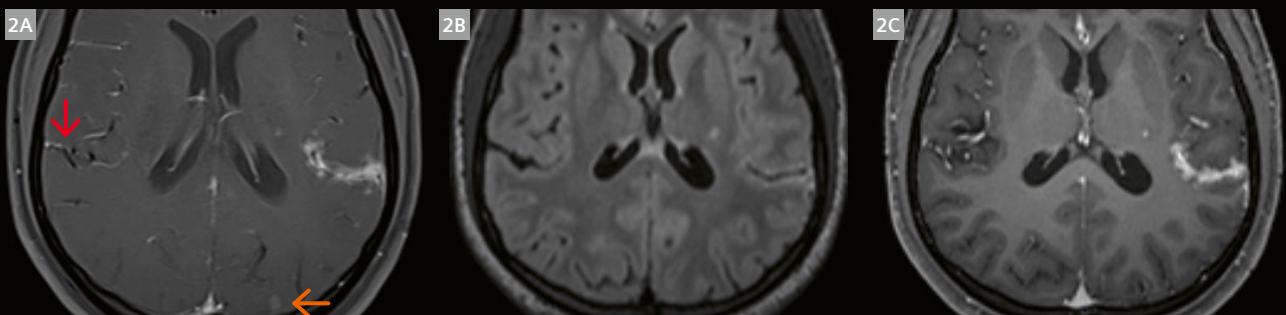
All studies were performed using a 3T MRI system (MAGNETOM Skyra, Siemens Healthcare, Erlangen, Germany). Gadolinium was administered intravenously at a dose of 0.1 mmol/kg. The MR studies were started

about 60–120 seconds after contrast injection. The post-contrast 3D T1 MPRAGE sequence was performed first, followed by the post-contrast 3D T1 SPACE and the 3D SPACE FLAIR.



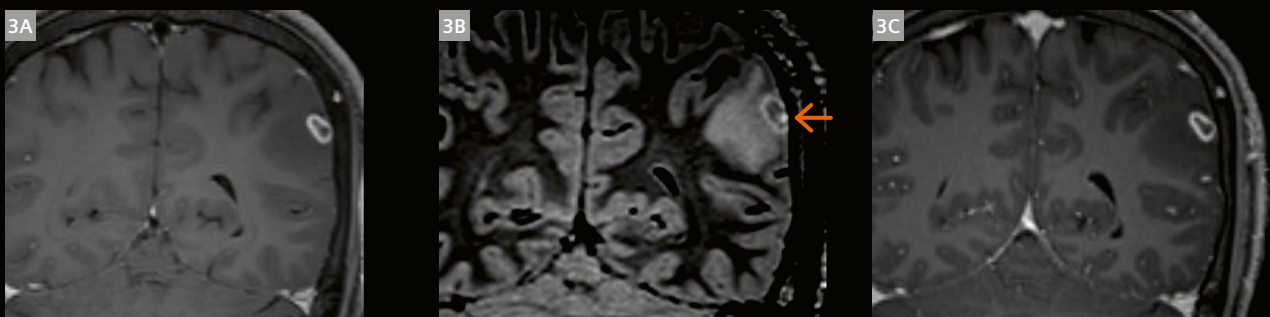
### 1 Nodular enhancing discrete lesion

(1A) Post-contrast 3D T1 SPACE image showing a heterogeneously enhancing nodule (arrow) in the right occipital lobe; lesions are less conspicuous in the (1B) post-contrast 3D SPACE FLAIR image and (1C) post-contrast 3D T1 MPRAGE image.



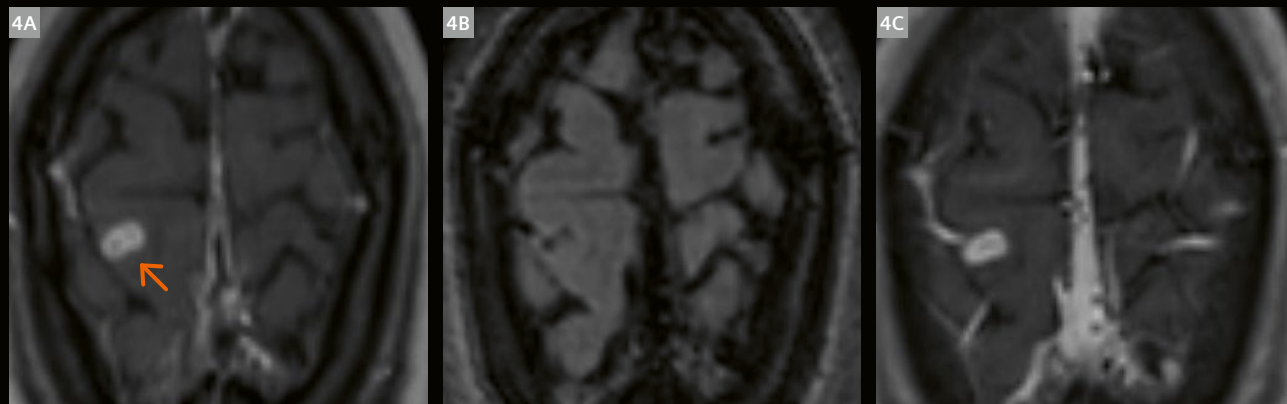
### 2 TB meningitis

(2A) Post-contrast 3D T1 SPACE; (2B) post-contrast 3D SPACE FLAIR and (2C) post-contrast 3D T1 MPRAGE; vessel enhancement particularly in the perisylvian region can be mistaken for meningeal enhancement in MPRAGE, but the 3D T1 SPACE image shows flow voids (red arrow). A nodular enhancing lesion (orange arrow) is visible in the left occipital lobe on 3D T1 SPACE, but not on the other sequences.

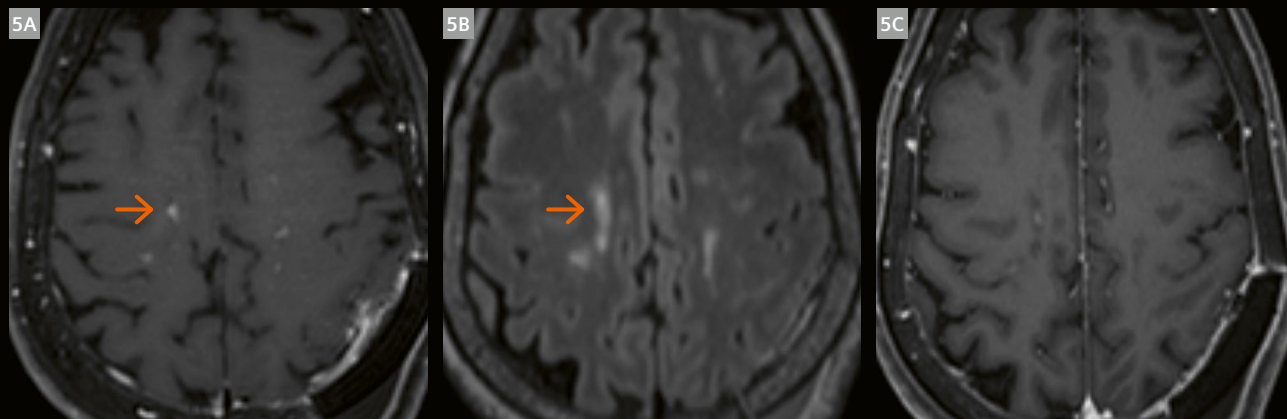


### 3 Neurocysticercosis

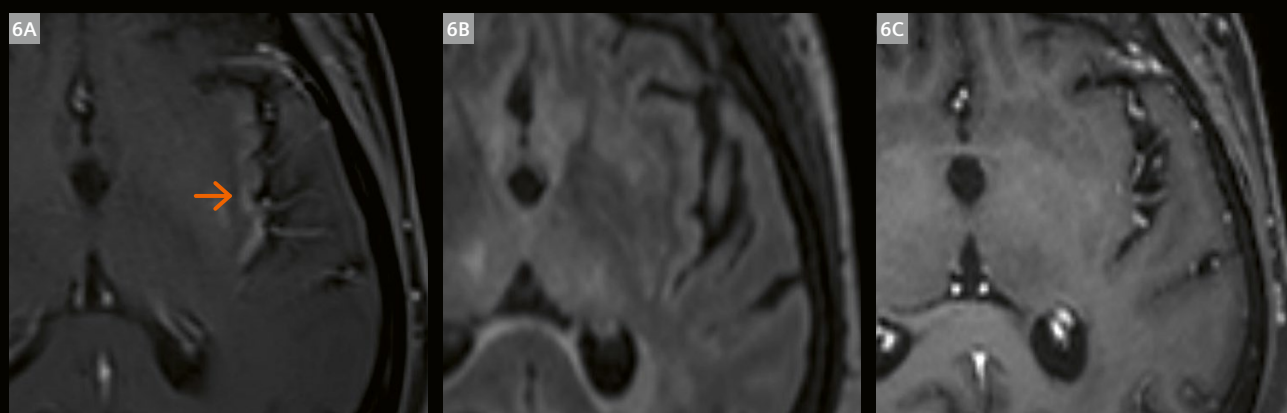
(3A) Post-contrast 3D T1 SPACE; (3B) post-contrast 3D SPACE FLAIR and (3C) post-contrast 3D T1 MPRAGE; the eccentric scolex is better seen on the 3D SPACE FLAIR image (orange arrow).

**4 Tuberculoma**

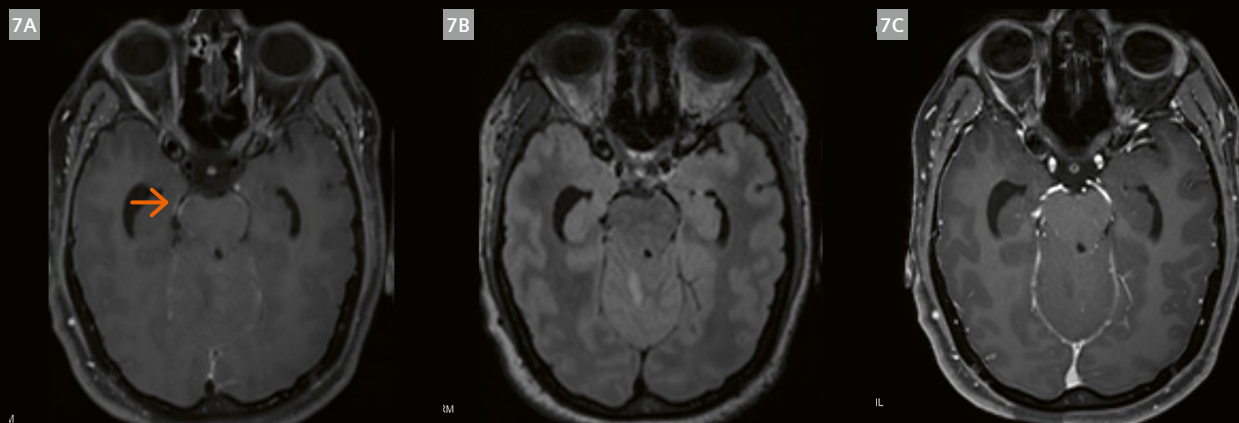
(4A) Post-contrast 3D T1 SPACE; (4B) post-contrast 3D SPACE FLAIR and (4C) post-contrast 3D T1 MPRAGE; tandem lesions better seen on the 3D T1 SPACE image (orange arrow).

**5 Demyelination**

(5A) Post-contrast 3D T1 SPACE; (5B) post-contrast 3D SPACE FLAIR and (5C) post-contrast 3D T1 MPRAGE; enhancing lesions better seen on the 3D T1 SPACE and 3D SPACE FLAIR images (orange arrows).

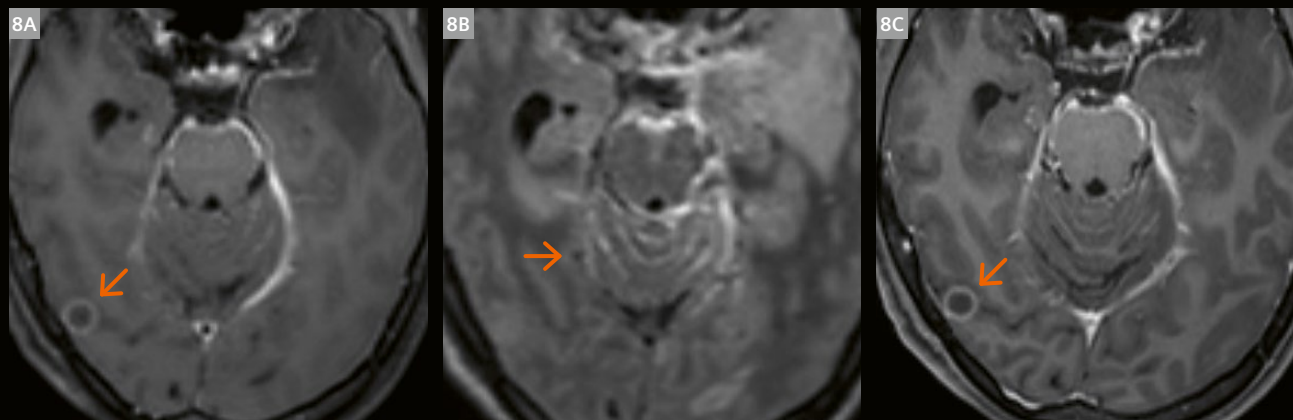
**6 Herpes encephalitis**

(6A) Post-contrast 3D T1 SPACE; (6B) post-contrast 3D SPACE FLAIR and (6C) post-contrast 3D T1 MPRAGE; gyriform enhancement in the left sylvian fissure better seen on the 3D T1 SPACE image (orange arrow).



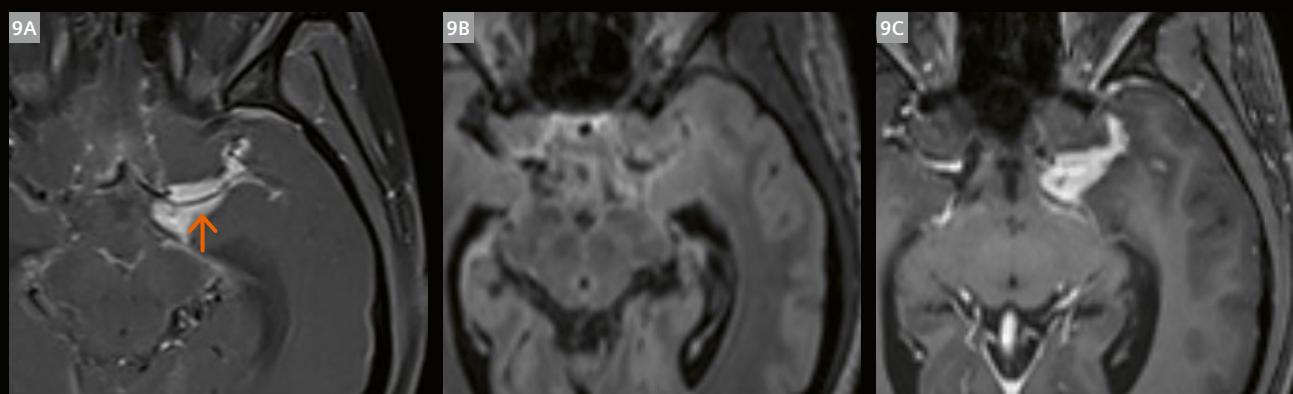
#### 7 Bacterial meningitis

(7A) Post-contrast 3D T1 SPACE; (7B) post-contrast 3D SPACE FLAIR and (7C) post-contrast 3D T1 MPRAGE; basal cistern meningeal enhancement better seen on the 3D T1 SPACE image (orange arrow).



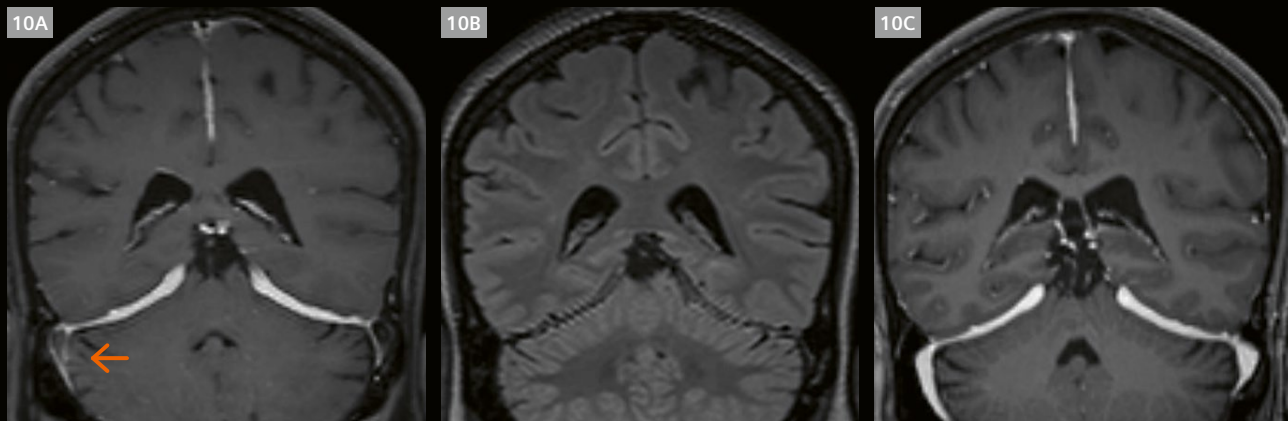
#### 8 Tuberculoma with meningoencephalitis

(8A) Post-contrast 3D T1 SPACE; (8B) post-contrast 3D SPACE FLAIR and (8C) post-contrast 3D T1 MPRAGE; superior cerebellar folia enhancement better seen on the 3D SPACE FLAIR image, while ring-enhancing lesions are better seen with 3D T1 SPACE and 3D SPACE FLAIR (orange arrows).



#### 9 TB meningitis

(9A) Post-contrast 3D T1 SPACE; (9B) post-contrast 3D SPACE FLAIR and (9C) post-contrast 3D T1 MPRAGE; thickening with enhancement of meninges in the left medial temporal region adjacent to the left middle cerebral artery is well seen on both, the 3D T1 SPACE and the 3D MPRAGE images; with MPRAGE the vessels could not be separately delineated, but with SPACE the vessels are seen as signal voids.



#### 10 Hypertrophic pachymeningitis

(10A) Post-contrast 3D T1 SPACE; (10B) post-contrast 3D SPACE FLAIR and (10C) post-contrast 3D T1 MPRAGE. Meningeal enhancement is seen in both SPACE and MPRAGE images, but the right sigmoid sinus could be separately delineated with 3D T1 SPACE.

### Standard MRI protocols used on the 3T MAGNETOM Skyra at Barnard Institute of Radiology (BIR) and at Rajiv Gandhi General Hospital (RGGH)

Parameters	3D T1 SPACE	3D SPACE FLAIR	3D T1 MPRAGE
Repetition time (TR)	700 ms	5000 ms	1800 ms
Effective echo time (TE eff)	11.0 ms	388 ms	2.32 ms
Inversion time		2000 ms	900 ms
Imaging time	5:07 min	4:47 min	3:34 min
Field of view	250 x 250 mm	250 x 250 mm	240 x 240 mm
Thickness	0.9 mm thick sections	0.9 mm thick sections	0.9 mm thick sections

The images were evaluated by two senior radiologists, who looked for brain parenchymal lesions and meningeal enhancement, and characterized lesions.

### Results

The ideal sequences for the different brain and meningeal pathologies are given in tables 1–4.

#### Parenchymal abnormalities

	3D T1 SPACE		3D SPACE FLAIR		3D T1 MPRAGE	
	Rad 1	Rad 2	Rad 1	Rad 2	Rad 1	Rad 2
< 1 cm	29	28	18	15	20	19
1–3 cm	84	83	65	63	78	76
> 3 cm	35	35	35	35	35	34

For detecting discrete lesions, the overall sensitivity of 3D T1 SPACE was highest (99.3%), followed by 3D T1 MPRAGE (88.5%), and 3D SPACE FLAIR (78%). 3D T1 SPACE performed well even for lesions < 1 cm (sensitivity: 98.3%), whereas the sensitivity was less for 3D SPACE FLAIR (56.9%) and 3D T1 MPRAGE (70.7%). All three sequences showed sensitivity above 98% for lesions > 3 cm.

Table 1: Number of discrete lesions identified.

3D T1 SPACE		3D SPACE FLAIR		3D T1 MPRAGE	
Rad 1	Rad 2	Rad 1	Rad 2	Rad 1	Rad 2
20	18	36	34	21	19

**Table 2:** Number of lesions with scolex.

For detecting lesions with scolex, the sensitivity of 3D SPACE FLAIR was higher (97.2%) than both 3D T1 MPRAGE (55.5%) and 3D T1 SPACE (52.8%).

	3D T1 SPACE		3D SPACE FLAIR		3D T1 MPRAGE	
	Rad 1	Rad 2	Rad 1	Rad 2	Rad 1	Rad 2
< 1 cm	23	24	15	14	18	18
1–3 cm	16	15	13	14	14	13
> 3 cm	6	6	6	6	6	6

**Table 3:** Number of conglomerate ring-enhancing lesions.

For detecting conglomerate ring-enhancing lesions, the overall sensitivity of 3D T1 SPACE was highest (98.5 %), followed by 3D T1 MPRAGE (83.3%) and 3D SPACE FLAIR (79.7%). 3D T1 SPACE performed well even for lesions < 1 cm (sensitivity 97.9%), while the sensitivity was less for 3D SPACE FLAIR (60.4%) and 3D T1 MPRAGE (75%). All three sequences showed 100% sensitivity for lesions > 3 cm.

	3D T1 SPACE		3D SPACE FLAIR		3D T1 MPRAGE	
	Rad 1	Rad 2	Rad 1	Rad 2	Rad 1	Rad 2

#### Supratentorial

Pachymeningeal enhancement	12	12	10	9	6	7
Leptomeningeal enhancement	25	24	22	23	18	15
Gyral enhancement	6	6	6	5	3	3

#### Infratentorial

Folial enhancement	9	9	8	9	4	5
Cisternal enhancement	25	26	23	22	17	15

**Table 4:** Number of cases with meningeal abnormalities.

For detecting meningeal abnormalities, the sensitivity of 3D T1 SPACE was highest (98.7%), followed by 3D SPACE FLAIR (87.8%) and 3D T1 MPRAGE (59.6%).

#### Distribution of abnormalities:

Tuberculosis	25%	Viral meningitis	10%
Metastases	13.33%	Demyelination	6.66%
Neurocysticercosis	10%	Neurosarcoidosis	3.33%
Bacterial meningitis	23.33%	Brain abscess	8.33%

## Discussion

The results of our study show that both 3D T1 SPACE and 3D SPACE FLAIR provide significantly more information than a routine post-contrast 3D T1 MPRAGE sequence alone. 3D T1 SPACE (black blood) offers several benefits. In brain tumors, it can differentiate vessel from tumor enhancement after contrast perfusion imaging, and can therefore better differentiate true from spurious enhancement. 3D T1 SPACE is also preferable in cases of meningitis, as are neuronavigation protocols for the same reason. 3D SPACE FLAIR is better able to demonstrate scolices.

Conglomerate lesions, typically seen in tuberculosis, were better delineated by 3D T1 SPACE than by 3D SPACE FLAIR and MPRAGE. Pachymeningeal enhancement is seen in, for instance, transient postoperative changes, spontaneous intracranial hypotension, granulomatous disease, and neoplasms such as meningiomas, metastatic disease, and secondary CNS lymphoma. In our study, we found that post-contrast 3D T1 SPACE is much better for demonstrating pachymeningeal involvement than 3D SPACE FLAIR and 3D T1 MPRAGE.

## Conclusion

Multiple 3D sequences are available and protocols vary between institutions. The choice of a particular 3D sequence can be tailored according to individual needs. We found that 3D T1 SPACE (black blood) was more robust and offered several benefits compared to 3D T1 MPRAGE and in many cases also compared to 3D SPACE FLAIR.

## Acknowledgments

The author would like to acknowledge the contributions of Dr. A. Mohideen Asraf, M.D., Assistant Professor at BIR and RGGH; Dr. Swarnalakshmi, M.D., of RGGH; and Dr. S. Harishpriya, DMRD, junior resident at BIR.

## References

- 1 Chang KH, Han MH, Roh JK, Kim IO, Han MC, Kim CW. Gd-DTPA-enhanced MR imaging of the brain in patients with meningitis: comparison with CT. *AJNR Am J Neuroradiol.* 1990;11(1):69–76.
- 2 Melhem ER, Bert RJ, Walker RE. Usefulness of optimized gadolinium-enhanced fast fluid-attenuated inversion recovery MR imaging in revealing lesions of the brain. *AJR Am J Roentgenol.* 1998;171(3): 803–7.
- 3 Komada T, Naganawa S, Ogawa H, Matsushima M, Kubota S, Kawai H, et al. Contrast-enhanced MR imaging of metastatic brain tumor at 3 tesla: utility of T(1)-weighted SPACE compared with 2D spin echo and 3D gradient echo sequence. *Magn Reson Med Sci.* 2008;7(1):13–21.
- 4 Essig M, Knopp MV, Schoenberg SO, Hawighorst H, Wenz F, Debus J, et al. Cerebral gliomas and metastases: assessment with contrast-enhanced fast fluid-attenuated inversion-recovery MR imaging. *Radiology.* 1999;210(2):551–7.
- 5 Mathews VP, Caldemeyer KS, Lowe MJ. Brain: gadolinium-enhanced fast fluid-attenuated inversion-recovery MR imaging. *Radiology.* 1999;211(1):257–63.
- 6 Tsuchiya K, Katase S, Yoshino A, Hachiya J. FLAIR MR imaging for diagnosing intracranial meningeal carcinomatosis. *AJR Am J Roentgenol.* 2001;176(6):1585–8.
- 7 Lee EK, Lee EJ, Kim S, Lee YS. Importance of Contrast-Enhanced Fluid-Attenuated Inversion Recovery Magnetic Resonance Imaging in Various Intracranial Pathologic Conditions. *Korean J Radiol.* 2016;17(1):127–41.
- 8 Singh SK, Agris JM, Leeds NE, Ginsberg LE. Intracranial leptomeningeal metastases: comparison of depiction at FLAIR and contrast-enhanced MR imaging. *Radiology.* 2000;217(1):50–3.
- 9 Chang C, Stuckey S, Alatakis S, Low K. Contrast Enhanced 3D T1-weighted SPACE: Pictorial Essay of Appearances, Advantages and Disadvantages Compared with Conventional Contrast Enhanced 3D T1-weighted Imaging (MPRAGE). Poster presented at: RANZCR-AOCR 2012. August 30 – September 2; Sydney, Australia. Available from: <http://www.ranzcr.edu.au>. [Last accessed on 2018 Apr 09].
- 10 Kumar S, Kumar S, Surya M, Mahajan A, Sharma S. To Compare Diagnostic Ability of Contrast-Enhanced Three-Dimensional T1-SPACE with Three-Dimensional Fluid-Attenuated Inversion Recovery and Three-Dimensional T1-Magnetization Prepared Rapid Gradient Echo Magnetic Resonance Sequences in Patients of Meningitis. *J Neurosci Rural Pract.* 2019;10(1):48–53.
- 11 Kato Y, Higano S, Tamura H. Usefulness of contrast-enhanced T1-weighted sampling perfection with application-optimized contrasts by using different flip angle evolutions in detection of small brain metastasis at 3T MR imaging: comparison with magnetization-prepared rapid acquisition of gradient echo imaging. *AJNR Am J Neuroradiol.* 2009;30(5):923–9.
- 12 Okada T, Kanagaki M, Yamamoto A, Sakamoto R, Kasahara S, Morimoto E, et al. Which to Choose for Volumetry: MPRAGE or SPACE? Proceedings of the ISMRM 19th Annual Meeting & Exhibition; 2011 May 7–13; Montreal, Quebec, Canada.
- 13 Hajnal JV, Bryant DJ, Kasuboski L, Pattany PM, De Coene B, Lewis PD, et al. Use of fluid attenuated inversion recovery (FLAIR) pulse sequences in MRI of the brain. *J Comput Assist Tomogr.* 1992;16(6):841–4.
- 14 De Coene B, Hajnal JV, Gatehouse P, Longmore DB, White SJ, Oatridge A, et al. MR of the brain using fluid-attenuated inversion recovery (FLAIR) pulse sequences. *AJNR Am J Neuroradiol.* 1992;13(6):1555–64.
- 15 Rydberg JN, Hammond CA, Grimm RC, et al. Initial clinical experience in MR imaging of the brain with a fast fluid-attenuated inversion-recovery pulse sequence. *Radiology* 1994;193(1):173–80.
- 16 Thurnher MM, Thurnher SA, Fleischmann D, Steuer A, Rieger A, Helbich T, et al. Comparison of T2-weighted and fluid-attenuated inversion-recovery fast spin-echo MR sequences in intracerebral AIDS-associated disease. *AJNR Am J Neuroradiol.* 1997 Oct;18(9):1601–9.
- 17 Fukuoka H, Hirai T, Okuda T, Shigematsu Y, Sasao A, Kimura E, et al. Comparison of the added value of contrast-enhanced 3D fluid-attenuated inversion recovery and magnetization-prepared rapid acquisition of gradient echo sequences in relation to conventional postcontrast T1-weighted images for the evaluation of leptomeningeal diseases at 3T. *AJNR Am J Neuroradiol.* 2010;31(5):868–73.
- 18 Griffiths PD, Coley SC, Romanowski CA, Hodgson T, Wilkinson ID. Contrast-enhanced fluid-attenuated inversion recovery imaging for leptomeningeal disease in children. *AJNR Am J Neuroradiol.* 2003;24(4):719–23.
- 19 Jeevanandham B, Kalyanpur T, Gupta P, Cherian M. Comparison of post-contrast 3D-T1-MPRAGE, 3D-T1-SPACE and 3D-T2-FLAIR MR images in evaluation of meningeal abnormalities at 3-T MRI. *Br J Radiol.* 2017;90(1074):20160834.

## Contact

Professor S. Babu Peter, MD DNB MNAMS FICR  
 Barnard Institute of Radiology  
 Madras Medical College  
 Rajiv Gandhi General Hospital  
 Opposite to Chennai Central Railway Station  
 Chennai, Tamil Nadu, India  
 drbabupeter@gmail.com



# T1 Relaxation-Enhanced Steady-State (T1RESS): An Improved Three-Dimensional Method for Contrast-Enhanced Imaging of Brain Tumors

Robert R. Edelman<sup>1,2</sup>, Ioannis Koktzoglou<sup>1,3</sup>, Nondas Leloudas<sup>1</sup>, Jianing Pang<sup>4</sup>

<sup>1</sup>Department of Radiology, NorthShore University HealthSystem, Evanston, IL, USA

<sup>2</sup>Department of Radiology, Northwestern University, Chicago, IL, USA

<sup>3</sup>Department of Radiology, University of Chicago Pritzker School of Medicine, Chicago, IL, USA

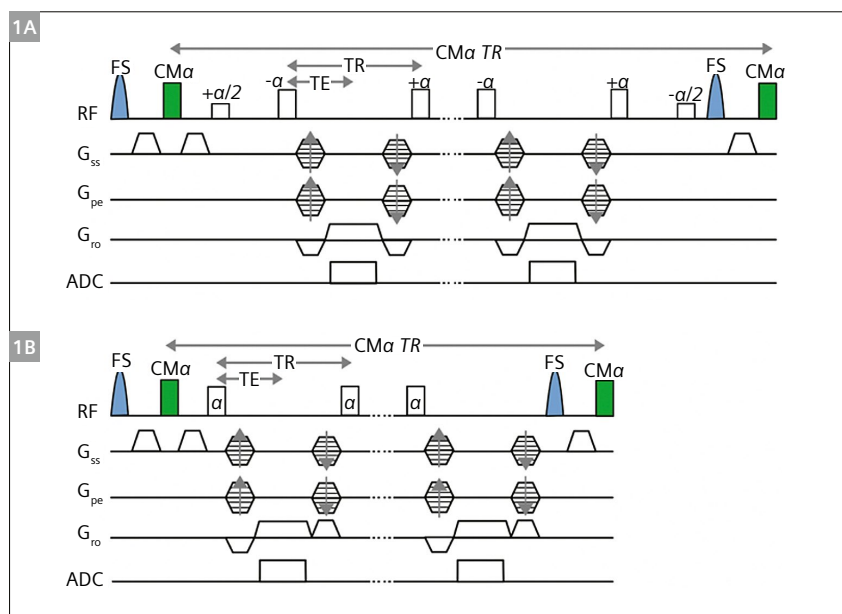
<sup>4</sup>Cardiovascular MR R&D, Siemens Medical Solutions USA, Inc., Chicago, IL, USA

## Introduction

We describe a new type of steady-state magnetic resonance imaging (MRI) pulse sequence, called T1 relaxation-enhanced steady-state (T1RESS)<sup>1</sup> [1], that overcomes limitations of standard-of-care post-contrast neuroimaging techniques. It considerably improves the visibility of brain tumors and other enhancing lesions while reducing scan

time through a novel pulse sequence architecture based on a steady-state free precession (SSFP) readout and periodic contrast-modifying radiofrequency (RF) pulses (Fig. 1).

T1RESS provides a flexible degree of T1 weighting while maintaining excellent signal-to-noise ratio (SNR) efficiency by repeatedly applying non-spatially selective



**1** T1RESS sequence. Comparison of balanced (1A) and unbalanced (1B) steady-state readouts.

$\alpha$  represents the imaging RF pulse, and FS denotes a fat saturation RF pulse. A non-spatially selective contrast-modifying RF pulse (CMa) is applied periodically over the entire duration of the echo train to introduce a flexible amount of T1 weighting (adapted from reference 1).

<sup>1</sup> Work in progress. The application is currently under development and is not for sale in the U.S. and in other countries. Its future availability cannot be ensured.

contrast-modifying (CM $\alpha$ ) RF pulses throughout the duration of the echo train. The CM $\alpha$  RF pulses can be adjusted independently of the imaging RF pulses. The amount of T1 weighting can be altered as needed by varying the values for the CM $\alpha$  flip angle and repetition time (TR), with larger flip angles and shorter TR resulting in more T1 weighting. For contrast-enhanced MRI of brain tumors, typical values for the CM $\alpha$  flip angle and TR are 75–90° and  $\approx$  400 milliseconds, respectively.

This sequence design has two main benefits:

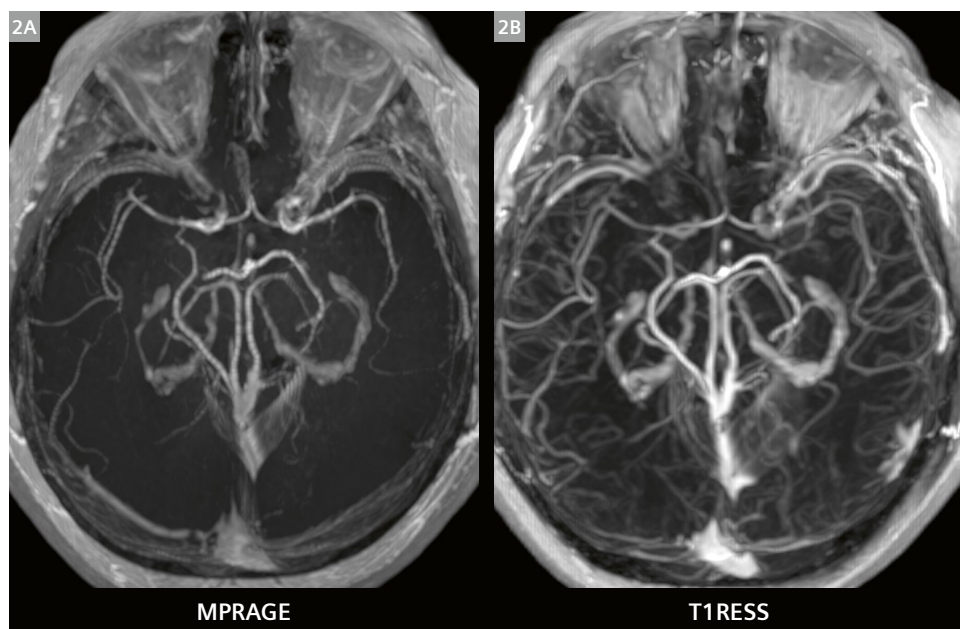
1. It provides flexible control over T1 weighting, so that sensitivity to the T1 shortening effects of paramagnetic contrast agents can be optimized for specific clinical indications.
2. It substantially reduces the signal intensity of non-enhancing background tissues, thereby improving the visibility of those enhancing lesions.

The high degree of background signal suppression results from several factors:

1. T1 weighting from the repeatedly applied CM $\alpha$  RF pulses;
2. the low T2/T1 ratio of healthy tissue, which in combination with the SSFP readout results in a substantially diminished signal intensity relative to a fast low-angle-shot (FLASH)-based acquisition;
3. magnetization transfer effects, which are much greater with T1RESS than FLASH due to the frequent application of short-duration, high-flip-angle imaging, and CM $\alpha$  RF pulses [2].

Two main versions of T1RESS have been implemented to date. One version, which we call “balanced” T1RESS (bT1RESS), uses a fully balanced SSFP readout and thus has native bright-blood contrast. A second “unbalanced” version (uT1RESS) uses an unbalanced SSFP readout, thus suppressing blood vessel signal based on flow-dependent dephasing. To test the diagnostic performance of T1RESS for brain tumors, we performed a proof-of-concept study that was approved by the hospital institutional review board. Contrast-enhanced MRI of the brain was performed at 3 Tesla (MAGNETOM Skyra and MAGNETOM Skyra<sup>fit</sup>, Siemens Healthcare, Erlangen, Germany) in 54 adult subjects with suspected or known brain tumors. 0.1 mmol/kg of gadobutrol (Bayer, Berlin, Germany) was administered intravenously followed by standard-of-care sequences, after which additional post-contrast scans were obtained consisting of balanced and unbalanced T1RESS as well as 3D FLASH and/or magnetization-prepared rapid acquisition gradient echo (MPRAGE). For both bT1RESS and uT1RESS, data were acquired using a Cartesian 3D k-space trajectory as a single shot along the phase-encoding direction, whereas the acquisition was segmented along the 3D partition-encoding direction.

For both versions of T1RESS, the periodic application of contrast-modifying RF pulses was essential for generating T1 contrast and to suppress the signal intensity of cerebrospinal fluid and soft-tissue edema. Bright-blood bT1RESS dramatically outperformed 3D FLASH and MPRAGE in creating angiographic renderings of the intracranial vessels during the equilibrium phase of contrast enhancement (Fig. 2), while with uT1RESS the blood vessels appeared dark.

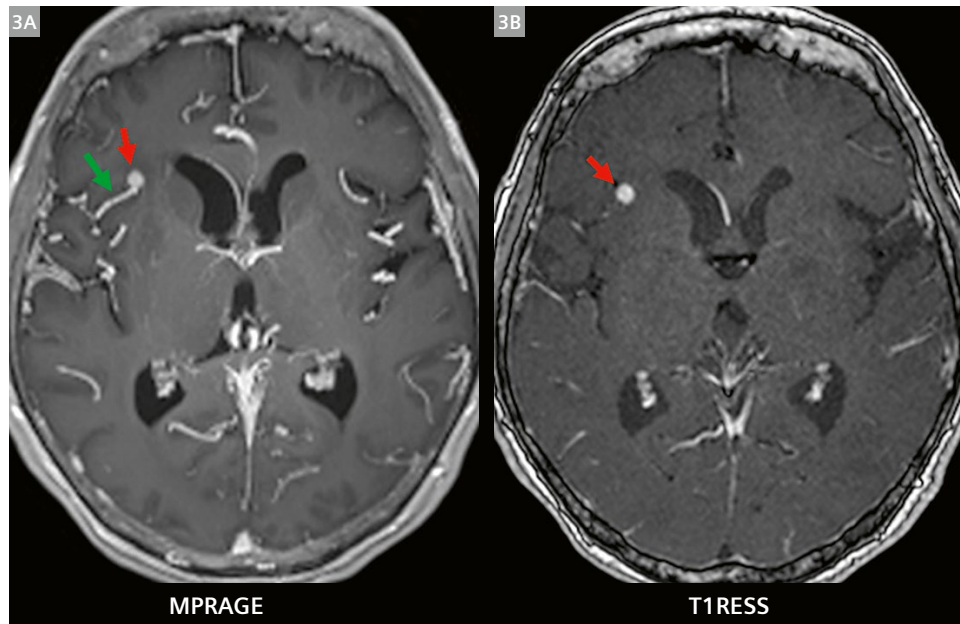


**2** Post-contrast vascular imaging. 47 mm thick maximum intensity projections from MPRAGE (2A) and bT1RESS (2B). Note that small branch vessels are much better seen with bT1RESS because of the improved SNR and greater background tissue suppression.

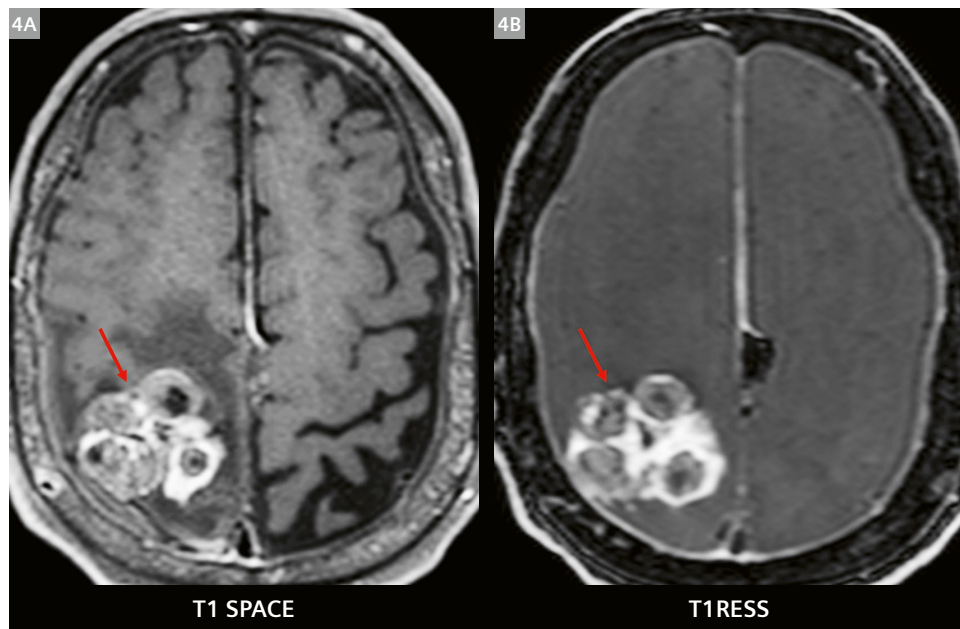
With uT1RESS, enhancing tumors appear particularly conspicuous against a background in which blood vessels and non-enhancing tissues all appear relatively dark. We found that this method could unambiguously identify even small metastatic tumor deposits that were difficult to distinguish from blood vessels on 3D FLASH or MPRAGE images (Fig. 3).

We also compared uT1RESS with the dark-blood T1-weighted sampling perfection with application-optimized contrasts using different flip angle evolution (SPACE) technique, which has been shown to have superior performance compared with MPRAGE for detecting small brain metastases [3]. We found that brain tumors appeared

significantly more conspicuous with uT1RESS than T1 SPACE (Fig. 4). Comparing uT1RESS with T1 SPACE using matched spatial resolution and scan time to evaluate 32 tumors in 14 patients, the respective values for mean tumor-to-brain contrast-to-noise ratios (CNR) were  $180.32 \pm 92.34$  vs.  $60.34 \pm 54.88$ ,  $p = 8.75 \times 10^{-7}$ . The values for mean tumor-to-brain contrast were  $1.76 \pm 0.76$  vs.  $0.89 \pm 0.43$ ,  $p = 7.95 \times 10^{-7}$ . Moreover, uT1RESS does not suffer from the same limitations as the T1 SPACE technique, which include sensitivity to  $B_1$  field inhomogeneity, blurring related to T2 decay over the lengthy fast spin-echo train, and the need for additional flow dephasing gradients to achieve uniform suppression of the blood-pool signal.



**3** Patient with small right frontal brain metastasis from renal cell carcinoma. Comparison of axial multiplanar reconstruction from uT1RESS (3B) and MPRAGE (3A); while MPRAGE makes it difficult to distinguish the bright signal of the metastasis (red arrow) from that of a nearby blood vessel (green arrow), uT1RESS makes the metastasis more conspicuous due to the suppression of vascular signal in combination with the lower signal intensity of normal brain tissue.



**4** Patient with large right occipital brain metastasis. (4A) T1 SPACE, (4B) uT1RESS. While both techniques demonstrate the enhancing mass and suppress vascular signal, the tumor-to-brain contrast is much higher with uT1RESS.

## Discussion

In this study of brain tumors at 3T using post-contrast scans, uT1RESS provided a more than twofold improvement in tumor visibility compared with either MPRAGE or T1 SPACE, which are both widely used neuroimaging techniques. For oncological applications, enhancing blood vessels distract from, and could potentially be confused with, enhancing tumors [4]. uT1RESS renders blood vessels dark by using an unbalanced steady-state gradient-echo readout in which the phase-encoding gradients are rewound and the frequency-encoding gradient is unbalanced [5–7]. The resultant suppression of intravascular signals is a consequence of flow- and diffusion-related phase dispersion that gradually accumulates with each sequence repetition [8]. Because the 3D uT1RESS acquisition utilizes a very large number ( $\approx 40,000$ ) of sequence repetitions, intravascular phase dispersion is complete, resulting in marked suppression of intravascular signal regardless of vessel orientation. Unbalanced steady-state sequences are reported to be more motion-sensitive than balanced SSFP or FLASH [9]. However, we found that bulk motion artifacts were minimal or absent despite the effective suppression of the blood-pool signal. This is partly due to the fact that uT1RESS uses a very weak dephasing gradient – which, along with the large number of sequence repetitions, ensures that the phase dispersion is gradual and consistently applied in every sequence repetition.

Another interesting feature of uT1RESS is its high SNR efficiency. For instance, the default scan time on our 3T scanners for a whole-brain MPRAGE or T1 SPACE acquisition with 1 mm slice thickness is typically on the order of four to seven minutes. By comparison, using uT1RESS, we have implemented an accelerated version of the technique that allows us to complete a whole-brain scan with 1 mm slice thickness in less than one minute. Other potentially useful versions of the technique are also feasible. For instance, we can obtain water-only and fat-only images using a two-echo Dixon implementation of uT1RESS. The uT1RESS and bT1RESS techniques can also be applied at 1.5T.

## Contact

Robert R. Edelman, M.D.  
Clinical Professor of Radiology  
NorthShore University HealthSystem  
Suite G503  
2650 Ridge Ave  
Evanston IL 60201  
USA  
Phone: +1 847-570-2098  
REdelman@northshore.org



While our initial work has focused on the imaging of brain tumors, the methodology can be applied to a broad range of clinical applications. Future efforts will include using dark-blood uT1RESS to evaluate tumors in the breast, liver, and pancreas, for breath-hold 3D imaging of cardiac morphology and of late gadolinium enhancement in the myocardium, and for the improved depiction and characterization of plaque in the carotid and peripheral arteries. With regard to bright-blood bT1RESS, this technique has the potential to significantly improve image quality and vessel conspicuity for contrast-enhanced MR angiography of the head and neck and other vascular regions.

## References

- 1 Edelman R, Leloudas N, Pang J, Bailes J, Merrell R, Koktzoglou I. Twofold improved tumor-to-brain contrast using a novel T1 relaxation-enhanced steady-state (T1RESS) MRI technique. *Sci Adv.* 2020;6(44):eabd1635.
- 2 Bieri O, Scheffler K. On the origin of apparent low tissue signals in balanced SSFP. *Magn Reson Med.* 2006;56(5):1067–74.
- 3 Park J, Kim J, Yoo E, Lee H, Chang JH, Kim EY. Detection of small metastatic brain tumors: comparison of 3D contrast-enhanced whole-brain black-blood imaging and MP-RAGE imaging. *Invest Radiol.* 2012;47(2):136–41.
- 4 Yang S, Nam Y, Kim MO, Kim EY, Park J, Kim DH. Computer-aided detection of metastatic brain tumors using magnetic resonance black-blood imaging. *Invest Radiol.* 2013;48(2):113–9.
- 5 Chavhan GB, Babyn PS, Jankharia BG, Cheng HL, Shroff MM. Steady-state MR imaging sequences: physics, classification, and clinical applications. *Radiographics.* 2008;28(4):1147–60.
- 6 Sekihara K. Steady-state magnetizations in rapid NMR imaging using small flip angles and short repetition intervals. *IEEE Trans Med Imaging.* 1987;6(2):157–64.
- 7 Elster AD. Gradient-echo MR imaging: techniques and acronyms. *Radiology.* 1993;186(1):1–8.
- 8 Markl M, Leupold J. Gradient echo imaging. *J Magn Reson Imaging.* 2012;35(6):1274–89.
- 9 Yu Z, Zhao T, Asslander J, Lattanzi R, Sodickson DK, Cloos MA. Exploring the sensitivity of magnetic resonance fingerprinting to motion. *Magn Reson Imaging.* 2018;54:241–248.

# HASTE Diffusion-weighted Imaging at 3 Tesla: Evaluation of Non-EPI Diffusion for the Detection of Cholesteatomas

Thomas Troalen, Ph.D.<sup>1</sup>; Arnaud Pellerin, M.D.<sup>2</sup>; David Bertrand, M.D.<sup>2</sup>; Yohann Michelot<sup>1</sup>; Jonas Svensson, Ph.D.<sup>3</sup>; Frederik Testud, Ph.D.<sup>4</sup>

<sup>1</sup>Siemens Healthcare SAS, Saint-Denis, France

<sup>2</sup>IRIS GRIM Radiologie, L'Hôpital Privé du Confluent, Nantes, France

<sup>3</sup>Skånes Universitetssjukhus (SUS), Lund, Sweden

<sup>4</sup>Siemens Healthcare AB, Malmö, Sweden

## Introduction

A cholesteatoma is a hyperproliferative disease of keratinocytes characterized by mass formation due to the accumulation of continuous desquamation of keratin, leading to local invasive destruction of surrounding tissues in the middle ear [1]. It can be caused by a birth defect, but it is mostly caused by repeated middle-ear infections. A cholesteatoma often develops as a cyst that sheds layers of old skin. As these dead skin cells accumulate, the growth can increase in size and destroy the delicate bones of the middle ear. This may affect hearing, balance, and the functioning of facial muscles.

Cholesteatomas are managed surgically, generally by a complete excision of the lesion via tympanoplasty or radical or modified radical mastoidectomy. This is often followed by a second-look procedure performed to check for residual or recurrent disease. This second-look is conducted 6–18 months after the initial operation because most cholesteatomas recur within the first two postoperative years, with 60% occurring in the first year after surgery [2]. The second-look surgery is mainly to assess residual or recurrent disease because both cannot adequately be diagnosed solely by clinical examination [3].

Cholesteatomas are visualized either by computed tomography (CT) or magnetic resonance imaging (MRI). CT imaging is still the method of choice for detecting and assessing the exact location, the extent, and possible complications prior to surgery. MRI with diffusion-weighted imaging (DWI) is, however, a powerful tool for initial evaluation and diagnosis or to detect local recurrence or residual cholesteatoma [4].

To date, various different DWI-techniques have been used: These can essentially be divided into echo-planar imaging (EPI)-based and non-EPI-based techniques. The choice of the technique is mainly influenced by the fact that imaging must be performed near the skull base

where problems due to different artifacts (e.g., field inhomogeneities, motion) can occur. Several reviews have compared both approaches [4, 5]: Non-EPI MRI has become established as the modality of choice in detecting and localizing post-operative, middle-ear cholesteatoma at 1.5T [6, 7].

Half-Fourier acquisition single-shot turbo spin-echo (HASTE) DWI is a non-EPI technique that has been used for many years to detect cholesteatomas at 1.5T. HASTE DWI has the advantage of providing a very clear hyperintensity at the location of the cholesteatoma, with no artifactual hyperintensities at the air-bone interface of the temporal bone [8]. In addition, due to the higher spatial resolution, reduced slice thickness, and artifacts, HASTE DWI has been shown to be superior to single-shot EPI-based DWI for small sized cholesteatoma (< 5 mm) [6] and is therefore considered as the gold standard for detecting cholesteatomas using MRI.

Advanced neurological investigations are now performed predominantly on 3T clinical MRI scanners [9] as they have become more accessible over the last two decades. Thus, there is also a role for 3T MRI in investigating patients with cholesteatomas.

HASTE DWI applied at 3T has already been reported on older MAGNETOM scanners [10] but it has been challenging in the past due to interference patterns emerging from various possible sources (slice cross-talk, undesired coherence pathways, and violation of CPMG conditions). Readout segmented EPI, also referred to as RESOLVE [11], has been proposed as a better alternative to single-shot echo-planar DWI [12]. Although RESOLVE is a segmented EPI-based imaging technique with shortened readout reducing susceptibility artifacts, coronal images are still prone to image artifacts. This is because signal hyperintensities due to these inhomogeneities can overlap with cholesteatoma locations, therefore resulting in potential misdiagnosis. However, this particular study

did not compare RESOLVE with non-EPI DWI techniques, in particular with HASTE DWI.

Due to newer hardware and improved  $B_0$  homogeneity of the newer MR systems, the use of the HASTE DWI sequence at 3T for cholesteatoma has been revisited again. This article presents several representative cases from two hospitals and with different 3T MRI scanners to demonstrate the feasibility of HASTE DWI at 3T for patients with suspected cholesteatomas.

## Case reports

### 1. Experience from Lund, Sweden:

#### Comparison between 1.5T and 3T

Four patients (ranging in age from 27 to 74 years, mean age 49 years) underwent an MRI examination at 1.5T and at 3T because of suspected cholesteatomas on a MAGNETOM Aera and MAGNETOM Prisma (Siemens Healthcare, Erlangen, Germany), respectively. Written informed consent was obtained for all participants.

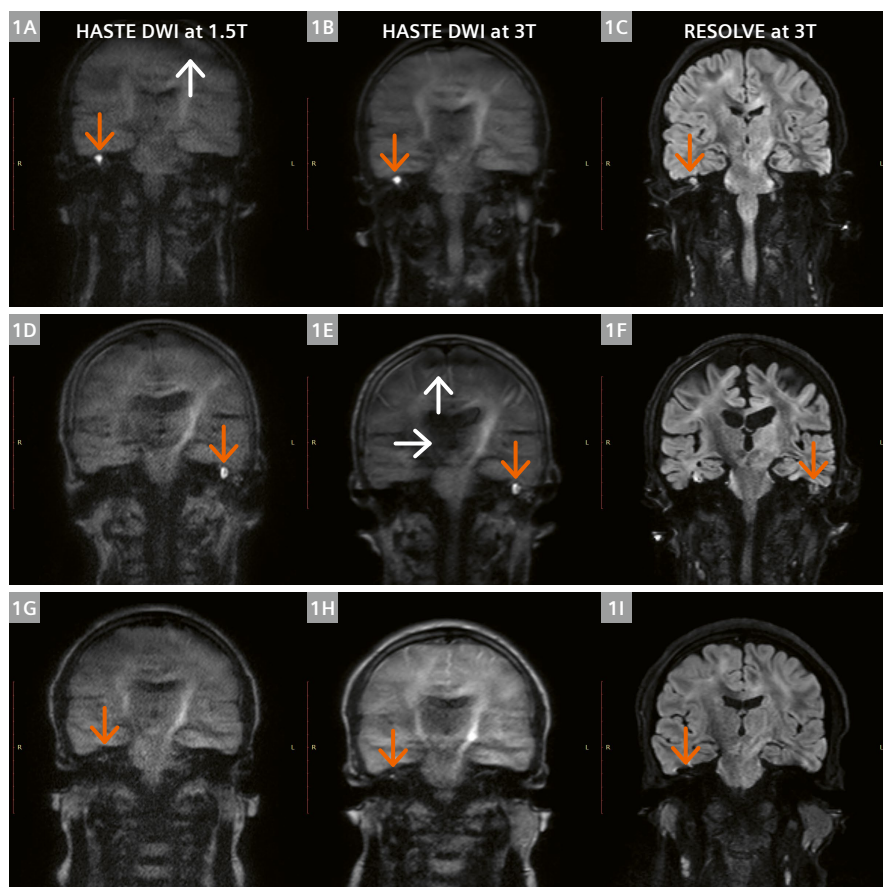
At 1.5T, the MR exam consisted, among other acquisitions, of two HASTE DWI acquisitions each with different b-values which had the following parameters: TE/TR = 103 ms / 2000 ms, flip angle 150°, 3.5 mm slice thickness, in-plane resolution  $0.6 \times 0.6 \text{ mm}^2$  after interpolation, FOV  $220 \times 220 \text{ mm}^2$ , iPAT factor 2 and 10 averages for each diffusion acquisition with  $b = 0 \text{ s/mm}^2$  and  $b = 1000 \text{ s/mm}^2$  in 3-dimensional (3D) diagonal diffusion mode. The total acquisition time for 18 slices was 5 minutes for each b-value acquisition.

The protocols for the prototype HASTE DWI acquisition at 3T<sup>1</sup> were essentially identical, apart from TE, which was 105 ms.

Among other MR acquisitions at 3T, RESOLVE acquisitions were performed which had the following parameters: TE/TR = 42 ms / 2150 ms, flip angle 180°, 3.5 mm slice thickness, in-plane resolution  $1.1 \times 1.1 \text{ mm}^2$  after interpolation, FOV  $220 \times 220 \text{ mm}^2$ , 2 and 5 averages for the diffusion-weighted acquisition with  $b = 0 \text{ s/mm}^2$  and  $b = 1000 \text{ s/mm}^2$  in 3D diagonal diffusion mode, respectively, and iPAT factor 3. The total acquisition time was 3.5 minutes for 15 slices.

RESOLVE and HASTE diffusion-weighted images acquired with  $b = 1000 \text{ s/mm}^2$  from three of the four cases are shown in Figure 1. In the top and middle rows of Figure 1, the cholesteatoma lesion is visible as a bright spot (orange arrow) and easy to detect in the HASTE diffusion-weighted images at both field strengths. The lesions

<sup>1</sup>The sequence used in the article was a prototype.



**1** Comparison of HASTE DWI at 1.5T (left-hand column, MAGNETOM Aera) and 3T (middle column, MAGNETOM Prisma) for a 28-year-old, a 74-year-old, and a 27-year-old patient in the top, middle and bottom rows, respectively. RESOLVE at 3T from the same slice as in the middle column is depicted in the right-hand column. In all cases, diffusion-weighted images with  $b = 1000 \text{ s/mm}^2$  are shown. Orange and white arrows point to the position of the cholesteatoma and image artifacts, respectively.  
Images courtesy of Skåne University Hospital, Lund, Sweden.

are also visible on the RESOLVE images (Figs. 1C and F) but have the same contrast as the healthy brain tissue next to it. In Figure 1F, a region with signal hyperintensity is visible above the right middle-ear cavity. Dark band artifacts are visible in the neck in Figures 1 A-E, and within the brain in Figures 1A and E (white arrows). In the last row, a patient with a small hyperintense region is visible on HASTE DWI at 3T (Fig. 1H) but hardly distinguishable on HASTE DWI at 1.5T (Fig. 1G) or RESOLVE at 3T (Fig. 1I). The presence of a small cholesteatoma was confirmed later by surgery. The fourth patient (images not shown here) did not show a cholesteatoma.

## 2. Experience from Nantes, France:

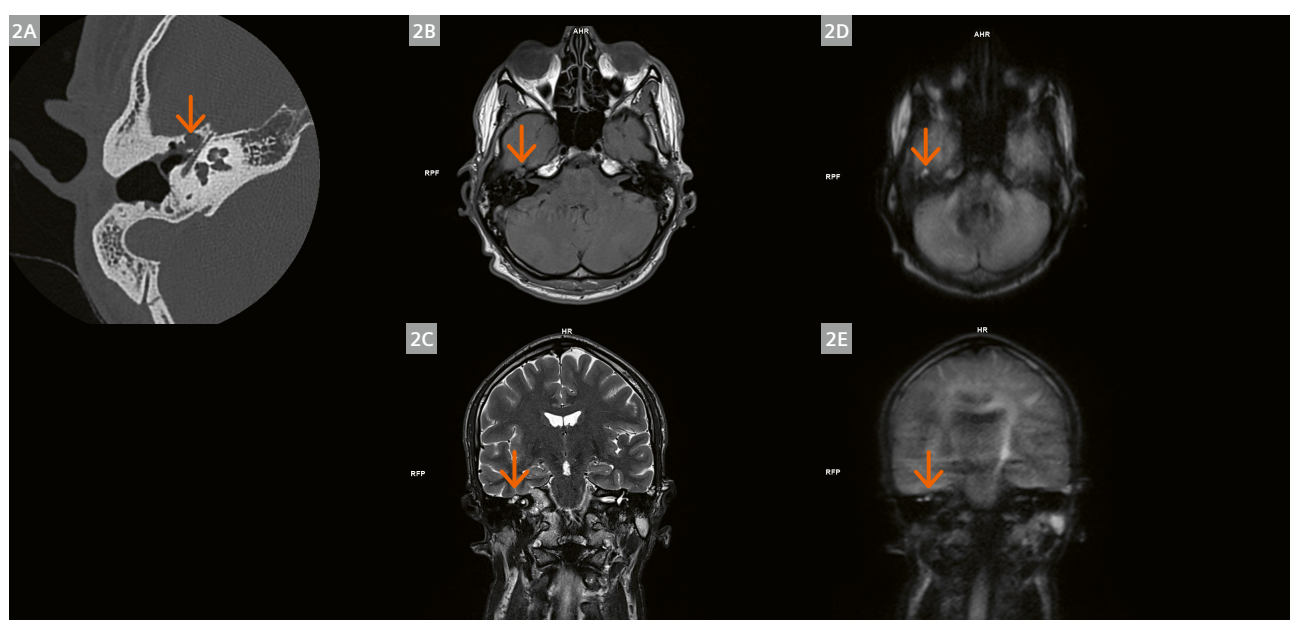
### Diagnostic validation with CT and surgery

A robust clinical protocol has been defined in the radiology department of the Private Hospital of Confluent, Nantes, France, and consisted of transversal and coronal HASTE DWI image series, in combination with transversal or coronal T1-weighted and T2-weighted TSE sequences. The 3T HASTE DWI sequence<sup>1</sup> was acquired using the exact same protocol as in Lund, except that only 15 slices and 8 averages were acquired for a total scan time of 4 minutes. No  $b = 0 \text{ s/mm}^2$  images were acquired. All images were obtained on a 3T MAGNETOM Lumina (Siemens Healthcare, Erlangen, Germany).

Figure 2 presents a case of a 29-year-old male patient with possible recurrent cholesteatoma in the right middle-ear cavity after primary mastoidectomy and tympanoplasty performed ten years ago. Clinical recurrence was suspected based on otoscopy and audiology: right hearing loss and tinnitus were observed, but without any facial nerve palsy. Recurrent cholesteatoma was confirmed from the 3T images, and a second-look surgery was indicated. Histological analysis confirmed the collection of keratinous debris lined by stratified squamous epithelium trapped in the right ear.

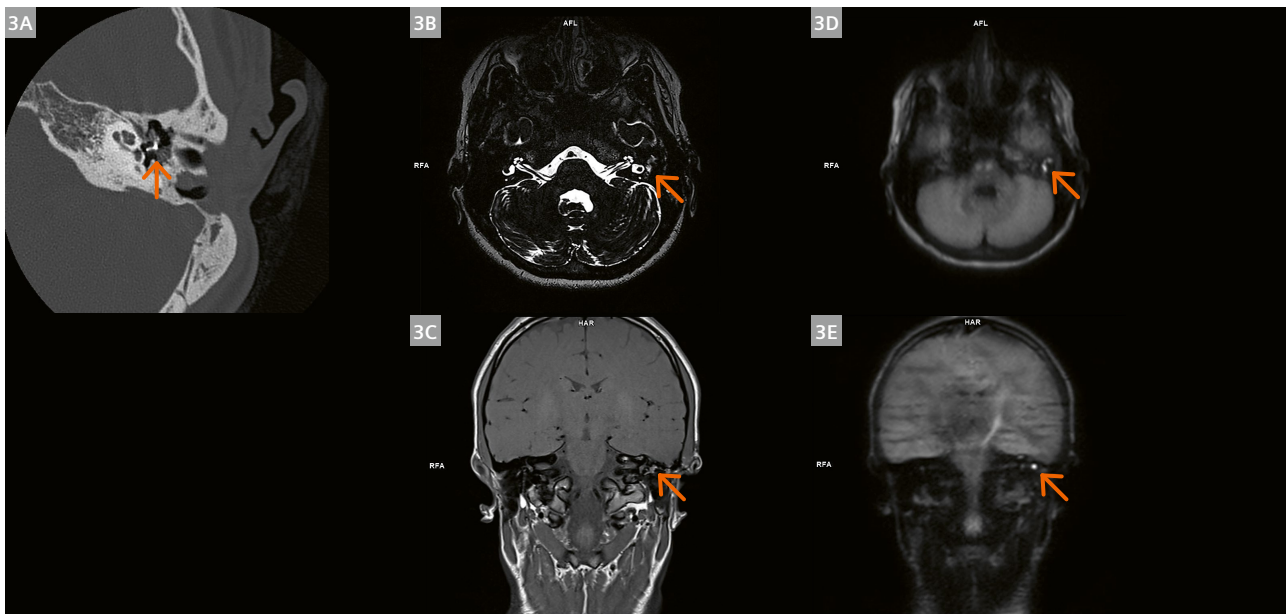
A second case of a 16-year-old woman with possible recurrent cholesteatoma in the left middle-ear cavity after primary tympanoplasty including ossiculoplasty is presented in Figure 3. Clinical recurrence was suspected with the patient complaining about worsening of her hearing. The ENT doctor noticed an otorrhea and an uncontrollable retraction pocket. Following the MR exam, a second-look surgery was indicated, with new ossiculoplasty.

A third case is presented in Figure 4 of a 42-year-old woman previously treated in 2005 for a right cholesteatoma. The patient presented an attic retraction pocket poorly tolerated and was suffering from severe conductive hearing loss.



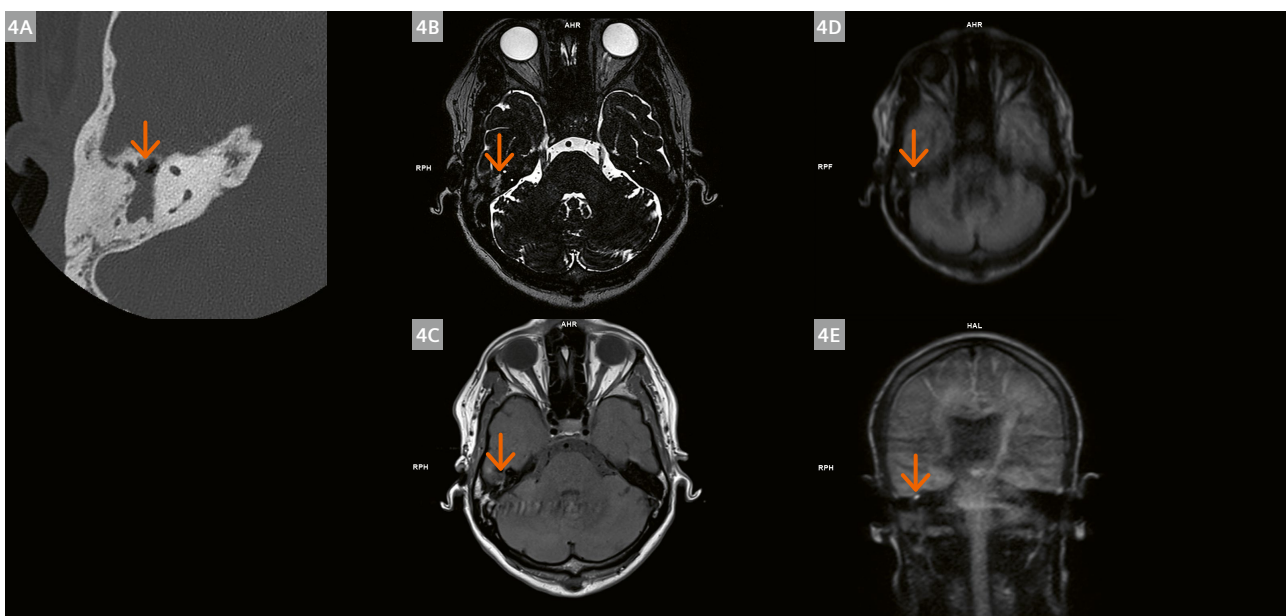
- 2** Clinical case of a 29-year-old male patient with possible recurrent cholesteatoma in the right middle-ear cavity after primary mastoidectomy and tympanoplasty performed ten years ago.

Imaging findings: (2A) Transverse reconstruction of the CT scan showed a convex lesion located at the anterior epitympanic recess with tegmen erosion. Proximity to a geniculate ganglion and secondary tympanic part of the facial nerve was observed. (2B) Transverse T1-weighted image showed a lesion of iso signal intensity, which was observed as a moderate hyperintense lesion on the coronal T2-weighted image (2C). Close contact to the basi-temporal meningeal was depicted (2D, E). At this location, two little spots with increased DW signal intensity were visible on the transverse and coronal HASTE diffusion-weighted images, suggesting a cholesteatoma.



**3** Clinical case of a 16-year-old female with possible recurrent cholesteatoma in the left middle-ear cavity after primary tympanoplasty including ossiculoplasty.

Imaging findings: (3A) Transverse reconstruction of the CT scan showed a nodular lesion within the tympanic cavity adjacent to the ossicular prosthesis that appeared to be dislocated. 3T images revealed a recurrent cholesteatoma at this location. (3B) Transverse spin-echo T2-weighted image showed a middle-ear lesion with high signal intensity, which was barely visible on the coronal spin-echo T1-weighted image (3C). (3D, E) At this location, increased DW signal intensity (5 mm in size) was observed on both transversal and coronal HASTE diffusion-weighted images, indicative of cholesteatoma. This was not a false negative case despite the potential prosthetic artifact. One can note that the filling of the mastoidectomy cavity appeared as a scar or granulation tissue as no DW hyperintensity was observed.



**4** Clinical case of a 42-year-old woman previously treated in 2005 for a right cholesteatoma.

Imaging findings: (4A) Transverse reconstruction of the CT scan showed a non-specific complete filling of right middle-ear cavity and of additus ad antrum. 3T images confirmed a small recurrent cholesteatoma within this filling. The transverse and coronal HASTE diffusion-weighted images (4D, E) presented a very small (size < 3 mm) hyperintensity located anteriorly in the middle-ear cavity that could be correlated with small hyperintense signal intensity on the transverse spin-echo T2-weighted image (4B), and low signal on spin-echo T1-weighted image (4C), suggesting a cholesteatoma. Close contact to the basi-temporal meninge was noticed.

## Discussion

A comparison study and case reports from two sites have been summarized both at 1.5T and 3T and on different MRI scanners.

In the comparison study examining HASTE DWI at 1.5T and 3T, HASTE diffusion-weighted images at both field strengths allowed the detection of cholesteatoma lesions. This was not always the case with RESOLVE as illustrated in the case of the third patient (last row in Fig. 1). RESOLVE acquisitions can indeed suffer from some residual geometric distortions and artifacts, especially in the region of the ear cavity, where the susceptibility differences between air, soft tissue, and bone induce very strong local spatial magnetic field variations. The improved signal-to-noise ratio of the 3T examination as compared with 1.5T was beneficial in detecting a small cholesteatoma using HASTE DWI (Fig. 1, bottom row).

As presented in the case reports, HASTE DWI was included in the examination on clinical 3T MRI scanners to investigate the presence of cholesteatomas in the clinical workflow and allowing successful treatment of patients. HASTE DWI has some limitations of which the most obvious is the low signal-to-noise ratio and low contrast in the other regions visible within the field of view. The latter is probably only a minor drawback in most scenarios because other contrasts are acquired by default, as is the case at the French and Swedish institutions. The sequence still requires considerable acquisition time, in particular if both  $b = 0 \text{ s/mm}^2$  and  $b = 1000 \text{ s/mm}^2$  are acquired, for example to estimate the apparent diffusion coefficient (ADC), or when both coronal and axial acquisitions are needed. This can be partly mitigated by acquiring just the high  $b$ -value image where the cholesteatoma is clearly visible; if surgery is to be performed, a CT scan is acquired for planning. This is the strategy adopted by the French institution. In some cases artifacts are visible on the HASTE DWI, for example reduced signal intensities. They originate from the violation of the CPMG conditions and are more predominant at some distance from the isocenter. An axial rather than a coronal acquisition centered around the isocenter can therefore be used to avoid regions distant from the isocenter. An alternative method to avoid these artifacts is to apply a phase insensitive preparation [13] after the diffusion-encoding block. This would, however, lead to even larger echo times and therefore a further reduction in SNR.

This article provides case reports and experiences from a limited number of sites and patients. It is, however, not a state-of-the-art, large-scale clinical study to investigate the image quality qualitatively and quantitatively of HASTE DWI for detecting cholesteatomas at 3T. This will therefore be part of a future study.

## Conclusion

In conclusion, cholesteatoma findings with HASTE DWI were always in agreement between 1.5T and 3T in the cases presented. It was shown that the RESOLVE technique may not depict a cholesteatoma in every case, because of local susceptibility variations induced by magnetic field inhomogeneities, resulting in artifacts or signal cancellation making the diagnosis sometimes difficult. HASTE DWI is intrinsically less sensitive to susceptibility variations and is therefore a well-suited method for the detection of pathologies in regions with large magnetic susceptibility variations on a clinical 3T scanner.

## Acknowledgment

The HASTE diffusion-weighted imaging prototype sequence has been shared as a Core Competence Partnership (C<sup>2</sup>P) agreement with other institutions by Skåne University Hospital, Lund, Sweden.

## References

- 1 J.D. Swartz, Cholesteatomas of the middle ear. Diagnosis, etiology, and complications, *Radiol. Clin. North Am.* 22 (1984) 15–35.
- 2 K. Gyo, Y. Sasaki, Y. Hinohira, N. Yanagihara, Residue of middle ear cholesteatoma after intact canal wall tympanoplasty: surgical findings at one year, *Ann. Otol. Rhinol. Laryngol.* 105 (1996) 615–619. <https://doi.org/10.1177/000348949610500805>.
- 3 A.C. Yiğiter, E. Pınar, A. İmre, N. Erdoğan, Value of Echo-Planar Diffusion-Weighted Magnetic Resonance Imaging for Detecting Tympanomastoid Cholesteatoma, *J. Int. Adv. Otol.* 11 (2015) 53–57. <https://doi.org/10.5152/iao.2015.447>.
- 4 B. Henninger, C. Kremsler, Diffusion weighted imaging for the detection and evaluation of cholesteatoma, *World J. Radiol.* 9 (2017) 217. <https://doi.org/10.4329/wjr.v9.i5.217>.
- 5 M. Jindal, A. Riskalla, D. Jiang, S. Connor, A.F. O'Connor, A Systematic Review of Diffusion-Weighted Magnetic Resonance Imaging in the Assessment of Postoperative Cholesteatoma, *Otol. Neurotol.* 32 (2011) 1243–1249. <https://doi.org/10.1097/MAO.0b013e31822e938d>.
- 6 B. De Foer, J.-P. Vercruyse, B. Pilet, J. Michiels, R. Verriest, M. Pouillon, T. Somers, J.W. Casselman, E. Offeciers, Single-shot, turbo spin-echo, diffusion-weighted imaging versus spin-echo-planar, diffusion-weighted imaging in the detection of acquired middle ear cholesteatoma, *AJNR Am. J. Neuroradiol.* 27 (2006) 1480–1482.
- 7 S. Khemani, R.K. Lingam, A. Kalan, A. Singh, The value of non-echo planar HASTE diffusion-weighted MR imaging in the detection, localisation and prediction of extent of postoperative cholesteatoma: Localisation and prediction of postoperative cholesteatoma, *Clin. Otolaryngol.* 36 (2011) 306–312. <https://doi.org/10.1111/j.1749-4486.2011.02332.x>.
- 8 T. Moritani, A. Hiwatashi, J. Zhong, Pitfalls and Artifacts of Diffusion-Weighted Imaging, in: T. Moritani, A.A. Capizzano (Eds.), *Diffus.-Weight. MR Imaging Brain Head Neck Spine*, Springer International Publishing, Cham, 2021: pp. 29–41. [https://doi.org/10.1007/978-3-030-62120-9\\_3](https://doi.org/10.1007/978-3-030-62120-9_3).
- 9 J. Alvarez-Linera, 3T MRI: advances in brain imaging, *Eur. J. Radiol.* 67 (2008) 415–426. <https://doi.org/10.1016/j.ejrad.2008.02.045>.

## Contact

Thomas Troalen, Ph.D.  
Siemens Healthcare SAS  
40 Avenue des Fruitières  
93210, Saint Denis  
France  
[thomas.troalen@siemens-healthineers.com](mailto:thomas.troalen@siemens-healthineers.com)



Frederik Testud, Ph.D.  
Siemens Healthcare AB  
Pulpetgången 6  
215 32, Malmö  
Sweden  
[frederik.testud@siemens-healthineers.com](mailto:frederik.testud@siemens-healthineers.com)

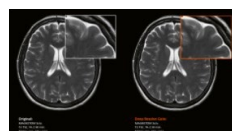


- 10 F.B. Pizzini, F. Barbieri, A. Beltramello, F. Alessandrini, F. Fiorino, HASTE Diffusion-Weighted 3-Tesla Magnetic Resonance Imaging in the Diagnosis of Primary and Relapsing Cholesteatoma, *Otol. Neurotol.* 31 (2010) 596–602. <https://doi.org/10.1097/MAO.0b013e3181dbb7c2>.
- 11 D.A. Porter, R.M. Heidemann, High resolution diffusion-weighted imaging using readout-segmented echo-planar imaging, parallel imaging and a two-dimensional navigator-based reacquisition: EPI With Parallel Imaging and 2D Reacquisition, *Magn. Reson. Med.* 62 (2009) 468–475. <https://doi.org/10.1002/mrm.22024>.
- 12 O. Algin, H. Aydin, E. Ozmen, G. Ocakoglu, S. Bercin, D.A. Porter, A. Kutluhan, Detection of cholesteatoma: High-resolution DWI using RS-EPI and parallel imaging at 3 tesla, *J. Neuroradiol.* 44 (2017) 388–394. <https://doi.org/10.1016/j.neurad.2017.05.006>.
- 13 D.C. Alsop, Phase insensitive preparation of single-shot RARE: Application to diffusion imaging in humans, *Magn. Reson. Med.* 38 (1997) 527–533. <https://doi.org/10.1002/mrm.1910380404>.

Advertisement

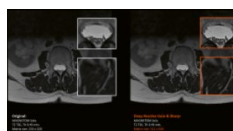
## Try them on your system

Trial licenses for many of the applications featured in this issue of MAGNETOM Flash are available as a trial license free of charge for a period of 90 days.



### Deep Resolve Gain

Deep Resolve Gain is an advanced image reconstruction technology that achieves intelligent denoising.



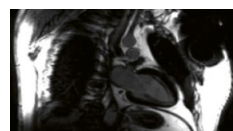
### Deep Resolve Sharp

Deep Resolve Sharp is an AI-powered image reconstruction technology with a deep neural network at its core that increases the sharpness of the image.



### MR Protocols Module

Centrally manage & distribute your standardized protocols.



### High Bandwidth Inversion Recovery

Cardiac inversion recovery for patients prone to susceptibility artefacts.



### Breast Dot Engine

The Breast Dot Engine supports consistent frequency selection for fat, water, saline or silicone.

For further details, product overviews, image galleries and general requirements visit us at:

[www.siemens-healthineers.com/magnetic-resonance-imaging/  
options-and-upgrades](http://www.siemens-healthineers.com/magnetic-resonance-imaging/options-and-upgrades)

# Magnetic Resonance Fingerprinting – The Future of Quantitative MR Neuroimaging

Gregor Kasprian, M.D.; Victor Schmidbauer, M.D.

Division of Neuroradiology, Department of Biomedical Imaging and Image-guided Therapy,  
Medical University of Vienna, Austria

By providing the possibility to acquire a variety of unique tissue contrasts, magnetic resonance imaging (MRI) is the gold standard for diagnostic brain imaging. However, current MRI strategies are compromised by time-consuming image data acquisitions, limitations in the comparability of quantitative imaging data, artifacts, and inter-scanner variability.

Improvements in quantitative imaging techniques will guide us toward a new era in diagnostic neuroradiology. The possibility to complement the subjective assessment of non-invasive brain imaging by quantitative data will lead to better, more reliable, and objectifiable diagnoses of diseases of the central nervous system. Moreover, robust quantitative data will serve as ideal input for artificial intelligence-based algorithms, which – in combination with radiological expertise – will improve diagnostic and prognostic precision and thereby optimize personalized treatment for many patients. To date, quantitative MR techniques have been time consuming and complex in data post-processing, and thus limited to research. To achieve clinical practicability and feasibility, these traditional approaches had to be reinvented.

## MR signals translated into tissue-specific fingerprints

Magnetic Resonance Fingerprinting (MRF)<sup>1</sup> is a pioneering approach in the field of MR technology. MRF relies on the principle that each tissue examined evolves its own unique signal – *fingerprint* – after the application of a technically appropriate stimulus [1]. In contrast to conventional MRI, MRF is characterized by variation of the technical parameters, e.g., repetition time, and radiofrequency excitation angle, throughout the sequence acquisition to generate the evolution of the tissue's *fingerprint* [2]. Initially, this tissue fingerprint appears as complex and abstract data, which needs to be translated into an image. As for any

translation, a pre-existing standard of reference or dictionary is required. A dictionary-based recognition process connects the acquired signal-derived information to quantitative MR metrics – such as, but not limited to, relaxation parameters and diffusion properties – in a voxel-wise manner [1, 2]. The MRF dictionary contains a collection of simulated fingerprints to represent all tissue-specific properties within the physiological range [3]. Since MRF pattern recognition takes a variety of different parameters into account, the tissue characterization process is considered highly accurate and robust [2]. In summary, three hallmarks characterize the entire MRF process. The first step – signal evolution and acquisition – is MR scanner and sequence dependent. The second and third steps are characterized by automatized data processing: dictionary-based pattern recognition and tissue-specific, property-based visualization [2, 3].

## Quantitative MRI and multiple image contrasts in less than eight minutes

Based on a single sequence acquisition of less than eight minutes, MRF provides a variety of multiparametric imaging information for qualitative and quantitative non-invasive neuro MR diagnostics. By choosing physical MR properties as the bedrock of the technical concept, MRF demonstrates excellent inter-scanner reproducibility [4]. This approach allows a robust and objective method to detect, characterize, and quantify physiological and pathological changes of the central nervous system [5, 6]. Furthermore, MRF is regarded as a highly promising technique for eliminating artifacts in MR imaging [2, 7], as each voxel is subjected to the pattern recognition process individually. Overall, MRF is leading the way into the future of MRI, providing structural diagnostic, quantitative, robust, less artifact prone imaging data in a short imaging time.

<sup>1</sup>MR Fingerprinting is not commercially available in some countries. Due to regulatory reasons its future availability cannot be ensured.

## Clinical experiences in MRF

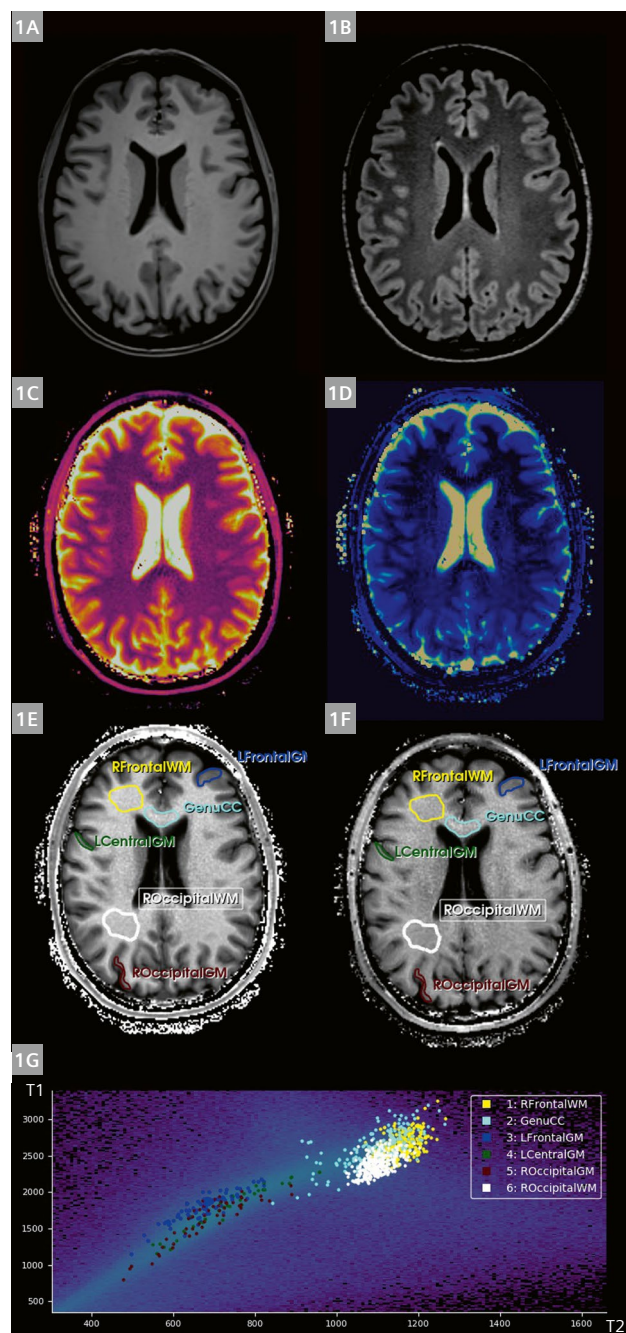
Clinical experiences using this novel approach are still scarce. At the same time, as MRF technology is continuously improving, specific areas of interest in the neuroradiological application of this technology are currently being identified. MRF will be particularly valuable in diagnosing diseases that were previously difficult to assess and evaluate based on the subjective impression of individual radiologists. As MRF is sensitive to multiple MR parameters at once, it offers a variety of in-depth MR imaging markers of pathologically altered brain parenchyma. Pathological brain tissue, which so far might have been categorized as "normal-appearing" brain parenchyma by traditional subjective visual radiological assessment, could be detected more sensitively using MRF. This will allow better quantification and evaluation of the burden of disease in individual patients and will help better understand the current status and progress in a variety of neurological disorders. As a consequence, MRF can help monitor the effect of treatment more reliably than ever before.

Furthermore, time-saving, in-depth multiparametric characterization of pathologically altered brain tissue – after acquisition of a single MRF sequence – may further improve the diagnostic specificity of MRI, allowing to optimize the differentiation of similar-appearing signal changes into specific pathological entities. Ultimately, the resulting reduction in overall MR scan time may also grant easier and faster access to high-end MR diagnostics to the benefit of many patients.

Here, we would like to demonstrate some initial clinicoradiological experiences with MRF in different areas of diagnostic neuroimaging.

## Basic MRF findings in normal subjects

MRF allows characterization of the fingerprint of specific brain compartments. Figure 1 shows the MR images of a 45-year-old normal subject. The upper row depicts sequentially acquired conventional T1-weighted (1A) and fluid-attenuated T2-weighted 3D sequences at 3 Tesla (MAGNETOM Vida, Siemens Healthcare, Erlangen, Germany) totaling an imaging time of up to 8 minutes. The results of a single acquisition using MRF (7 minutes acquisition time) are shown in Figure 1. A T1 map (1C) and a T2 map can be visualized with color coding according to the local T1 and T2 values. Advanced quantitative analysis using the MR Robust Quantitative Tool (MR RoQT) allows characterization of specific gray (dark colors) and white matter (bright colors) compartments, which can be distinguished from each other on the scatterplot graph (bottom row). The scatterplot indicates the T2 (x-axis) and T1 (y-axis) values of the analyzed regions of interest and



**1** 45-year-old healthy subject. (1A, B) T1-weighted (1A) and fluid-attenuated T2-weighted 3D sequences (1B) at 3T. (1C, D) MR Fingerprinting acquisition. (1E, F) T1 map (1E) and T2 map (1F) with color coding according to the local T1 and T2 values. (1G) MR RoQT scatterplot characterizing specific gray (dark colors) and white matter (bright colors) compartments. The scatterplot indicates the T2 (x-axis) and T1 (y-axis) values of the analyzed regions of interest and shows the normal variation of values within one tissue compartment.

shows the normal variation of values within one tissue compartment. Except for distinct differences between white and gray matter, there are also regional differences in the quantified T1 and T2 values. In addition to structural MR data, MRF also provides quantitative data, which cannot be extracted from conventional T2-weighted and T1-weighted MRI sequences, without investing further acquisition time. MRF is quite a robust quantitative MR technology, which is feasible in a clinical setting.

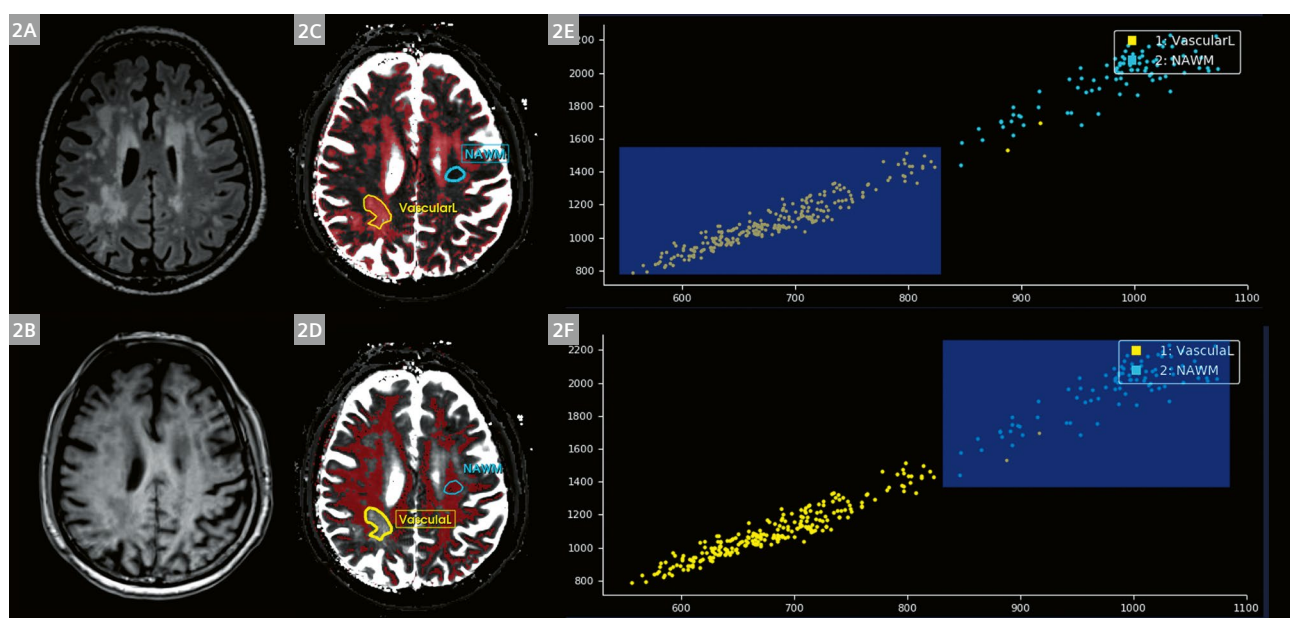
## MRF findings in brain pathologies

In addition to the quantitative characterization of regional variations of brain tissue fingerprints, a detailed analysis of the MR characteristics of abnormal brain regions is also possible. Figure 2 depicts a 67-year-old patient with severe vascular leukoencephalopathy. Conventional FLAIR (2A) sequences depict the T2-weighted hyperintense white matter alterations, which are less conspicuous on T1-weighted sequences (2B). By using MRF and generating T2 maps (2C, D), lesional (yellow) and non-lesional (turquoise) brain regions can be automatically segmented based on their T1 and T2 quantitative characteristics, shown in the scatterplots (2E, F). By either selecting the lesional (yellow) or non-lesional (turquoise) range of T1/T2 values, these

tissue types can be distinguished and separated as well as quantified. This will allow a more accurate semi-automated follow-up analysis of brain imaging data, and allows better monitoring of the course of a disease or the effectiveness of therapeutic measures.

## MRF in amyotrophic lateral sclerosis

MRF can be particularly valuable if qualitative findings need to be objectified. This may be especially important in cases of neurodegenerative disorders such as amyotrophic lateral sclerosis (ALS). The hyperintense T2-weighted signal change of the corticospinal tract has been a useful sign of Wallerian degeneration in ALS. However, the sign is often subtle and sometimes non-specific. A reliable quantitative analysis of these changes might help to identify this sign with greater confidence and diagnostic certainty. Figure 3 shows the results of an MRI examination of a 71-year-old patient with clinically suspected ALS: The T1-weighted (3A), T2-weighted (3B), and FLAIR (3C) 3D sequences were sequentially acquired at 3 Tesla. The second row shows the results of the MRF analysis in the same patient, depicting the T1 map (3D) and the T2 map (3E). The arrows point to the left internal capsule. Please note the slight T2-weighted hyperintense signal alteration of the

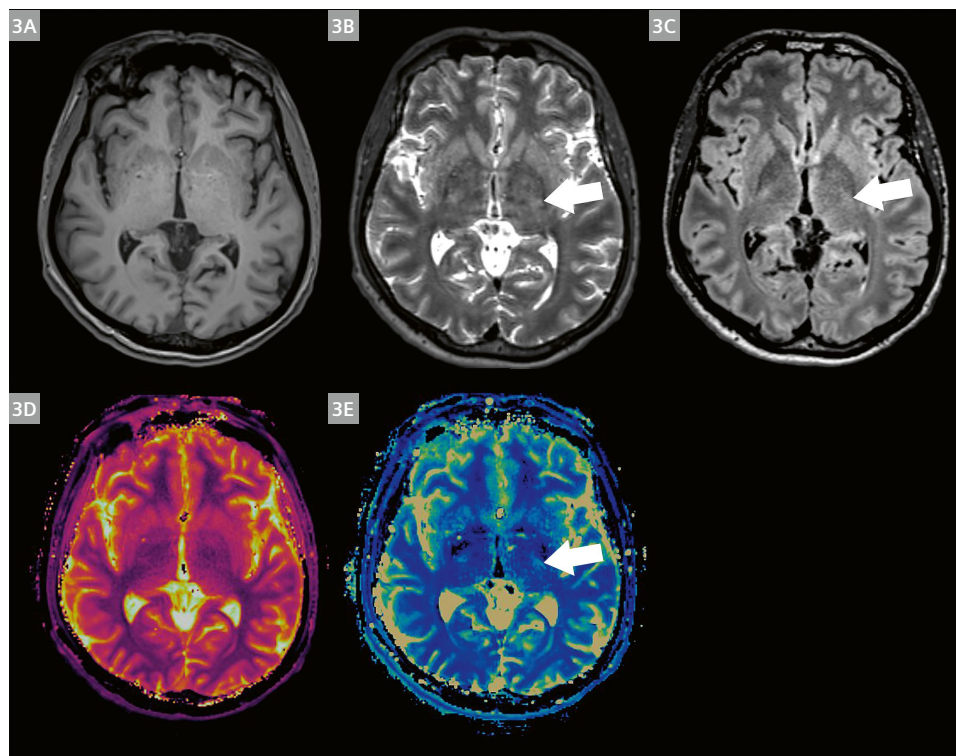


- 2** A 67-year-old patient with severe vascular leukoencephalopathy. (2A) Conventional FLAIR depict the T2-weighted hyperintense white matter alterations, which are less conspicuous on (2B) T1-weighted sequences. (2C, D) By using MRF lesional (yellow) and non-lesional (turquoise) brain regions can be automatically segmented based on their quantitative R1 (x-axis) and R2 (y-axis) characteristics, shown in the scatterplots (2E, F).

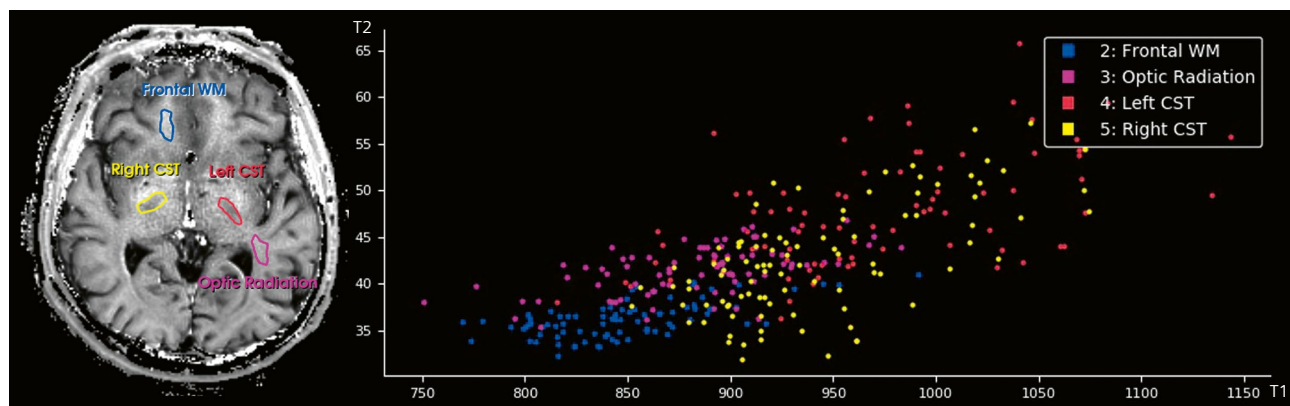
corticospinal tract, which is confirmed on the T2 map of the MRF analysis.

If the local T1 (x-axis) and T2 (y-axis) values are analyzed using the postprocessing software MR RoQT, an unequivocal difference between the corticospinal tract fingerprints (red and yellow) and those of the optic radiation (pink) or the frontal white matter (blue) can

be identified (Fig. 4). This improves the diagnostic confidence of the radiologist and leads to a smaller interrater variability in the imaging assessment of this disorder. Further, these findings can be combined with diffusion tensor imaging (DTI) based parameters (FA, diffusivity) or diffusion-weighted imaging (DWI) based ADC measurements to increase the diagnostic sensitivity of this sign.



**3** A 71-year-old patient with clinically suspected ALS. T1-weighted (3A), T2-weighted (3B), and FLAIR (3C) 3D sequences sequentially acquired at 3T. (3D, E) show the results of the MRF analysis in the same patient, depicting the T1 map (3D) and the T2 map (3E). The arrows point to the left internal capsule. The slight T2-weighted hyperintense signal alteration of the corticospinal tract is confirmed on the T2 map of the MRF analysis.



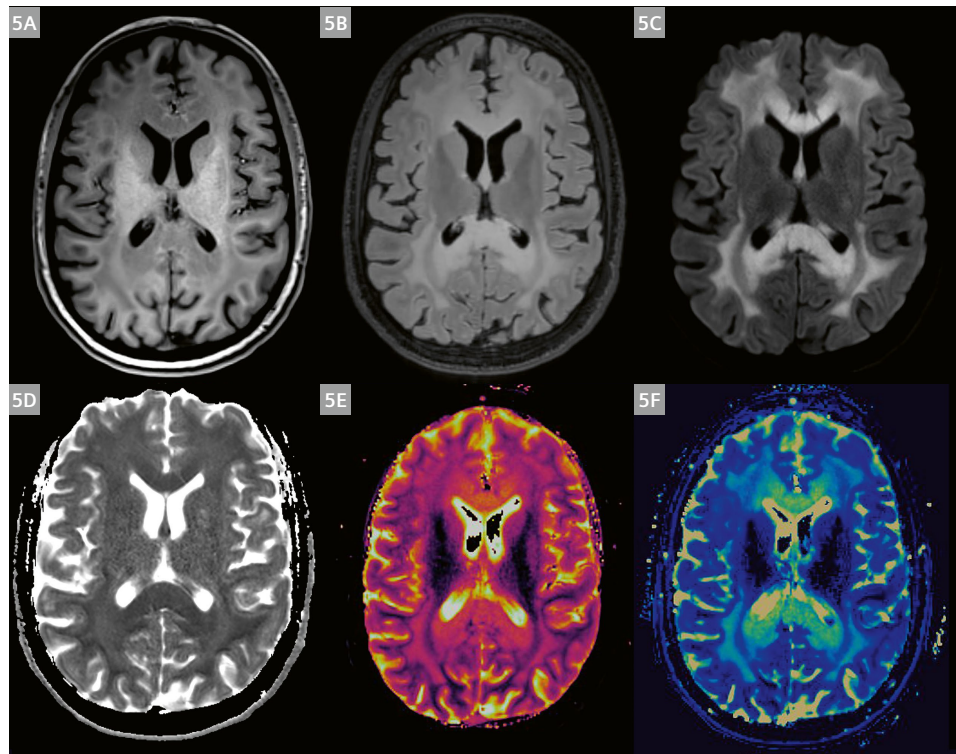
**4** Postprocessing of the patient data shown in Figure 3 using the MR Robust Quantitative Tool (MR RoQT). T1 values are indicated on the x-axis, T2 values are plotted on the y-axis. The left and right corticospinal tracts show a distinctive difference in their T1 and T2 fingerprints compared to other white matter regions.

## MRF in metabolic disorders or leukodystrophies

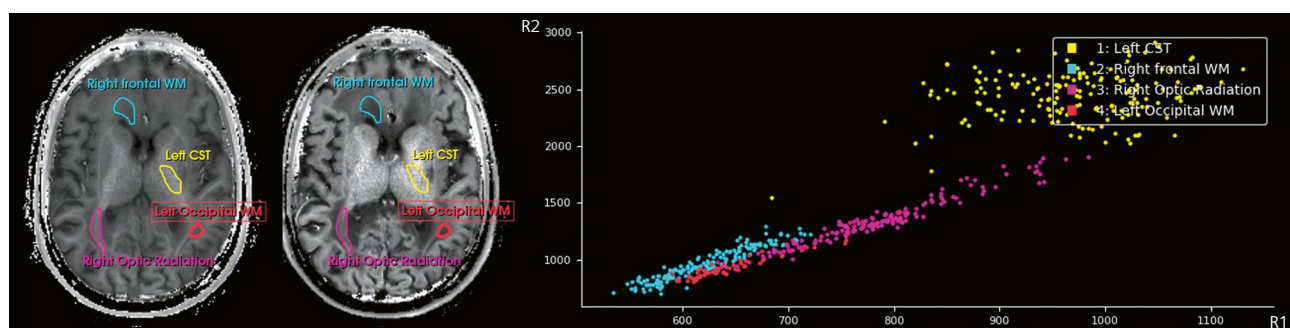
MRF may also be beneficial in neurological disorders, characterized by widespread signal alterations of the gray and white matter, such as leukodystrophies or mitochondriopathies. Figure 5 shows the MR images of a 6-year-old girl with glutaric aciduria type I – a metabolic disorder/mitochondriopathy. Please note the extensive white matter signal alterations on T1 (5A) FLAIR (5B) and DWI (5C, D). There is extensive white matter diffusion restriction. MRF (5E, F) quantifies the regional signal changes on T1 (5E) and T2 (5F) maps,

indicating the relative sparing of the corticospinal tract and basal ganglia.

Using MRF-based quantification on T1 and T2 maps (Figure 6), regional variations in the pathology associated fingerprints can be identified. There is massive T1 and T2 shortening (turquoise) of the right frontal white matter. The optic radiation (pink) is less severely affected and the left corticospinal tract shows T2 (x-axis) and T1 (y-axis) values, which are in the normal range (compare Fig. 1). Combined with semiautomated segmentation tools (MR RoQT), this approach helps monitor disease progression and further refine specific disease-related patterns and fingerprints.



**5** A 6-year-old girl with glutaric aciduria. Extensive white matter signal alterations on T1 (5A) FLAIR (5B) and DWI (5C, D). MRF (5E, F) quantifies the regional signal changes on T1 (5E) and T2 (5F) maps indicating the relative sparing of the corticospinal tract and basal ganglia.



**6** MRF-based quantitative R1 (x-axis) and R2 (y-axis) values show a severe shortening of the right frontal WM (turquoise). The right optic radiation (pink) as well as the left occipital WM (red) are less affected. Normal-appearing R1 and R2 values can be found in the left corticospinal tract (yellow).

## Summary

MRF leads the way into a new era of neuro MRI. The possibility to provide multiple quantitative MR parameters based on a single data acquisition in less than 8 minutes results in quantitative data suitable for characterizing normal and pathologically altered tissue compartments of the central nervous system. As the regional neuroanatomical tissue diversity can be mapped non-invasively, MRF opens new possibilities in the non-invasive characterization of normal brain structure and its developmental changes across human lifespan. Further, pathological processes can be objectified and quantified, leading to greater confidence in the diagnosis of metabolic and neurodegenerative disorders. The extent of tissue pathology can be mapped and monitored over time, which is helpful in neurovascular disorders and inflammatory and/or demyelinating conditions. Lastly, disease-specific fingerprints of metabolic disorders and abnormal myelination processes are quantifiable and will be easier to identify. In the future, MRF will serve as an important backbone for artificial intelligence-based algorithms, aiming to automatically identify lesion-specific fingerprints. This will ultimately change the daily practice of neuroradiology.

## References

- 1 Ma D, Gulani V, Seiberlich N, Liu K, Sunshine JL, Duerk JL, et al. Magnetic resonance fingerprinting. *Nature*. 2013 Mar;495(7440):187–92.
- 2 Panda A, Mehta BB, Coppo S, Jiang Y, Ma D, Seiberlich N, et al. Magnetic resonance fingerprinting – An overview. *Curr. Opin. Biomed.* 2017 Sep;3:56–66.
- 3 Tippareddy C, Zhao W, Sunshine JL, Griswold M, Ma D, Badve C. Magnetic resonance fingerprinting: an overview. *Eur J Nucl Med Mol Imaging [Internet]*. 2021 May 26 [cited 2021 Aug 19]; Available from: <https://link.springer.com/10.1007/s00259-021-05384-2>
- 4 Körzdörfer G, Kirsch R, Liu K, Pfeuffer J, Hensel B, Jiang Y, et al. Reproducibility and Repeatability of MR Fingerprinting Relaxometry in the Human Brain. *Radiology*. 2019 Aug;292(2):429–437.
- 5 Dubois J, Alison M, Counsell SJ, Hertz-Pannier L, Hüppi PS, Benders MJNL. MRI of the Neonatal Brain: A Review of Methodological Challenges and Neuroscientific Advances. *J Magn Reson Imaging*. 2021 May;53(5):1318–43.
- 6 Badve C, Yu A, Dastmalchian S, Rogers M, Ma D, Jiang Y, et al. MR Fingerprinting of Adult Brain Tumors: Initial Experience. *AJNR Am J Neuroradiol*. 2017 Mar;38(3):492–9.
- 7 Cloos MA, Knoll F, Zhao T, Block KT, Bruno M, Wiggins GC, et al. Multiparametric imaging with heterogeneous radiofrequency fields. *Nat Commun*. 2016 Nov;7(1):12445.

## Contact

Associate Professor Gregor Kasprian, M.D., MBA  
 Department of Biomedical Imaging and Image-guided Therapy  
 Medical University of Vienna  
 Währinger Gürtel 18-20  
 1090 Vienna  
 Austria  
 Tel.: (+43) 1 40400 48950  
[gregor.kasprian@meduniwien.ac.at](mailto:gregor.kasprian@meduniwien.ac.at)



Gregor Kasprian



Victor Schmidbauer

Advertisement

## Learn more about Magnetic Resonance Fingerprinting

For technical explanations, articles, lectures,  
 imaging examples and much more  
 on MR Fingerprinting, visit us at

[magnetomworld.siemens-healthineers.com/  
 hot-topics/mr-fingerprinting](http://magnetomworld.siemens-healthineers.com/hot-topics/mr-fingerprinting)

*MR Fingerprinting is not commercially available in some countries.  
 Due to regulatory reasons its future availability cannot be ensured.*



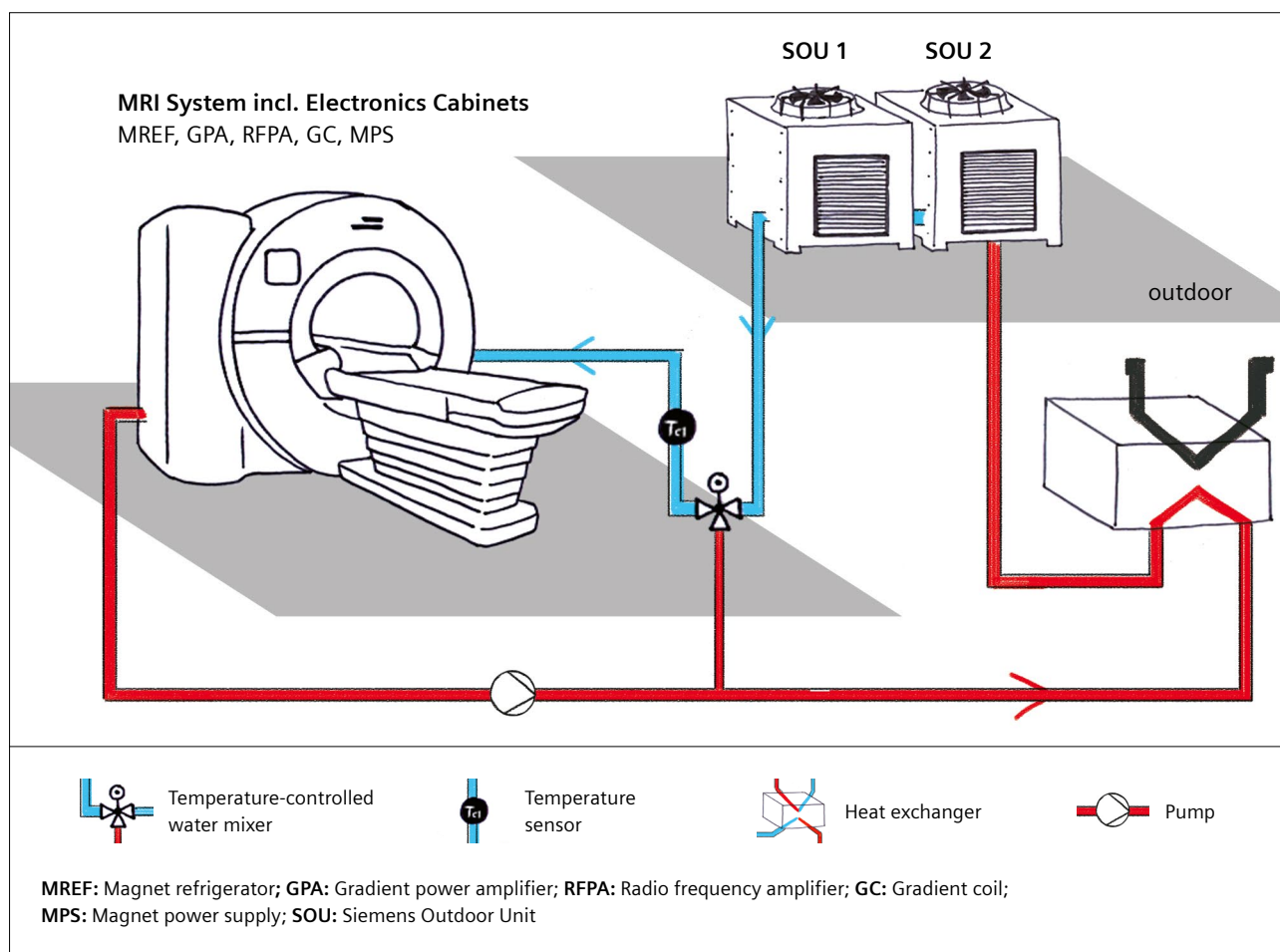
# MAGNETOM Free.Max: Keeping a Hot System Cool

Stephan Biber, Ph.D.

Senior System Architect & Principal Key Expert at Siemens Healthineers, R&D AEP, Erlangen, Germany

Helium is a rare element on Earth. Once released into the atmosphere, it is so lightweight that it leaves Earth's gravitational field and diffuses into space. DryCool technology, one of the key innovations on MAGNETOM Free.Max, reduces the helium demand in MR systems and removes the need to handle liquid helium during system installa-

tion. It also saves helium and prevents it from being released into the atmosphere during both normal system operation and failures such as quench events. However, the dramatic reduction of liquid helium to 0.7 liters contained in each MR magnet reduces the heat capacity of the magnet. If a conventional magnet loses cooling – e.g., due



**1** Active cooling system with external chillers.

to a power outage or a failure of the cooling system – the liquid helium slowly starts evaporating. Once a certain pressure threshold is exceeded (usually after less than 1 hour), the magnet loses helium into the ambient atmosphere. Depending on the filling level, a conventional magnet can stay cold by continuously evaporating its helium reservoir for many days without losing superconductivity. This is because the helium reservoir contains several hundred liters of helium. Reducing the helium down to less than 1 liter for DryCool magnets therefore also reduces the tolerance of such systems against infrastructure failures. The main types of failure are power outages and failures of the cooling system. This paper describes how MAGNETOM Free.Max can provide high availability of the MRI scanner despite a liquid helium inventory of only 0.7 liters.

## Power outages

Power outages are external events, out of control of the MRI system. The system can only react accordingly; it cannot avoid the situation itself. With DryCool technology, a small integrated uninterruptible power supply (UPS) keeps the magnet electronics running even during a power outage. If the power outage persists, the magnet electronics will ramp down the magnet after a certain waiting time in order to avoid a quench event, which would turn all the energy in the magnetic field into heat and warm up the system significantly. With MAGNETOM Free.Max, ramping the magnet down and then back up to field is now an automatic procedure which no longer requires an onsite visit from a service technician, due to the integrated magnet power supply. After a controlled ramp down, the magnet heats up very slowly. Once power returns, it can be recooled and ramped up again [1]. In regions where power reliability is poor, the system can also be buffered with a large UPS which not only keeps the system cold, but also enables continuous scanning even during brownouts or blackouts of the power grid.

## Cooling system failures

Unlike power outages, the reliability of the cooling system is very much under the control of the MRI system design. For an imaging modality like MRI, which relies so much on cooling, the reliability of the cooling system is essential for guaranteeing high availability of the MRI system. The MAGNETOM Free.Max cooling system was developed with the need for high reliability in mind from the very beginning. The following section explains the redundancy-focused architectural measures which were applied to MAGNETOM Free.Max.

A liquid helium temperature of 4 K is achieved using a cryocooler ("cold head") which is driven by a compressor. The compressor (magnet refrigerator = MREF) requires approximately 6–8 kW of power to generate ~1 W cooling power on the 4 K level. In order to ensure permanent operation of the compressor, which keeps the magnet cold, the MREF must be supplied with electricity and cooling water. Cold water for MAGNETOM Free.Max can be provided by two different options:

### Active cooling system

One option is to buy an external chiller which is tailored to operate with the MRI system. The flow diagram in Figure 1 shows that, in this case, the same water running through the MR components (MREF, gradient coil, amplifiers) is also running through the outdoor units SOU 1 and SOU 2. In such a configuration, the MRI system is self-contained and does not rely on any external water supply. This makes the setup very reliable because it avoids clogging of water flow or corrosion due to dirt and debris from external cooling water.

Chillers are located outside the building, often on rooftops or parking lots, where they use the ambient air to dissipate the heat from the MRI system. As they are located outdoors, chillers are exposed to all kinds of weather conditions: Temperatures can range from -20°C to +45°C, and dirt, dust, or leaves can block the heat exchangers. In highly reliable cooling systems, the outdoor units are a weak point in the chain. If an outdoor unit fails, the helium compressor will stop working and this will soon cause the magnet to ramp down. For the new DryCool technology, the chillers were designed with built-in redundancy to overcome this problem. During heavy-load scanning (mainly diffusion imaging) MAGNETOM Free.Max can



**2** Active cooling system with two ~17 kW Siemens Outdoor Units (SOU).

require up to 33 kW of cooling power, with demand primarily coming from the gradient system (coil and amplifier), the magnet cooling, and the RF amplifier. The cooling power is provided by two separate ~17 kW outdoor units (Siemens Outdoor Unit: SOU 1 and SOU 2; Fig. 2), which can work mostly independently from one another. During times when the system is in standby or scanning with less power-demanding sequences (TSE, GRE), only one of the two chillers is needed and the other one is turned off to save energy. If there is a failure with one of the 17 kW chillers, the second one automatically takes over to guarantee a permanent cold water supply and avoid a magnet ramp-down and the associated system downtime. The system can even continue scanning in this mode. Furthermore, during normal operation when one chiller is enough, the chillers are switched on and off in alternating mode to make sure both chillers are always operational and the energy consumption is optimized.

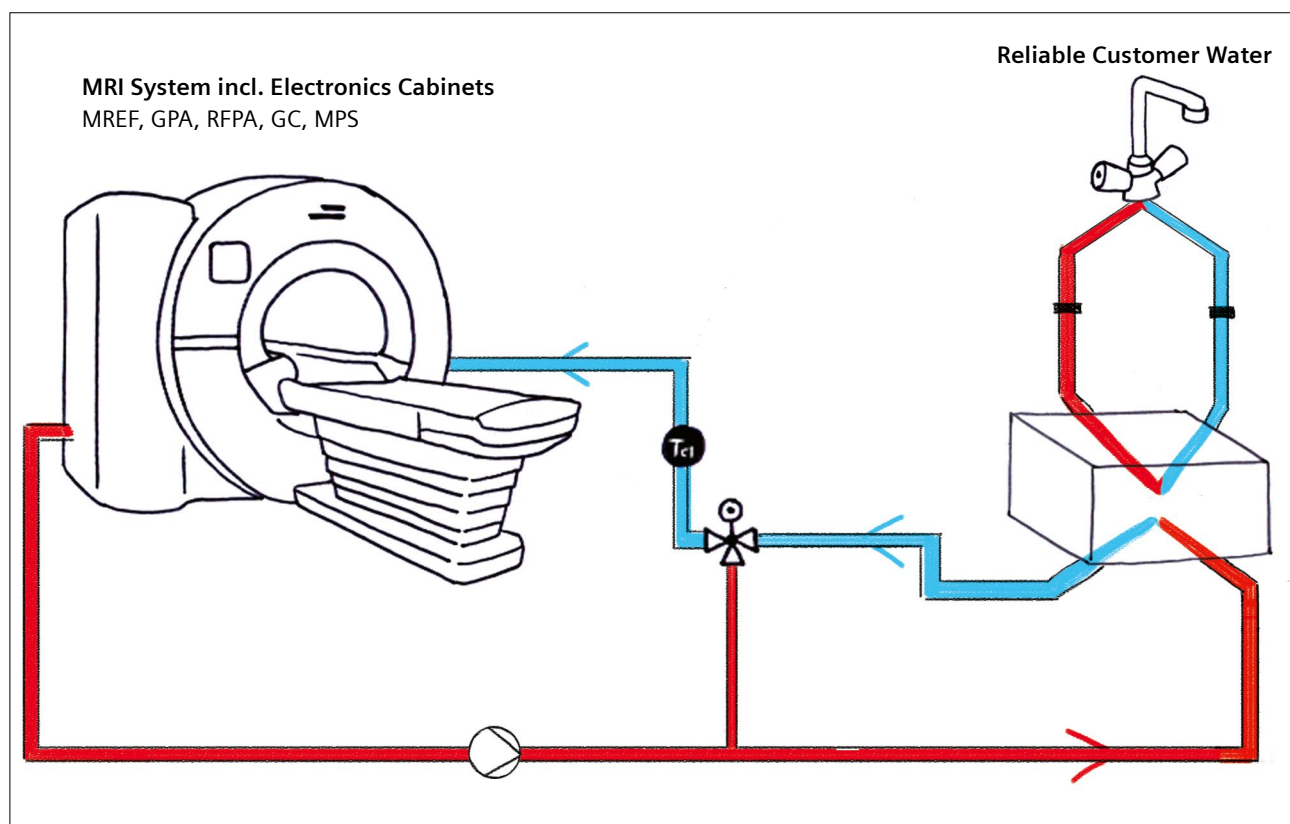
The splitting of the cooling modules requires little additional effort, as the 33 kW cooling power is needed anyway for system operation. This means that there is no extra cooling power added to provide redundancy for the magnet cooling, because the 6–8 kW required for magnet cooling is less than half of the total cooling power of a single unit. Redundancy can therefore be achieved just

by providing the overall cooling power from two separate units with half the total system power – without the need to install any unused cooling power, which would add extra effort and costs.

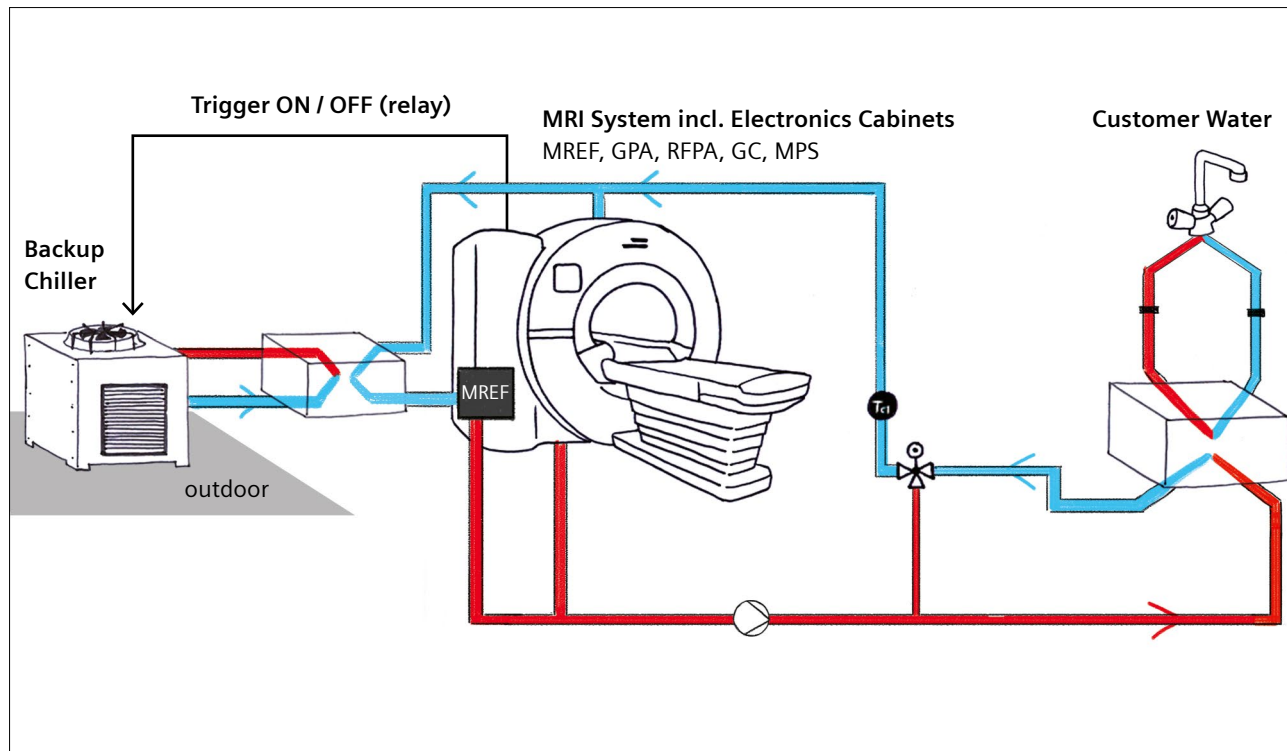
### Passive cooling system

In many large institutions, cooling water is centrally supplied and the MRI system can profit from the fact that no extra chillers are needed. The so-called “passive cooling option” cools the MRI system using a heat exchanger which separates the water provided by the central cooling supply from the water circulating through the MRI system components (Fig. 3A).

In cases where the central water supply from the hospital is not considered to be reliable enough, there is also a possibility to connect a locally sourced “backup chiller” to the system. This can provide the cooling power needed to keep only the magnet refrigeration running in case the central water supply fails. The cold water for the MREF coming from the backup chiller is provided to the system through an additional heat exchanger. The system automatically detects cases where the cooling power from the central water supply is insufficient and sends a signal to trigger the backup chiller (Fig. 3B).



**3A** Passive cooling system with reliable water from a central customer supply.



**3B** Passive cooling system with automatically triggered backup chiller.

## Remote monitoring and service

Despite the best efforts to ensure high reliability, cooling systems with high water flow rates and pressure – such as those used in MRI systems – require regular service. With the MR cooling system running 24/7, most failures (leakage, clogging, corrosion, dirt on outdoor units) can be detected and solved by qualified service personnel before they cause the system to stop working. Furthermore, the built-in cooling system is connected to our online service and all parameters available via sensors are also transmitted and evaluated online to allow remote diagnostics and preventive maintenance. In particular, the magnet refrigerator (MREF) is equipped with sophisticated temperature and pressure sensors. Preventive maintenance makes it possible to detect problems by watching the trends of these parameters over time. As a result, many problems can be detected before they lead to a complete failure of a component.

## Contact

Stephan Biber, Ph.D.  
Siemens Healthcare GmbH  
SHS DI MR R&D AEP  
Postbox 32 60  
91050 Erlangen  
Germany  
[stephan.biber@siemens-healthineers.com](mailto:stephan.biber@siemens-healthineers.com)



## Summary

The above overview shows how the system architecture, both for the cooling system and the system control, is tailored to deal with the new challenges of DryCool magnets and deliver maximum availability. Three different configurations are provided to achieve a high-reliability cooling system adapted to the individual needs and conditions of different sites. The basic principle is to provide redundancy for those parts that have an unacceptably high chance of failure. Combining this with remote monitoring, regular servicing, and automatic ramping guarantees extremely high availability for DryCool systems and independency of the scarce natural resource helium.

## Reference

- 1 Calvert S. MAGNETOM Free.Max: from Concept to Product, a Brief History of the DryCool Magnet Development. MAGNETOM Flash. 2021; MAGNETOM Free.Max special issue: 44–48.  
Available from: <https://www.magnetomworld.siemens-healthineers.com/hot-topics/lower-field-mri>

# Meet Siemens Healthineers

Siemens Healthineers: Our brand name embodies the pioneering spirit and engineering expertise that is unique in the healthcare industry. The people working for Siemens Healthineers are totally committed to the company they work for, and are passionate about their technology. In this section we introduce you to colleagues from all over the world – people who put their hearts into what they do.

## Cheng Shi, Ph.D.

I have a bachelor's degree in biomedical engineering from Tsinghua University. I earned my Ph.D. working under Professor Ed X Wu in the Laboratory of Biomedical Imaging and Signal Processing at the University of Hong Kong. After graduating, I joined SSMR in 2015 as a protocol developer.



Shenzhen, China



### How did you first come into contact with MRI?

I majored in biomedical engineering, so I learned a bit about MRI, CT, and PET in an introductory course on medical imaging techniques in my sophomore year in 2007. I was intrigued by MRI's lack of radiation, multi-functionality, and most of all the anatomical details it provides. But it was not until my third year, when I chose a course on MRI basics, that I really began to understand the terms "T1-weighted", "T2-weighted", and "k-space". I've been fascinated ever since. The first MRI system that I worked on was a Bruker 7T small animal scanner during my doctoral studies on subcortical visual function in rats. When I learned that Siemens Healthineers had developed an ultra-high 7T system for human studies, I was really impressed. But I wasn't surprised – I figured that if any company was going to do that, it would be Siemens Healthineers. Now that I'm part of Siemens Healthineers, I'm working to inspire the same confidence in other people. I hope that when our 0.55T MAGNETOM Free.Max hits the wider market, people also won't be surprised.

### What do you find motivating about your job?

The opportunities for self-improvement motivate me. As a protocol developer, I set up and test the protocols and workflows. Over the past five years, I've integrated many large and small application features to make the protocols faster and the workflow smarter. For example, one of the biggest challenges with MAGNETOM Free.Max is the lower SNR concomitant with lower field strength of 0.55T. A novel SMS averaging technique was developed by Dr. Liu Wei to improve SNR by taking advantage of

both the conventional SMS technique and the fact that MAGNETOM Free.Max requires multiple averages. While it is understood how this technique should help, it is up to me as a protocol developer to identify the best application scenarios – such as body regions, contrasts, and coil settings – and the optimal parameter settings to push its limits. I love the fact that we strive to improve for the benefit of our customers and ourselves, and for each and every product we develop.

### What are the biggest challenges in your job?

The biggest challenge is how to respond to MAGNETOM users' needs in the best possible way. Also, MAGNETOM Free.Max presented many challenges linked to the lower field strength. One of the main challenges I encountered was the SWI application. Ever since it was first published, SWI has been widely used for the detection of microbleeds and calcification. The longer echo time needed for the susceptibility effect proportional with field strength caused a further drop in SNR. I spent quite some time working on it until I had to conclude that optimizing the old GRE-based SWI was a dead end. But I didn't want to just give up on such an useful application. Supported by the whole application team and especially by Dr. Liu Wei, we developed an SWI sequence based on a partially flow-compensated 3D EPI sequence. Using the 3D technique greatly improved the SNR. Though it was not without its flaws, repeated volunteer testing in the factory and working on feedback from clinical sites led to the EPI-based SWI finally being provided. In the end, we have done our best to serve the users' needs by enabling SWI for MAGNETOM Free.Max.

### What are the most important developments in healthcare?

Medical imaging is one of the top ten medical advances and it has transformed healthcare. With MAGNETOM Free.Max, we have worked hard to make this revolutionary modality accessible to more people. With a lower field strength it is easy to install and promotes MR applications that profit from reduced susceptibility artifacts such as imaging in the presence of metal or lung imaging. Moreover, the new platform will further revolutionize healthcare by helping to network data and enable AI training based on big data.

### What would you do if you could spend a month doing whatever you wanted?

If I had a whole month, my first choice would be a meditation retreat. Ever since I read about it in a novel (can anyone guess what it is?), I've wanted to experience it for myself. I'd enjoy having the time to really focus on myself, on my breathing, and on observing myself without judgement. My second choice would be to take a trip with my children. Ideally, we'd all go to India for a meditation retreat together when they are old enough. Before that, I might choose to work for the month because the company gives me the flexibility to go home early (since I go to work early) and spend time with my kids. Also, I take part in the dance and yoga classes that are held in the company's gym with other kindred spirits every lunchtime. It's a very enjoyable daily routine. And by the way – the novel that inspired me to visit a meditation retreat is *Eat, Pray, Love* by Elizabeth Gilbert.

## Visit MAGNETOM World

Find more portraits of our colleagues around the world!

[www.magnetomworld.siemens-healthineers.com/meet-siemens-healthineers](http://www.magnetomworld.siemens-healthineers.com/meet-siemens-healthineers)

The collage consists of six portrait cards arranged in two rows of three. Each card features a grayscale map of a country with a black dot indicating the location, followed by the colleague's name in orange text and a small portrait photo.

- Melanie Habatsch**: Erlangen, Germany
- Emily Lucchese**: Melbourne, Australia
- Cordell Fields, Esq.**: Malvern, PA, USA
- Lars Filipsson**: Stockholm, Sweden
- Miguel Contreras**: Santiago, Chile
- Zhang Le, Ph.D.**: Shenzhen, China

The entire editorial staff at New York University, Grossman School of Medicine, USA and at Siemens Healthineers extends their appreciation to all the radiologists, technologists, physicists, experts, and scholars who donate their time and energy – without payment – in order to share their expertise with the readers of MAGNETOM Flash.

#### MAGNETOM Flash – Imprint

© 2021 by Siemens Healthcare GmbH,  
All Rights Reserved

##### Publisher:

**Siemens Healthcare GmbH**  
Magnetic Resonance,  
Karl-Schall-Str. 6, D-91052 Erlangen, Germany

##### Editor-in-chief:

Antje Hellwich  
(antje.hellwich@siemens-healthineers.com)

##### Guest Editor:

Jan Fritz, M.D., P.D., D.A.B.R., R.M.S.K.  
New York University, Grossman School of Medicine,  
NYU Langone Health, Department of Radiology,  
New York, NY, USA

##### Editorial Board:

Jane Kilkenny; Nadine Leclair, M.D.;  
Heiko Meyer, Ph.D.; Rebecca Ramb, Ph.D.;  
Wellesley Were

##### Review Board:

Gaia Banks, Ph.D.; André Fischer, Ph.D.; Daniel Fischer;  
Christian Geppert, Ph.D.; Maria Ringholz;  
Gregor Thörmer, Ph.D.

##### Copy Editing:

Sheila Regan, Jen Metcalf, UNIWORKS,  
[www.uni-works.org](http://www.uni-works.org)  
(with special thanks to Kylie Martin)

##### Layout:

Agentur Baumgärtner,  
Friedrichstr. 4, D-90762 Fürth, Germany

##### Production:

Norbert Moser,  
Siemens Healthcare GmbH

##### Printer:

G. Peschke Druckerei GmbH,  
Taxetstr. 4, D-85599 Parsdorf b. Munich, Germany

Note in accordance with § 33 Para.1 of the German Federal Data Protection Law: Despatch is made using an address file which is maintained with the aid of an automated data processing system.

MAGNETOM Flash is sent free of charge to Siemens Healthineers MR customers, qualified physicians, technologists, physicists and radiology departments throughout the world. It includes reports in the English language on magnetic resonance: diagnostic and therapeutic methods and their application as well as results and experience gained with corresponding systems and solutions. It introduces from case to case new principles and procedures and discusses their clinical potential. The statements and views of the authors in the individual contributions do not necessarily reflect the opinion of the publisher.

The information presented in these articles and case reports is for illustration only and is not intended to be relied upon by the reader for instruction as to the practice of medicine. Any health care practitioner reading this information is reminded that they must use their own learning, training and expertise in dealing with their individual patients. This material does not substitute for that duty and is not intended by Siemens Healthcare to be used for any purpose in that regard. The drugs and doses mentioned herein are consistent with the approval labeling for uses and/or indications of the drug. The treating physician bears the sole responsibility for the diagnosis and treatment of patients, including drugs and doses prescribed in connection with such use. The Operating Instructions must always be strictly followed when operating the MR system. The sources for the technical data are the corresponding data sheets. Results may vary.

Partial reproduction in printed form of individual contributions is permitted, provided the customary bibliographical data such as author's name and title of the contribution as well as year, issue number and pages of MAGNETOM Flash are named, but the editors request that two copies be sent to them. The written consent of the authors and publisher is required for the complete reprinting of an article.

We welcome your questions and comments about the editorial content of MAGNETOM Flash. Please contact us at [magnetomworld.team@siemens-healthineers.com](mailto:magnetomworld.team@siemens-healthineers.com)

Manuscripts as well as suggestions, proposals and information are always welcome; they are carefully examined and submitted to the editorial board for attention. MAGNETOM Flash is not responsible for loss, damage, or any other injury to unsolicited manuscripts or other materials. We reserve the right to edit for clarity, accuracy, and space. Include your name, address, and phone number and send to the editors, address above.

---

**MAGNETOM Flash is also available online:**

**[www.siemens-healthineers.com/magnetom-world](http://www.siemens-healthineers.com/magnetom-world)**

Not for distribution in the US

On account of certain regional limitations of sales rights and service availability, we cannot guarantee that all products included in this brochure are available through the Siemens sales organization worldwide. Availability and packaging may vary by country and is subject to change without prior notice. Some/All of the features and products described herein may not be available in the United States.

The information in this document contains general technical descriptions of specifications and options as well as standard and optional features which do not always have to be present in individual cases, and which may not be commercially available in all countries.

Due to regulatory reasons their future availability cannot be guaranteed. Please contact your local Siemens organization for further details.

Siemens reserves the right to modify the design, packaging, specifications, and options described herein without prior notice. Please contact your local Siemens sales representative for the most current information.

Note: Any technical data contained in this document may vary within defined tolerances. Original images always lose a certain amount of detail when reproduced.

---

#### **Siemens Healthineers Headquarters**

Siemens Healthcare GmbH

Henkestr. 127

91052 Erlangen, Germany

Phone: +49 9131 84-0

[siemens-healthineers.com](http://siemens-healthineers.com)